Structure Prediction in Materials Science and characterisation with EELS in the low-loss regime

A thesis submitted for the degree of

Doctor of Philosophy in Materials

Xinlei Liu

St Edmund Hall College

University of Oxford

Trinity 2023

Abstract

Electron Energy Loss (EEL) spectroscopy is a complementary spectroscopic method that is adopted in (scanning) transmission electron microscope ((S)TEM). The low-loss region of the corresponding Electron Energy Loss spectrum (EELS) is associated with plasmon excitation. It is closely related to the optical properties of the sample and can reveal a wealth of crystallographic information, such as structures and bondings. To fully interpret experimental EELS, it is vital to develop a protocol to accurately simulate EELS.

This thesis focuses on enhancing the accuracy of computationally modelled EELS, especially in the low-loss region. Within the density functional theory (DFT), several functionals are tested: the Becke-Johnson functional (BJ), the Tran-Blaha functional (TB), and the SCAN functional. The functionals are reported to provide better descriptions of the excited properties of materials but have not been thoroughly studied in the context of EELS modelling. Beyond DFT, we employ the time-dependent DFT (TDDFT) and state-of-art GW method combined with the Bethe-Salpeter Equation (BSE) method. In addition, we also apply the method to a case study of the corrosion products of beryllium tiles from nuclear reactors. During this study, we have found a new approach to simulate the core-loss spectrum of beryllium. The approach could potentially be applied to other elements with semi-core electrons, such as lithium.

List of Publications and Presentations

Xinlei Liu, Carmen Makepeace, Rebecca Nicholls, Sergio Lozano-Perez, Jonathan Yates, *Beryllium Corrosion within the JET Tokamak*, Poster presented at MMM Hub Conference and User Meeting 2019

Xinlei Liu, Carmen Makepeace, Rebecca Nicholls, Sergio Lozano-Perez, Jonathan Yates, *Understanding the degradation of Be tiles in the JET tokamak reactor using EELS and DFT*, Poster Flash Talk and presentation in the Energy and Energy Storage Materials (EMAG) session at Microscience Microscopy Congress 2021

Xinlei Liu, Carmen Makepeace, Anna Widowson, Sergio Lozano-Perez, Jonathan Yates, Rebecca Nicholls, *Electron energy loss spectroscopy as a tool to distinguish between different beryllium compounds*, in preparation

Xinlei Liu, Rebecca Nicholls, Jonathan Yates, *A new pseudopotential approach to model the core-loss EELS with valence holes*, in preparation

Acknowledgements

Above all, I would like to express my heartfelt gratitude to my supervisors, Jonathan Yates and Rebecca Nicholls, for granting me the opportunity to continue my studies at Oxford after my undergraduate. Throughout my DPhil journey, I have received an immeasurable amount of support and guidance from both of them. Words cannot adequately convey how grateful I am, particularly in the face of the unexpected disruptions caused by the Covid-19 pandemic.

I extend my sincere thanks to my scientific collaborators, Sergio Lozano-Perez and Carmen Makepeace, for their invaluable assistance with the experimental data.

I am deeply appreciative of my parents, Lijin Zhao and Yong Liu, for their unwavering encouragement and understanding. Their steadfast support has served as the bedrock upon which I have constructed my academic pursuits.

In addition, I would like to acknowledge my girlfriend, Xuanli Sun, with profound gratitude. Her patience, understanding, and unwavering belief in me have provided an enduring wellspring of strength.

Contents

Abstract **i**

Acknowledgements **iii**

1 Introduction **1**

1.1 Summary of the Thesis 2

2 Introduction to Electron Energy Loss Spectroscopy **5**

2.1 Electron Microscopes 5

2.2 EEL Spectrum 9

2.3 Inelastic Scattering 10

2.4 Plasmon Excitation 11

2.5 Single-electron Excitation and Excitons 13

2.6 Core-electron Excitation 14

2.7 ELNES and EXELFS 15

2.8 Processing of the Experimental Data 17

2.8.1 Zero-loss Peak Removal 17

2.8.2 Background Subtraction 17

2.8.3 Deconvolution 18

3 Previous Approaches to Model EELS **20**

3.1 Core-loss EELS 21

3.1.1 The Effect of Core Hole 24
3.2 Low-loss EELS 26
3.2.1 Motivations 29

4 Density Functional Theory and Beyond 31
4.1 Density Functional Theory 32
4.1.1 Many-body Schrödinger Equation 32
4.1.2 The Hohenberg and Kohn Theorem 33
4.1.3 Kohn-Sham Equations 34
4.1.4 Exchange and Correlation 37
4.2 Time-Dependent Density Functional Theory 43
4.3 GW Approximation 43
4.3.1 The Single-particle Green's Function 44
4.3.2 Dyson's equation 46
4.3.3 Self Energy and Quasi-particle 48
4.3.4 Hedin's equations 50
4.4 Practical Calculations 53
4.4.1 Convergence in DFT 54
4.4.2 Convergence in GW 58

5 The Theory of EEL Spectrum Modelling 61
5.1 Density of States (DOS) 62
5.2 Dielectric Function 63
5.2.1 Independent Particle Approximation 64
5.2.2 Macroscopic Dielectric Function 65
5.2.3 The Local Field 66
5.2.4 Random Phase Approximation 68
5.2.5 Linear-response Theory 70
5.2.6 Bethe-Salpeter Equation 73

5.3 Predicted Transition Energy 77
5.4 Practical Calculations 78
5.4.1 Convergence in IPA 79
5.4.2 Convergence in RPA with LFE 80
5.4.3 Convergence in Linear-response TDDFT 81
5.4.4 Convergence in BSE 82
5.4.5 Energy Broadening 83
5.5 Computational Details 84
5.5.1 Example of Convergence Tests 84
5.5.2 Computational Setup for Chapters 5 and 6 88
5.5.3 Computational Setup for Chapter 7 90
5.5.4 Computational setup for Chapter 8 92

6 Case Study - System Containing Beryllium Oxides 99

6.1 Beryllium in the fusion reactor 100
6.2 Candidate Structures 101
6.3 Benchmark - The As-Received Sample 102
6.4 Beryllium Samples from JET 106
6.4.1 Eroded Outer Wall Sample 108
6.4.2 Eroded Inner Wall Sample 111
6.4.3 Deposited Inner Wall Sample 112
6.4.4 Melted Upper Dump Plate Sample 113
6.5 Summary 114

7 A New Approach to Model Core-loss EELS for Be 116

7.1 A Brief Outline of the Methodology 118
7.2 Accuracy of the Modified Pseudopotential 121
7.3 EELS Modelling using the New Approach 124
7.4 Predicted Transition Energy 127

7.4.1 Costs of Calculations . . . 131
7.5 Summary . . . 132

8 Simulating EELS within DFT 134

8.1 Geometry Optimisation . . . 135
8.2 Band Structures . . . 137
8.3 Low-loss EELS within IPA . . . 144
8.3.1 Diamond . . . 144
8.3.2 Graphite . . . 145
8.3.3 LiF . . . 147
8.3.4 Silicon . . . 148
8.3.5 Rutile . . . 149
8.3.6 Monoclinic ZrO_2 . . . 151
8.3.7 Hexagonal and Orthorhombic ZrO . . . 153
8.3.8 Costs of Calculations . . . 156
8.4 Summary . . . 157

9 Simulating EELS Beyond DFT 159

9.1 Low-loss EELS with LFE . . . 160
9.1.1 Non-transition Elements . . . 162
9.1.2 Transition Elements . . . 166
9.2 Low-loss with TDDFT . . . 167
9.3 Low-loss EELS with GW + RPA . . . 171
9.4 Low-loss with GW+BSE . . . 175
9.4.1 Diamond . . . 176
9.4.2 LiF . . . 177
9.4.3 Silicon . . . 178
9.4.4 Rutile . . . 179
9.5 Costs of Calculations . . . 180

9.6 Summary 182

10 Conclusions **184**

10.1 Summary 184

10.2 Outlook 186

Bibliography **188**

Chapter 1

Introduction

In a scanning transmission electron microscope (STEM), a beam of electrons of known energy is focused onto a specimen. The electrons interact with the specimen and during the interaction, some of them lose energy (inelastic) while others do not (elastic). The resulting energy distribution of a beam of electrons is measured using Electron Energy Loss (EEL) spectroscopy and is presented as an Electron Energy Loss spectrum (EELS) [1, 2]. The spectrum can be divided into three regions based on the energy range and among them, the most relevant ones for this thesis are the low-loss region which is associated with the plasmon excitation (up to about 50 eV) and the core-loss region related to the core-electrons excitation (from 10 up to 1000s eV). The core-loss region has consistently garnered significant research interest [3–17]. Nevertheless, the low-loss region also contains additional information about the materials. It can offer supplementary crystallographic information not provided by the core-loss region, e.g. the ZrO phase at zirconium/zirconium oxide interfaces [18].

To better interpret experimental EELS, a precise theoretical description of the optical properties of materials is necessary, in order to generate accurate computationally modelled EELS. A literature review regarding different levels of methods

to model the core-loss and the low-loss regions of EELS is given in the later chapter. The quantum-mechanical methods investigated in this thesis are based on the fact that the experimental EELS is closely related to the dielectric function, which provides a possible route for the simulation. The low-loss region requires the description of the full dielectric function while the core-loss region can be approximated using the imaginary part of the dielectric function. The most widely adopted method to simulate EELS is based on the density functional theory (DFT), which although being a ground-state theory, is capable of reproducing some experimental features of EELS. Since the excitation of either plasmons or the core-electrons is associated with the excited properties of the material, there is a question as to whether standard static DFT is an appropriate level of theoretical treatment or if more advanced theories are needed.

This thesis mainly focuses on improving the simulated low-loss region of EELS, together with a case study of a system containing beryllium oxides that is used in nuclear reactors and a new approach to simulate the beryllium K-edge spectrum.

1.1 Summary of the Thesis

The thesis is organised into 10 chapters, including this introduction. Chapter 2 discusses aspects of experimental EEL spectroscopy and the methods needed to post-process the data. The different scattering processes behind each region and how they are influenced by the local bonding environment are illustrated. Chapter 3 is a literature review of previous approaches used to model EELS, both for the core-loss and low-loss regions. The motivation of the research work presented in thesis is shown at the end of Chapter 3.

Chapters 4 and 5 discuss the theoretical background of the computational methods used throughout the studies presented in this thesis. Chapter 4 mainly focuses

on the theories of DFT and methods beyond static DFT. One notorious problem of DFT is the underestimation of the band gap, which is closely related to the single-electron excitation peak that is observed in the low-loss region. Outer-shell electrons (valence electrons), after absorbing enough energy from the incident electron, are excited across the band gap to the conduction band. Thus to begin with, a series of new functionals within DFT that are reported to predict better band gaps are introduced. In addition, to go beyond DFT, time-dependent DFT (TDDFT) and the GW method based on the single particle's Green's function are tested. At the end of Chapters 4 and 5, the technical details required for practical calculations are also discussed and the computational details of the calculations are presented.

Other than the band gap, another problem with calculating electron excitations is related to the challenging problem of describing the electron correlation and the electron-hole interaction. Chapter 5 starts with methods of calculating the density of states (DOS), followed by different levels of methods to deal with the electron correlation that is crucial for EELS modelling. The simplest independent particle approximation is based on the assumption that electrons and holes do not interact at all. The first level of including the correlation is the so-call local-field effect (LFE), which takes the fluctuation of the polarisation of the system into account. In addition, the linear-response theory for TDDFT and the Bethe-Salpeter Equation (BSE) method that runs on top of GW calculations will be covered.

Chapter 6 is a case study of the application of simulated and experimental EELS to explore the corrosion products of beryllium tiles that were used in a nuclear fusion reactor. Both the low-loss and core-loss regions of EELS are modelled and compared with the experimental spectra of samples taken from different parts of the Joint European Torus (JET) tokamak. During this study, the fact that the

pseudopotential of beryllium has all four electrons explicitly described as valence electrons (a pseudised all-electron potential) led to a new approach to simulate the Be K-edge of the core-loss EELS. Chapter 7 will be dedicated to that new method.

In Chapter 8, the results of simulating EELS, within independent particle approximation and using functionals within DFT will be presented and are compared to the spectra calculated with the standard PBE functional. Chapter 9 discusses the state-of-art methods to simulate EELS, by either going beyond DFT (excited-state method) or involving more electron-hole interactions in the calculation, or using combined methods. Finally, Chapter 10 will present the conclusion of this thesis.

Chapter 2

Introduction to Electron Energy Loss Spectroscopy

In this chapter, I am going to illustrate the physics of Electron Energy Loss (EEL) spectroscopy. In particular, the theoretical background to how energy is lost when the incident electrons pass through samples in a transmission electron microscope (TEM). This chapter starts with an introduction to the EEL spectroscopy. Then we focus on the low-loss and core-loss peaks and the associated techniques required to process the experimental data.

2.1 Electron Microscopes

Transmission Electron Microscopy (TEM) is an experimental technique that reveals structure details at the atomic scale using a beam of electrons. There are two major types of TEM instruments: the conventional TEM and the scanning transmission electron microscope (STEM). A TEM is composed of five major parts: a high-voltage electron source, the microscope column, a vacuum system, the detectors, and the control computers.

The vacuum system is needed to ensure that the electron beam only interacts with the sample. As for the electron source, there are mainly two families: thermionic electron sources and field emission electron sources. Thermionic electron sources rely on the principles of thermionic emission, where electrons are emitted when the material is heated to a high temperature. Tungsten filament and LaB6 (Lanthanum Hexaboride) crystal are examples of such sources. The field emission electron sources are based on field emission, where electrons are emitted from a sharp metal tip in the presence of a strong electric field. Examples involve a Schottky source that uses a heated tungsten tip and a cold field emission source that adopts a cold tungsten tip. Different electron sources result in different energy resolutions and brightness. For the thermionic electron sources, the typical energy width ranges between 1 and 2 eV and the brightness is low. For field emission electron sources, the energy width ranges from 0.3 to 0.7 eV. Schottky field emitters combine a high brightness with relative stability compared to thermionic emitters and the highest brightness and lowest energy spread is offered by the cold field emission gun, with an energy spread of 0.3 eV or lower [2, 19].

The microscope column is composed of sets of electromagnetic lenses and apertures to focus the electron beams down to the atomic scale and magnify them to get an image. Electromagnetic lenses are made of copper wire coils surrounded by ferromagnetic materials. When current passes through the coils, a magnetic field is created within the column and is concentrated into a small region by the ferromagnetic materials. Apertures are circular holes in thin strips of heavy metal, limiting the amount of electrons striking the specimen and the x-ray generation.

The microscope column can be further split into three parts: the condenser lens system, the objective lens system, and the projector lens system. The condenser lens system is responsible for primary beam formation, which takes the electron

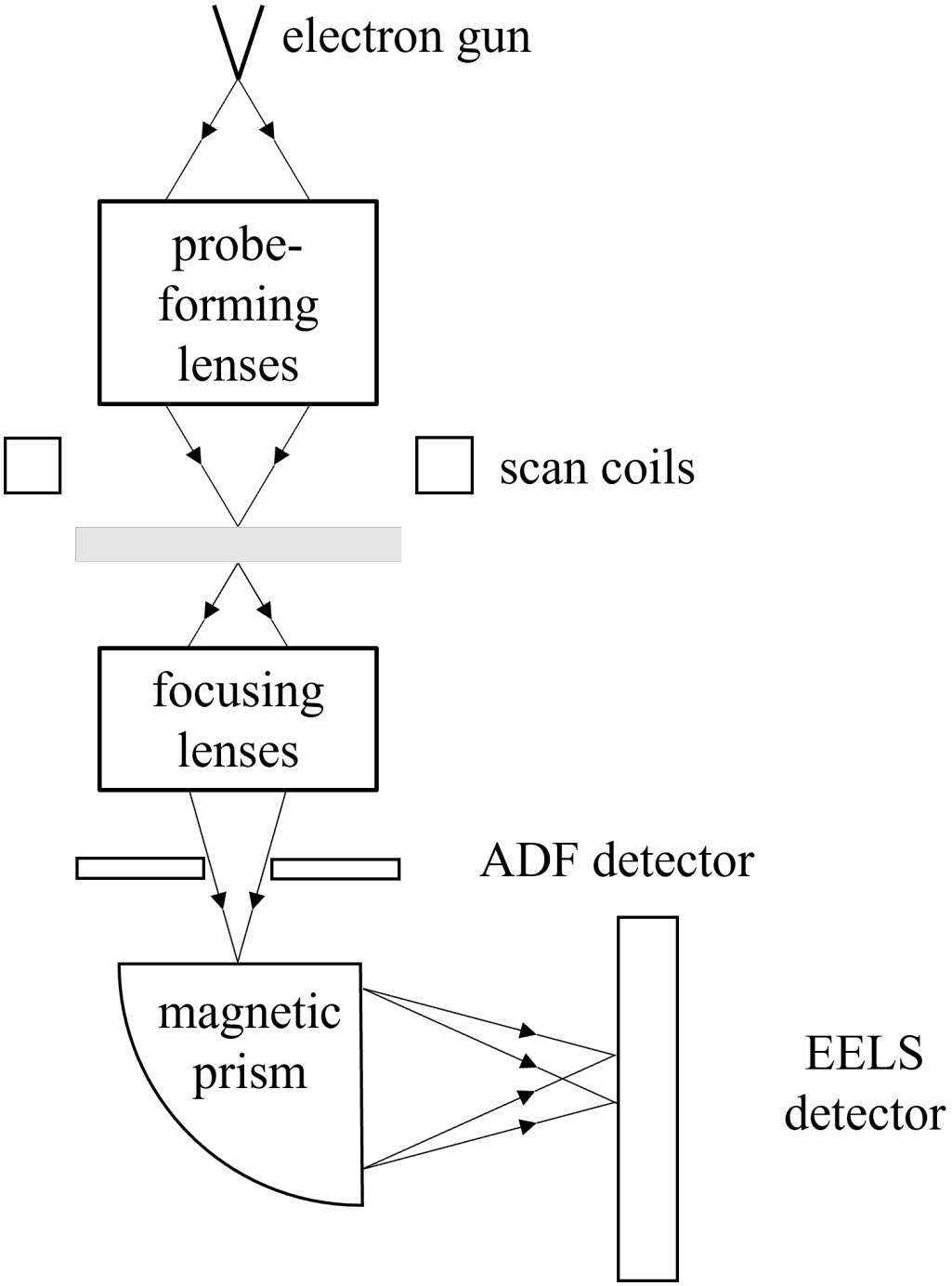


Figure 2.1: Schematic of electron energy-loss spectroscopy (EELS) experiment in a scanning transmission electron microscope (STEM).

beam from the electron source and guides it to the sample. In conventional TEM mode, the condenser lenses are adjusted to form a broad and parallel beam at the sample. The objective lens below the specimen is used to produce the intermediate images and diffraction patterns that are further magnified by the projector lens. The overall magnification of the TEM is determined by the combined magnifications of the objective, intermediate, and projector lenses. In STEM mode, however, a convergent beam is required and it is formed by using an objective lens above the sample, and the images are formed by scanning. A simplified STEM diagram is shown in Figure 2.1 [2, 19].

The key part of TEM-EELS instrumentation is a spectrometer based on a magnetic prism. Within the magnetic field, electrons are deflected by about 90 degrees and then dispersed according to their different kinetic energies. The spectra are then recorded with a charge-coupled device (CCD camera) [1, 2, 20].

The energy resolution of an EEL spectrum is limited by several factors. Firstly, as discussed earlier, it is determined by the electron source used. The intrinsic energy spread of the electrons emitted by the electron source significantly affects the energy resolution. Secondly, the aberrations of the electron spectrometer are also crucial and are directly related to the ability of the spectrometer to focus and separate electrons of different energy losses accurately. The adoption of a combination of a magnetic prism with curved edges and weak multipole lenses helps design the aberration-corrected spectrometers [2, 21]. Thirdly, the energy resolution can be further improved by monochromation, in which an energy filter is inserted after the electron source. The energy resolution of EELS carried out in the latest electron microscope is around 10 meV [22].

2.2 EEL Spectrum

As shown in Figure 2.2, an EEL spectrum is mainly composed of three regions: the zero-loss peak (region 1),the low-loss region (region 2) and the core-loss region (region 3).

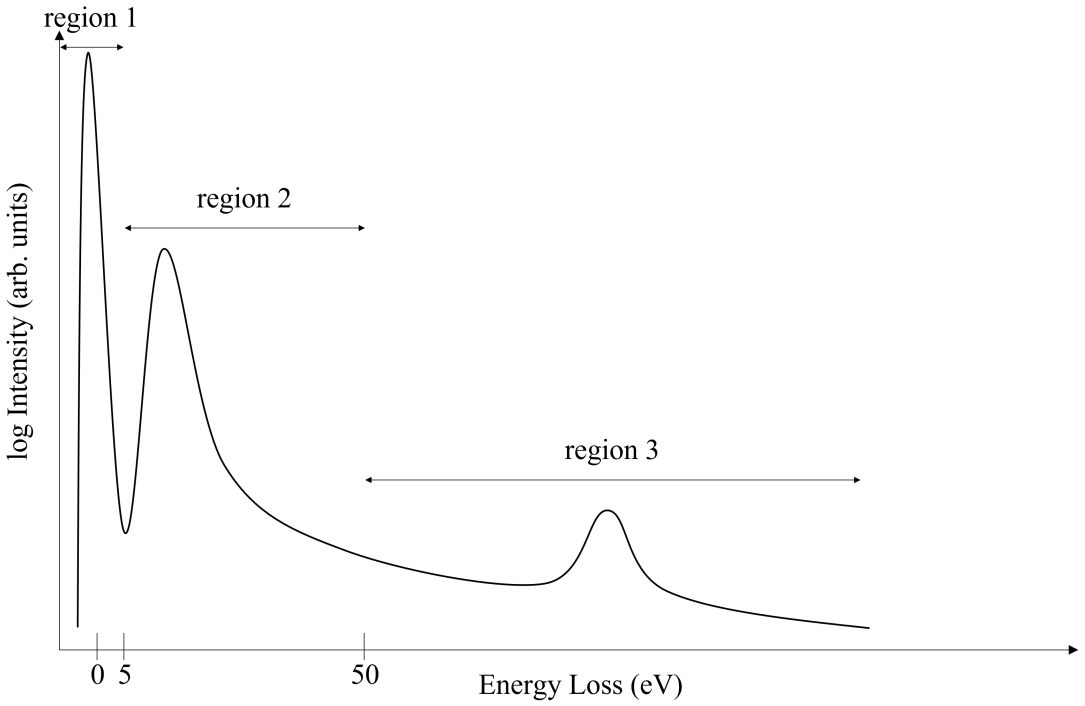


Figure 2.2: Schematic representation of a typical EEL spectrum.

The zero-loss peak represents the transmitted electrons and elastically scattered electrons for which the energy transfer is negligible. However, since experimentally there exists an energy resolution limit, the zero-loss region also involves electrons that are quasielastically scattered, with energy loss less than the limit. And thus, the width of the zero-loss peak defines the resolution of the spectrum [1, 2]. Beyond the zero-loss peak and up to hundreds of meV, there exist phonon peaks as a result of atomic vibrations. With the advent of the latest generation of TEM, phonon vibrations have become observable using EEL spectroscopy [22]. In this thesis, we limit our discussion of EEL spectroscopy to only the low-loss and core-loss regions and further reading regarding the phonon spectroscopy can

be found in [23].

The low-loss region, also regarded as the plasmon peak, is caused mainly by the oscillation in the electron cloud of the solid. In addition to the collective response, single-electron excitations are also possible and add fine-structure peaks to the plasmon peaks. The low-loss region can be used to determine the electrical and optical properties of the sample (e.g. band structure, band gap) and it also gives crystallographic information such as bonding [1, 2].

The core-loss region is composed of ionisation edges as a result of core-electron excitations. The core-loss edges are superimposed on a background consisting of the tails of the zero-loss peak, the plasmon peaks, and those from ionisation edges with lower threshold energies and energy loss due to the bremsstrahlung radiation. And thus one of the major difficulties in experimental EEL spectroscopy is to extract information about the weak core-loss edges. Specific procedures to process the raw experimental data are needed which are discussed further in this chapter. The core-loss region gives information about which elements occur within the sample. For very thin specimens, the edges also inform the relative concentration of corresponding elements [1, 2].

2.3 Inelastic Scattering

Both the low-loss and the core-loss regions of EELS correspond to the inelastic scattering where the kinetic energy of the incident electron is not conserved. It occurs when the incident electrons interact with the atomic electrons surrounding the nucleus. The inelastic scattering can be divided into two types: inner-shell electron excitation and outer-shell electron excitation. The first type occurs when an inner-shell electron, after absorbing an amount of energy from the incident electron, makes an upward transition to a higher energy level (interband transition) and leaves a vacant core hole. It contributes to the core-loss region in

EELS (50 eV or more). The outer-shell electron excitation which dominates in the low-loss region in EELS (a few eV or tens of eV), can be further divided into two types: single-electron excitation and many-electron excitation. As for single-electron excitation, an electron could either undergo interband transition across the band gap (insulators or semiconductors) or to a higher energy state (metals) or intraband transition within the same energy level (metals). A many-electron excitation, usually known as plasmon excitation, is a collective oscillation of the electron density which is prominent in many solids [2, 24].

2.4 Plasmon Excitation

The plasmon excitation results from the fact that the outer-shell electrons are only weakly bound to the atoms. As a result, in the simplest situation, they behave as free particles, constituting a free electron gas. However, they are also coupled to each other via electrostatic forces and can be considered as a set of coupled oscillators. When an incident electron passes through the electron sea, it repels the atomic electrons close to it and thus leaves a positively charged region behind it (a correlation hole). This positively charged region exerts a backward attraction force on the incident electron and results in energy loss. This process can be interpreted as the creation of pseudoparticles known as plasmons and the energy loss is known as plasmon loss. The movement of atomic electrons is oscillatory and thus plasmons are defined as collective oscillations of the free electron gas density. The plasmon generation at each inelastic scattering event denotes a peak shown in EELS [2, 25].

Similar to the electric field created by the incident electron, an electromagnetic wave incident onto the specimen will also generate plasmons. In other words, the EELS of a material is closely related to its optical properties. The optical constants of a material can be described by the dielectric function ϵ [2, 25]:

$$\varepsilon = \varepsilon_1 + i\varepsilon_2 \tag{2.1}$$

which is a measure of how a material responds to an electric field. Its real part ε_1 indicates the degree to which a material can be polarised while the imaginary part ε_2 is associated with the dielectric losses.

The energy loss function is related to the complex permittivity by [2, 25]:

$$\mathrm{Im}\left[\frac{-1}{\varepsilon}\right] = \mathrm{Im}\left[\frac{-1}{\varepsilon_1 + \mathrm{i}\varepsilon_2}\right] = \frac{\varepsilon_2}{{\varepsilon_1}^2 + {\varepsilon_2}^2} \tag{2.2}$$

And thus experimentally, information obtained from EELS intensity in the low-loss region (plasmon peaks), combined with Kramers-Krönig relation [26], produces the real part and hence the full function (complex permittivity) [2, 25, 27]. Theoretically, it also provides a route for the low-loss region to be simulated, which is the key to this project. The dielectric function will be discussed further in later chapters. Other applications of the Kramer-Krönig relation in EEL spectroscopy involve the determination of the sample thickness and further reading can be found in [28–30].

Other than the bulk plasmon, before the incident electron enters the bulk sample, its electric charges also polarise the surface and generate surface-charge waves. This kind of phenomenon is called surface plasmon excitation. As a result, additional peaks can be seen at a lower energy than the volume plasmon excitation. For example, for a dielectric/metal boundary, the energy loss due to surface plasmon is inversely proportional to $(1 + \varepsilon_1)^{\frac{1}{2}}$. In the simplest case that the interface is between a vacuum and a free electron metal, $\varepsilon = 1$ and thus the energy is reduced from the bulk value by a factor of $2^{\frac{1}{2}}$ [2, 24, 25, 31].

2.5 Single-electron Excitation and Excitons

A competing phenomenon to plasmon excitation is single-electron excitation, which involves the direct transfer of energy from an incident electron to a single atomic electron. One obvious effect of the interband transitions is the addition of fine-structure peaks above or below the plasmon peaks. The spectral intensity of the fine-structure peaks is related to the band structure and the corresponding joint density of states [2, 24]. In semiconductors or insulators, in addition to the interband transition from the top of the valence band to the bottom of the conduction band, there are also transitions from the valence band top to a Rydberg series of states which lie just below the bottom of the conduction band. Such states are caused by excitons which are coupled excited electrons in the conduction band and electron holes in the valence band. The energy difference between the bottom of the conduction band and the exciton states is given by the exciton binding energy. As a result, additional peaks are seen below the bandgap energy known as the exciton peaks [2, 24, 25].

Other than the fine-structure peaks, the single-electron excitation also causes the broadening of plasmon peaks. In materials such as alkali metals and silicon, sharp plasmon peaks can be seen. However, in materials such as carbon and organic compounds, the plasmon peaks are broader as a result of plasmon damping. The damping is caused by the transfer of the plasmon energy to single-electron excitation and is more predominant in materials where the valence electrons are more tightly bound [2, 24, 25]. Another important effect of the single-electron excitation is the shifting of the peaks due to polarisation. If interband transitions occur at an energy below the plasmon energy, the polarisation of the bound electrons makes it hard for free electrons to return to their equilibrium position, and thus increases the resonance energy, and the plasmon peak is shifted to higher energy [2, 24, 32].

2.6 Core-electron Excitation

A core-electron excitation is a result of the inelastic interaction between an incident electron with an inner-shell electron which lies on an energy level hundreds or thousands of eV below the Fermi level. During the interaction, the inner-shell electron absorbs the specific amount of energy and is excited to the unoccupied states above the Fermi level. Due to energy conservation, an equal amount of energy is lost by the incident electron. The fact that an electron near the core (nucleus) is excited gives the name core-loss to the high-energy region of EEL spectroscopy [2].

Electrons in atomic states are defined by four quantum numbers: Principal quantum number (n), Azimuthal quantum number (l), Magnetic quantum number (m) and Spin quantum number (s). The principal quantum number describes the size of the orbitals. As n increases, the number of electron shells increases and the electron is further away from the nucleus and thus less tightly bonded. The principal quantum number 1-5 is represented by K, L, M, N and O and each level has energy [2]:

$$E_n = -R(Z - \sigma_n)^2/n^2 \tag{2.3}$$

where R is the Rydberg energy (13.6 eV) and $Z - \sigma_n$ is the effective atomic number including the effect of electron screening. Thus core-electron binding energies are different for each element and each shell. The core-loss edges can hence be used to identify elements present in the sample. As each ionisation edge is on top of a downward-sloping background caused by other energy-loss processes, if the background is subtracted appropriately, the intensity can give information regarding how much of each element is present in the sample.

The Azimuthal (angular) quantum number describes the shape of the orbitals.

There are l=0, 1, 2, ...n-1 possible values which are denoted by s, p, d, f, etc. The magnetic quantum number describes the orientation in space of a particular orbital. The value of m can range from $-l$ to l in integer steps including 0 and thus there are 1, 3, 5, 7 orbitals in each s, p, d, f subshell. The fact that electrons are self-rotating gives the fourth quantum number s which describes the intrinsic spin angular momentum of electrons. It has value $\frac{1}{2}$ and $-\frac{1}{2}$ which represent upward and downward spin respectively. The total angular momentum quantum number $j = s + l$ cannot be negative. And thus for a 2s electron, $l = 0$ and only $j = \frac{1}{2}$ can be found while for a 2p electron, $l = 1$ and j can be $\frac{1}{2}$ or $\frac{3}{2}$. The p orbital is thus further divided into $\mathrm{p}_{\frac{1}{2}}$ and $\mathrm{p}_{\frac{3}{2}}$ with energy difference due to spin-orbit coupling. The results split the L shell into three subshells L_1, L_2 and L_3 and the core-loss edges on EEL spectrum are labelled according to where the electrons being excited originated from [25].

As the probability of an incident electron being scattered (the intensity) is inversely proportional to the energy loss which is proportional to Z^2 as shown in equation 2.3, core-loss EEL spectroscopy is best working with light elements and energy losses beyond 1000- 2000 eV are hence rarely used [2, 25, 28].

2.7 ELNES and EXELFS

The core-loss EELS is actually composed of two parts: the energy-loss near-edge structure (ELNES) and the extended energy-loss fine structure (EXELFS). ELNES is formed by inner-shell electrons being excited into one of the low-lying unoccupied states and thus it gives information about the energy density of the unoccupied states close to the Fermi energy. Since the core states are highly localised, the fine structures between edges representing different elements in the same sample or the same elements in different samples could be significantly different due to the local density of states (LDOS). One good example is the

difference in the number of peaks and their energies of the carbon K-edges presented in different organic compounds [30,33]. This difference is caused by carbon atoms in different compounds experiencing different bonding environments (e.g. double bond or single bond). Another good example is the carbon K-edges for graphite and diamond as shown in figure 2.3. In a diamond, only one major peak can be seen which represents the sp^3 bonding (σ bond). In graphite, there is an additional peak due to the sp^2 bonding (π bond) [2, 25, 31, 34, 35].

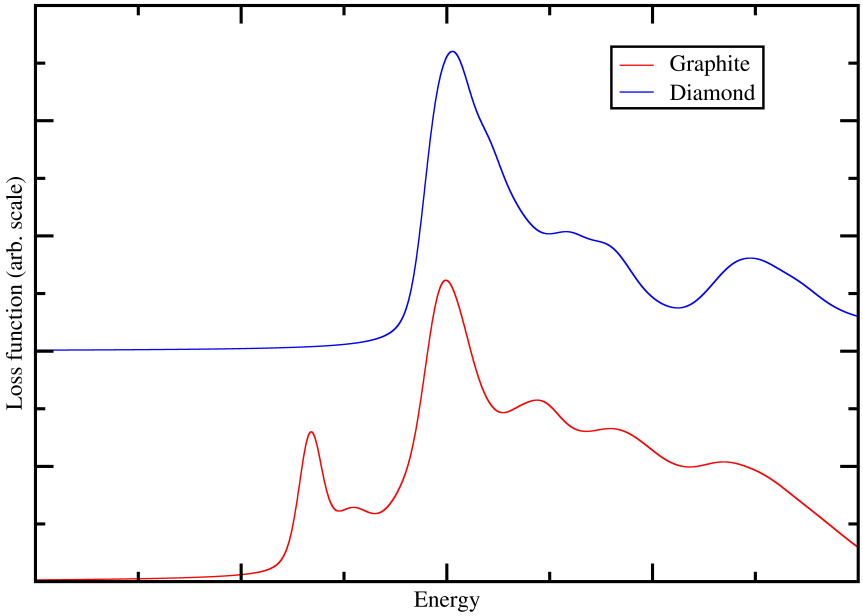


Figure 2.3: Theoretically modelled EELS of Graphite (Red) and Diamond (Blue) using PBE functional. No shifts have been applied and both graphs start at an arbitrary zero.

Beyond ELNES exists EXELFS which appears as a tail of an edge up to energy losses of about 100-200 eV beyond it. When energy exceeds the binding energy of a core edge only to a small extent, electrons are ejected from the atom with a relatively small energy. The ejected electrons are then scattered by neighbouring atoms. For electrons that are reflected back to the original atom, the reflected

wave could either constructively or destructively interfere (diffraction) [2, 25, 31]. Similar to extended x-ray absorption fine structure (EXAFS) in x-ray absorption spectra, EXELFS can be used to measure interatomic distances. Further reading can be found in reference [2, 36].

2.8 Processing of the Experimental Data

To extract the physical data about the specimen from its EELS and also to make a clearer comparison with the experimental data, we have applied several routines to post-process the raw data which are listed as follows:

2.8.1 Zero-loss Peak Removal

As the zero-loss peak corresponds to the electrons that do not undergo energy loss when passing through the sample, it is an experimental feature that is not meaningful to model. In addition, the tail of the zero-loss peak can contain a substantial amount of counts and thus alter the intensity or even the shape of the low-loss peak. Thus before making a comparison of the modelled low-loss EELS with the experimental one, it is vital to remove the zero-loss peak first. There are two methods used in this thesis to extract the zero-loss peak. The Reflected Tail method is based on the assumption that the zero-loss peak is symmetric and the right-side tail (the one that is overlapped with the low-loss peaks) is modelled using a reflection of the left-side tail. The Fitted Logarithm Tail method uses least-squares fitting to fit a logarithmic function to the zero-loss peak [37].

2.8.2 Background Subtraction

As discussed earlier, one major challenge of the experimental EEL spectroscopy is to extrapolate and subtract the background. For the low-loss edges, the background comes mainly from the asymmetries of the zero-loss peak that exhibits

a tail extending into the low-loss region, together with the energy loss due to the bremsstrahlung radiation. Excitations of lower binding energy will also contribute to the background. As for the core-loss edges, the background is a result of several processes such as the zero-loss or plasmon tails, the plural scattering, and the core edges which exist at lower energies. For background extrapolation in this thesis, we have adopted the power-law formalism in the form of:

$$I = AE^{-r} \tag{2.4}$$

where I is the spectral intensity, E is the energy loss and A and r are coefficients determined using least-squares fitting to the pre-edge background [2, 24, 37, 38].

The background is extrapolated as shown in Figure 2.4. A rectangular region of interest is selected over the desired region. The background function is then fitted to the selected background data and then the background is extrapolated to obtain a full background model, which is finally subtracted from the original spectrum [37].

2.8.3 Deconvolution

With the increase in the sample thickness, there is also an increase in the probability of multiple scattering, which is also known as plural scattering. It originates from electrons that have been scattered more than once. For the low-loss region, plural scattering will introduce additional spectral peaks that are repeated at multiples of their basic energy. For the core-loss region, such events alter the shapes of both the ELNES and EXELFS and thus must be removed before making the comparison. The plural scattering effects are removed by Fourier deconvolution with two different approaches: the Fourier-log and the Fourier-ratio techniques. Both methods require knowledge of the probability distribution represented by

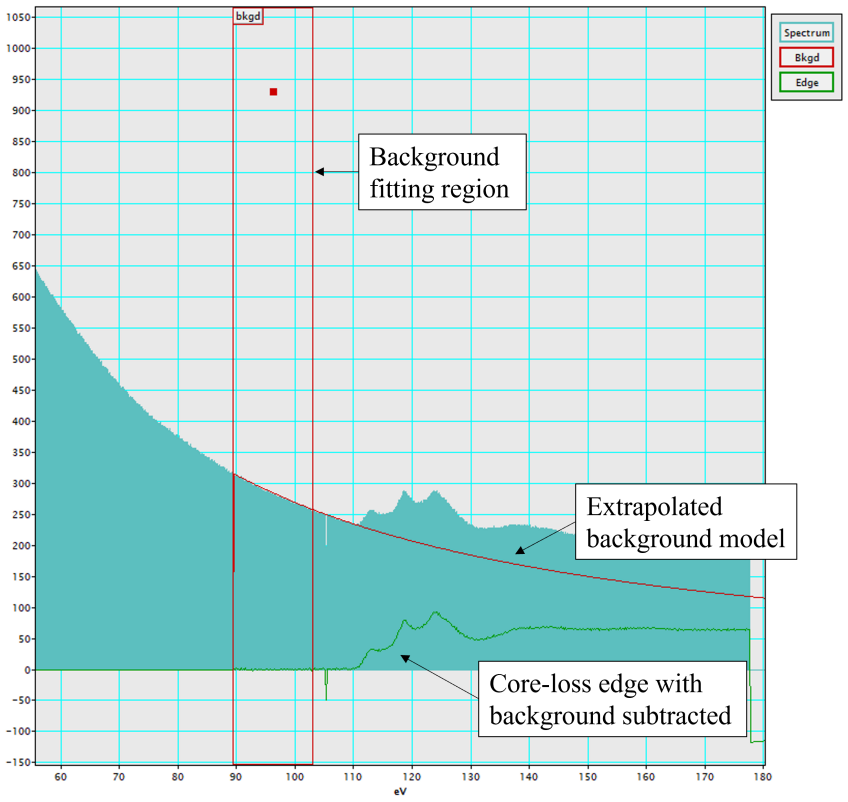


Figure 2.4: Power-law background modelling of a core-loss EEL spectrum

the low-loss peaks. Further reading can be found in [2, 24, 37, 39, 40].

Chapter 3

Previous Approaches to Model EELS

This chapter focuses on a literature review of various methods adopted in the modelling of EELS. There are several in-depth reviews of the various theoretical and computational methods for the modelling of EELS [3–5] while the main approaches are summarised in this chapter.

Both the core-loss and low-loss regions of EELS are closely related to the imaginary part of the dielectric function, although they involve different calculations. In addition, core-loss EELS is closely related to another experimental technique used to probe the unoccupied electronic states of condensed matter, known as X-ray absorption near edge spectroscopy (XANES). The details of the theories will be discussed in later chapters. In summary, for the core-loss region where $\varepsilon_1 \approx 1$, energy-loss near-edge structure (ELNES) is proportional to the $\mathrm{Im}(\varepsilon)$ and gives very similar experimental spectra to the X-ray absorption near-edge structures (XANES). Thus for the core-loss EELS, various methods initially used to calculate the XANES are also discussed.

This chapter starts with the calculations of the core-loss EELS, together with

the importance of the core hole. and followed by methods associated with the low-loss region.

3.1 Core-loss EELS

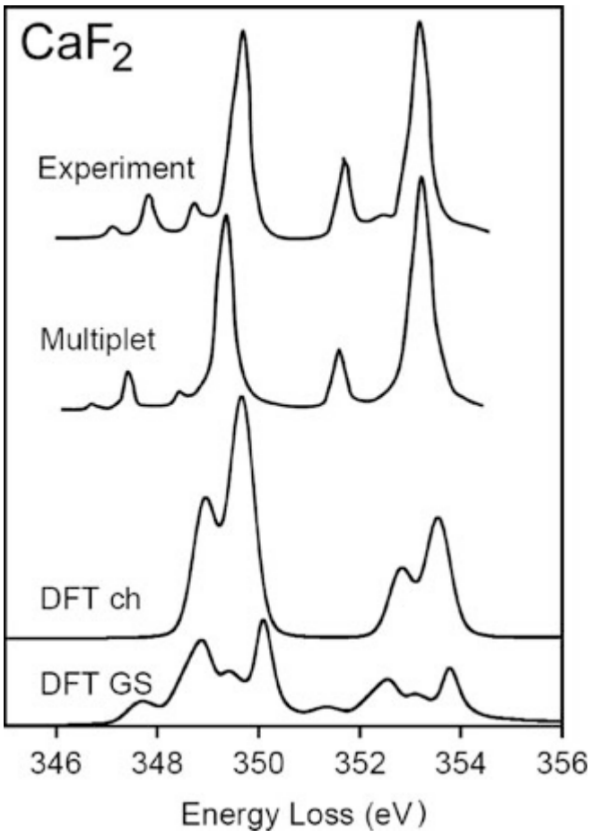


Figure 3.1: The Ca $L_{2,3}$ edge of CaF_2 comparing the DFT (ground state (GS) and core hole (ch)) calculations with multiplet calculations and with the experimental spectra. The figure is adapted from Reference [4] with permission.

The core-loss EELS contains the ionisation edges which measure the transition of an electron from a tightly bound core state to an unoccupied state above the Fermi level. The initial core-state wave function is well defined and thus the calculation of the fine structure in the edge, ELNES depends on the methods adopted for calculating the final unoccupied-state wave function. The simplest method is to assume that the atom is isolated and perform an atomic calculation using the atomic continuum and bound-state wave functions. Electron exchange

and correlation effects are then included by multiplet theory based on an atomic model rather than the single particle description. A review of different levels of theories for multiplet calculations can be found in reference [41]. For $3d$ transition metals, additional symmetry effects and the configuration-interaction effects of the neighboring atoms are involved via the crystal field theory [3,5,6]. In addition, the crystal field multiplet model can be further improved by combining the ground state configuration with other low-lying configurations [41]. Several codes have been developed for the multiplet calculations: CTM4XAS [6, 42], Xclaim [43] and Quanty [44]. The calculation results of the $L_{2,3}$ edges for the transition metals [7, 42, 45] and the $M_{4,5}$ edges for the rare-earth elements [8] agree well with the experiments. The Ca $L_{2,3}$ edge of CaF_2 is shown in Figure 3.1, adapted from Reference [4]. The figure suggests that for the Ca $L_{2,3}$ edge of CaF_2, a better agreement with the experiment data is given by the multiplet calculations, compared to that of the bandstructure approach of DFT calculations.

Another approach is the scattering theory which describes the interaction of the outgoing spherical wave representing the ejected electron and backscattered waves due to the potential of the neighboring atoms. For the excited electron high in energy, it has a short mean-free path and thus only one scattering event is likely to occur before it leaves the immediate vicinity of the atom, which results in the extended fine structure (EXELFS). At lower energies, the mean-free path of the outgoing electron is much longer and thus multiple scattering could happen with other atoms in the material, which gives rise to the ELNES. The multiple scattering (MS) method is associated with solving the Green's function as described in Section 4.3.1. The FEFF code adopts the multiple scattering theory in calculating the ELNES [9] and various calculation results have been reported: in Reference [10], satisfactory results are obtained for both the N K edge and Ga $L_{2,3}$ edges for the cubic and hexagonal phases of GaN. As shown in Figure 3.2, for cubic GaN, the MS calculation reproduces a more satisfactory result while for

the hexagonal phase, better matching near the threshold is given by the band-structure method as described below. In Reference [46], the author reproduced the graphite C K edge using the MS method. A practical guide in using FEFF8 to calculate EELS was provided by Moreno [47], together with examples of the N K edge and Ga $L_{2,3}$ edges of hexagonal GaN. Further reading regarding the theories can be found in the reference [11, 12].

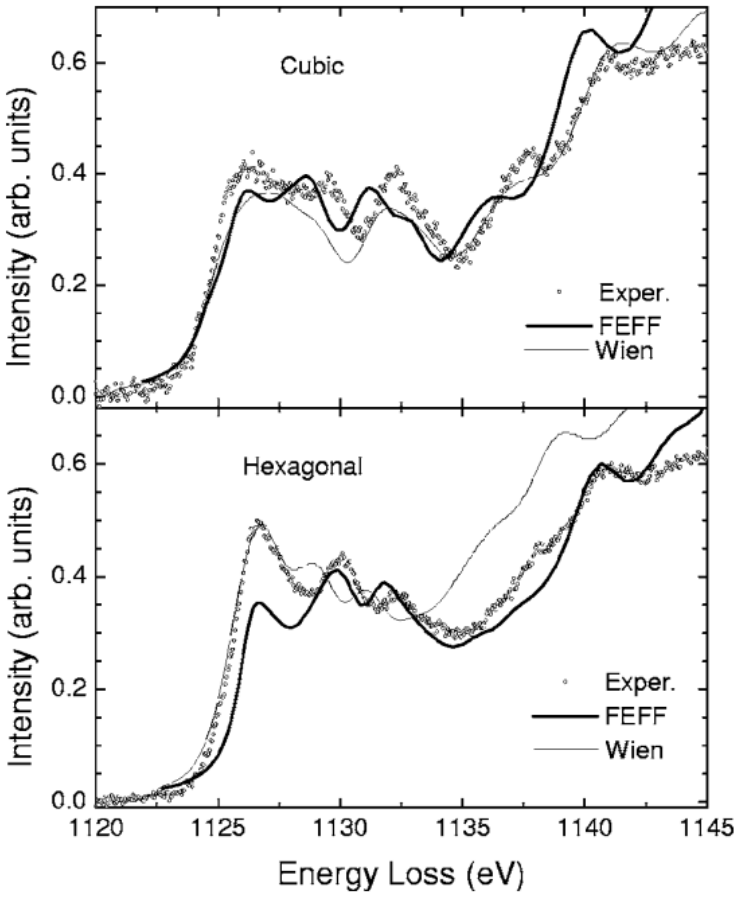


Figure 3.2: Experimental and calculated Ga L_3 edge for cubic and hexagonal phases of GaN, comparing multiple scattering method (FEFF) and DFT (Wien). The figure is adapted from the Reference [10] with permission.

The method adopted in this thesis to calculate the core-loss EELS is known as the bandstructure approach which uses the density functional theory to calculate the ground-state electronic structures. Based on the independent one-electron approximation, the excitation process is approximated as a transition of a single

electron from an initial to a final excited state. There are several codes available and two popular ones are the pseudopotential code CASTEP [48] using plane wave basis set and the all-electron code WIEN2k [49, 50] with the linearised augmented plane wave basis set. These codes have been used to study a wide variety of materials including: Jiang used the WIEN2k code to calculate the O K edge of rutile; Keast adopted the method to study the electronic structure of GaN and $In_xGa_{1-x}N$ measured with electron energy-loss spectroscopy; Jayawardane calculated the B and N K edges in cubic BN which agree well with the experiments; Gao presented a comparison of the simulated results with the experiments for N K edge of group-III nitrides (AlN, GaN, InN) [14] and B K edge of CaB_6 [13]. An overview of calculating EELS using CASTEP was written by Milman [51].

3.1.1 The Effect of Core Hole

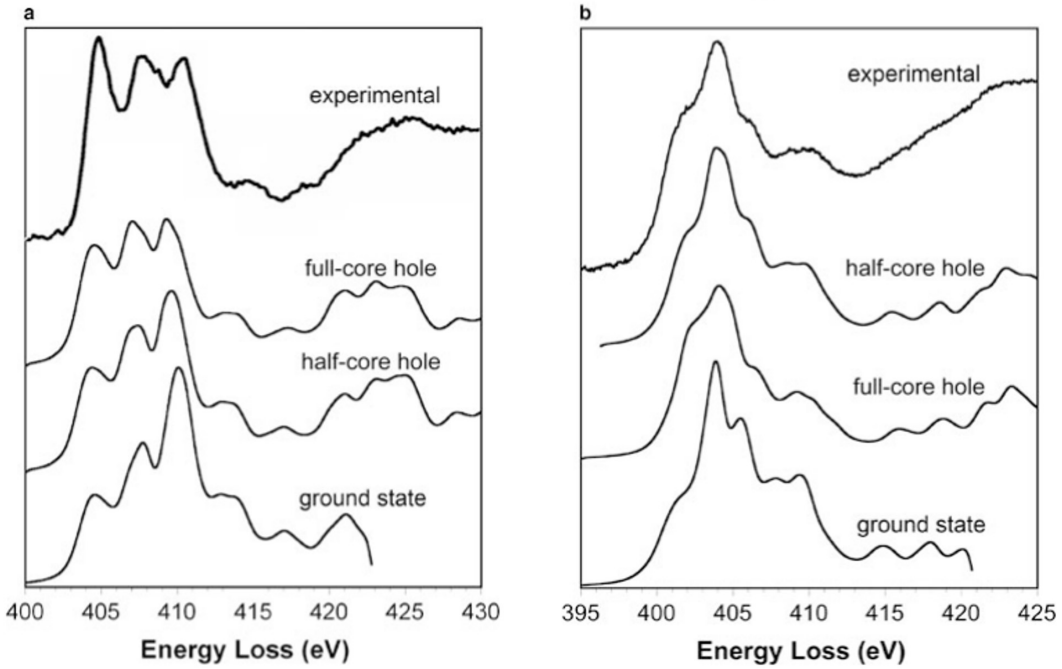


Figure 3.3: Calculated and experimental spectra for (a) AlN and (b) GaN. Calculations are performed with no core hole, half a core hole, and a full core hole. The figure is adapted from Reference [10] with permission.

Another important aspect of the ELNES calculation is the core hole. A core hole

is a positively-charged vacancy left by an electron that has been excited from one of the inner atomic orbitals. The core hole effect is included in the multiple scattering codes [9, 10]. For the bandstructure approach, it is straightforward to include the core hole effect using the all-electron code and the method has been employed in many previous studies [52–54]. For example, in the WIEN2k, there are three types of core hole calculations available. The first one is the Z + 1 method which replaces the excited atom with the next heavier atom with an extra proton [15, 55, 56]. The second method is by removing one electron from the appropriate core state of the excited atom and placing it in the valence. The third method is to remove the core electron and add the corresponding charge as a background charge. It is also possible to only remove a fraction of the core electron and perform a partial core hole calculation [49]. For the pseudopotential method, the core hole effect can be taken into account using similar approaches. The core-loss calculations presented in this thesis adopt the specially designed pseudopotential method which is discussed in more detail in the Reference [16,17,57,58]. In addition, one half a core hole can also be achieved via a Slater transition [59].

However, for different materials, there is a question about whether to use no, partial or full core hole in the calculations. In certain metals, the effect of the core–hole is almost completely screened out [4, 59]. The author of reference [10] states that a core hole is usually essential for insulators. In reference [4], the author states that the best agreement with the experiment is obtained with a full core hole for AlN, half a core hole for GaN (as shown in Figure 3.3), and no core hole for Cu. The general trend is to adopt a full core hole for ELNES calculations of non-metals. In reference [17], the author claims that core hole effects are more vital for cations in ionic compounds or elements with lower electronegativity in covalent compounds, shown in Figure 3.4. There is no globally agreed answer to the above question as intrinsically, DFT provides a static approximation to the

actual dynamic and many-body excitation process.

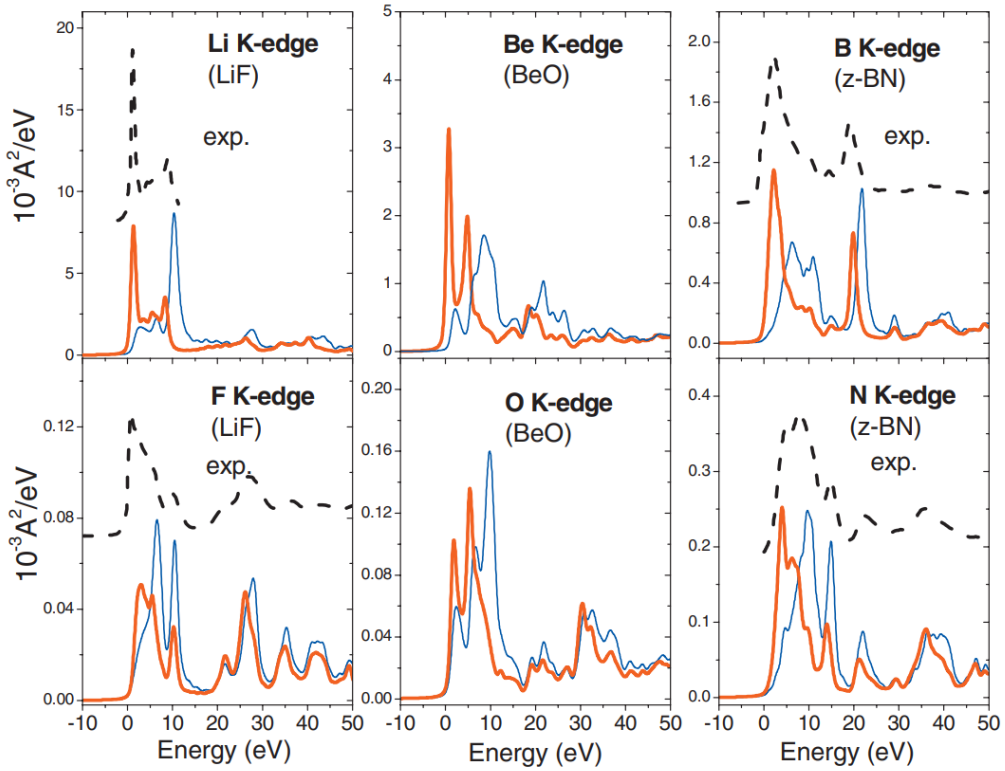


Figure 3.4: Experimental and calculated core-loss EELS for LiF, BeO, and cubic BN with (red) and without (blue) core holes. The figure is adapted from Reference [10] with permission.

3.2 Low-loss EELS

The low-loss EELS measures the excitations of the valence electrons. To model the low-loss EELS, the simplest method is to use classical electrodynamics which predicts the low-loss EELS using the dielectric function obtained experimentally as discussed in Section 2.4. Such analytical method, however, is limited only to relatively simple geometries such as planar interfaces and spherical particles [4, 60]. Similar to the bandstructure approach for the ELNES calculations, the low-loss EELS calculations can be performed using DFT to obtain the ground-state valence and conduction wave functions. The independent particle approximation (IPA) is also adopted to calculate the imaginary part of the dielectric function and

additional calculations are required to obtain the real part using Kramers-Krönig relation [26]. LDA and GGA are two common exchange and correlation potentials used in the DFT calculations. The next level of approximation is to include the local field effect (LFE) using the Random Phase Approximation (RPA). A good agreement of RPA + LFE with the experimental results of Au and $AuAl_2$ were presented in reference [5,61]. Studies on the theoretical and experimental low-loss EELS of ZrO_2 have been performed with and without LFE in reference [18, 62]. The authors of references [62, 63] both emphasise on the importance of LFE for materials with *d*-state electrons with examples of ZrO_2 (as shown in Figure 3.5) and TiO_2. Beyond ground-state RPA, there are two broad classes of approaches. One way is based on the many-body perturbation theory and uses quasiparticle corrections to better calculate the excited-states properties, known as the GW approximations. The GW approximation can be applied with RPA, or with the Bethe–Salpeter equation (BSE) to include the excitonic effects. Another approach to address the many-body problem is a time-dependent reformulation of DFT (TDDFT). TDDFT, RPA on top of GW calculations and BSE calculations were carried out and compared for silicon in reference [64]. The author showed an overall satisfactory agreement between the RPA curve with respect to the experimental spectrum. The inclusion of excitonic effects improves the results with respect to both the RPA, and more drastically, with respect to the GW calculations.

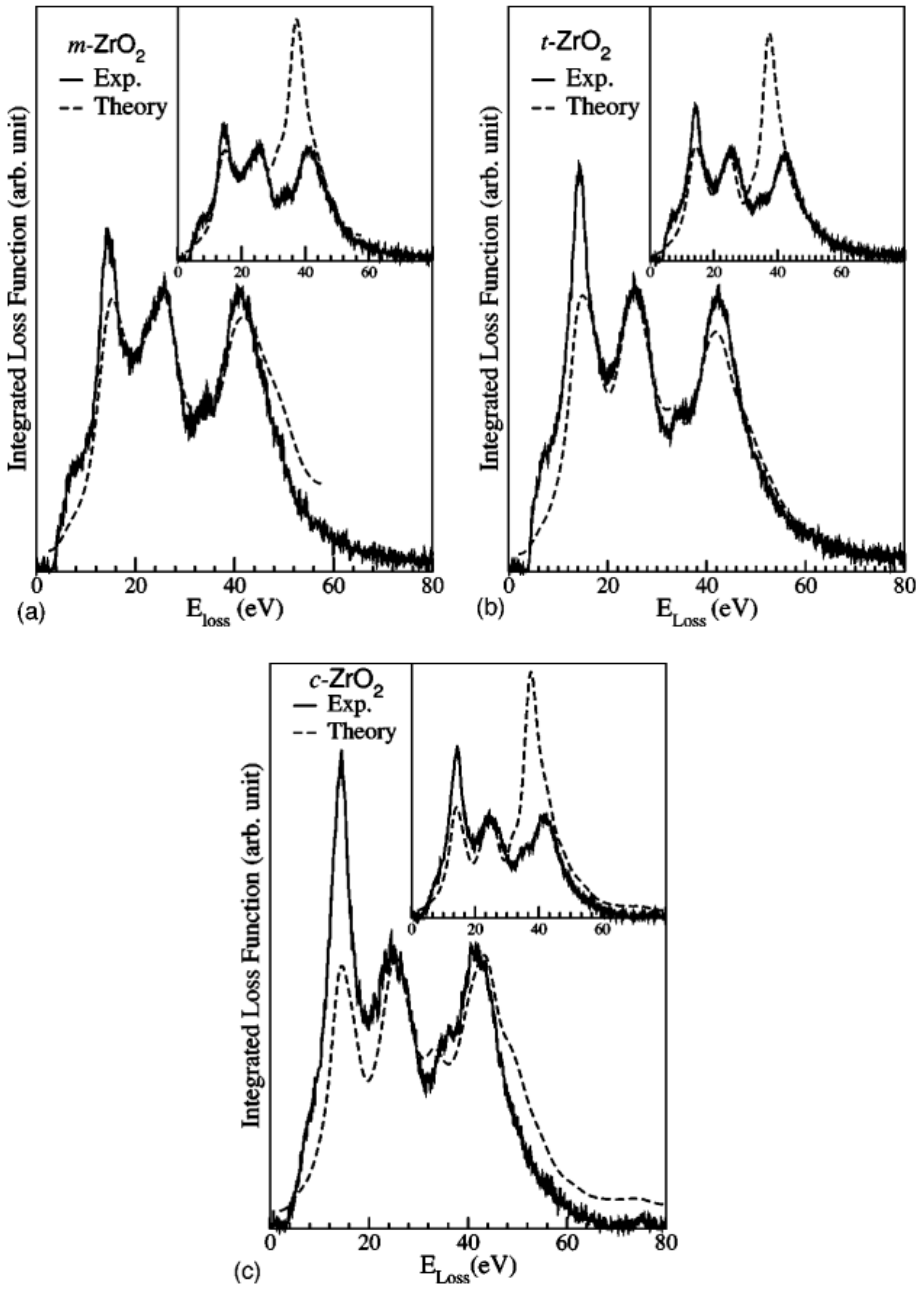


Figure 3.5: Integrated loss function for pure zirconia: (a) monoclinic, (b) tetragonal, and (c) cubic phases. The experimental (solid) and calculated results with LFE (dashed) are shown in the main figures while the inset shows the comparison of calculations with (solid) and without (dashed) LFE. The figures are adapted from Reference [62] with permission.

3.2.1 Motivations

Although core-loss EELS has long been a major area of interest in EELS modelling, the experimental low-loss region also contains additional valuable information. In the example of the ZrO phase at zirconium/zirconium oxide interfaces [18], the author demonstrates that stronger features are observed in the experimental low-loss EELS across the interface region of the sample compared to the experimental oxygen K-edge and zirconium $L_{2,3}$ edges. As the structure at the metal–oxide interface is unknown, it is vital to perform calculations to better interpret the experimental EELS spectrum. In addition, modelling the low-loss EELS can help develop a more direct relationship between the experimentally obtained dielectric function and the electronic structure of the material.

On the computational modelling side, within DFT, various functionals have been developed trying to solve the notorious band-gap problem. How these functionals could improve the computationally modelled EELS is still waiting to be answered. Additionally, due to the advance of computational resources, for advanced methods like GW and BSE, it is now possible to perform low-loss EELS calculations for more complex structures. For core-loss EELS, however, due to the presence of core hole, the 'defect' structure requires far more computational resources than the low-loss EELS. Performing relatively-cheaper low-loss EELS calculations allows more advanced methods to be investigated.

The main target of the research work presented in this thesis is to examine different levels of quantum mechanical theories to computationally model the low-loss EELS and develop a protocol regarding methods selection for different materials, considering both accuracy and efficiency. The first approach is to stay within ground-state DFT, while adopting exchange and correlation functionals which are reported to provide better descriptions of the excited properties of materials. Compared to standard LDA and GGA functionals, the Becke-Johnson functional

(BJ) [65], the Tran-Blaha functional (TB) [66], and the SCAN functional [67,68] has been known to make better predictions of the band gaps [69] but has not been thoroughly studied in the context of EELS modelling. The second approach is to go beyond DFT and tackle the many-body problem with the GW approximations and TDDFT methods. In addition, the assumption of IPA that electrons and holes are independent may not be adequate. To go beyond the one-electron picture in IPA, the many-body picture is drawn by first including the LFE, and subsequently the linear-response theory associated with TDDFT and BSE method on top of GW approximations. In all cases, the calculations involve a substantial increase in theoretical complexity and computational effort. Thus, aside from accuracy, other factors to consider include: first, the feasibility of performing calculations for materials with more complex structures, and second, whether the additional computational efforts are worthwhile.

The method is then applied to solve the material problem of the corrosion products of beryllium tiles used in nuclear reactors, thus better understanding the oxidation process. During the research, a new pseudopotential approach to simulate the beryllium K-edge spectrum is also developed.

Chapter 4

Density Functional Theory and Beyond

In this chapter, I discuss the theories behind the calculation of electronic structure which is the starting point for modelling the low-loss and core-loss regions of EELS. Density Functional Theory (DFT) is a ground-state theory which serves as the starting point of this thesis. Within DFT, a key part of this thesis is to use different levels of approximations of the exchange and correlation functional to simulate EELS, from the simplest Local Density Approximation (LDA) [70, 71], to PBE [72] which belongs to the family of the generalised gradient approximation (GGA) functionals, and to meta-GGAs including the functional proposed by Becke and Johnson [65], a modified version of the Becke-Johnson functional by Tran and Blaha [66] and the rSCAN functional [73], which is an improved regularized version of the SCAN (Strongly Constrained and Appropriately Normed) functional [67, 68]. However, since EELS involves plasmon and electron excitations which are related to the excited states of a material, the ground-state theory is potentially not enough to fully recreate the features that we have seen in an experimental spectrum. Beyond DFT, Time-dependent Density Functional Theory

(TDDFT) and the GW approximation (GWA) are applied in this thesis, which are well-known for working with excited-state properties, i.e. the band gaps and the absorption spectrum.

This chapter begins with the core theories of DFT, followed by theories of TDDFT and GWA. We will also make a brief discussion of the convergence parameters for practical calculations. Further reading can be found in references [74–76].

4.1 Density Functional Theory

4.1.1 Many-body Schrödinger Equation

The many-body Schrödinger equation (in atomic units) of a system with M nuclei and N electrons takes the form [74]:

$$\begin{aligned}&\Bigg[-\sum_i \frac{\nabla_i^2}{2} - \sum_I \frac{1}{M_I}\frac{\nabla_I^2}{2} - \sum_{i,I}\frac{Z_I}{|\mathbf{r}_i - \mathbf{R}_I|} \\ &+ \frac{1}{2}\sum_{i,j}\frac{1}{|\mathbf{r}_i - \mathbf{r}_j|} + \frac{1}{2}\sum_{I,J}\frac{Z_I Z_J}{|\mathbf{R}_I - \mathbf{R}_J|}\Bigg]\Psi(\mathbf{r_1},\ldots,\mathbf{r_N};\mathbf{R_1},\ldots,\mathbf{R_M}) \\ &= E_{TOT}\Psi(\mathbf{r_1},\ldots,\mathbf{r_N};\mathbf{R_1},\ldots,\mathbf{R_M})\end{aligned} \tag{4.1}$$

where E_{TOT} is the total energy and Ψ is the electron wavefunction of the whole system. The first two terms represent the kinetic energies of electrons and nuclei respectively with M_I being the nucleus mass. The following three terms denote to the Coulomb interactions between electrons and nuclei, electrons and electrons and nuclei and nuclei. Z_I and Z_J are the atomic numbers of different nuclei and $\mathbf{r}$ and $\mathbf{R}$ are vector positions of electrons and nuclei. The energy associated with Coulomb interactions is defined to be positive for repulsion and negative for attraction. All five terms inside the big bracket together is defined as the

Hamiltonian $\hat{H}$ operator. It is too computationally intensive to directly solve the many-body Schrödinger equation. It is simplified by several procedures.

The first approximation made is that, as nuclei are much heavier than electrons, in practice all nuclei are frozen in a lattice, M_I=∞. And thus the term representing the kinetic energy of nuclei can be removed. Equation 4.1 is simplified into [74]:

$$\begin{aligned}&\left[-\sum_i \frac{\nabla_i^2}{2} - \sum_{i,I} \frac{Z_I}{|\mathbf{r_i} - \mathbf{R_I}|} + \frac{1}{2}\sum_{i,j} \frac{1}{|\mathbf{r_i} - \mathbf{r_j}|}\right]\Psi(\mathbf{r_1}, \ldots, \mathbf{r_N}) \\ &= E\Psi(\mathbf{r_1}, \ldots, \mathbf{r_N})\end{aligned} \tag{4.2}$$

where E is the total electronic energy when the positions of the nuclei are fixed [74]:

$$E = E_{TOT} - \frac{1}{2}\sum_{I,J} \frac{Z_I Z_J}{|\mathbf{R_I} - \mathbf{R_J}|} \tag{4.3}$$

However, although the contribution of the nuclei is simplified, the question remains complex for a system with N electrons as it involves $3N$ Cartesian coordinates in the many-body wavefunction $\Psi(\mathbf{r_1}, \ldots, \mathbf{r_N})$. Before moving on with the simplification, we will first introduce the core concept of DFT, the Hohenberg-Kohn theorem [77].

4.1.2 The Hohenberg and Kohn Theorem

Equation 4.2 can be rewritten by expressing the total electronic energy E as a functional of the many-body wavefunction $\Psi(\mathbf{r_1}, \ldots, \mathbf{r_N})$ [74]:

$$E = \langle\Psi|\hat{H}|\Psi\rangle = \int \mathrm{d}\mathbf{r_1}...\mathrm{d}\mathbf{r_N}\Psi^*(\mathbf{r_1}, \ldots, \mathbf{r_N})\hat{H}\Psi(\mathbf{r_1}, \ldots, \mathbf{r_N}) \tag{4.4}$$

where the Hamiltonian of the many-body equation is:

$$\hat{H} = -\sum_{i} \frac{\nabla_i^2}{2} - \sum_{i,I} \frac{Z_I}{|\mathbf{r_i} - \mathbf{R_I}|} + \frac{1}{2} \sum_{i,j} \frac{1}{|\mathbf{r_i} - \mathbf{r_j}|} \tag{4.5}$$

The Hohenberg-Kohn Theorem [77] states that if the system is in its ground state, then the associated total energy E is a function of electron density n only, which is a function of a single position variable [74, 78]:

$$n(\mathbf{r}) = N \int \mathrm{d}\mathbf{r_2} ... \mathrm{d}\mathbf{r_N} \Psi^*(\mathbf{r_1}, \ldots, \mathbf{r_N}) \hat{H} \Psi(\mathbf{r_1}, \ldots, \mathbf{r_N}) \tag{4.6}$$

The proof of the Hohenberg-Kohn Theorem is beyond the scope of this thesis, and full derivation can be found in [74, 77]. Remarkably the theorem simplifies the problem of determining the energy of the quantum state, which initially depends on the entire wavefunction with $3N$ variables to the electron density with only three variables, although limiting DFT to a ground-state theory.

4.1.3 Kohn-Sham Equations

To construct the functional that the Hohenberg-Kohn Theorem mentioned, we first simplify the equation 4.2, by defining the Coulomb interaction between electrons and nucleus as the external nuclear potential V_N [74]:

$$V_N(\mathbf{r}) = -\sum_{i,I} \frac{Z_I}{|\mathbf{r_i} - \mathbf{R_I}|} \tag{4.7}$$

The next important step taken to simplify the problem is the independent electrons approximation [74] which assumes that electrons do not interact with each other and thus there is no Coulomb repulsion between electrons. Thus the many-body problem turns into solving the single-electron Schrödinger equations of N electrons where the overall electron wavefunction Ψ is written as:

$$\Psi(\mathbf{r_1}, \mathbf{r_2}, \ldots, \mathbf{r_N}) = \frac{1}{\sqrt{N!}} \begin{vmatrix} \phi_1(\mathbf{r_1}) & \phi_1(\mathbf{r_2}) & \ldots & \phi_1(\mathbf{r_N}) \\ \phi_2(\mathbf{r_1}) & \phi_2(\mathbf{r_2}) & \ldots & \phi_2(\mathbf{r_N}) \\ \vdots & \vdots & \ddots & \vdots \\ \phi_N(\mathbf{r_1}) & \phi_N(\mathbf{r_2}) & \ldots & \phi_N(\mathbf{r_N}) \end{vmatrix} \tag{4.8}$$

where ϕ_i is the single-electron wavefunction. The matrix determinant is known as the Slater determinant [79] and is used to ensure that the many-body wavefunction Ψ obeys the Pauli's exclusion principle [74, 80].

The total energy E also becomes the sum of individual electron energies ϵ_i [74]:

$$E = \epsilon_1 + \epsilon_2 + \cdots + \epsilon_N \tag{4.9}$$

However, one obvious drawback of the independent electrons approximation is that the energy associated with the Coulomb repulsion between electrons is of the same magnitude as the other terms in the equation 4.1. To take the Coulomb interaction into account, we assume that electrons, instead of directly repelling each other, interact via a mean field they generate. This approximation is know as the mean-field approximation and the associated potential is known as Hartree potential $V_H(\mathbf{r})$ [74]:

$$V_H(\mathbf{r}) = \int \frac{n(\mathbf{r'})}{|\mathbf{r} - \mathbf{r'}|} d\mathbf{r'} \tag{4.10}$$

which is given by Poisson's equation [81] as a function of electron density $n(\mathbf{r})$:

$$n(\mathbf{r}) = \sum_i |\phi_i(\mathbf{r})|^2 \tag{4.11}$$

Based on the Hohenberg-Kohn Theorem, we could now write the total energy as a functional of the electron density [74, 82]:

$$
\begin{aligned}
E &= F\left[n\right] \\
&= \overbrace{\underbrace{\int d\mathbf{r}\ n(\mathbf{r})V_n(\mathbf{r})}_{\text{External potential}} - \underbrace{\sum_i \int d\mathbf{r}\ \phi_i^*(\mathbf{r})\frac{\nabla^2}{2}\phi_i(\mathbf{r})}_{\text{Kinetic energy}} + \underbrace{\frac{1}{2}\int\int d\mathbf{r}\ d\mathbf{r}'\frac{n(\mathbf{r})n(\mathbf{r}')}{|\mathbf{r}-\mathbf{r}'|}}_{\text{Hartree energy}}}^{\text{Total energy in the independent electrons approximation}} + \underbrace{E_{xc}[n]}_{\text{XC energy}}
\end{aligned}
\tag{4.12}
$$

The additional term E_{xc} is the exchange and correlation energy, which arises from the difference between the Coulomb repulsion between electrons and the Hartree potential.

Hohenberg and Kohn [77] also discovered that the ground-state density n_0 corresponds to the function that minimises the total energy. This is known as the Hohenberg-Kohn variational principle:

$$
\left.\frac{\delta E[n]}{\delta n}\right|_{n_0} = 0 \tag{4.13}
$$

And thus the exchange and correlation potential $V_{xc}(\mathbf{r})$ can be defined as [82]:

$$
V_{xc}(\mathbf{r}) = \left.\frac{\delta E_{xc}[n]}{\delta n}\right|_{n(\mathbf{r})} \tag{4.14}
$$

$V_{xc}(\mathbf{r})$ is crucial in DFT as it includes all many-body effects in principle. The effect of these exchange and correlation interactions is to reduce the classical value of the electron density at one electron due to the presence of a second electron nearby. And thus each electron creates a depletion or hole of electron density around itself. However, it has no known analytic form and thus requires certain

approximations which are discussed in the next section.

The single-particle Schrödinger equation is thus:

$$\left[-\frac{1}{2}\nabla_i^2 + V_N(\mathbf{r}) + V_H(\mathbf{r}) + V_{xc}(\mathbf{r}) \right] \phi_i(\mathbf{r}) = \epsilon_i \phi_i(\mathbf{r}), \tag{4.15}$$

The whole set of equations 4.7, 4.10, 4.11, 4.14 and 4.15 are known as the Kohn-Sham equations [82].

To simplify equation 4.15, we define the Hamiltonian operator $\hat{H}$:

$$\hat{H} = -\frac{1}{2}\nabla_i^2 + V_N(\mathbf{r}) + V_H(\mathbf{r}) + V_{xc}(\mathbf{r}) \tag{4.16}$$

and equation 4.15 is simplified into:

$$\hat{H}\phi_i(\mathbf{r}) = \epsilon_i \phi_i(\mathbf{r}), \tag{4.17}$$

4.1.4 Exchange and Correlation

As described in previous section, the key determinant of the practicality of the ground-state DFT is to find an accurate but not time-consuming approximation of the exchange and correlation potential V_{xc}. For the DFT calculations presented in this thesis, we used five types of exchange and correlation potential (LDA [71], PBE [72], Becke-Johnson [65], Tran-Blaha [66] and rSCAN [67, 68, 73]) and they are discussed below.

Local Density Approximation

The simplest model of electrons in a solid is the free electron gas (FEG) [83]. It is based on the assumption that electrons do not interact with each other and all physical properties of the system depends on the electron density $n(\mathbf{r})$. The

FEG model forms the basis of the Local Density Approximation (LDA) to DFT in which the exchange energy E_x is expressed as [70, 83]:

$$E_x[n(\mathbf{r})] = -\frac{3}{4}\Big(\frac{3}{\pi}\Big)^{\frac{1}{3}} n^{\frac{4}{3}}(\mathbf{r}) \tag{4.18}$$

There are several different methods to calculate the correlation energy of the FEG model E_c. One of the most established one is obtained by directly solving the many-body Schrödinger equation using stochastic numerical methods [84] and then applying Perdew-Zunger parameterisation as [71]:

$$E_c = \begin{cases} -0.0480 + 0.0311 ln r_s - 0.0116 r_s + 0.002 r_s ln r_s & \text{if } r_s < 1, \\ -0.1423(1 + 1.0529\sqrt{r_s} + 0.3334 r_s)^{-1} & \text{if } r_s \geq 1, \end{cases} \tag{4.19}$$

where r_s is the Wigner-Seitz radius [85]. Although based on the FEG model, LDA however, has been found to produce accurate results for not only the near-free electron gas, but also the inhomogeneous systems (i.e. atoms and molecules).

Generalised Gradient Approximation

The success of LDA has lead to the development of the Generalised Gradient Approximation (GGA). In LDA functional, the exchange and correlation energy E_{xc} only depends on the local density [23, 75] while the GGA also takes into account the gradient of the charge density $|\nabla n|$. There are many types of GGA functionals. One of the most widely used GGA functional, PBE was developed by Perdew, Burke, and Ernzefhof [72] in which the exchange energy E_x takes the form [72, 86]:

$$E_x^{\text{PBE}} = -\int n^{\frac{4}{3}}(\mathbf{r}) \left[\frac{3}{4}\Big(\frac{3}{\pi}\Big)^{\frac{1}{3}} + \frac{\mu s^2}{1 + \mu s^2/\kappa}\right] \mathrm{d}\mathbf{r} \tag{4.20}$$

where $\mu = 0.21951$ and $\kappa = 0.804$. s is a dimensionless reduced gradient that depends on the charge density $|\nabla n|$ [72, 86]:

$$s = \frac{|\nabla n|}{2n^{\frac{4}{3}}(3\pi^2)^{\frac{1}{3}}} \tag{4.21}$$

The correlation energy E_c has been more difficult to develop. The exact equation can be found in reference [72] and it also depends on the gradient of the charge density $|\nabla n|$. Both LDA and PBE functionals produce geometries and electronic structures which are in good agreement with experiments. However, they do have some limitations. It has been shown that GGA functionals tend to overestimate the lattice constants while LDA functional tends to underestimate, with similar overall error [87]. The most notorious problem is the underestimation of band-gaps [74], which is a general problem for DFT as it is a ground-state theory. The eigenfunctions and eigenvalues obtained by solving the single-electron Schrödinger equation, although working qualitatively quite well for reproducing the shape of the band structure, are actually Lagrange multipliers with no physical meanings and thus result in Kohn-Sham band gaps which underestimate the measured gaps by about 40% [74]. To better model EELS which involves electron excitations, we propose to use functionals which are reported to produce band gaps in better agreement with the experiment, the meta-GGAs.

Meta-GGAs (Becke-Johnson and Tran-Blaha Functionals)

Compared to GGAs, meta-GGAs include the higher order derivatives of the electron density or the kinetic energy density $\tau(\mathbf{r})$ to introduce more nonlocal effects. Before discussing more about meta-GGAs, it is worth giving a brief discussion of another fundamental but possible approach to represent the exchange potential V_X which can be calculated exactly using the non-local Hartree-Fock (HF) formalism [74, 88]:

$$V_X^{\mathrm{HF}}(\mathbf{r},\mathbf{r}') = -\sum_j \frac{\phi_j^*(\mathbf{r}')\phi_j(\mathbf{r})}{|\mathbf{r}-\mathbf{r}'|} \tag{4.22}$$

Note that this Hartree-Fock exchange potential V_X^{HF} is exact and thus different to the ones approximated in LDA or GGAs. However, as its evaluation involves an integration over the additional variable $\mathbf{r}'$, thus making it non-local, the HF method is computationally more expensive and it grossly overestimates band gaps in solids [74, 89]. The HF exchange potential is also orbital dependent. To remove its orbital dependence, the Slater potential [70] was proposed, which is the Coulomb potential due to the HF exchange hole [90]:

$$V_x^{\mathrm{S}}(\mathbf{r}) = -\sum_i \frac{|\phi_i(\mathbf{r})|^2}{n(\mathbf{r})} V_X^{\mathrm{HF}}(\mathbf{r}) \tag{4.23}$$

The Becke-Johnson (BJ) exchange potential [65] was proposed as a sum of the Slater potential and an additional term related to the kinetic energy density $\tau(\mathbf{r})$:

$$V_x^{\mathrm{BJ}}(\mathbf{r}) = V_x^{\mathrm{S}}(\mathbf{r}) + \frac{1}{\pi}\sqrt{\frac{5}{12}}\sqrt{\frac{2\tau(\mathbf{r})}{n(\mathbf{r})}} \tag{4.24}$$

where the kinetic energy density $\tau(\mathbf{r})$ is:

$$\tau(\mathbf{r}) = \frac{1}{2}\sum_i |\nabla\phi_i(\mathbf{r})|^2 \tag{4.25}$$

The BJ exchange potential is used in combination with the LDA correlation potential and is referred to as the Becke-Johnson functional.

The modified Becke-Johnson exchange and correlation potential was proposed by Tran and Blaha (TB) in the form [66]:

$$V_x^{\mathrm{TB}}(\mathbf{r}) = cV_x^{\mathrm{BR}}(\mathbf{r}) + (3c-2)\frac{1}{\pi}\sqrt{\frac{5}{12}}\sqrt{\frac{2\tau(\mathbf{r})}{n(\mathbf{r})}} \tag{4.26}$$

The Becke-Russel (BR) exchange potential $V_x^{\mathrm{BR}}(\mathbf{r})$ [91] is given by the expression [66, 91–93]:

$$V_x^{\mathrm{BR}}(\mathbf{r}) = -\frac{1}{b(\mathbf{r})}\left(1 - e^{-x(\mathbf{r})} - \frac{1}{2}x(\mathbf{r})e^{-x(\mathbf{r})}\right) \tag{4.27}$$

where b is defined as

$$b(\mathbf{r}) = \left[\frac{x^3(\mathbf{r})e^{-x(\mathbf{r})}}{8\pi n(\mathbf{r})}\right]^{1/3} \tag{4.28}$$

And $x(\mathbf{r})$ is determined from an equation involving the electron density $n(\mathbf{r})$, its spatial gradient and Laplacian [66, 92, 93]. The BR exchange potential is a good approximation of the Slater potential and is computationally cheaper [65, 90].

The only unknown left now is c. With $c = 1$, equation 4.26 is almost identical to equation 4.24 with the only difference being the BR exchange potential. Tran and Blaha proposed to determine c as a function of the electron density:

$$c = \alpha + \beta\left(\frac{1}{V_{\mathrm{cell}}}\int_{\mathrm{cell}} \mathrm{d}\mathbf{r}\frac{|\nabla n(\mathbf{r})|}{n(\mathbf{r})}\right)^{1/2} \tag{4.29}$$

where the parameters α and β were fitted to reproduce the band gaps of different materials. Similar to the Becke-Johnson functional, the TB exchange potential is also used together with the LDA correlation potential. The TB functional is reported to produce the best band gap results among LDA, GGAs, and meta-GGAs functionals [69]. The exact implementation of the BJ and TB potential into CASTEP, which is used for the associated calculations discussed in this

thesis, can be found in reference [92].

Meta-GGAs (SCAN)

The Strongly Constrained and Appropriately Normed (SCAN) functional is a recently developed, nonempirical meta-GGA functional [67, 68]. It is developed by satisfying all 17 known exact constraints on the behavior of semi-local functionals and the remaining free parameters are fitted to accurately describe particular systems for which exact results are known (e.g. homogeneous electron gas described by LDA), which are known as norms. SCAN is dependent on the dimensionless density gradient s as described by equation 4.21 and the kinetic energy density τ via a dimensionless quantity known as the isoorbital indicator function α [73]:

$$\alpha = \frac{\tau - \tau_W}{\tau_U} \tag{4.30}$$

where $\tau_W = |\nabla n|^2/8n$ and $\tau_U = (3/10)(3\pi^2)^{2/3}n^{5/3}$ are the single-orbital and uniform-density limit of τ respectively. α is able to recognise different local bonding environments (i.e. covalent single, metallic, and weak bonds) and select the appropriate local approximations of the exchange and correlation energies [67,73]. Compared to PBE, the SCAN functional is reported to show significant improvement in predicting the formation energies of strongly bound compounds [94]. In terms of band gaps, it is reported to produce results similar to the BJ functional and better than LDA and PBE functionals [69].

For calculations using SCAN functionals discussed in this thesis, we used CASTEP in which a regularised form of the SCAN functional (rSCAN) is implemented [73]. It is modified for enhanced numerical stability while retaining the same level of accuracy as the original SCAN.

4.2 Time-Dependent Density Functional Theory

As described in section 4.1.1, the many-body Schrödinger equation is approximated into a one-particle non-interacting Schrödinger equation that is represented in the Kohn-Sham approach. The application of the Hohenberg-Kohn Theorem then, on the one hand, helps solve the KS equations while on the other hand, limits the calculations to the ground-state properties. Even in the field of ground-state properties, failures have been reported, such as the overestimation of the dielectric constant [95]. Also, as DFT is a static ground-state theory, excited-state properties cannot be accurately calculated using the theory. The notorious band gap problem is just one example. By definition, the KS eigenvalues are different from the electron addition or removal energies. There are two approaches to yield such energies. The first one is known as the time-dependent density functional theory (TDDFT) by adding a time-dependent external potential and calculating the evolution of the density in time. As for EELS calculations, the time-dependent external perturbation due to the electron is weak and the system does not deviate strongly from its initial state. Thus instead of finding the full-time density, the response function is calculated from the external potential and the induced density using the linear-response theory, which is discussed in detail in the next chapter. Further reading regarding the time-dependent density functional theory, the Runge-Gross theorem , and how to solve the time-dependent Kohn-Sham Equations can be found in references [96–99].

4.3 GW Approximation

As we discussed in previous sections, DFT is a ground-state theory while EELS involves excited states and thus intrinsically DFT is not suitable for EELS calculations. Within DFT, we have been looking for methods that are reported to produce better band gaps. Before we start the introduction of the next level of

approximations, we shall first define what the band gap is. A formal definition of the band gap is that it is the difference between ionisation potential and electron affinity. The ionisation potential corresponds to the energy required to remove an electron from the bound initial state of the neutral sample while the electron affinity is defined as the energy liberated when an electron is added to a neutral atom. Thus in the picture of the total energy, the band gap can be expressed as [100, 101]:

$$E_{\text{gap}} = [E(N+1) - E(N)] - [E(N) - E(N-1)] \tag{4.31}$$

where N corresponds to the number of electrons. $E(N)$ is the total energy of the ground-state while $E(N+1)$ and $E(N-1)$ correspond to the total energy of a system with one more or one less electron. Thus intuitively, a better way to calculate the excited-state properties is to find a quantum mechanical expression that describes the addition and removal of an electron. The expression is known as the single-particle Green's function, which is also called propagator and it is solved via a technique known as the GW approximation.

4.3.1 The Single-particle Green's Function

The GW approximation is an approach to directly solve the many-body Schrödinger equation. The single-particle Green's function $G(\mathbf{r}, \mathbf{r}', t-t')$, in the time-domain, is the probability amplitude that a particle is created or destroyed at position $\mathbf{r}$, which is influenced by an adjoint process taking place at position $\mathbf{r}'$. The expression, in an N-particle ground state with total energy $E(N)$, is given as [101–103]:

$$G(\mathbf{r}, \mathbf{r}', t-t') = -i\langle N|\hat{T}[\hat{\psi}(\mathbf{r}, t)\hat{\psi}^{\dagger}(\mathbf{r}', t')]|N\rangle \tag{4.32}$$

where $\hat{\psi}^\dagger$ and $\hat{\psi}$ are the creation and annihilation field operators and $\hat{T}$ is the time ordering operator. $\hat{T}$ is involved to arrange the field operators such that the whole creation and annihilation process is physically meaningful: the creation operator $\hat{\psi}^\dagger$ will create an electron at position $\mathbf{r}'$ at time t' which propagates through the system to position $\mathbf{r}$ at time t and is annihilated by the annihilation operator $\hat{\psi}$ (assuming $t > t'$). If we do a Fourier transformation from the time domain to the frequency domain $t - t' \to \omega$, we get the Lehman representation of $G(\mathbf{r}, \mathbf{r}', \omega)$ [102]:

$$G(\mathbf{r}, \mathbf{r}', \omega) = \sum_s \frac{f_s(\mathbf{r}) f_s^*(\mathbf{r}')}{\omega - [E_s + i\delta \mathrm{sgn}(E_F - E_s)]} \tag{4.33}$$

where E_F is the Fermi energy and E_s is the energy of the bound state and together with $f_s(\mathbf{r})$ is defined as [101]:

$$f_s(\mathbf{r}) = \begin{cases} \langle N|\hat{\psi}(\mathbf{r})|N+1, s\rangle, & E_s > E_F \\ \langle N-1, s|\hat{\psi}(\mathbf{r})|N\rangle, & E_s < E_F \end{cases} \tag{4.34}$$

and

$$E_s(\mathbf{r}) = \begin{cases} E(N+1, s) - E(N), & E_s > E_F \\ E(N) - E(N-1, s), & E_s < E_F \end{cases} \tag{4.35}$$

where $|N+1, s\rangle$ is an eigenstate of the $(N+1)$-electron system with energy $E(N+1, s)$ and the small imaginary part δ is added for the convergence of the Fourier transform to frequency space [102].

As we can see from 4.33, in the denominator, we have the many-body energy eigenvalues. Thus the single-particle Green's function has poles at the true excitation energies of the many-electron system.

4.3.2 Dyson's equation

The problem now becomes how to obtain the single-particle Green's function $G(\mathbf{r}, \mathbf{r}', \omega)$. We take a look at what will happen if a particle is added to a system. It may first go a certain distance without interacting with anything at all and such a propagator is called the non-interacting Kohn-Sham Green's function G^0 which can be obtained from any mean field system like LDA via the expression [78, 104]:

$$G^0(\mathbf{r}, \mathbf{r}', \omega) = \sum_i \frac{\phi_i(\mathbf{r})\phi_i^*(\mathbf{r}')}{\omega - \epsilon_i - i\delta} \tag{4.36}$$

where ϕ_i and ϵ_i are the single-particle wavefunctions and the associated eigenvalues when solving the single-particle Schrödinger equation described by equation 4.15.

But then there are some scattering events and then the two process repeat. To sum up over all scattering paths, we define the electronic self energy Σ, which can be treated as an effective potential that arises from the exchange and from the response of the rest of the electrons to the addition of the foreign particle. Possible scattering events include electronic exchange, screening of first order, excitonic contribution, vertex function, etc. Thus the Green function of the interacting system is [104]:

$$G = G^0 + G^0\Sigma G^0 + G^0\Sigma G^0\Sigma G^0 + ... = G^0 + G^0\Sigma G \tag{4.37}$$

If we keep the terms up to one-scattering event $G^0\Sigma G$, the equation is known as Dyson's equation. The self energy is, in general, complex, non-local in space and has an energy dependence. The energy dependence, caused by the screening effect, is physically meaningful: a slow electron traveling through the many-

electron system will face stronger screening than a faster one [102]. As mentioned in the previous chapter, the problem that the GW approximation tries to solve is still the many-body Schrödinger equation. If we rewrite the Kohn-Sham single-particle Schrödinger equation from equation 4.15 as:

$$\left[-\frac{1}{2}\nabla_i^2 + V_N(\mathbf{r}) + V_H(\mathbf{r}) \right] \phi_i(\mathbf{r}) + V_{xc}(\mathbf{r})\phi_i(\mathbf{r}) = \epsilon_i \phi_i(\mathbf{r}), \tag{4.38}$$

By comparing equation 4.33 and equation 4.36 defining the two Green's function, we could write an expression for the quasi-particle energies E_i using the Kohn-Sham single particle wavefunctions $\phi_i(\mathbf{r})$ via a Schrödinger-like equation [76, 99]:

$$\left[-\frac{1}{2}\nabla_i^2 + V_N(\mathbf{r}) + V_H(\mathbf{r}) \right] \phi_i(\mathbf{r}) + \int \Sigma(\mathbf{r}, \mathbf{r}', E_i)\phi_i(\mathbf{r}')d\mathbf{r}' = E_i \phi_i(\mathbf{r}) \tag{4.39}$$

The major difference between equation 4.38 and equation 4.39 is that, by replacing the exchange and correlation potential V_{xc} in DFT with the self energy Σ, we get the quasi-particle energies which are the true excitation energies instead of the Kohn-Sham eigenvalues of a fictitious system. The approach is known as the many-body Perturbation Theory (MBPT) and the definition of the quasi-particle will be explored in the next section. In practice, the quasi-particle energies E_i are obtained as a correction of the Kohn-Sham eigenvalues ϵ_i via the expression [76, 78, 99, 105]:

$$E_i = \epsilon_i + \langle \phi_i | \Sigma(E_i) - V_{xc} | \phi_i \rangle \tag{4.40}$$

The equation is non-linear as it has energies on both sides and thus need to be solved iteratively. Another simplification to make is by doing Taylor expansion

of the self energy in the first order:

$$\Sigma(E_i) = \Sigma(\epsilon_i) + \Sigma'(\epsilon_i)(E_i - \epsilon_i) \tag{4.41}$$

which turns the direct solution of the quasi-particle energies into a linearised solution:

$$E_i = \epsilon_i + Z_i\langle\phi_i|\Sigma(\epsilon_i) - V_{xc}|\phi_i\rangle \tag{4.42}$$

where Z_i is a renormalisation factor:

$$Z_i = (1 - \langle\phi_i|\Sigma'(\epsilon_i)|\phi_i\rangle)^{-1} \tag{4.43}$$

Thus to solve the single-particle Green's function $G(\mathbf{r}, \mathbf{r}', \omega)$, we have introduced a new quantity, the self energy $\Sigma(\mathbf{r}, \mathbf{r}', E_i)$ which contains all the many-body exchange and correlation effects. The next step is thus to find an expression for the quasi-particle self energy.

4.3.3 Self Energy and Quasi-particle

To calculate the quasi-particle self energy, we need the Hartree-Fock (HF) method, which is briefly introduced in previous section 4.1.4 when introducing the meta-GGAs, as a starting point. In the HF formalism, the electron-electron interaction is treated as the bare Coulomb interaction V_X^{HF} described by equation 4.22 (From now on we will use v for simplicity). The HF self energy is thus the product of the non-interacting Green's function and the bare Coulomb interaction [76, 103, 106]:

$$\Sigma^{HF} = iG^0 v \tag{4.44}$$

However, in reality, an electron in the many-body system will repel all the electrons in its neighborhood and thus a positively-charged polarisation cloud is formed around the central electron as shown in the right-hand side of Figure 4.1. The central electron and the screening cloud are known as the quasi-particle. Quasi-particles have much weaker interactions between each other, known as the screened Coulomb interaction W. As screening is a dynamic process, the quasi-particle self energy is much harder to calculate as it depends on time or frequency. The quasi-particle self energy is thus [76, 103, 106]:

$$\Sigma^{GW} = iG^0 W \tag{4.45}$$

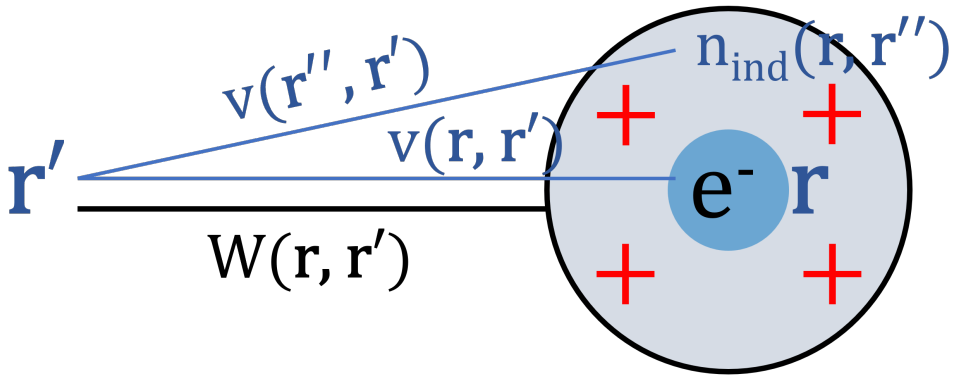


Figure 4.1: Quasi-particle is composed of an electron and its polarisation cloud, which give rise to a weaker screened Coulomb interaction W. The figure is remade from Reference [107]

The screened interaction W is the potential created by the quasi-particle and thus can be divided into two parts: the Coulomb interaction coming from the central electron $v(\mathbf{r}, \mathbf{r}'')$ and the induced charge from the polarisation cloud $n_{\text{ind}}(\mathbf{r}'', \mathbf{r}')$ which gives the effect of screening [107]:

$$W(\mathbf{r}, \mathbf{r}', \omega) = v(\mathbf{r}, \mathbf{r}') + \int v(\mathbf{r}'', \mathbf{r}') n_{\text{ind}}(\mathbf{r}, \mathbf{r}'', \omega) \mathrm{d}\mathbf{r}'' \tag{4.46}$$

The induced charge is calculated using the linear-response theory by applying the polarisation function P which is a time-ordered density response function. The polarisation function, multiplying the perturbing potential gives the induced density [107]:

$$n_{ind} = Pv + PvPv + PvPvPv \tag{4.47}$$

and thus the screened interaction W becomes:

$$W = v + vPv + vPvPv + vPvPvPv + ... = v + vPW \tag{4.48}$$

and the self energy becomes:

$$\Sigma = iGW = iGv + iGvPv + iGvPvPv + ... \tag{4.49}$$

4.3.4 Hedin's equations

So far we have seen that, to calculate Green's function G, we have introduced the self energy Σ, the screened interaction W and the polarisability P. Hedin proposed to approximate the self energy using an iterative scheme [103, 106]. The scheme consists of five coupled integral equations on five quantities which are known as Hedin's equations. To simplify the expressions, we use the following notations: $1 = (\mathbf{r_1}, \sigma_1, t_1)$ and $1^+ = (\mathbf{r_1}, \sigma_1, t_1 + \delta)$ where δ is a small positive constant and different numbers correspond to different variable sets. Hence Hedin's equations are listed as follows with the graphical representation shown in Figure 4.2a [99]:

$$G(1,2) = G^0(12) + \int \mathrm{d}(34) G^0(1,3)\Sigma(3,4)G(4,2) \tag{4.50}$$

$$\Sigma(1,2) = i \int \mathrm{d}(34) G(1,3)\Gamma(3,2,4)W(4,1^+) \tag{4.51}$$

$$\Gamma(1,2,3) = \delta(1,2)\delta(1,3) - \int \mathrm{d}(4567) \frac{\delta\Sigma(1,2)}{\delta G(4,5)} G(4,6)G(7,5)\Gamma(6,7,3) \tag{4.52}$$

$$W(1,2) = v(1,2) + \int \mathrm{d}(34) v(1,3)\tilde{P}(3,4)W(4,2) \tag{4.53}$$

$$\tilde{P}(1,2) = -i \int \mathrm{d}(34) G(1,3)G(4,1^+)\Gamma(3,4,2) \tag{4.54}$$

where we have introduced a new quantity the vertex function Γ, defined as the response of the Green's function to the variation of the total potential δU, which is the sum of the external potential and the Hartree potential [99]:

$$\Gamma(1,2,3) = -\frac{\delta G^{-1}(1,2)}{\delta U(3)} = -\frac{\delta G^{-1}(1,2)}{\delta[V_{ext}(3) + V_H(3)]} \tag{4.55}$$

Also, we are using an irreducible polarisability $\tilde{P}$ in the Hedin's equations, which is defined as the response of the induced density δn with respect to the variation of the total potential δU [99]:

$$\tilde{P}(1,2) = \frac{\delta n(1)}{\delta U(2)} = \frac{\delta n(1)}{\delta[V_{ext}(2) + V_H(2)]} \tag{4.56}$$

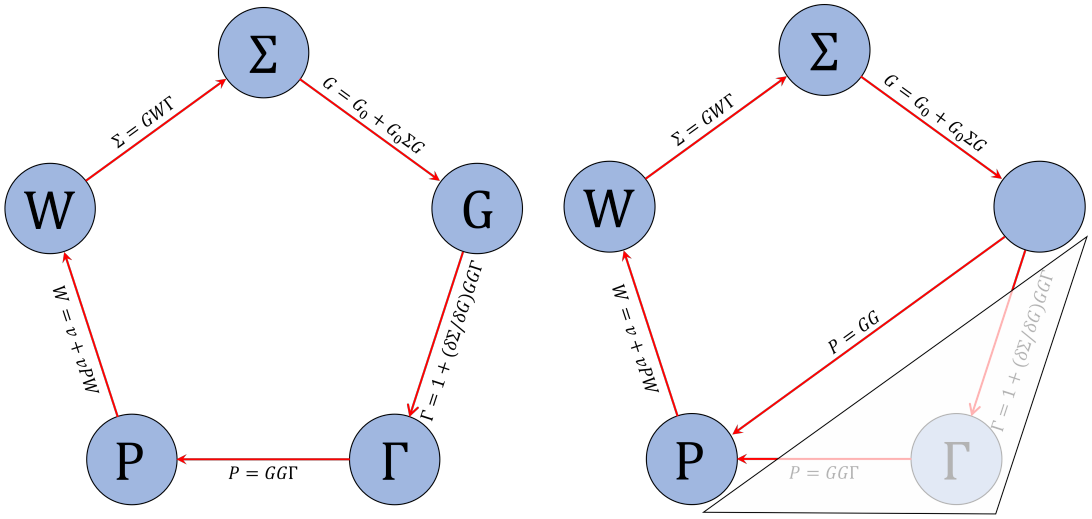
We can also define the reducible polarisability P as the response of the induced density δn due to the change of the external potential δV_{ext} [99]:

$$P(1,2) = \frac{\delta n(1)}{\delta V_{ext}(2)} \tag{4.57}$$

The relationship between the two polarisabilities will be discussed in the next chapter.

As for the screened interaction, it is related to the bare Coulomb interaction via $W = \varepsilon^{-1}v$ in which the time-ordered dielectric function ε is defined as [99]:

$$\varepsilon(1,2) = \delta(1,2) - \int \mathrm{d}3 v(1,3)\tilde{P}(3,2) \tag{4.58}$$



(a) (b)

Figure 4.2: (a) Schematic representation of the Hedin's equations (b) Schematic representation of the simplified version of Hedin's equations used for the standard GW Approximation ($\Sigma^{\mathrm{GW}} = G^0W^0$). The figure is remade from Reference [99]

Hedin's equations in principle can be solved by iteration. Starting from G^0 which is obtained from the ground-state DFT calculation using equation 4.36, iterating the pentagon, we can reach a full self-consistent solution. However, such calculation is computationally expensive and only few have been performed [108–111]. In practice, the non-self-consistent calculations are more popular which correspond to the first iteration of the pentagon with certain approximations as shown in Figure 4.2b. The first approximation is to set the vertex function Γ^{GW} to a delta function [99, 101, 103]:

$$\Gamma^{\mathrm{GW}}(1,2,3) = \delta(1,2)\delta(1,3) \tag{4.59}$$

And the polarisability P^0, the screened interaction W^0 and the self energy Σ are simplified into [99, 101, 103]:

.

$$P^0(1,2) = -iG^0(1,2)G^0(2,1^+) \tag{4.60}$$

$$W^0(1,2) = v(1,2) + \int \mathrm{d}(34)v(1^+,3)P^0(3,4)W^0(4,2) \tag{4.61}$$

$$\Sigma(1,2) = iG^0(1,2)W^0(1^+,2) \tag{4.62}$$

Starting from $\Sigma = 0$ and calculating quantities listed in the simplified version of the Hedin's pentagon as shown in Figure 4.2b through one iteration, we obtain a new self energy $\Sigma^{\mathrm{GW}} = G^0W^0$. And finally we can use Equation 4.42, to calculate the quasi-particle energies as a correction of the Kohn-Sham energies, which correspond to the true excitation energies of the many-electron system.

4.4 Practical Calculations

In this section, we will discuss the practical calculations based on the theories discussed so far. We will give a brief introduction to some additional approximations needed for running the calculations and also the principal convergence parameters for running the DFT calculations with different exchange and correlation functionals and GW calculations. As for TDDFT, since we are interested in EELS modelling which is associated with a weak time-dependent external perturbation, instead of calculating the full time-dependent density, we adopt the linear-response TDDFT which will be discussed further in the next chapter, together with the convergence parameters.

The DFT calculations with different exchange and correlation functionals are performed using CASTEP [48]. As for the GW calculations, which also require

the ground-state calculations, we use Quantum Espresso [112, 113] for the associated DFT calculations and YAMBO [105] for the actual GW calculations. The convergence tests for calculations shown in the results sections are outlined below.

4.4.1 Convergence in DFT

Plane Waves

All materials studied in this thesis are crystalline solids that have ordered arrangements of atoms. In real space, the entire structure can be generated by rigid translations of the unit cell which corresponds to the smallest group of particles that constitutes the repeating pattern. Taking the advantage of the crystal periodicity and by using the Block theorem, we can rewrite the Kohn-Sham eigenfunctions as [74]:

$$\phi_{i\mathbf{k}}(\mathbf{r}) = e^{i\mathbf{kr}} u_{i\mathbf{k}}(\mathbf{r}) \tag{4.63}$$

where $\mathbf{k}$ is the crystal momentum vector and $u_{i\mathbf{k}}(\mathbf{r})$ is a periodic function with the same periodicity as the crystal, known as the Bloch function. Now after solving the Schrödinger equation inside one crystalline unit cell, we can extend it to the whole cell by applying the periodic boundary condition.

To solve the Kohn-Sham equations, we need to expand the Bloch function $u_{i\mathbf{k}}(\mathbf{r})$ in a certain basis set. For both CASTEP and Quantum Espresso, the plane-wave basis set is used, which represents the wavefunctions using a Fourier series. Thus, the reciprocal lattice is used with the reciprocal lattice vectors $\mathbf{G}$. The corresponding primitive cell in the reciprocal lattice is known as the first Brillouin zone. The wavefunctions in the plane-wave basis set are expressed as [74]:

$$\phi_i(\mathbf{r}) = \sum_{\mathbf{G}} c_i(\mathbf{G}) e^{i\mathbf{G}\mathbf{r}} \tag{4.64}$$

in which $c_i(\mathbf{G})$ is the Fourier coefficients. As in practice, the total number of $\mathbf{G}$ is finite, the precision of the calculation is determined by the largest $\mathbf{G}$ included. The largest $\mathbf{G}_{max}$ is called the plane wave cutoff and is controlled by the kinetic energy cutoff according to the equation [74]:

$$E_{cut} = \frac{1}{2}|\mathbf{G}_{max}|^2 \tag{4.65}$$

The kinetic energy cutoff requires careful convergence study.

Also, the Bloch function $u_{i\mathbf{k}}(\mathbf{r})$ is evaluated over a finite number of k-point samples in the Brillouin zone. As the number of k-points increases, the evaluation is more accurate. However, there is also an increase in the calculation cost if more k-points are included. Thus finding a balance between the precision and cost is crucial and is done by performing the k-points convergence test. In the self-consistent calculations to solve the Kohn-Sham equations and to find the electronic ground state, a convergence test of k-points is required with respect to energy. As for the non-self-consistent calculations such as for the optical properties, additional convergence tests of k-points need to be done with respect to the spectral features. For the band structure calculations, the high-symmetry path in the Brillouin zone should also be explicitly given. The convergence parameters for the spectral calculations will be discussed further in the next chapter.

Pseudopotential

An intuitive way to reduce the computational cost of running DFT calculations and make the plane-wave basis set practical is by introducing the pseudopotential approach. The electrons in an atom can be classified as either core electrons or

valence electrons. Core electrons are the inner electrons that are bound tightly to the nucleus. The core electrons are localised and are not sensitive to the change in the surrounding chemical environment. Valence electrons, on the other hand, are more actively participated in the chemical bonding and thus determine the properties of the material. In addition, due to Pauli's exclusion principle [80], the valence electron wavefunctions must be orthogonal to the core wavefunctions, and stronger oscillations are observed in the region near the nucleus as shown in Figure 4.3. In a plane-wave basis set, it requires more plane waves to describe the wavefunctions and thus becomes more computationally expensive. To reduce the size of the basis set, the Frozen Core Approximation is made such that the core states are eliminated and only the valence electrons are explicitly described by pseudo-wavefunctions [74, 114].

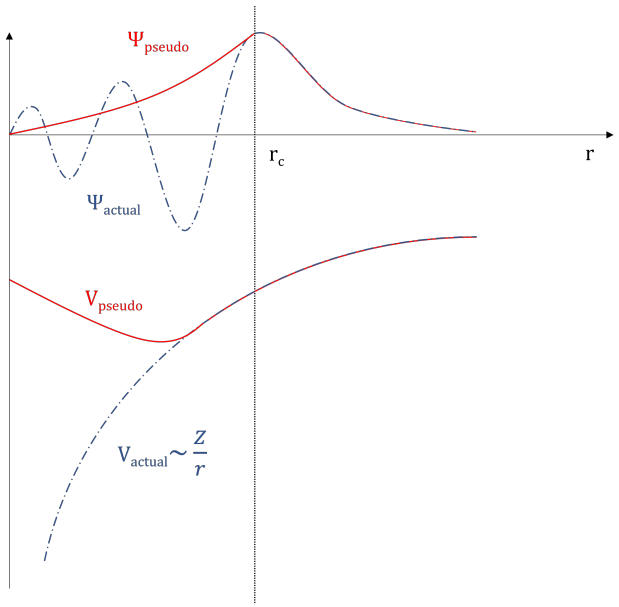


Figure 4.3: Comparison of the pseudo-wavefunction and pseudopotential (red) to the actual wavefunction and Coulomb potential (blue). Both the wavefunctions and the potentials match beyond a certain cutoff radius r_c. Below r_c, the pseudo-wavefunctions are smoother than the actual wavefunction. The figure is remade from Reference [114]

Useful pseudopotentials must be transferable (can be used for calculations on different configurations, from isolated atom to crystalline systems) and efficient

(both soft - requires smaller basis sets and thus computationally cheaper and accurate). Pseudopotentials with larger cutoff radius r_c are softer but less accurate and transferable [74]. In this thesis, we have used two types of pseudopotentials for the ground-state calculations - norm-conserving and ultrasoft pseudopotentials. For both pseudopotentials, the pseudo-wavefunctions are identical to the all-electron wavefunctions beyond the cutoff radius r_c. As for the norm-conserving pseudopotentials, below the cutoff radius r_c, the norm of each pseudo-wavefunction is identical to its corresponding all-electron wavefunction. In other words, the pseudised charge density within the core radius is the same as the all-electron charge density [115]. As for the ultrasoft pseudopotentials, such constraint is removed and the valence charge density is compensated by augmentation in the core regions [116]. Ultrasoft pseudopotentials are softer by reducing the necessary basis set size. And thus calculations using ultrasoft pseudopotentials require fewer plane waves and are typically cheaper than calculations using norm-conserving pseudopotentials. For calculations discussed in this thesis, most of the DFT functionalities are implemented for ultrasoft pseudopotentials. However, for calculations using the YAMBO code such as TDDFT and GW, which require ground-state DFT calculations as a starting point, only the norm-conserving pseudopotentials are supported and thus applied.

However, one obvious drawback of the pseudopotential approach is the absence of the core electrons information, which is problematic when running the core-loss EELS calculations, i.e. the initial states are in principle unknown. The problem is solved by using pseudopotentials specially designed for the excited atom with a core hole. The all-electron wavefunction is reconstructed using the Projector Augmented Wave (PAW) approach proposed by Van de Walle and Blöchl [117]. The associated excited pseudopotential is constructed by reducing the occupation of the core level of the reference configuration by one. Further reading regarding the exact method of construction can be found in reference [114].

4.4.2 Convergence in GW

The quasi-particle energies take the form [76, 99, 105]:

$$E_i = \epsilon_i + Z_i \langle \phi_i | \Sigma(\epsilon_i) - V_{xc} | \phi_i \rangle \tag{4.66}$$

And the key part is to find an expression for the self energy $\Sigma(\omega)$. In practice, the self energy is split into two parts: the exchange (x) part and the correlation (c) part [105]:

$$\Sigma(\omega) = \Sigma_x + \Sigma_c(\omega) \tag{4.67}$$

Exchange Self Energy

The exchange part of the self energy is the Fock-term of the Hartree-Fock self energy and can be directly computed from the DFT orbitals [101, 105]:

$$\Sigma_x = \langle \phi_{i\mathbf{k}} | \Sigma_x | \phi_{i\mathbf{k}} \rangle = -\sum_j \int_{BZ} \frac{d\mathbf{q}}{(2\pi)^3} \sum_{\mathbf{G}} v(\mathbf{q}+\mathbf{G}) |\rho_{ij}(\mathbf{k},\mathbf{q},\mathbf{G})|^2 f_{j(\mathbf{k}-\mathbf{q})} \tag{4.68}$$

where the summations are performed with respect to the index j which runs over all occupied states f is the occupation factor and $\rho_{ij}(\mathbf{k},\mathbf{q},\mathbf{G})$ is [105]:

$$\rho_{ij}(\mathbf{k},\mathbf{q},\mathbf{G}) = \langle \phi_{i\mathbf{k}} | e^{i(\mathbf{q}+\mathbf{G}).\mathbf{r}} | \phi_{j(\mathbf{k}-\mathbf{q})} \rangle \tag{4.69}$$

and the Fourier transform of the Coulomb potential is:

$$v(\mathbf{q}+\mathbf{G}) = \frac{4\pi}{|\mathbf{q}+\mathbf{G}|^2} \tag{4.70}$$

here both the reciprocal lattice vector $\mathbf{G}$ and the vector $\mathbf{q}$ which sample the first Brillouin zone requires convergence tests.

Correlation Self Energy

The correlation self energy is a complex quantity and is frequency-dependent [101, 105]:

$$\begin{aligned}\Sigma_c &= \langle \phi_{i\mathbf{k}} | \Sigma_c(\omega) | \phi_{i\mathbf{k}} \rangle \\ &= i \sum_j \int_{BZ} \frac{d\mathbf{q}}{(2\pi)^3} \sum_{\mathbf{G},\mathbf{G}'} \frac{4\pi}{|\mathbf{q}+\mathbf{G}|^2} \rho_{ij}(\mathbf{k},\mathbf{q},\mathbf{G}) \rho^*_{ij}(\mathbf{k},\mathbf{q},\mathbf{G}') \\ &\times \int d\omega' G^0(\omega-\omega') \varepsilon^{-1}_{\mathbf{G}\mathbf{G}'}(\mathbf{q},\omega')\end{aligned} \tag{4.71}$$

where G^0 is the non-interacting Green's function evaluated from the ground-state DFT calculation [101, 105]:

$$G^0(\omega) = \frac{f_{i\mathbf{k}}}{\omega - \epsilon_{i\mathbf{k}} - i\delta} + \frac{1 - f_{i\mathbf{k}}}{\omega - \epsilon_{i\mathbf{k}} + i\delta} \tag{4.72}$$

In contrast with the case of the exchange self energy Σ_x, the summation over bands now extends over all bands (including the unoccupied ones), and thus requires convergence tests. In addition, the screened Coulomb interaction $W_{\mathbf{G}\mathbf{G}'}(\mathbf{q},\omega)$ ($W = \varepsilon^{-1} v$) is adopted via the dielectric function $\varepsilon^{-1}_{\mathbf{G}\mathbf{G}'}(\mathbf{q},\omega)$. The dielectric function is a dynamical matrix, calculated at the random phase approximation (RPA) level and including local field effects which will be discussed further in the next chapter. The evaluation of the dielectric function requires three more convergence tests: the $\mathbf{q}$-point sampling determined by the choice of k-point sampling which is generally the same as the one used for the exchange self energy, the size of the dielectric matrix in $\mathbf{G}$ space determined by the number of $\mathbf{G}$ vectors

and the number of bands entering in the sum over states in the RPA response function. The last two convergence parameters will be further explored in the corresponding section in the next chapter.

The fact that the inverse dielectric function is a frequency-dependent matrix makes it difficult to calculate the frequency integral in equation 4.71. To simplify the problem, YAMBO [105] adopts the generalised plasmon pole model (PPM) proposed by Godby-Needs [118]:

$$\varepsilon^{-1}_{\mathbf{GG'}}(\mathbf{q},\omega) \approx \delta_{\mathbf{GG'}} + \mathbf{R}_{\mathbf{GG'}}(\mathbf{q})\Big[\frac{1}{\omega - \mathbf{\Omega}_{\mathbf{GG'}}(\mathbf{q}) + i\delta}\frac{1}{\omega + \mathbf{\Omega}_{\mathbf{GG'}}(\mathbf{q}) - i\delta}\Big] \tag{4.73}$$

which approximates the frequency dependence of the dielectric matrix with a single pole function. The two parameters $\mathbf{R}_{\mathbf{GG'}}$ and $\mathbf{\Omega}_{\mathbf{GG'}}$ are obtained by fitting to reproduce the RPA dielectric matrix at two frequencies: the static limit $\omega = 0$ and an imaginary frequency close to the plasma frequency [99, 101, 102, 104, 105, 118]. The effects of different PPM can be found in [101, 119].

Chapter 5

The Theory of EEL Spectrum Modelling

In previous chapter we have explored the underlying theory to obtain the ingredients required for the EELS modelling. In this chapter, we will focus on different approaches to calculate EELS. We will start with different types of density of states (DOS) calculations, which serve as a bridge between the band structure and the dielectric function. Then we will explore different methods to calculate the dielectric functions, from the independent particle approximation (IPA), to the random phase approximation (RPA) with the local-field effect (LFE), to the linear-response theory associated with TDDFT and finally to the Bethe-Salpeter equation (BSE), including more many-body effects step by step. In addition, we will also talk about the predicted transition energy, which is important to the comparison of modelled core-loss EELS to the experimental results. And in the end, main convergence parameters that need to be taken into consideration when running practical calculations are illustrated.

5.1 Density of States (DOS)

Before discussing how EELS can be modelled, it is important to illustrate the concept of density of states (DOS). The DOS of a system describes the number of states that an electron can occupy in the energy interval between $\epsilon_{i\mathbf{k}}$ and E [120]:

$$\rho(E) = \frac{1}{N_k} \sum_{i,\mathbf{k}} \delta(\epsilon_{i\mathbf{k}} - E) \tag{5.1}$$

where N_k is the number of k-points and $\epsilon_{i\mathbf{k}}$ is the energy eigenvalues of the i^{th} state at a specific wave vector $\mathbf{k}$. In OptaDOS, the delta function is approximated by several broadening schemes: Gaussian broadening uses fixed-width Gaussian function; Extrapolative scheme divides Brillouin zone into equal-size tetrahedra and then extrapolates from each k-point; Adaptive broadening scheme takes the gradient of the energy band into consideration which modifies the width of the Gaussian [120, 121].

The projected density of states (pDOS) describes the contribution of each atomic orbital to the DOS. It is calculated by adding an additional matrix element [120]:

$$pDOS(E) = \frac{1}{N_k} \sum_{i,\mathbf{k}} |\phi_{i\mathbf{k}}|\phi_{atomic,\mathbf{k}}|^2 \delta(\epsilon_{i\mathbf{k}} - E) \tag{5.2}$$

The joint density of states (jDOS) describes the number of allowed transitions between the occupied valence states and unoccupied conduction states. For metals, jDOS starts from zero as the highest occupied band is partially filled. For semiconductos and insulatos, jDOS starts at the energy of the band gap below which no optical transitions are allowed. The band gap is the difference in energy between the top of the valence band and the bottom of the conduction band.

jDOS takes the form [120]:

$$jDOS(E) = \frac{1}{N_k} \sum_{i,j,\mathbf{k}} \delta(\epsilon_{i\mathbf{k}} - \epsilon_{j\mathbf{k}} - E) \tag{5.3}$$

5.2 Dielectric Function

The dielectric function $\varepsilon(\mathbf{q}, \omega)$ describes the dielectric response of a material to the application of an alternating electric field. Its real part $\varepsilon_1(\mathbf{q}, \omega)$ gives information about the polarisability of the system while the imaginary part $\varepsilon_2(\mathbf{q}, \omega)$ is related to the actual electronic transitions. As described in previous section, both core-loss and low-loss EELS are related to the complex dielectric function $\varepsilon = \varepsilon_1 + i\varepsilon_2$ via the loss function:

$$\text{EELS} = \text{Im}\left[\frac{-1}{\varepsilon}\right] = \text{Im}\left[\frac{-1}{\varepsilon_1 + \text{i}\varepsilon_2}\right] = \frac{\varepsilon_2}{{\varepsilon_1}^2 + {\varepsilon_2}^2} \tag{5.4}$$

And thus, to simulate EELS, the vital part is to correctly calculate the dielectric function. There are several mechanisms: The simplest one is the independent particle approximation (IPA) which is based on the assumption that electrons and holes do not interact at all. The next level of calculation includes the inhomogeneities of the system and is the so-called random phase approximation (RPA) with the local-field effects (LFE). Although still lying in the DFT range which corresponds to cheap calculations, RPA yields results of reasonable accuracy [23]. Beyond DFT, there are two main methods that are employed in this thesis: the linear-response theory associated with the adiabatic approximations of the time-dependent density functional theory and the Bethe-Salpeter equations on top of the GW approximation.

5.2.1 Independent Particle Approximation

The dielectric function in the long-wavelength limit, at the independent particle level is given by Ehrenreich and Cohen [122]:

$$\varepsilon(\mathbf{q},\mathbf{q};\omega) = 1 - \frac{4\pi}{q^2\Omega}\sum_{v,c,\mathbf{k}}\frac{f(c)-f(v)}{\omega-\epsilon_{c\mathbf{k}}+\epsilon_{v\mathbf{k}}+i\delta}\left|\left\langle\phi_{c\mathbf{k}}\middle|e^{-i\mathbf{q}.\mathbf{r}}\middle|\phi_{v\mathbf{k}}\right\rangle\right|^2 \tag{5.5}$$

where $\mathbf{q}$ is the momentum transfer. Since the wavelength of electron is very small, the transmitted momentum can usually be neglected. Ω is the volume of the unit cell and $f(i)$ is the Fermi-Dirac distribution function. $e^{-i\mathbf{q}.\mathbf{r}}$ describes the probability of vertical transitions from the initial occupied state $\left|\phi_{v\mathbf{k}}\right\rangle$ to the final unoccupied state $\left|\phi_{c\mathbf{k}}\right\rangle$. In OptaDOS [120, 121], the imaginary part of the dielectric function is obtained using the approach outlined by Pickard [114]:

$$\varepsilon_2(\omega) = \frac{4\pi}{q^2\omega}\sum_{v,c,\mathbf{k}}\left|\left\langle\phi_{c\mathbf{k}}\middle|e^{i\mathbf{q}.\mathbf{r}}\middle|\phi_{v\mathbf{k}}\right\rangle\right|^2\delta(\epsilon_{c\mathbf{k}}-\epsilon_{v\mathbf{k}}-\omega) \tag{5.6}$$

ε_2 can be thought of as jDOS modified by the transition matrix element. The exponential term $e^{-i\mathbf{q}.\mathbf{r}}$ can be expanded as a Taylor series and is further simplified by the dipole approximation, as the scattering vector $\mathbf{q}$ is very small for inelastic scattering which removes the q^2 and the higher order terms:

$$\left|\left\langle\phi_{c\mathbf{k}}\middle|e^{i\mathbf{q}.\mathbf{r}}\middle|\phi_{v\mathbf{k}}\right\rangle\right| = q\left|\left\langle\phi_{c\mathbf{k}}\middle|\mathbf{u}.\mathbf{r}\middle|\phi_{v\mathbf{k}}\right\rangle\right| \tag{5.7}$$

where $\mathbf{u}$ is the unit vector in the direction of the momentum transfer vector $\mathbf{q}$. For core-loss calculations, the dipole selection rules state that the change in angular quantum number Δl must be equal to ± 1. For example, in terms of K edges, only transitions to unoccupied p-state ($l = 1$) are allowed as the initial state is a s-state ($l = 0$) [4]. In addition, as the system is not strongly polarised, $\varepsilon_1 \approx 1$

and since $\varepsilon_2 << \varepsilon_1$, the loss function is further simplified into:

$$\mathrm{EELS}_{\mathrm{core}} = \mathrm{Im}\left[\frac{-1}{\varepsilon}\right] = \varepsilon_2 \tag{5.8}$$

This approximation does not hold for the low-loss calculation and thus both ε_1 and ε_2 are involved for the loss function. After ε_2 is calculated using equation 5.6, ε_1 is calculated using the Kramers-Krönig relation [26, 120].

5.2.2 Macroscopic Dielectric Function

Before moving on to the local-field effects, it is vital to first find the connection between the microscopic point of view (i.e. band structure) and the macroscopic one (the actual spectrum seen in the experiments). The microscopic dielectric function in the reciprocal space is $\varepsilon_{\mathbf{GG'}}(\mathbf{q}, \omega)$ where $\mathbf{G}$ stands for a vector in the reciprocal lattice and $\mathbf{q}$ is a vector in the first Brillouin zone. It is a matrix that depends on frequency or time. To obtain the actual spectrum, we need to calculate the macroscopic dielectric function ε_M which is a spatial integral taken on the microscopic one. Both equation 5.5 and 5.6 calculate the macroscopic functions via [99, 123]:

$$\varepsilon'_M(\omega) \sim \int d\mathbf{r} d\mathbf{r'} e^{i\mathbf{q}.(\mathbf{r}-\mathbf{r'})} \varepsilon_{\mathbf{rr'}}(\mathbf{q}, \omega) \tag{5.9}$$

and can be rewritten in reciprocal space as [99]:

$$\varepsilon'_M(\omega) = \lim_{\mathbf{q}\to 0} \varepsilon(\mathbf{q}, \omega)_{\mathbf{G}=\mathbf{G'}=\mathbf{0}} \tag{5.10}$$

However, macroscopically speaking, when an external field is applied, a local electric dipole moment is induced. According to Maxwell's equations, the total electric field $\mathbf{E}$ is related to the electric displacement field $\mathbf{D}$ via:

$$\mathbf{E} = \varepsilon^{-1}\mathbf{D} \tag{5.11}$$

And thus the correct average should be taken on ε^{-1} instead which leads to a different equation to calculate the macroscopic dielectric function [97, 99, 122–125]:

$$\varepsilon_M(\omega) = \lim_{\mathbf{q}\to 0} \frac{1}{[\varepsilon^{-1}(\mathbf{q},\omega)]_{\mathbf{G}=\mathbf{G}'=\mathbf{0}}} \tag{5.12}$$

The EEL spectrum for vanishing momentum transfer is then determined by:

$$\text{EELS} = \text{Im}\left[\frac{-1}{\varepsilon_{\text{M}}}\right] \tag{5.13}$$

An explicit discussion of the difference between ε_M and ε'_M can be found in Sottile's PhD thesis [99]. Here we will only limit the discussion to the final conclusion that to take the local-field effects into consideration, equation 5.12 is used and is further discussed in the next section.

5.2.3 The Local Field

In previous section, we have introduced how to calculate the macroscopic dielectric function from the microscopic one. In this section, we will introduce an alternative method to obtain the microscopic dielectric function $\varepsilon_{\mathbf{GG}'}(\mathbf{q},\omega)$ using the retarded microscopic polarisability $\tilde{\chi}_{\mathbf{GG}'}(\mathbf{q},\omega)$:

$$\varepsilon = 1 - v\tilde{\chi} \tag{5.14}$$

or alternatively:

$$\varepsilon_{\mathbf{GG'}}(\mathbf{q},\omega) = \delta_{\mathbf{GG'}} - v_{\mathbf{G}}(\mathbf{q})\tilde{\chi}_{\mathbf{GG'}}(\mathbf{q},\omega) \tag{5.15}$$

where v or $v_{\mathbf{G}}(\mathbf{q})$ is the bare Coulomb potential. In the case of the homogeneous electron gas, the microscopic dielectric function ε is diagonal in $\mathbf{G}$ space. And thus ε_M and ε'_M are identical. However, such a relationship does not hold for an inhomogeneous system where the dielectric matrix is no longer diagonal. The microscopic dielectric function is both distance and position-dependent. To do the matrix inversion, the off-diagonal elements of $\varepsilon_{\mathbf{GG'}}$ must be taken into account which is known as the local-field effects (LFE). LFE is related to the fluctuation of the polarization of the system on the atomic scale and can be interpreted as a basic approximation of the electron-hole approximation [99, 123].

As for the EEL spectrum, it is also useful to define an additional retarded microscopic function χ that is related to the inverse of the dielectric function via:

$$\varepsilon^{-1} = 1 + v\chi \tag{5.16}$$

and it is related to the retarded microscopic polarisability $\tilde{\chi}$ via a Dyson-like screening equation:

$$\chi = \tilde{\chi} + \tilde{\chi}v\chi \tag{5.17}$$

For simplicity, $\tilde{\chi}$ is referred to as the irreducible microscopic polarisability and χ is referred to as the reducible microscopic polarisability later in this thesis.

From section 4.3.4, we have seen two similar quantities in the Many Body Perturbation Theory (MBPT): the time-ordered irreducible polarisability $\tilde{P}$ and the time-ordered reducible polarisability P. The polarisability we have discussed in this section so far corresponds to the retarded polarisability which works in the

(Time-dependent) Density Functional Theory. The real parts of the retarded and the time-ordered reducible polarisabilities have the same value and are just used to represent the response functions in different theories [99]. For the imaginary parts, they depend on the sign of the frequency ω. Similarly, we have an equation for the time-ordered polarisabilities:

$$P = \tilde{P} + \tilde{P}vP \tag{5.18}$$

it is also interesting to note that the bare Coulomb potential v can be further divided into a term $\bar{v}$ which represents the Coulomb term without the long-range component v_0:

$$\bar{v} = \begin{cases} v_{\mathbf{G}} & \mathbf{G} \neq 0 \\ 0 & \mathbf{G} = 0 \end{cases} \tag{5.19}$$

and $\bar{v}$ is responsible for the LFE [99]. As for the macroscopic dielectric function without the local field effects (NLF) [99]:

$$\varepsilon_M^{NLF} = \lim_{\mathbf{q}\to 0} \varepsilon_{00}(\mathbf{q},\omega) = \lim_{\mathbf{q}\to 0}[1 - v_0(\mathbf{q})\tilde{\chi}_{00}(\mathbf{q},\omega)] = \varepsilon'_M \tag{5.20}$$

So equation 5.6 that is used in OptaDOS neglects the LFE.

5.2.4 Random Phase Approximation

Based on equation 5.11 and 5.14, we could see that if the system is not polarisable ($\tilde{\chi} = 0$), the total electric field is the same as the external field. Within DFT and the independent particle approximation, the Random Phase Approximation corresponds to the irreducible microscopic polarisability $\tilde{\chi}$ approximated by an independent particle polarisability χ^0 [97, 99, 123]:

$$\chi^0_{\mathrm{DFT}}(\mathbf{G};\mathbf{G}',\omega) = 2\sum_{v,c,\mathbf{k}} \frac{\langle\phi_{v\mathbf{k}}|e^{-i\mathbf{G}.\mathbf{r}}|\phi_{c\mathbf{k}}\rangle\langle\phi_{c\mathbf{k}}|e^{i\mathbf{G}'.\mathbf{r}'}|\phi_{v\mathbf{k}}\rangle}{\omega - (\epsilon_{c\mathbf{k}} - \epsilon_{v\mathbf{k}}) + i\delta} \tag{5.21}$$

where $\phi_{i\mathbf{k}}$ and $\epsilon_{i\mathbf{k}}$ are the Kohn-Sham eigenfunctions and eigenvalues. Then using $\varepsilon = 1 - v\chi^0$ we are able to calculate the microscopic dielectric function. Within DFT-RPA, the xc effects in the response are neglected and the Coulomb potential is given by the time-independent Hartree potential.

One thing to note is that here we are using a two-electron approximation of Fermi's golden rule for consistency with the correct macroscopic dielectric function (equation 5.12) and the LFE is included. For the RPA calculations in this thesis, we use the YAMBO code [105, 126]. In contrast, in OptaDOS [120, 121], equation 5.6 is applied and an average operation described by 5.9 is used which neglects the LFE.

Beyond DFT, we have also discussed the GW approximation that gives the quasi-particle energies which are the true excitation energies. Thus another choice for the Random Phase Approximation is the GW-RPA which has similar expression to equation 5.21 by replacing the DFT eigenvalues with the quasi-particle energies E_i [99]:

$$P^0_{\mathrm{GW}}(\mathbf{G};\mathbf{G}',\omega) = 2\sum_{v,c,\mathbf{k}} \frac{\langle\phi_{v\mathbf{k}}|e^{-i\mathbf{G}.\mathbf{r}}|\phi_{c\mathbf{k}}\rangle\langle\phi_{c\mathbf{k}}|e^{i\mathbf{G}'.\mathbf{r}'}|\phi_{v\mathbf{k}}\rangle}{\omega - (E_{c\mathbf{k}} - E_{v\mathbf{k}}) + i\delta} \tag{5.22}$$

As for the GW approximation, a more promising method to calculate the polarisability is to use the Bethe-Salpeter equation which involves the electron-hole interaction and will be fully explored later in this chapter.

5.2.5 Linear-response Theory

Going beyond DFT, we have introduced the time-dependent density functional theory (TDDFT) in section 4.2. TDDFT is more physically accurate as it describes the response of a fully interacting many-electron system when exposed to a time-dependent external potential, which in the case of EELS corresponds to the field of an external electron. This time-dependent external perturbation is weak and the system does not deviate strongly from its initial state. Under this circumstance, calculating the full time-dependent density will give the correct results but is not necessary [98]. It is preferable to calculate these small deviations directly instead of extracting them from the full solutions. This is achieved by using linear-response theory. In the case of the system initially in the ground-state with a small time-dependent external potential switched on at t_0, the induced charge density is related to the external potential via [97–99]:

$$n_{\mathrm{ind}}(\mathbf{r},t) = \int \mathrm{d}\mathbf{r}'\mathrm{d}t'\chi(\mathbf{r},\mathbf{r}',t-t')V_{ext}(\mathbf{r}',t') \tag{5.23}$$

where the linear density-response function $\chi(\mathbf{r},\mathbf{r}',t-t')$, also known as the full polarisability (reducible) is given by:

$$\chi(\mathbf{r},\mathbf{r}',t-t') = \left.\frac{\delta n(\mathbf{r},t)}{\delta V_{ext}(\mathbf{r}',t')}\right|_{V_{ext}(\mathbf{r}',t')=V^0_{ext}(\mathbf{r}')} \tag{5.24}$$

By using the Lehmann representation, it can also be written in the frequency domain as [98, 99]:

$$\begin{aligned}\chi(\mathbf{r},\mathbf{r}',\omega) = \sum_{n=1}^{\infty}\Big\{ &\frac{\langle\Psi_0|n(\mathbf{r},0)|\Psi_n\rangle\langle\Psi_n|n(\mathbf{r}',0)|\Psi_0\rangle}{\omega-(E_n-E_0)+i\delta} \\ &- \frac{\langle\Psi_0|n(\mathbf{r}',0)|\Psi_n\rangle\langle\Psi_n|n(\mathbf{r},0)|\Psi_0\rangle}{\omega+(E_n-E_0)+i\delta}\Big\}\end{aligned} \tag{5.25}$$

where Ψ_0 and Ψ_n are the ground-state and n^{th} excited-state wavefunction and E_0 and E_n are the corresponding energies. It can be seen that the full polarisability $\chi(\mathbf{r}, \mathbf{r}', \omega)$ has poles at the excitation energies of the N-particle system.

It is also possible to describe the induced charge density using the time-dependent Kohn-Sham potential V_{ks} via:

$$n_{\text{ind}}(\mathbf{r}, t) = \int \mathrm{d}\mathbf{r}' \mathrm{d}t' \chi^0(\mathbf{r}, \mathbf{r}', t - t') V_{ks}(\mathbf{r}', t') \tag{5.26}$$

where the independent particle polarisability as depicted in equation 5.21 describes the linear response of the non-interacting Kohn-Sham system. Equation 5.21 can be rewritten in the real space and frequency domain as:

$$\chi^0(\mathbf{r}, \mathbf{r}', \omega) = \sum_{v,c,\mathbf{k}} \frac{(f_v - f_c)\phi^*_{v\mathbf{k}}(\mathbf{r})\phi_{c\mathbf{k}}(\mathbf{r})\phi^*_{c\mathbf{k}}(\mathbf{r}')\phi_{v\mathbf{k}}(\mathbf{r}')}{\omega - (\epsilon_{c\mathbf{k}} - \epsilon_{v\mathbf{k}}) + i\delta} \tag{5.27}$$

where ϕ_c and ϕ_v are the Kohn-Sham eigenfunctions, ϵ_c and ϵ_v are the corresponding energies and f_v and f_c are Fermi occupation numbers. it is obvious to see that the independent particle polarisability $\chi^0(\mathbf{r}, \mathbf{r}', \omega)$ has poles at the excitation energies of the fictitious Kohn-Sham system.

The two response functions χ and χ^0 are related to each other, as shown in [97–99]:

$$\chi = \chi^0 + \chi^0(v + f_{xc})\chi \tag{5.28}$$

$$\chi = (1 - \chi^0 v - \chi^0 f_{xc})^{-1}\chi^0 \tag{5.29}$$

with v being the functional derivative of the Hartree potential (equation 4.10)

with respect to the density which equals to the bare Coulomb potential. And the exchange and correlation kernel f_{xc} is defined as the functional derivative of the time-dependent exchange and correlation potential with respect to the time-dependent density, evaluated at the ground-state density n_0:

$$f_{xc}(\mathbf{r}, \mathbf{r}', t, t') = \left. \frac{\delta V_{xc}[n](\mathbf{r}, t)}{\delta n(\mathbf{r}', t')} \right|_{n(\mathbf{r}', t')=n_0(\mathbf{r}')} \tag{5.30}$$

In terms of the adiabatic local density approximation (ALDA), the exchange part is given by [98]:

$$f_x(\mathbf{r}, \mathbf{r}') = \frac{\delta^2 E_x^{\mathrm{LDA}}[n_0]}{\delta n_0(\mathbf{r}) \delta n_0(\mathbf{r}')} = -\delta(\mathbf{r} - \mathbf{r}') \Big[\frac{1}{9\pi n_0^2(\mathbf{r})} \Big]^{1/3} \tag{5.31}$$

and the correlation part can be calculated using the same method on the static LDA correlation energy.

The microscopic dielectric function can thus be calculated using equation 5.29 together with a retarded version of equation 5.16:

$$\varepsilon^{-1}_{\mathbf{G}\mathbf{G}'}(\mathbf{q}, \omega) = \delta_{\mathbf{G}\mathbf{G}'} + v_{\mathbf{G}}(\mathbf{q}) \chi_{\mathbf{G}\mathbf{G}'}(\mathbf{q}, \omega) \tag{5.32}$$

Comparing the methods to calculate the microscopic dielectric function that we have discussed so far, it is possible to see that they are interlinked. The independent particle approximation (IPA) corresponds to the case of setting to zero the terms in equation 5.29 coming from the variation of the Hartree ($v = 0$) and the exchange and correlation ($f_{xc}^{\mathrm{IPA}} = 0$) potentials. From equation 5.32, we could see that such approximation neglects the all the off-diagonal components of the matrix $\varepsilon^{-1}_{\mathbf{G}\mathbf{G}'}$ and thus the local field effects (LFE) is not included. The next level of calculation, the random phase approximation (RPA) neglects only

the exchange and correlation kernel ($f_{xc}^{\mathrm{RPA}} = 0$) and the LFE is included. And finally in TDDFT, or more specifically, ALDA (also known as TDLDA), both the microscopic components of the induced Hartree potential and the variations of the exchange and correlation potential are involved, together with the LFE.

5.2.6 Bethe-Salpeter Equation

In experimental EELS, the features are a result of the collective excitations and the electron-hole interband transitions, or a coupled superposition of both. The GW-RPA method discussed in the previous section includes the true excitation energies. However, the effects related to the two-particle interaction between an excited electron and the associated hole are still neglected. Such effects are known as the excitonic effects, which are large for insulators and small for narrow-gap semiconductors. Excitons in metals are rarely reported due to their short life time. This is caused by the the abundance of free conducting electrons in metals, which reduces the Coulomb interaction of electron-hole pairs by the shielding effect and thus the exciton state of electron-hole pairs can not be maintained. The description of the excitonic effects can be achieved by the inclusion of the vertex function as described in the Hedin's equations and using the Bethe-Salpeter equation (BSE) [64, 99, 127–129].

In the case there is no interaction between the electron and the hole, the two-particle correlation function L^0 describes the independent motion of an electron (from point 3 to point 1) and a hole (from point 2 to point 4) which is represented by a single-particle Green's function [99, 127]:

$$L^0(1,2,3,4) = -iG(1,3)G(4,2) \tag{5.33}$$

To describe the electron-hole interactions, we first need a two-particle Green's function [99, 127]:

$$G(1,2,3,4) = (-i)^2 = \langle N|\hat{T}[\hat{\psi}(1)\hat{\psi}(3)\hat{\psi}^\dagger(4)\hat{\psi}^\dagger(2)]|N\rangle \tag{5.34}$$

As for the two-particle correlation function of the interacting particles L, it is a 4-point (reducible) polarisability [99, 127]:

$$L(1,2,3,4) = L^0(1,2,3,4) - G(1,2,3,4) \tag{5.35}$$

and it can also be calculated by a Dyson equation called the Bethe-Salpeter equation (BSE) [99, 127]:

$$\begin{aligned} L(1,2,3,4) &= -i\frac{\delta G(1,2)}{\delta V_{ext}(3,4)} \\ &= L^0(1,2,3,4) + \int \mathrm{d}(5678) L^0(1,2,5,6) K(5,6,7,8) L(7,8,3,4) \end{aligned} \tag{5.36}$$

where the kernel K is defined as [99, 127]:

$$\begin{aligned} K(5,6,7,8) &= v(5,6,7,8) + i\frac{\delta\Sigma(5,6)}{\delta G(7,8)} \\ &= v(5,7)\delta(5,6)\delta(7,8) + i\frac{\delta\Sigma(5,6)}{\delta G(7,8)} \end{aligned} \tag{5.37}$$

where $v(5,6,7,8)$ is the 4-point extension of the Coulomb potential.

The self energy $\Sigma(5,6)$ is further approximated using the quasi-particle self energy $\Sigma(5,6) = iG(5,6)W(6,5)$as:

$$\frac{\delta\Sigma}{\delta G} = \frac{\delta(GW)}{\delta G} = W + G\frac{\delta(W)}{\delta G} \approx W \tag{5.38}$$

and thus the kernel K becomes [99, 127]:

$$K(5,6,7,8) = v(5,7)\delta(5,6)\delta(7,8) - W(5,6)\delta(5,7)\delta(6,8) \tag{5.39}$$

Here, the v corresponds to the repulsive bare Coulomb interaction while W is the screened Coulomb attraction between electron and hole. The GW approximation used corresponds to the first iteration of the Hedin's pentagon with the self energy described by equation 4.62. In other words, we are using the GW quasi-particle energies with the DFT wavefunctions [99, 128]. Another approximation is that for the screened interaction W, a static approximation is used due to the fact that the dynamical effects in the electron-hole screening and in the one-particle Green's function tend to cancel each other and are thus both neglected [99, 128, 130, 131].

In practice, expecting that only a limited number of electron-hole (eh) pairs will contribute to each excitation, equation 5.36 for the polarisability L is usually transformed in an eigen value problem for an effective 2-particle Hamiltonian by representing the basis set by pairs of single-particle eigenfunctions [99, 132–134]:

$$L_{(vc)(v'c')} = [H^{exc} - I\omega]^{-1}_{(vc)(v'c')}(f_{v'} - f_{c'}) \tag{5.40}$$

where I is the identity operator and the excitonic Hamiltonian H^{exc} is defined as [99, 128, 133, 134]:

$$H^{exc}_{(vc)(v'c')} = \begin{pmatrix} H^{reso}_{(vc)(v'c')} & H^{coupling}_{(vc)(c'v')} \\ -\left[H^{coupling}_{(vc)(c'v')}\right]^* & -\left[H^{reso}_{(vc)(v'c')}\right]^* \end{pmatrix} \tag{5.41}$$

the matrix H^{reso} corresponds to the resonant contributions, which are active for

positive frequencies, and $-\left[H^{reso}\right]^*$ corresponds to the anti-resonant ones, that contribute to negative frequencies. The off-diagonal matrices are the coupling terms that describe the mixing of the positive and negative frequency transitions [99, 128, 134]:

$$H^{reso}_{(vc)(v'c')} = H^{diag}_{(vc)(v'c')} + 2v_{(vc)(v'c')} - W_{(vv')(cc')} \tag{5.42}$$

$$H^{coupling}_{(vc)(c'v')} = 2v_{(vc)(c'v')} - W_{(vc')(cv')} \tag{5.43}$$

The diagonal part involves the quasi-particle energies obtained from the GW approximation [99, 128, 134]:

$$H^{diag}_{(vc\mathbf{k})(v'c'\mathbf{k}')} = (E_{c\mathbf{k}} - E_{v\mathbf{k}})\delta_{vv'}\delta_{cc'}\delta_{\mathbf{k}\mathbf{k}'} \tag{5.44}$$

and $v_{(vc)(v'c')}$ is the repulsive electron-hole exchange and $W_{(vv')(cc')}$ is the attractive screened electron-hole interaction [99, 134]:

$$v_{(vc\mathbf{k})(v'c'\mathbf{k}')} = \frac{4\pi}{\Omega}\sum_{\mathbf{G}\neq 0}\frac{1}{|\mathbf{G}|^2}\langle c\mathbf{k}|e^{i\mathbf{G}.\mathbf{r}}|v\mathbf{k}\rangle\langle v'\mathbf{k}'|e^{-i\mathbf{G}.\mathbf{r}}|c'\mathbf{k}'\rangle \tag{5.45}$$

and

$$W^{scr}_{(vc\mathbf{k})(v'c'\mathbf{k}')} = \frac{4\pi}{\Omega}\sum_{\mathbf{G}\mathbf{G}'}\frac{\varepsilon^{-1}_{\mathbf{G}\mathbf{G}'}(\mathbf{q})}{|\mathbf{q}+\mathbf{G}|^2}\langle c\mathbf{k}|e^{i(\mathbf{q}+\mathbf{G}).\mathbf{r}}|c'\mathbf{k}'\rangle\langle v'\mathbf{k}'|e^{-i(\mathbf{q}+\mathbf{G}').\mathbf{r}'}|v\mathbf{k}\rangle\delta_{\mathbf{k}-\mathbf{k}',\mathbf{q}.} \tag{5.46}$$

The coupling terms are much smaller than the resonant and anti-resonant terms and are usually neglected in the calculation of the absorption spectrum. However, for the modelling of EELS, which involves the real part of the dielectric

matrix, the coupling terms can no longer be neglected as it contains transitions at both positive and negative frequencies by the Kramers-Krönig relation [26,64,99]. Compared to TDDFT, BSE is physically more straightforward by involving the excitonic effects and quasi-particle energies, though it is computationally more demanding.

5.3 Predicted Transition Energy

In some materials, atoms of the same elements can exist at two or more atomic sites and thus experience a completely different chemical environment. For example, in Fe_3O_4, Fe coexists at two cation sites: octahedral and tetragonal. The experimental EELS gives us an overall spectrum that includes the effects of atoms from both sites. However, in EELS modelling, the spectrum is obtained separately for each individual site and thus it is vital to correctly align them with the predicted transition energy and sum up for comparison. There are two methods applied in this thesis to obtain the theoretical transition energy, Δ Self-Consistent-Field method (Δ SCF) in all-electron calculations [135–137] and the method proposed by Mizoguchi [138] for pseudopotential calculations.

In all-electron calculation (AE), the ΔSCF method is applied where the predicted transition energy E_{TE} is equal to the total energy difference between the excited and the ground states. The excited state corresponds to the state in which there is a core hole with the missing electron occupying the lowest unoccupied level of the ground-state system:

$$E_{TE} = E_{AE}^{exc} - E_{AE}^{gro} \tag{5.47}$$

Such evaluation is not valid when pseudopotentials (PS) are used due to the frozen core approximation which neglects the impact of core electrons. Thus

an additional term that includes the contribution of core orbitals is necessary E_{atom}^{core}:

$$E_{TE} = E_{PS}^{exc} - E_{PS}^{gro} + \Delta E_{atom}^{core} \tag{5.48}$$

where E_{PS}^{exc} and E_{PS}^{gro} correspond to the total energy of the excited state calculated with the corehole pseudopotential and the ground state performed with the non-corehole pseudopotential. ΔE_{atom}^{core} is evaluated by the isolated atom calculation via:

$$\Delta E_{atom}^{core} = \Delta E_{AE(atom)} - \Delta E_{PS(atom)} \tag{5.49}$$

where $\Delta E_{AE(atom)}$ is the energy difference between the excited state and ground state obtained in the all-electron calculations with an isolated atom instead of the whole structure. $\Delta E_{PS(atom)}$ is the energy difference of the isolated atom calculations with the corehole pseudopotential and with the non-core hole pseudopotential. $\Delta E_{PS(atom)}$ represents the contribution of valence orbitals to $\Delta E_{AE(atom)}$ and is subtracted to avoid double-counting the energy of the valence electron.

The predicted transition energy is the energy required to create a core hole and thus similar to bandgap in JDOS, in EELS, below E_{TE} no edges should be seen. It hence provides information regarding the edge onset which is vital when summing up individual spectra.

5.4 Practical Calculations

In this section, we will illustrate the practical aspects of running the spectral calculations. The goal is to highlight the convergence parameters, in addition to the ones discussed in 4.4, specifically for the spectral calculations or in more

detail.

As for the band structure and DOS-related calculations, they are performed with OptaDOS [120, 121] on top of the DFT calculations using CASTEP [48]. While for the modelling of the low-loss EELS, there are five main types of spectral calculations: DFT-IPA, DFT-RPA, linear-response TDDFT, GW-RPA and GW-BSE. The DFT-IPA calculations are performed with OptaDOS [120, 121] with the DFT calculations with different exchange and correlation functionals using CASTEP [48]. The DFT-RPA calculations with and without LFE discussed in the thesis are performed with YAMBO [105] with the ground-state calculations using Quantum Espresso [112,113]. For the rest of the low-loss EELS calculations, the ground-state calculations are performed with Quantum Espresso [112, 113], the excited-state calculations (GW) are done with YAMBO [105] and the spectral calculations (RPA, linear-response TDDFT, and BSE) use YAMBO [105] as well. Regarding the core-loss EELS for the study of beryllium-oxide systems, OptaDOS [120, 121] is used together with CASTEP [48].

5.4.1 Convergence in IPA

For the independent particle approximation, the imaginary part of the dielectric function is calculated using equation 5.6 [120, 121]:

$$\varepsilon_2(\omega) = \frac{4\pi}{q^2\omega} \sum_{v,c,\mathbf{k}} \left| \left\langle \phi_{c\mathbf{k}} \middle| e^{i\mathbf{q}.\mathbf{r}} \middle| \phi_{v\mathbf{k}} \right\rangle \right|^2 \delta(\epsilon_{c\mathbf{k}} - \epsilon_{v\mathbf{k}} - \omega) \tag{5.50}$$

Thus, other than the Spectral k-point as discussed in the previous chapter, which requires a convergence test for all methods listed in this thesis, we also need to define the number of bands (occupied and unoccupied) used in the calculation. The number of unoccupied bands needs a careful convergence test until any further increase has no effect on the simulated spectrum within the targeted energy

range.

As for the core-loss EELS calculations, another important factor that needs to be considered is the core hole effect, which corresponds to the system with an inner-shell electron removed. It is achieved by using an excited pseudopotential for one atom and the interaction between the core hole and the excited electron was treated within the single-particle electronic structure method [16,17,58,114]. However, such an approach will introduce a defect into the crystal structure and thus break the translational symmetry of the crystal. To minimise the mutual interaction of excited atoms, the supercell approach is adopted which forms a large cell with only one of the atoms in each cell to be excited. The core hole is instantaneously screened by the valence electrons while the lattice is assumed to have no time to relax. The size of the supercell requires a convergence test with respect to the spectra, as the larger the size, the computationally more demanding the calculation is.

5.4.2 Convergence in RPA with LFE

To include the local-field effects (LFE) for the random phase approximation (RPA), we need to calculate the microscopic dielectric function which is a non-diagonal matrix for inhomogeneous systems [105]:

$$\varepsilon^{-1}_{\mathbf{GG'}}(\mathbf{q},\omega) = \delta_{\mathbf{GG'}} + v_{\mathbf{G}}(\mathbf{q})\chi_{\mathbf{GG'}}(\mathbf{q},\omega) \tag{5.51}$$

where the RPA response function $\chi_{\mathbf{GG'}}$ is given by a Dyson-like screening equation [105]:

$$\chi_{\mathbf{GG'}}(\mathbf{q},\omega) = \chi^0_{\mathbf{GG'}}(\mathbf{q},\omega) + \sum_{\mathbf{G_1},\mathbf{G_2}} \chi^0_{\mathbf{GG_1}}(\mathbf{q},\omega) v_{\mathbf{G_1}}(\mathbf{q}) \delta_{\mathbf{G_1G_2}} \chi_{\mathbf{G_2G'}}(\mathbf{q},\omega) \tag{5.52}$$

and the non-interacting response function $\chi^0_{\mathbf{GG'}}$ is given by [105]:

$$\chi^0_{\mathbf{GG'}}(\mathbf{q},\omega) = 2\sum_{v,c,\mathbf{k}} \int_{BZ} \frac{d\mathbf{k}}{(2\pi)^3} \rho^*_{cv\mathbf{k}}(\mathbf{q},\mathbf{G}) \rho_{cv\mathbf{k}}(\mathbf{q},\mathbf{G'}) f_{v\mathbf{k}-\mathbf{q}}(1-f_{c\mathbf{k}}) \times \Big[\frac{1}{\omega + \epsilon_{v\mathbf{k}-\mathbf{q}} - \epsilon_{c\mathbf{k}} + i\delta} - \frac{1}{\omega + \epsilon_{c\mathbf{k}} - \epsilon_{v\mathbf{k}-\mathbf{q}} - i\delta}\Big] \tag{5.53}$$

The size of the dielectric matrix in **G** space is determined by specifying the number of **G** vectors or energy cut off in the screening known as the response block size. It depends strongly on the system inhomogeneity and also on the sum of bands in determining the non-interacting response function $\chi^0_{\mathbf{GG'}}$. Thus for any RPA with LFE calculations (not only for the DFT/GW-RPA calculations but also for the determination of the correlation self energy as discussed in section 4.4.2), the two parameters are converged simultaneously [105].

5.4.3 Convergence in Linear-response TDDFT

In the linear-response TDDFT, the response function is calculated using an equation very similar to the RPA one described by equation 5.52 [105]:

$$\chi_{\mathbf{GG'}}(\mathbf{q},\omega) = \chi^0_{\mathbf{GG'}}(\mathbf{q},\omega) + \sum_{\mathbf{G_1},\mathbf{G_2}} \chi^0_{\mathbf{GG_1}}(\mathbf{q},\omega)[v_{\mathbf{G_1}}(\mathbf{q})\delta_{\mathbf{G_1G_2}} + f^{xc}_{\mathbf{G_1G_2}}\chi_{\mathbf{G_2G'}}(\mathbf{q},\omega) \tag{5.54}$$

with the addition of f^{xc} which is the time-dependent exchange and correlation kernel. For calculations involved in this thesis, we use the adiabatic local density approximation (ALDA) for the kernel. Thus for the ALDA calculations, other than the two convergence parameters discussed in 5.4.2 which determines the size of the dielectric matrix in the reciprocal space and the number of bands respectively, an additional parameter associated with the size of the exchange

and correlation kernel needs convergence study.

5.4.4 Convergence in BSE

BSE is rewritten as an eigenvalue problem for the two-particle Hamiltonian. Take the matrix element of the resonant contribution as an example, which is described by equation 5.42 and 5.44 [105]:

$$H^{reso}_{(vc\mathbf{k})(v'c'\mathbf{k}')} = (E_{c\mathbf{k}} - E_{v\mathbf{k}})\delta_{vv'}\delta_{cc'}\delta_{\mathbf{k}\mathbf{k}'} + (f_{c\mathbf{k}} - f_{v\mathbf{k}})[2v_{(vc\mathbf{k})(v'c'\mathbf{k}')} - W_{(vc\mathbf{k})(v'c'\mathbf{k}')}] \tag{5.55}$$

Thus other than the k-point mesh of the DFT calculations which defines the $\mathbf{k}$, convergence tests are also required for the range of bands from which the electron-hole basis of the BSE kernel is constructed. Both occupied and unoccupied bands are needed. Other than the bands range, as for the electron-hole exchange v:

$$v_{(vc\mathbf{k})(v'c'\mathbf{k}')} = \frac{4\pi}{\Omega}\sum_{\mathbf{G}\neq 0}\frac{1}{|\mathbf{G}|^2}\langle c\mathbf{k}|e^{i\mathbf{G}.\mathbf{r}}|v\mathbf{k}\rangle\langle v'\mathbf{k}'|e^{-i\mathbf{G}.\mathbf{r}}|c'\mathbf{k}'\rangle \tag{5.56}$$

and the screened electron-hole interaction W:

$$W^{scr}_{(vc\mathbf{k})(v'c'\mathbf{k}')} = \frac{4\pi}{\Omega}\sum_{\mathbf{G}\mathbf{G}'}\frac{\varepsilon^{-1}_{\mathbf{G}\mathbf{G}'}(\mathbf{q})}{|\mathbf{q}+\mathbf{G}|^2}\langle c\mathbf{k}|e^{i(\mathbf{q}+\mathbf{G}).\mathbf{r}}|c'\mathbf{k}'\rangle\langle v'\mathbf{k}'|e^{-i(\mathbf{q}+\mathbf{G}').\mathbf{r}'}|v\mathbf{k}\rangle\delta_{\mathbf{k}-\mathbf{k}',\mathbf{q}.} \tag{5.57}$$

separate convergence tests are required to truncate the summations over the $\mathbf{G}$ and $\mathbf{G}'$ vectors by setting the cutoff energy parameters.

5.4.5 Energy Broadening

In addition to the convergence parameters, broadening is required when generating the spectral features. The first part of the broadening is associated with the finite number of k-point samples as discussed in 4.4.1. Thus a broadening scheme is required to broaden the eigenenergies obtained at a discrete sampling of the Brillouin Zone to a continuous spectral function. For all CASTEP and OptaDOS calculations discussed in this thesis, including the band structure, density of states, and the low-loss and core-loss EELS calculations, an adaptive broadening scheme is applied with a relative smearing of 0.4 to the calculation of the dielectric function. The calculated function is broadened by a Gaussian function with its width being proportional to the energy band gradient as described in Reference [121].

For both the low-loss and core-loss EELS calculations, the energy resolutions are still far better than the results obtained by experiments. One major cause is instrumental broadening due to the measurement process. Experimentally, the energy resolution is determined by the full width at half maximum (FWHM) of the zero-loss peak [2, 37] and is found to be between 1.2 and 1.8 eV for the experimental data used in this thesis. A slightly higher value is usually selected to broaden the simulated spectra. For low-loss EELS calculations using CASTEP and OptaDOS, a further Gaussian broadening with a fixed width of 2.0 eV is applied to the simulated loss function [121]. For Yambo, the broadening is achieved by setting a damping coefficient of 1.0 eV, utilised in the form of Lorentzian peaks to compare with the experiments. The values are selected by comparing the broadened simulated spectra with the experimental ones.

For the core-loss EELS, the broadening of the experimental spectra is also caused by the lifetime of the core hole and the lifetime of the excited state [49, 121]. The broadening due to the core hole lifetime depends on the atom and the edge. It is

caused by the fact that the core hole does not have an infinite lifetime, but decays by radiative or Auger electronic transitions from some occupied higher-energy shells [139]. The core hole lifetime effect can be modeled by a Lorentzian [49,140]. The final states also have finite lifetimes as the excited electron loses energy by emitting plasmons or creating electron-hole pairs until it falls to the Fermi level. The final state lifetime broadening increases with increasing energy and is modeled by a Lorentzian function with an energy-dependent width, as proposed by [140]. The core-loss EELS calculations discussed in this thesis are performed using CASTEP and OptaDOS and the instrumental broadening effects are taken into account by using a fixed-width Gaussian broadening of 1.0 eV. A fixed-width Lorentzian function of 0.5 eV and an additional Lorentzian function with an energy-dependent width of scale 0.1 are also added such that the total width of the Lorentzian used is the sum of the width of the fixed Lorentzian function and the energy above the Fermi level times the scale. The value of the scale is the default value as recommended by the OptaDOS user guide and the widths are selected by comparing the broadened simulated spectra with the experimental ones.

5.5 Computational Details

5.5.1 Example of Convergence Tests

For each material presented in this thesis, two main factors influence the convergence parameters. The first one is the element and the associated pseudopotentials selected. Different elements have different requirements for the energy cutoff because the distribution of their electron density and the localization of core versus valence electrons vary. Different pseudopotentials, as discussed in Section 4.4.1, have different approximations and thus hardness, which require energy cutoff convergence tests respectively. The second factor is the structure

itself regarding the arrangement of atoms, which requires different k-point sampling. For example, separate k-point sampling convergence tests are required for diamond and graphite although both of them are made of carbon atoms. However, if the same pseudopotentials of carbon are used, the same energy cutoff can be adopted in both structures. In this section, diamond is presented as an example to demonstrate how convergence tests are performed for the geometry optimisation and the low-loss EELS calculations, and beryllium metal is used as an example for the convergence test of core-loss EELS calculations with respect to the distance between core holes. The convergence tests regarding pseudopotential parameters (TB) and band gap calculations are discussed later in this chapter.

For the geometry optimisation, convergence tests are performed for the cutoff energy and the k-point sampling to reach a convergence of the total energy to be within 1 meV/atom. For the cutoff energy, for computational efficiency, separate convergence tests are performed for isolated atoms, and the larger energy cutoff is selected for a compound system. For example, in the case of BeO, energy convergence tests are conducted separately on isolated Be and O atoms to determine the appropriate energy cutoff. The higher of these values is then chosen to ensure sufficient accuracy for the compound calculations. An example of the energy cutoff convergence tests of the carbon is shown in Figure 5.1. For each structure, the k-point sampling convergence test is carried out in similar procedures to the energy cutoff convergence test, with the variable being the k-point sampling instead of the energy.

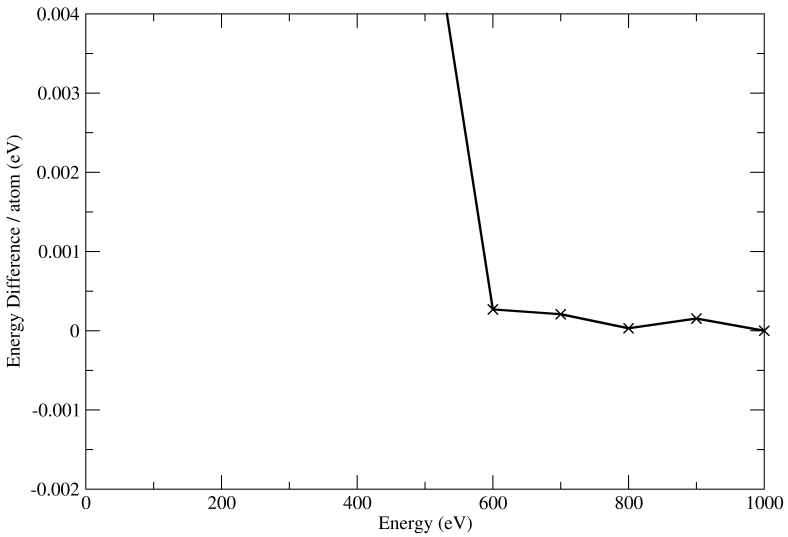


Figure 5.1: The convergence test of the energy cutoff for the total energy of carbon. The calculation is performed with CASTEP using PBE functional and is performed on an isolated carbon atom. The converged value of the energy cutoff is 600 eV.

For the low-loss EELS calculations of each structure, convergence tests of the cutoff energy, the k-point sampling for the self-consistent (scf) cycles, and the spectral one for the non-self-consistent (nscf) cycles, and the number of unoccupied bands have been performed such that any further increases have no effect on the simulated spectrum. An example of the convergence tests of the diamond is shown in Figure 5.2.

For the core-loss EELS calculations of each structure, excited pseudopotentials are generated for the interested core-loss edges by removing an electron from the 1s orbital. The convergence tests of the cutoff energy, the k-point sampling for the scf cycles and the spectral one for the nscf cycles, and the number of unoccupied bands are performed in similar procedures as for the low-loss EELS calculations. For minimisation of the mutual interactions of excited atoms, the supercell is used and the size is carefully checked with the additional convergence

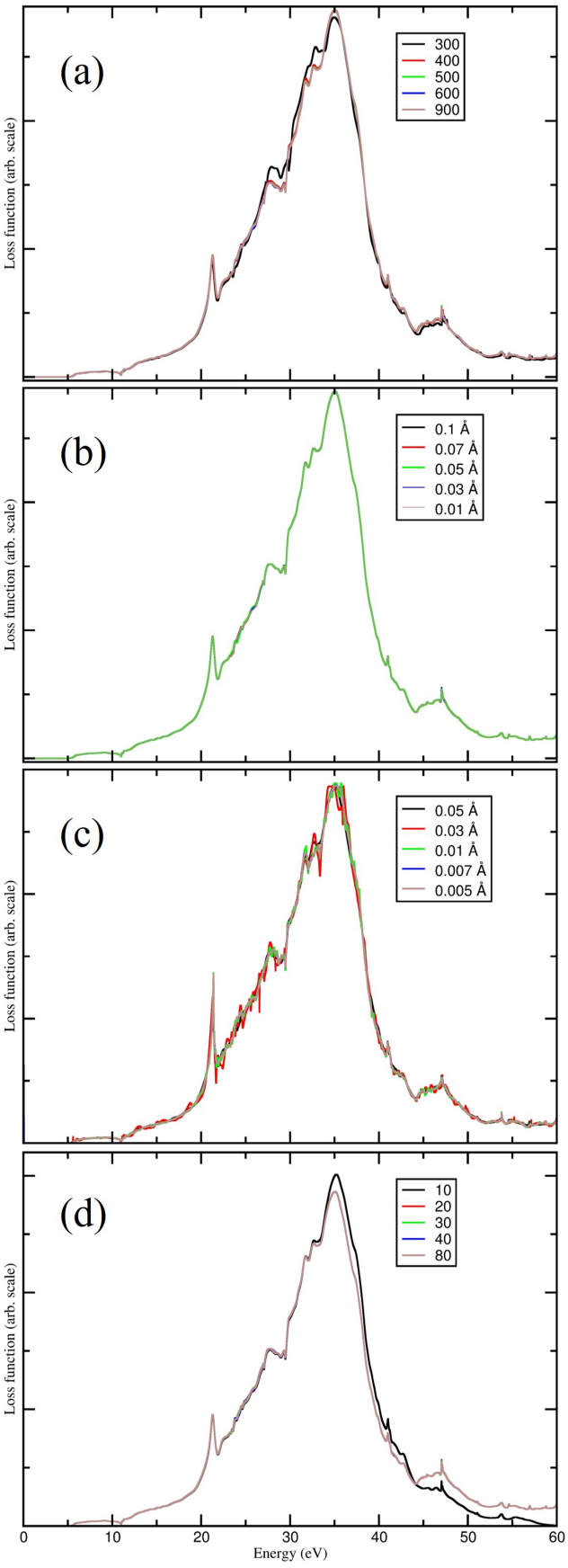


Figure 5.2: (Caption next page.)

Figure 5.2: (Previous page.) The convergence tests of calculated low-loss EELS of diamond with respect to (a) kinetic energy cutoff (b) k-point sampling (c) spectral k-point sampling (d) number of conduction bands. The calculations are performed with CASTEP using PBE functional. The converged values are kinetic energy cutoff = 500 eV, k-point sampling = $2\pi \times 0.1$Å, spectral k-point sampling = $2\pi \times 0.007$Å and number of conduction bands = 40.

test. An example of the convergence test with respect to the distance between core holes of beryllium metal is shown in Figure 5.3.

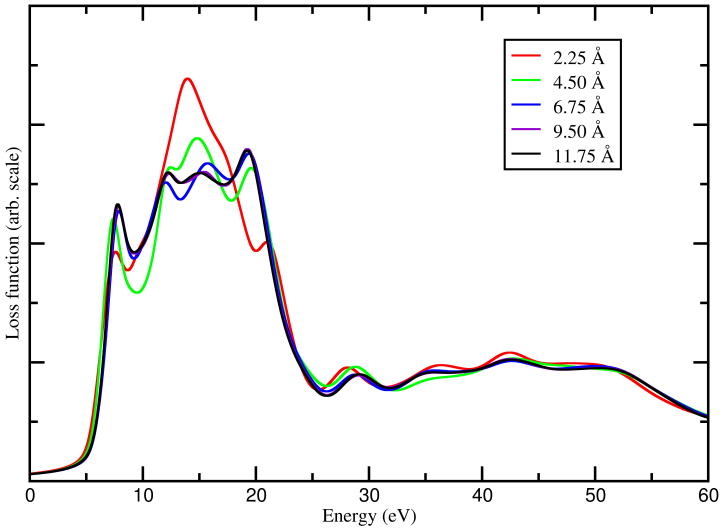


Figure 5.3: The convergence test of calculated core-loss EELS of Be metal with respect to the distance between core holes. The calculation is performed with CASTEP using PBE functional. Convergence is observed at a distance of 9.50 Å with minor differences in spectral features. However, the distance of 11.75 Å is selected for subsequent calculations to ensure higher accuracy.

5.5.2 Computational Setup for Chapters 5 and 6

Pseudopotentials

There are three elements involved in these two chapters: Be, O and H. The calculations have been performed with the CASTEP code [48] and OptaDOS [120,121] using ultrasoft pseudopotentials and the PBE exchange-correlation functional.

The default on-the-fly (OTF) pseudopotentials are used for oxygen and hydrogen for all calculations. As for beryllium, as described in Chapter 7, the OTF pseudopotential is used for geometry optimisation and low-loss EELS simulation, which treats all four electrons of beryllium ($1s^2 2s^2$) as valence electrons. For the Be K-edge EELS calculations, a modified pseudopotential is used which treats the inner $1s$ electrons as core electrons.

Convergence Parameters

The convergence tests are performed following the procedures outlined in 5.5.1. The energy cutoff convergence tests are carried out for each isolated atom of Be, O and H and the highest value is found to be 1000 eV as shown in Table 5.1. Thus the geometry optimisation calculations have been performed for each structure using a cutoff energy of 1000 eV and a k-point sampling of $2\pi \times 0.01$Å to reach a convergence of the total energy to be within 1 meV/atom.

Element	Energy cutoff (eV))
Be	1000
O	900
H	700

Table 5.1: Energy cutoff of Be, O and H.

For the low-loss EELS calculations of each structure, a cutoff energy of 1000 eV, a k-point sampling of $2\pi \times 0.01$Å for both scf and nscf cycles are used and the number of unoccupied bands, ranging between 30 and 200 are selected for different materials, such that any further increases do not affect the simulated spectrum.

For the core-loss EELS calculations of each structure, excited pseudopotentials are generated for the Be K-edge (with modified pseudopotential) and O K-edge by removing an electron from the $1s$ orbital. A cutoff energy of 1000 eV, a k-point sampling of $2\pi \times 0.08$Å for the scf cycles and a spectral k-point sampling

of $2\pi \times 0.03$Å, and a higher number of unoccupied bands for each structure are used, with converged supercell sizes respectively.

5.5.3 Computational Setup for Chapter 7

Pseudopotentials

There are seven elements involved in this chapter: C, Li, F, Si, Ti, O, and Zr. The calculations have been performed with the CASTEP code [48] using on-the-fly ultrasoft pseudopotentials and OptaDOS [120, 121]. There are four different functionals compared and discussed in this chapter: the Becke-Johnson functional (BJ), the Tran-Blaha functional (TB), the RSCAN functional and the standard PBE functional.

As described in the previous chapter, the cutoff pseudisation radius must be chosen such that the wavefunctions are pseudised close to the nucleus. The generation of BJ and TB pseudopotentials requires an accurate evaluation of the kinetic energy density. We have found that for transition elements that involve d-electrons, a smaller cutoff radius is required which makes the pseudopotential harder and the calculation more expensive. The cutoff radius is determined by performing atomic tests for the pseudopotential such that the eigenvalues of all-electron and pseudised atoms match. The cutoff radius of Ti is chosen to be $r_c = 0.5\,a_0$ for BJ and TB while for PBE and RSCAN the value is $r_c = 1.263\,a_0$. The cutoff radius of Zr is chosen to be $r_c = 1.0\,a_0$ for BJ and TB and $r_c = 1.471\,a_0$ for PBE and RSCAN.

In addition, for the TB calculation, we also need a convergence of the c parameter as described by equation 4.29, which is used to calculate the exchange potential. We first generate the pseudopotential using the BJ potential, i.e. $c = 1$, and start the plane-wave calculation. During the calculation, we have a second $\tilde{c}$ parameter which is calculated from the pseudodensity and varies self-consistently. Then we

start a new run with pseudopotential generated using the new $\tilde{c}$ and the process is repeated until $\tilde{c}$ does not change between runs [92]. The TB calculation is then performed by fixing the c parameter using the self-consistent $\tilde{c}$ value for both the pseudopotential generation and the electronic structure calculation. Further reading regarding the method can be found in reference [92]. A list of the self-consistent $\tilde{c}$ value can be found below:

Structure	Diamond	Graphite	LiF	Silicon	Rutile
$\tilde{c}$	1.19	1.30	1.54	1.09	1.47
Structure	ZrO_2 Monoclinic		ZrO Hexagonal		ZrO Orthorhombic
$\tilde{c}$	1.39		1.24		1.25

Table 5.2: Self-consistent $\tilde{c}$ values of the candidate structures.

The self-consistent $\tilde{c}$ values for diamond, LiF, and silicon as listed in Table 5.2 agree with the values from reference [92], with a difference less than 0.01. No reference values are found for the rest of the structures.

Convergence Parameters

For the geometry optimisation and low-loss EELS calculations, the convergence tests are performed following the procedures outlined in 5.5.1. The band structure calculations also follow a similar procedure as the low-loss EELS calculations.

The geometry optimisation calculations have been performed with the PBE and RSCAN functionals. A cutoff energy of 900 eV for both PBE and RSCAN and a k-point sampling of $2\pi \times 0.05$Å or less when setting the energy difference to be less than or equal to 1 meV/atom.

For the band structure calculations, the wavefunctions have been expanded in a plane wave basis set with a kinetic energy cutoff of 500 to 800 eV for different materials. A k-point sampling of $2\pi \times 0.05$Å has been used such that any further increases have no effect on the simulated band structures. The high symmetry

path has been obtained for each structure using SeeK-path [141].

For the Low-loss EELS calculations, the same $\tilde{c}$ parameters are adopted as listed in table 5.2 for the TB functional. We have carefully checked the convergence of the kinetic energy cutoff, the k-point sampling, and the spectral k-point sampling by comparing the simulated spectra. We have adopted similar parameters as for the band structures calculations with a kinetic energy cutoff of 500 to 800 eV, a k-point sampling of $2\pi \times 0.1$Å and a spectral k-point sampling of $2\pi \times 0.01$Å. In addition, as EEL spectroscopy involves the transition from the valence states to the excited states, we have also run a convergence test of the number of conduction bands for each material until any further increase makes no change to the simulated spectra.

5.5.4 Computational setup for Chapter 8

Pseudopotentials

There are seven elements involved in this chapter: C, Li, F, Si, Ti, O, and Zr. The ground-state DFT calculations are performed with Quantum Espresso [112,113] while the GW calculations and the optical spectra calculations are done with the YAMBO code [105]. As for the ground-state DFT calculations, the norm-conserving (NC) pseudopotentials are used as a requirement for the subsequent YAMBO calculations. The pseudopotentials are generated using the code ONCVPSP (Optimized Norm-Conserving Vanderbilt Pseudopotential) which is an accurate and relatively inexpensive type of norm-conserving pseudopotential [142]. For the IPA and RPA with LFE, both LDA and PBE functionals are used while the subsequent TDDFT (Linear-response Theory), GW, and BSE calculations are performed on top of LDA functional.

DFT Convergence Parameters

The geometry optimisation convergence tests are performed following the procedures outlined in 5.5.1. A cutoff energy of 80 Ry is used for both LDA and PBE functionals and the convergence of the k-point sampling is also carefully checked to reach an energy difference of less than or equal to 1 meV/atom.

GW Convergence Parameters

For the band structure calculations presented in section 9.3, different convergence parameters are tested with respect to the quasiparticle band gap, such that the energy difference is less than 0.03 eV. Overall there are five parameters that require convergence tests: the Exchange cutoff that governs the number of G-vectors used in the sum of the exchange self-energy; the Correlation band that specifies the range of bands entering in the sum over states in the correlation part of the self energy; the Dielectric cutoff corresponding to the number of G-vectors in the screening and thus the size of the dielectric matrix, which is required to be converged along with the RPA band that determines the number of bands entering in the sum over states in the RPA response function; the Brillouin zone sampling (k-point sampling) for both the exchange and correlation parts of the self energy. The converged parameters are shown in Table 5.3 and the convergence tests are shown in Figure 5.4.

Structure	Exchange cutoff (Ry)	RPA band	Dielectric cutoff (Ry)	Correlation band	k-point sampling
Diamond	10	50	14	80	9 9 9
LiF	60	80	15	140	6 6 6
Silicon	10	60	9	80	10 10 10
TiO2	50	80	11	180	2 4 2
ZrO_2 Monoclinic	40	90	11	190	5 5 5
Rutile	40	90	11	170	3 3 6

Table 5.3: Converged parameters for the GW calculations.

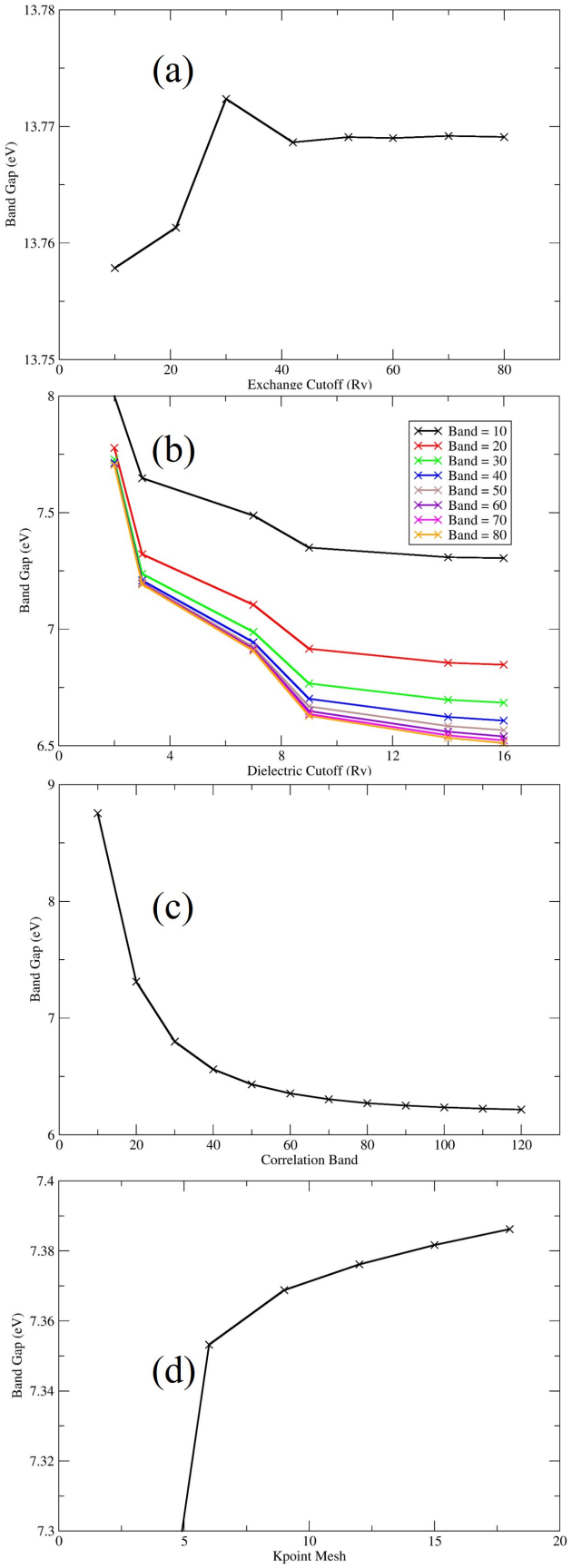


Figure 5.4: (Caption next page.)

Figure 5.4: (Previous page.) The convergence tests of quasiparticle band gap of diamond with respect to (a) exchange cutoff (b) RPA band and dielectric cutoff (c) correlation band (d) k-point sampling. The calculations are performed with YAMBO using GW method on top of LDA and the converged parameters can be found in Table 5.3.

RPA and TDDFT Convergence Parameters

For RPA and the subsequent TDDFT and BSE calculations, the parameters are chosen by performing convergence tests such that any further increases have no effect on the simulated spectrum. For RPA calculations, there are three parameters to be converged: the Dielectric cutoff and the RPA band as described in the previous section and the k-point sampling. As for the TDDFT calculations using YAMBO, there is an additional parameter, the Kernel cutoff that specifies the size of the exchange and correlation kernel. Same convergence parameters are used for RPA calculations using LDA and PBE functionals and TDDFT calculations as shown in Table 5.4. The convergence tests are shown in Figure 5.5.

Structure	Kernel cutoff* (mRy)	RPA band	Dielectric cutoff (Ry)	k-point sampling
Diamond	500	40	11	15 15 15
Graphite	500	60	11	21 21 7
LiF	2500	120	9	8 8 8
Silicon	5000	50	9	8 8 8
TiO2	1000	220	9	3 6 3
ZrO Hexagonal	5000	140	7	4 8 4
ZrO_2 Monoclinic	1000	240	7	4 4 4
ZrO Orthorhombic	1000	250	5	8 8 4
Rutile	5000	100	13	5 5 10

Table 5.4: Converged parameters for the RPA and TDDFT calculations. Kernel cutoff* is used only for the TDDFT calculations.

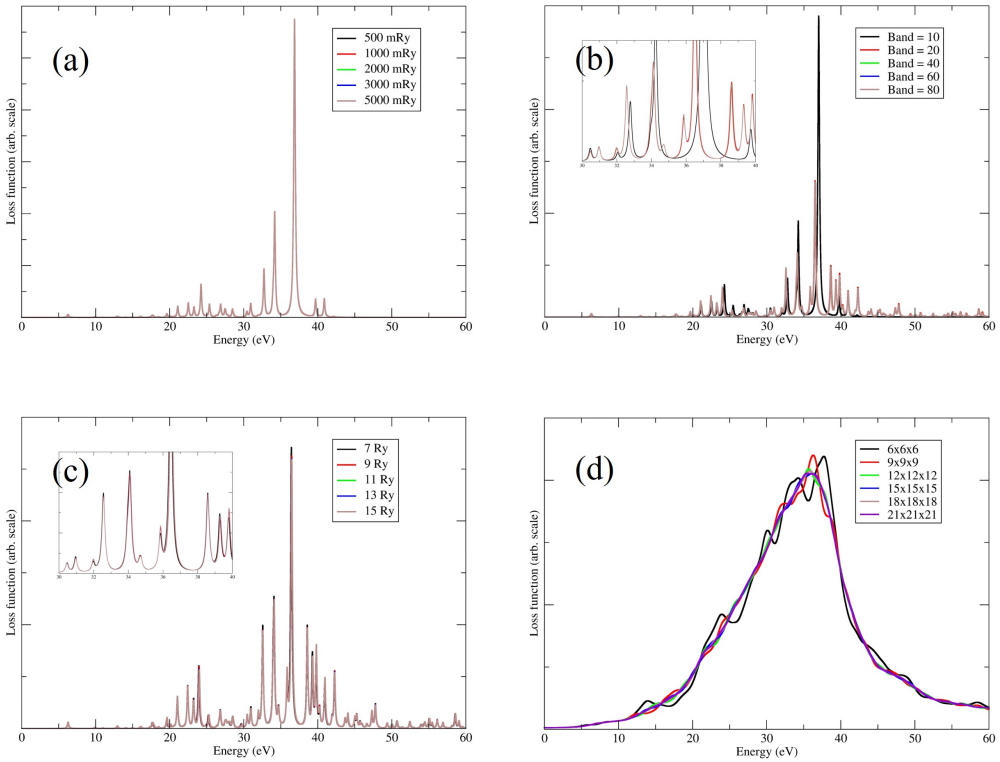


Figure 5.5: The convergence tests of calculated EELS of diamond with respect to (a) kernel cutoff (b) RPA band (c) dielectric cutoff (d) k-point sampling. In practice, the RPA band and the dielectric are converged simultaneously. Separate graphs of (b) and (c) are just shown for clarity. A damping coefficient of 0.1 eV is applied except for the k-point sampling, in which a damping coefficient of 1.0 eV is used due to the large increase in the computational cost of increasing the k-point sampling. The converged parameters are shown in Table 5.4.

BSE Convergence Parameters

BSE is rewritten as an eigenvalue problem for the two-particle Hamiltonian with the size of a matrix $[N_v \times N_c \times K_{BZ}] \times [N_v \times N_c \times K_{BZ}]$ with N_v, N_c and K_{BZ} correspond to the number of valence bands, number of conduction bands and the number of k-points in the Brillouin zone. Thus, two parameters that require careful convergence tests are the band range and the k-point sampling. Another two parameters are the Exchange cutoff and the Interaction cutoff which govern the number of G-vectors used in the electron-hole exchange v (Equation 5.56

and the screened electron-hole interaction W (Equation 5.57 respectively. The convergence parameters are listed in the Table 5.5. The convergence tests are shown in Figure 5.6.

Structure	Exchange cutoff (Ry)	Interaction cutoff (Ry)	Band range (Ry)	k-point sampling
Diamond	20	1	1-14	15 15 15 0 0 0
LiF	20	1	5-60	8 8 8 0 0 0
Silicon	10	5	1-27	12 12 12 0 0 0
Rutile	20	4	3-120	7 7 14 0 0 0

Table 5.5: Converged parameters for the BSE calculations.

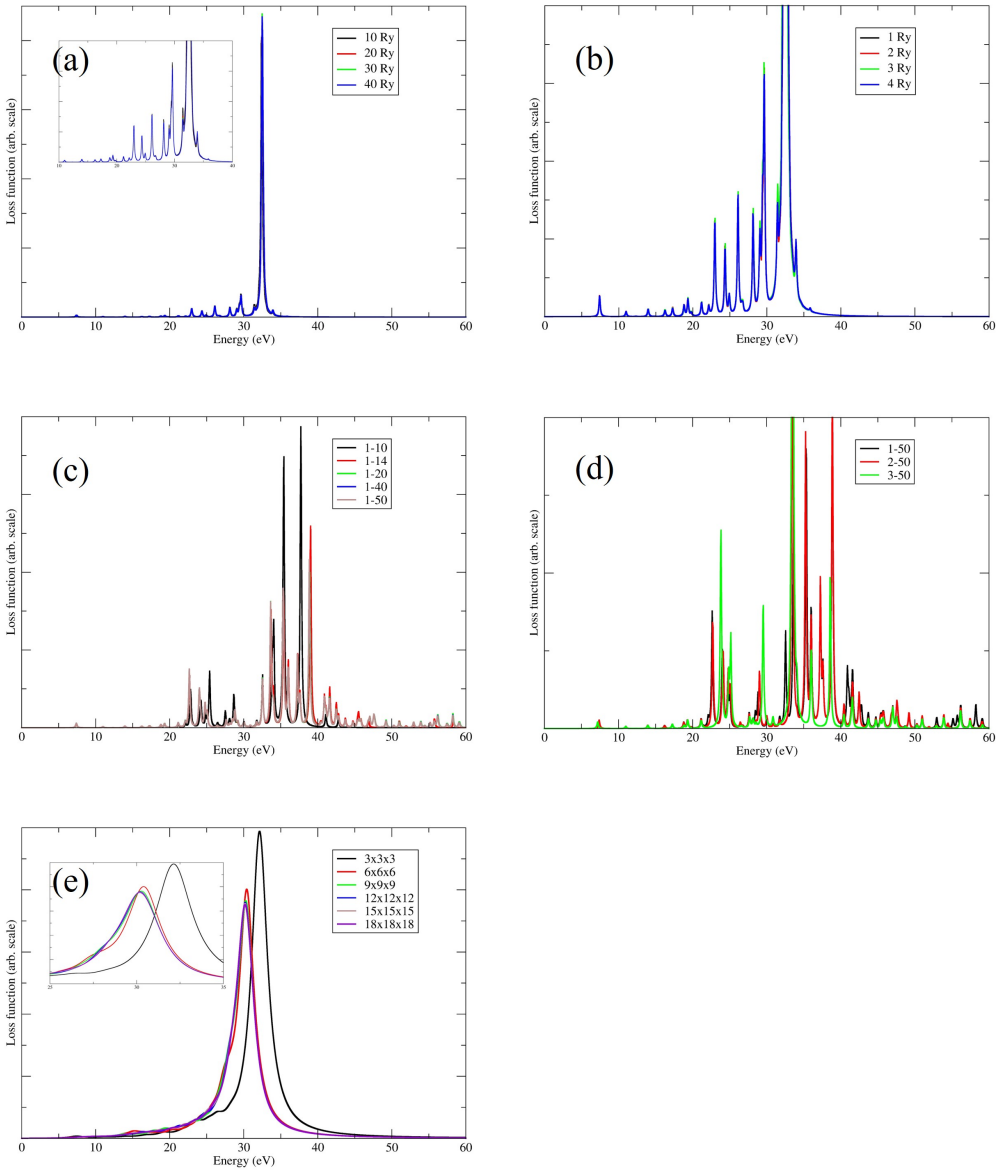


Figure 5.6: The convergence tests of calculated EELS of diamond with respect to (a) exchange cutoff (b) interaction cutoff (c) number of valence bands (d) number of conduction bands (e) k-point sampling. A damping coefficient of 0.1 eV is applied except for the k-point sampling, in which a damping coefficient of 1.0 eV is used due to the large increase in the computational cost of increasing the k-point sampling. The converged parameters are shown in Table 5.5.

Chapter 6

Case Study - System Containing Beryllium Oxides

This chapter explores an application of EELS modelling in materials science. The subject of interest is the corrosion of beryllium used as the wall material in the Joint European Torus (JET), currently the world's largest fusion reactor. The experimental spectra were kindly provided by Dr. Carmen Makepeace (University of Oxford) and measured using Scanning TEM (STEM) in a JOEL-ARM200F TEM. Full details regarding the experiments can be found in Carmen's thesis [143]. The experimental data was post-processed by Professor Rebecca Nicholls and Professor Sergio Lozano-Perez from the University of Oxford. The simulated spectra were calculated using the PBE functional in DFT with CASTEP and OptaDOS for selected structures which are discussed later in this chapter. The experimental and simulated EELS, both in the low-loss and core-loss regions, are compared to better understand how hydrogen isotopes are retained in beryllium.

This chapter starts with a brief introduction of the application of beryllium in the fusion reactor and possible corrosion mechanisms. The experimental samples and the selected structures for modelling are then discussed and finally the comparison

of the experimental and simulated spectra is presented, along with a discussion of potential phases present in the experiment.

6.1 Beryllium in the fusion reactor

Beryllium is a chemical element with atomic number 4. It is a silver-white metal with a hexagonal close-packed structure. Beryllium is used as a plasma-facing component (PFC) for the International Thermonuclear Experimental Reactor (ITER) first wall. The reason behind is that it has limited reactivity with hydrogen isotopes which results in lower fuel retention in JET-ILW compared to carbon PFCs [144, 145]. It also has a low atomic number which decreases fuel dilution and power losses [144]. In addition, it has a strong affinity for oxygen and thus good oxygen gettering from the plasma [144, 146].

In the Joint European Torus (JET) tokamak, beryllium tiles are subject to both power and particle loads. There are several mechanisms involved in the erosion and deposition processes. Firstly, like aluminium, beryllium tends to oxidise, forming BeO when exposed to air. On untreated Be surfaces, oxidation can occur to 4 nm monolayer depth [147]. The oxidation rate decreases with the square root of oxide thickness [147]. However, the phenomenon is exaggerated at elevated temperatures as beryllium atoms beneath the protective oxide layers diffuse to the surface to re-getter the oxygen from the plasma [147, 148].

Secondly, normally hydrogen or hydrogen isotopes do not dissolve in beryllium metals thus preventing high hydrogen isotope retention. However, beryllium has low surface binding-energy which results in strong physical sputtering [149]. As the beryllium atoms from the edge plasma redeposited onto PFC surfaces, there is a co-deposition of hydrogen with beryllium [146]. Deuterium, one of two stable isotopes of hydrogen, can be retained either in the atomic form or the molecular form. The atomic part of trapping is associated with the formation of beryllium

hydroxide which takes place in the beryllium oxide layer. The molecular part is caused by structure defects of the oxide layer which leads to bubble growth [150]. Deuterium retention in bulk beryllium was reported in reference [151–153].

Despite knowing that oxygen and hydrogen isotopes both exist in the beryllium tiles, the exact structures are still unknown. Knowledge of the structures formed is crucial in understanding the mechanism of corrosion of the material. Commonly used methods for structure determination such as X-ray crystallography cannot be performed as the area analysed contains multiple phases. In EELS, a smaller region is examined, which reduces the possibility of having more than one phase. This provides the incentive to deduce the structures present in the corrosion product by comparing the experimental and the DFT simulated EELS.

6.2 Candidate Structures

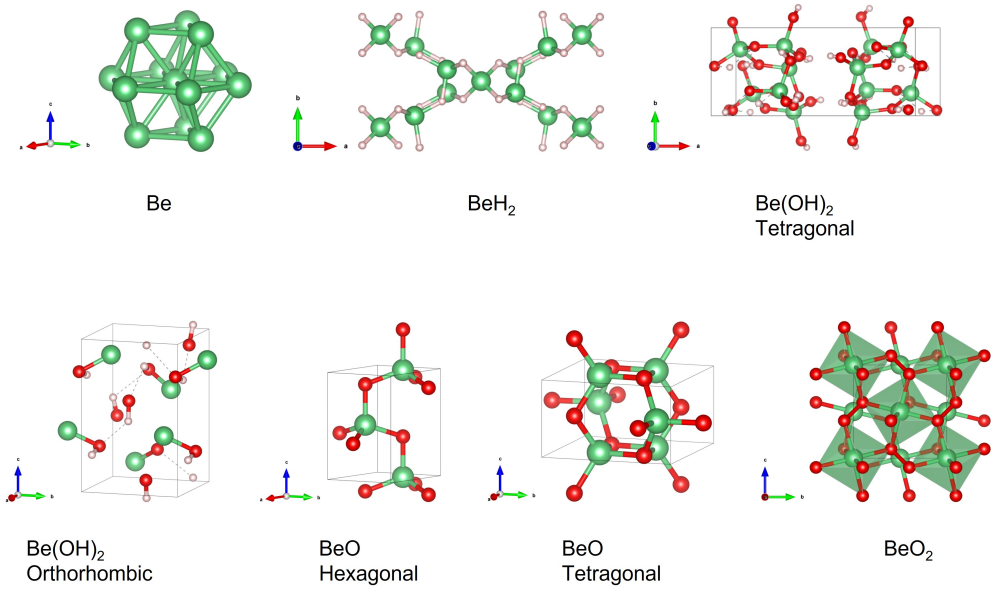


Figure 6.1: Selected structures in the Be-O-H system that are used to simulate the EELS with green beryllium atom, red oxygen atom, and white hydrogen atom.

Overall, as shown in Figure 6.1, seven structures have been taken into consideration: Be metal, BeH_2, α-$Be(OH)_2$ (tetragonal), β-$Be(OH)_2$ (orthorhombic), α-BeO (hexagonal), β-BeO (tetragonal) and BeO_2. The first five are all structures

that are stable at room temperature within the Be-O-H ternary system listed on ICSD [154]. H_2O and O_2 are not taken into consideration as they are gaseous at the operational scenario in the JET. Also, considering the high-temperature environment, the high-temperature phase β-BeO [155, 156] and pressure-induced structure BeO_2 are also considered [157].

Beryllium hydride was long believed to be a three-dimensional polymer consisting of infinite chains containing hydrogen bridges [158]. The exact structure, found in 1988 from powder diffraction is body-centered [159]. $Be(OH)_2$ has three known polymorphs: amorphous, metastable tetragonal α-$Be(OH)_2$ and orthorhombic β-$Be(OH)_2$ [160, 161]. Due to computational limitations, we only consider the tetragonal and the orthorhombic structures. Beryllium oxide finds its application in electronic technology due to its superior thermal conductivity while being an electrical insulator. It has a hexagonal wurtzite structure α-BeO at room temperature which transforms into a tetragonal phase at higher temperature [155, 156, 162]. Beryllium peroxide BeO_2 is predicted by computational modelling to exist at pressures above 89.6 GPa through the chemical reaction of BeO and oxygen. It crystallises in a FeS_2-type structure with Be occupying the face-centered sites, surrounded by six nearest neighbors of oxygen atoms [157]. The computational details of all the results presented in this chapter can be found in The Appendix.

6.3 Benchmark - The As-Received Sample

To begin with, a sample that has not been exposed to plasma was examined and its EELS results were used as a benchmark to test the accuracy of the modelling results. As it is not exposed to hydrogen, the only elements that should possibly be present are beryllium and oxygen. Two different regions of the sample were examined and they are labeled as the metallic and the oxide as shown in Figure

6.2.

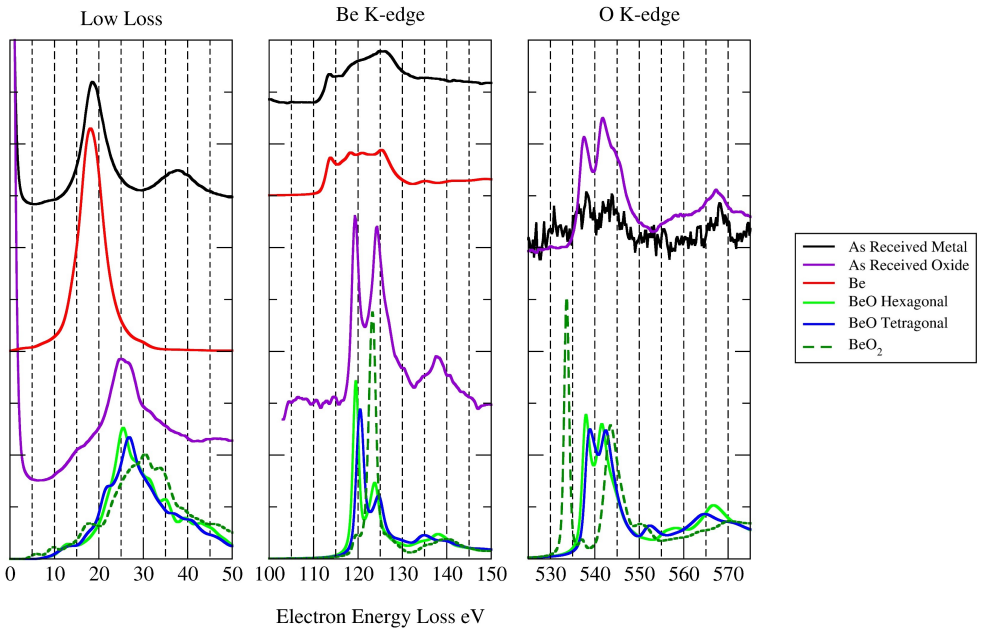


Figure 6.2: Comparison of the experimental EELS of the metallic region and the oxide region of the non-exposed as-received sample with the DFT simulated EELS of candidate structures. The ZLP was retained for the low-loss EELS and the multiple scattering effect was not removed by deconvolution. The core-loss EELS were background subtracted and had the multiple-scattering deconvoluted using the Fourier-log method.

As shown in Figure 6.2, for the experimental EELS of the metallic region shown in black, almost no oxygen signal is observed. The strong Be K-edge signal indicates that experimentally the selected position of the sample contains beryllium. The simulated EELS of Be metal are in good agreement with the experimental ones. For the low-loss EELS, the small peak at around 38 eV is due to multiple scattering effects and as such the feature is not reproduced computationally.

The EELS data of the oxide region of the as-received sample is shown in purple in Figure 6.2. For comparison, simulated spectra of hexagonal BeO, tetragonal BeO, and BeO_2 are presented. The Energy-dispersive X-ray spectroscopy (EDX) result suggests an atomic ratio of 43% Be and 57% O which is closest to BeO.

Computationally speaking, we could eliminate the existence of BeO_2 (dashed dark green), as for the O K-edge, an additional sharp peak at 533 eV is seen for BeO_2 which is not seen experimentally.

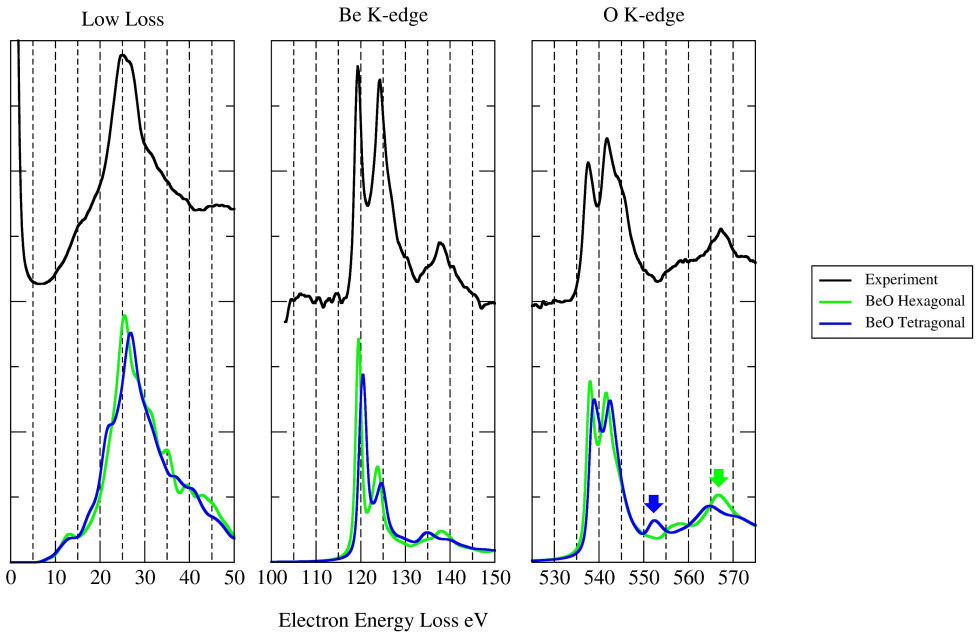


Figure 6.3: Comparison of the experimental EELS of the oxide region of the non-exposed as-received sample with the DFT simulated EELS of two polymorphs of BeO.

The EELS data of the two polymorphs of BeO are very similar as shown in Figure 6.3. The major difference lies in the O K-edge for which the tetragonal BeO shows an additional small peak at 552 eV which is not seen in the experimental spectrum. Thus, the structure that has EELS data closest to the experimental ones is hexagonal BeO. However, it is possible that the oxide sample contains some tetragonal BeO as well. Computationally at 0 K and 0 Pa, the two polymorphs of BeO are equally stable with an energy difference of less than 0.02 eV/atom.

Furthermore, there are still some discrepancies between the experimental and simulated spectra as shown in Figure 6.4. For the low-loss EEL spectrum, experimentally there is a small peak at 15 eV while computationally the peak is shifted

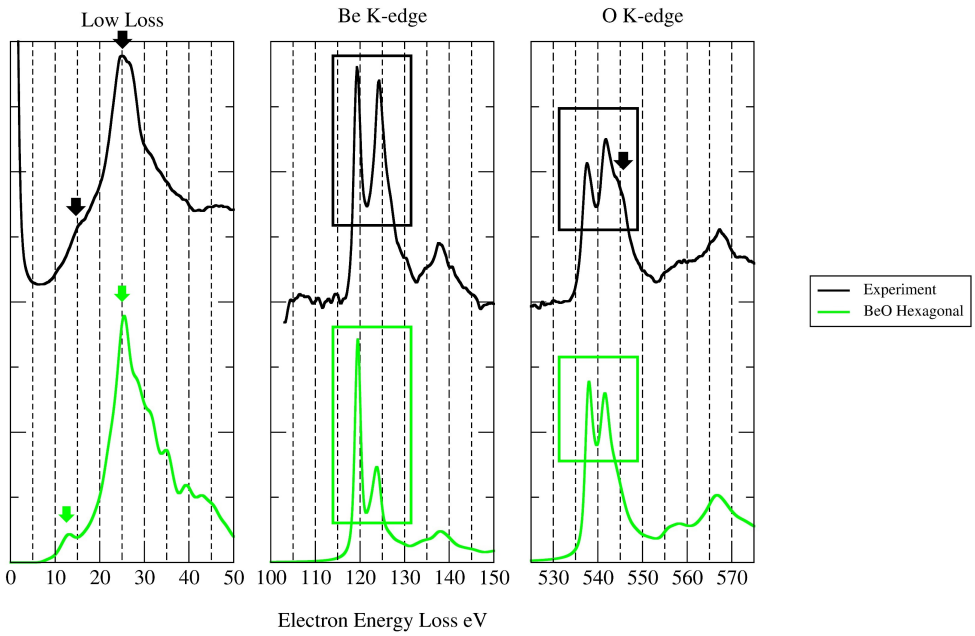


Figure 6.4: Highlighted differences between the experimental EELS of the oxide region of the non-exposed as-received sample and the DFT simulated EELS of hexagonal BeO.

to 13 eV. In addition, a sharp peak 25 eV is seen in the simulated spectrum while a broader peak is observed experimentally. The difference is caused by the lower broadening applied to the simulated spectrum in which the fine features are not physical. For the Be K-edge, although two peaks are seen both experimentally and computationally, the relative intensities of the two peaks are different. Peaks of similar heights are observed experimentally while the second peak is about half the intensity of the first one in the simulated spectrum. As for the O K-edge, experimentally the second peak is higher than the first one with a small shoulder. Such a feature is not seen in the simulated spectrum of hexagonal BeO.

There could be several reasons for the differences. Firstly, experimentally since the zero-loss peak is not removed, it could affect the shape of the spectrum. Or theoretically, DFT is not enough or it fails to simulate all the features that are seen experimentally. Secondly, the EDX suggests a higher atomic percentage

of oxygen. The DFT simulated EELS of hexagonal BeO could be correct and the difference is caused by another oxygen-containing Be_xO_y structure. This could be true if we bring BeO_2 back into discussion. Shown in Figure 6.2, if we ignore the sharp peak at 533 eV in the O K-edge spectrum of BeO_2, the addition of simulated features of BeO_2 to hexagonal BeO could improve the simulated spectra for the core-loss edge. For the low-loss, as the plasmon peak of BeO_2 is at relatively higher energy, the combination of the plasmon peaks of the two structures will result in a broader peak. For the Be K-edge, the single peak of the BeO_2 spectrum is at a similar position to the second peak of the hexagonal BeO spectrum. Adding the two peaks together could amend the height difference. Similarly, for O K-edge, the addition of BeO_2 will decrease the height difference and add the small shoulder that is currently missing. Clearly, the existence of the sharp peak can not be ignored and thus the additional structure is not BeO_2. However, it indicates the possibility of improving the current simulated spectrum by including another Be_xO_y structure. Finally, the difference could be caused by the contamination of the sample with copper. As stated in Carmen's thesis [143], the EDX signals suggest the existence of Cu which could potentially alter the local stoichiometry and bonding.

6.4 Beryllium Samples from JET

There were in total three first wall beryllium tiles taken from JET, which were subject to the actual fusion reaction: the inner wall limiter, the outer wall limiter, and the upper dump plate as shown in Figure 6.5. Erosion was found at the central part of both the inner and the outer wall limiters and one eroded area from each sample was analysed using EELS. Deposition is presented on the sides of both limiters as well. However, most regions of the deposited samples had many other metallic elements (Ni, Fe, and W) and only an inner wall deposited region

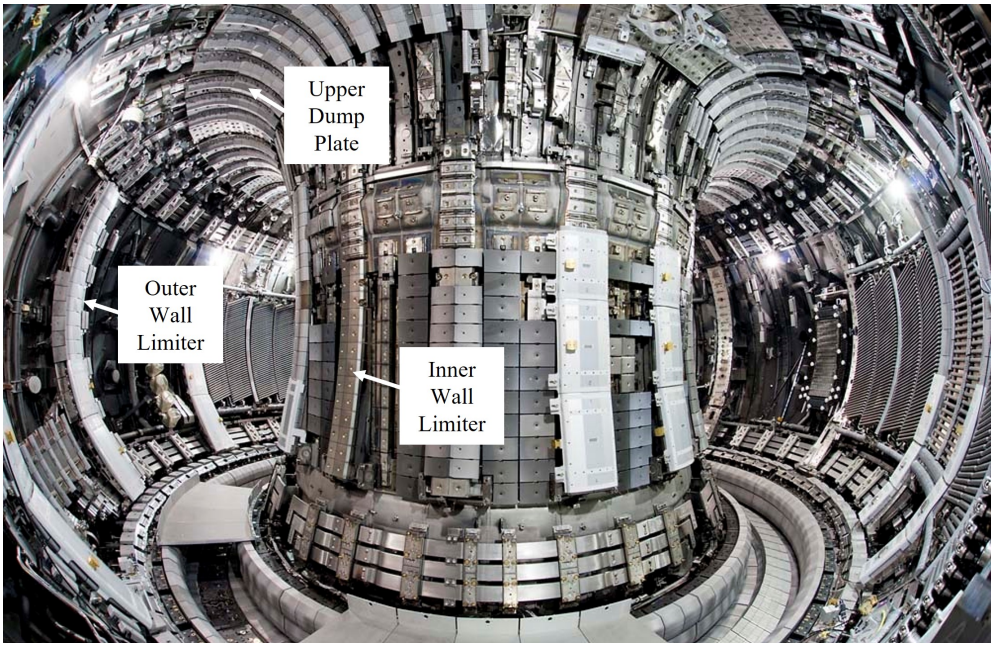


Figure 6.5: Overview of the beryllium limiter tiles in and around the JET tokamak. Figure is remade from Reference [163].

was examined. The dump plate samples underwent high thermal loads during plasma interactions and two melted regions of the sample were investigated. The experimental analysis was provided by Dr. Carmen Makepeace [143] and the above observations agree with what is stated in Reference [164].

To begin with, a comparison of the experimental EELS of different samples is presented, together with the atomic percentage. The experimental data was processed by Professor Rebecca Nicholls and Professor Sergio Lozano-Perez:

As shown in Figure 6.6, distinctive spectra are observed for eroded regions of the outer wall limiter. The spectra of the rest of the samples are similar to those of the oxide region of the as-received sample, with some additional fine features: for example, a sharper small peak at around 15 eV for the low-loss EELS. The major difference is the relative heights of the two peaks, both for the Be K-edge and the O K-edge. There is a trend that except for the eroded outer wall sample, the higher the atomic percentage of O, the higher the second peak.

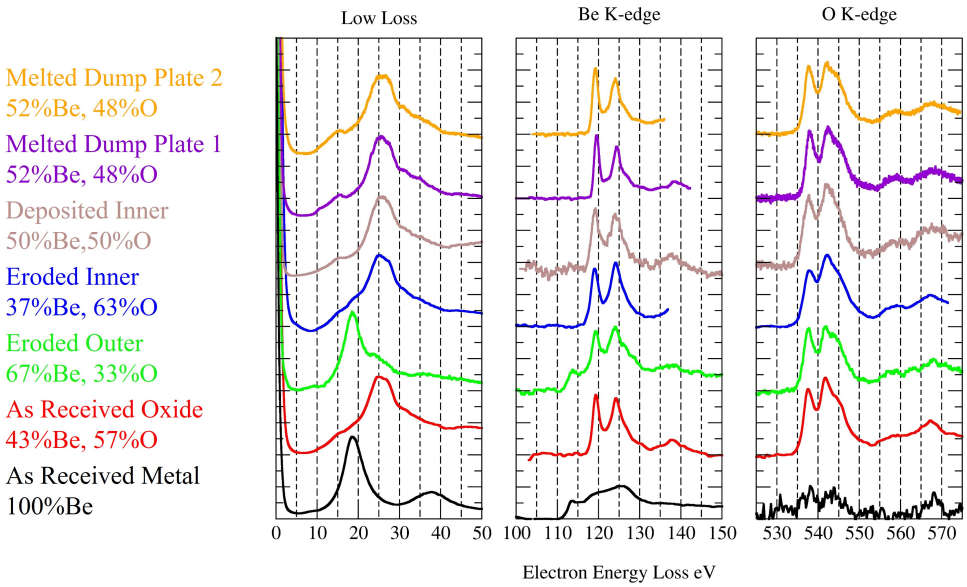


Figure 6.6: Experimental EELS of the as-received Be samples and samples from JET.

6.4.1 Eroded Outer Wall Sample

We start the discussion with the most distinctive specimen, the eroded outer wall sample. As shown in Figure 6.7, a strong oxygen signal is seen for the sample which indicates that the sample is oxidised. There are five candidate structures that could possibly contribute to the O K-edge: the two polymorphs of BeO as discussed in the previous section, BeO_2 which can already be removed from discussion as the sharp peak at 533 eV is not seen in any experimental spectra and the two polymorphs of $Be(OH)_2$. However, for both polymorphs of $Be(OH)_2$, a peak is observed between 545 and 550 eV in the simulated O K-edge EELS. Such features are not seen in the experimental spectrum of the eroded outer wall sample or in any of the rest of the JET samples. It suggests that neither polymorph of $Be(OH)_2$ is present in the samples. Similar to the as-receive oxide sample, no small peak is seen at 552 eV which indicates that the oxygen signal is caused by either hexagonal or tetragonal BeO.

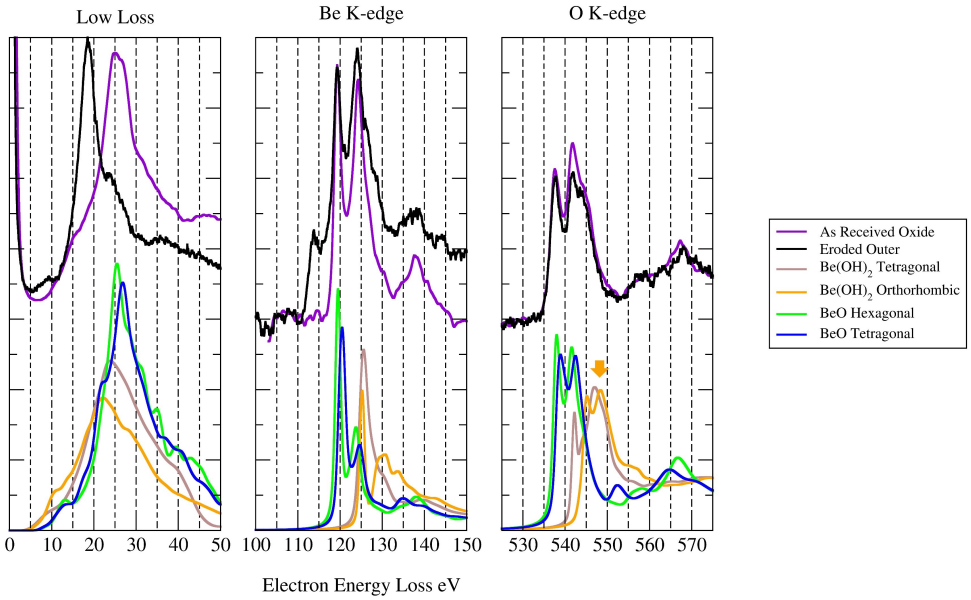


Figure 6.7: Comparison of the experimental EELS of the eroded region of the outer wall beryllium sample with the DFT simulated EELS of polymorphs of BeO and $Be(OH)_2$. The ZLP was retained for the low-loss EELS and the multiple scattering effect was not removed by deconvolution. The core-loss EELS were background subtracted and deconvoluted using the Fourier-ratio method. The spectra of the oxide region of the as-received sample are included for comparison and the same processing of the experimental data was adopted as stated in Figure 6.2.

For the Be K-edge and the low-loss EELS, Be and BeH_2 are included for discussion as shown in Figure 6.8. For the low-loss EELS, the plasmon peak at 18 eV is due to the presence of either Be metal or BeH_2 or both. The small shoulder at 19 eV is a result of hexagonal or tetragonal BeO. As for the Be K-edge spectrum, the peak at 114 eV suggests that Be metal exists in the sample. The sharp peak at 119 eV is due to the hexagonal BeO (or tetragonal BeO) as in the as-received oxide and the second peak at 124 eV could be a result of both hexagonal BeO and BeH_2.

However, as discussed in the previous section, there is a discrepancy in the height of the peak at 124 eV between the experimental result and the modelling result of hexagonal BeO. To make a better comparison, we combined the experimental

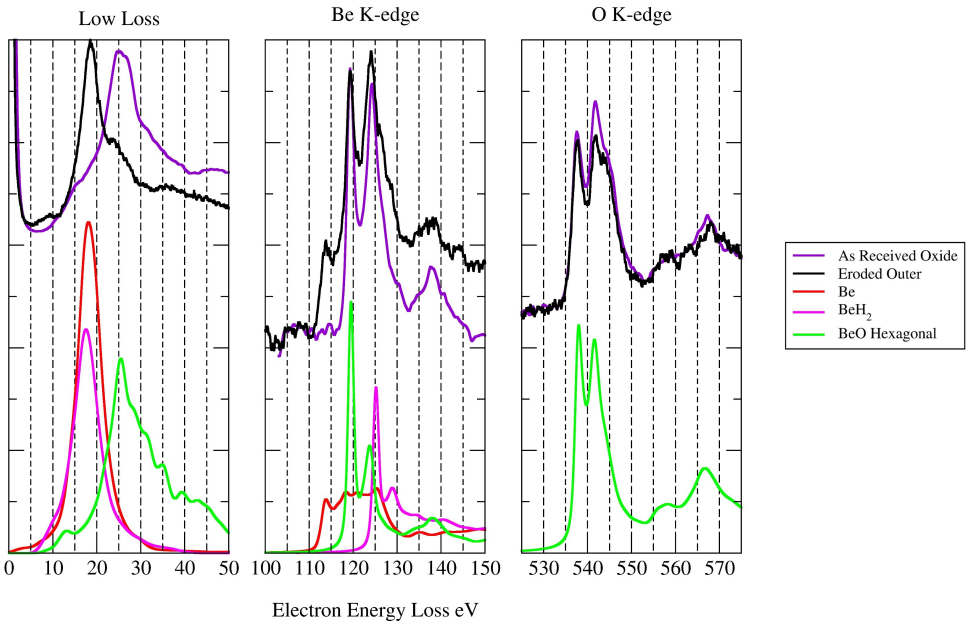


Figure 6.8: Comparison of the experimental EELS of the eroded region of the outer wall beryllium sample with the DFT simulated EELS of Be metal, BeH_2 and hexagonal BeO.

EELS of the metallic and oxide regions of the as-received sample to see if the experimental EELS of the eroded region could be replicated. As shown in Figure 6.9, the two graphs are very similar. For the low-loss EELS, the additional peak at 37 eV of the combined graph is due to the multiple scattering effect of the metallic region. For the Be K-edge spectrum, there are additional shoulders at 126 and 128 eV for the eroded sample, which could potentially be caused by the existence of BeH_2. In addition, compared to the experimental O K-edge spectra, a lower second peak is seen for the eroded outer wall sample. As the atomic percentage of O is significantly lower in the eroded sample (33%) than the as-received one (57%), this could be an indication that the second peak at 542 eV in O K-edge spectrum is due to an unknown oxygen-containing beryllium oxide structure. The major discrepancy between the two graphs is the atomic percentage, with 67% of Be and 33% of O for the eroded sample and 84% of Be and 16% of O for the combined one. In conclusion, both Be metal and hexagonal

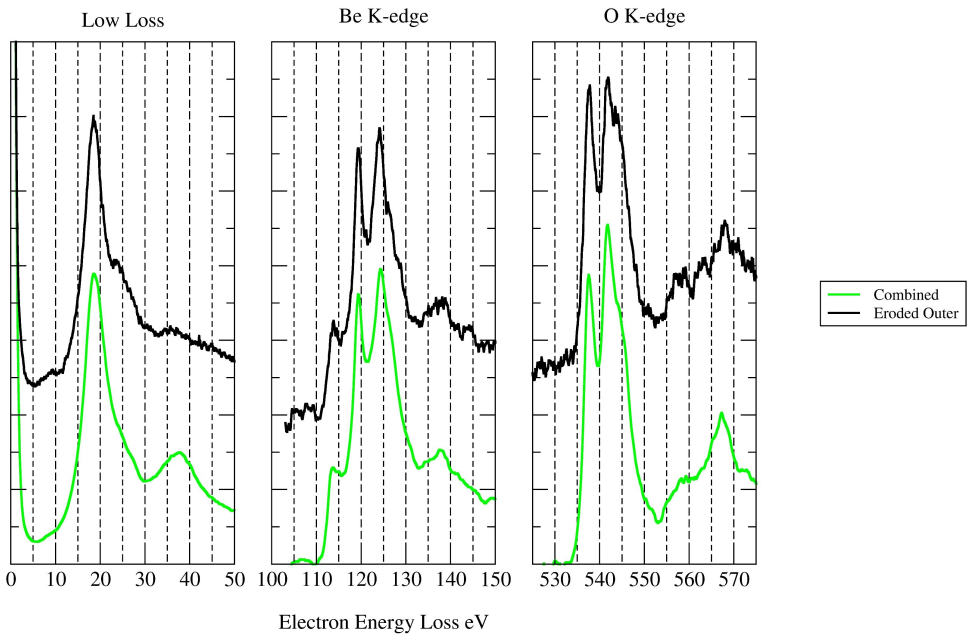


Figure 6.9: Comparison of the experimental EELS of the eroded region of the outer wall beryllium sample with the combined experimental EELS. The combined experimental EELS is obtained by adding together the experimental EELS of the metallic and oxide regions of the as-received sample with a ratio of Be : $Be_xO_y = 5 : 2$. The resulting combined structure has 84% of Be and 16% of O.

or tetragonal BeO are present in the structure. It is also possible that hydrogen retains as a form of BeH_2.

6.4.2 Eroded Inner Wall Sample

For the low-loss EELS of the eroded region of the inner wall sample as shown in Figure 6.10, there exists only the major plasmon peak at 25 eV. Also, for the Be K-edge spectrum, only the two sharp peaks at 119 and 124 eV can be observed. This indicates that there is no Be metal or BeH_2 present in the structure. A higher second peak is seen in both the Be K-edge and O K-edge spectrum and together with a higher atomic percentage of oxygen detected in the sample, it consolidates the previous assumption that both second peaks could be a result of

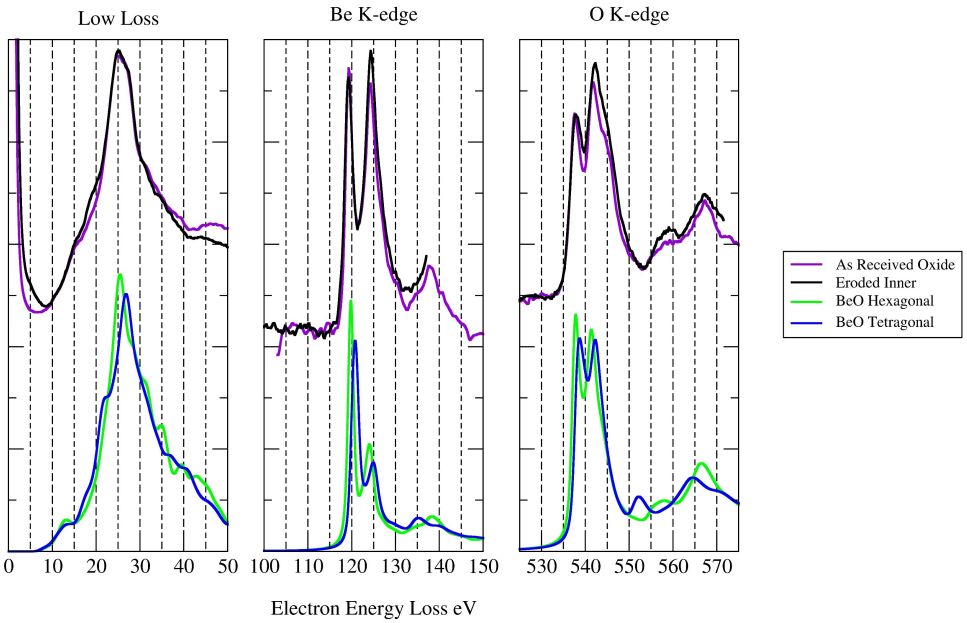


Figure 6.10: Comparison of the experimental EELS of the eroded region of the inner wall beryllium sample with the DFT simulated EELS of hexagonal and tetragonal BeO. Same post-processing of data was adopted as stated in Figure 6.7.

an additional unknown form of oxygen-containing beryllium oxide structure. In conclusion, the structure is hexagonal BeO (or tetragonal BeO) and no hydrogen retention is observed.

6.4.3 Deposited Inner Wall Sample

The overall spectra of the deposited region of the inner wall beryllium sample are very similar to those of the as-received oxide as shown in Figure 6.11. The major difference is that for the low-loss EELS, the small peak at 15 eV is sharper for the deposited sample. It could potentially be due to the existence of Be metal, which agrees with the relative higher atomic percentage of Be. As the Be K-edge spectrum contains lots of noise, the small peak at 114 eV corresponding to the presence of Be metal may not be able to be separated from the noise. In addition, it is hard to identify if there is a small shoulder at 123 eV for the Be

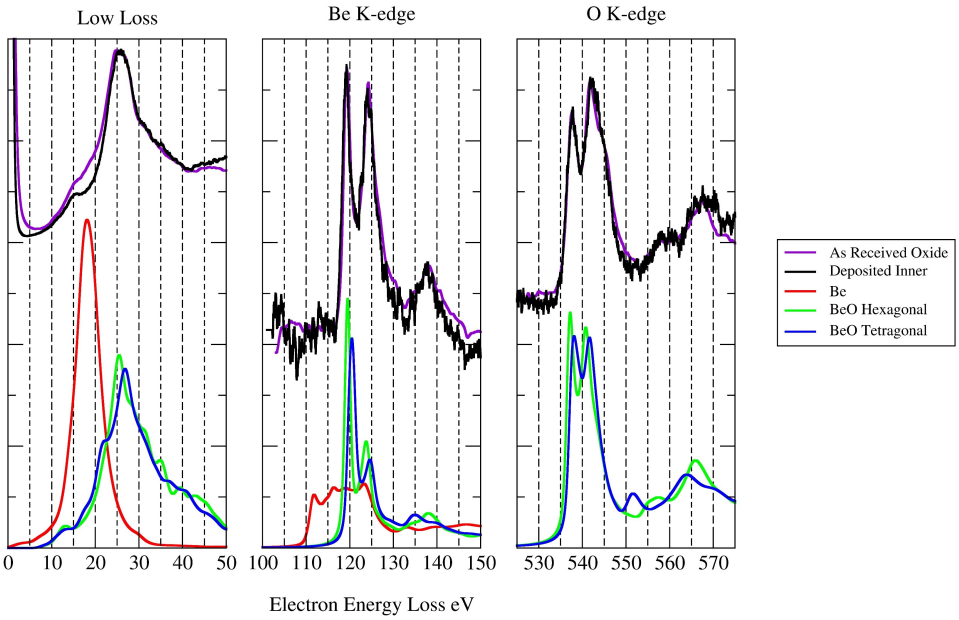


Figure 6.11: Comparison of the experimental EELS of the deposited region of the inner wall beryllium sample with the DFT simulated EELS of Be metal and two polymorphs of BeO. The same post-processing of data was adopted as stated in Figure 6.7.

K-edge spectrum and a small peak at 552 eV for the O K-edge spectrum. If they do exist, tetragonal BeO exists in the sample. In conclusion, the structure is hexagonal BeO with a small amount Be metal, with the possibility of the existence of tetragonal BeO.

6.4.4 Melted Upper Dump Plate Sample

The experimental EELS are very similar for the two melted regions of the upper dump plate as shown in Figure 6.12. For both samples, similar heights of the two peaks in the O K-edge spectra and the relatively higher atomic percentage of Be compared to the as-received oxide suggest the lower amount of the unknown oxygen-containing beryllium oxide structure present. In addition, a sharper small peak at 15 eV is observed in the low-loss spectra, which indicates the existence of Be or BeH_2. As for the Be K-edge however, no additional shoulder is seen for the

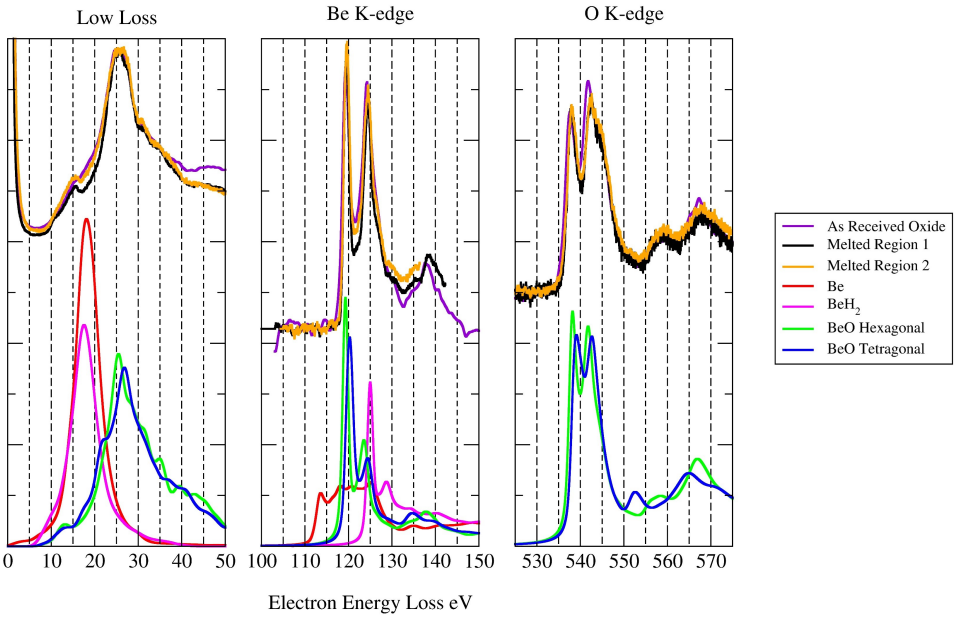


Figure 6.12: Comparison of the experimental EELS of the melted region of the upper dump plate beryllium sample with the DFT simulated EELS of Be metal and two polymorphs of BeO. The same post-processing of data was adopted as stated in Figure 6.7.

BeH_2. Thus, in conclusion, the structure is hexagonal or tetragonal BeO with Be metal.

6.5 Summary

In this chapter, we studied the corrosion products of beryllium tiles that were used in the Joint European Torus (JET) by comparing the experimental EELS with the simulated ones. Three types of EEL spectra were compared: low-loss, Be K-edge, and O K-edge. Seven candidate structures were selected for the EELS simulation: Be metal, BeH_2, α-$Be(OH)_2$ (tetragonal), β-$Be(OH)_2$ (orthorhombic), α-BeO (hexagonal), β-BeO (tetragonal) and BeO_2. And experimentally two regions of the non-exposed beryllium sample and five regions of the three actual JET samples were examined.

The metallic and oxide regions of the non-exposed beryllium are composed of Be metal and BeO respectively. Both the enthalpy and the simulated spectra of hexagonal and tetragonal BeO are very similar and it is hard to distinguish if either or both polymorphs present in the sample. The simulated spectra agree well with the experimental results for the metallic region while there are some discrepancies for the oxide region. Such difference of the spectra between the as-received sample and the simulated data makes it hard to set a standard. It is unclear what the oxide is and if the difference is caused by DFT being not good enough to simulate the spectra or if there is an unknown type of oxygen-containing beryllium oxide structure that is not hexagonal or tetragonal BeO or BeO_2.

The JET samples agree with the hypothesis that there is an unknown type of oxygen-containing beryllium oxide structure. The main corrosion product is still hexagonal or tetragonal BeO. Signals of Be metal are also observed in some low-loss and Be K-edge spectra. If hydrogen does retain in the beryllium tiles, it retains as BeH_2 but not as either polymorph of $Be(OH)_2$.

Chapter 7

A New Approach to Model Core-loss EELS for Be

In the last chapter, the simulated low-loss and Be K-edge spectra were presented. The calculations were performed using CASTEP with PBE pseudopotentials. An interesting problem arose when dealing with the pseudopotential of Be. The electronic configuration of Be is $1s^2 2s^2$ and its default CASTEP pseudopotential, known as the on-the-fly (OTF) pseudopotential, treats all four electrons as valence electrons. The valence electrons react to the crystal environment and participate in the formation of chemical bonding. On the contrary, a typical OTF pseudopotential, for example, the pseudopotential of oxygen, treats the outer $2s$ and $2p$ electrons as valence electrons while treating the inner $1s$ electrons as core electrons. The core electrons are frozen to their isolated atom states, which are precomputed using all-electron (AE) calculations and do not respond to the environment. For the research carried out in the last chapter, the calculations were performed using the default CASTEP core-loss calculation method with the modified pseudopotential of Be which treats the inner $1s$ electrons as core electrons. In this chapter, a new CASTEP approach is proposed to simulate the

Be K-edge EELS with the OTF pseudopotential that treats all four electrons as valence electrons.

In addition, for conventional core-loss EELS calculations using pseudopotentials, the energy onset of the peaks requires additional calculations to evaluate using Mizoguchi's method [138], due to the absence of information on the core electrons. However, since the OTF pseudopotential of Be contains the all-electron wavefunctions, theoretically the new approach is able to calculate the onset using the ΔSCF method [135–137], which is usually adopted in all-electron calculations.

The motivation for the research carried out in this chapter is first, if it is possible to perform all-electron EELS calculations in CASTEP with and without core hole and second, if the new method can regenerate the features and calculate the energy onset and the associated cost of calculations. In this chapter, we generate a new pseudopotential of Be with the $1s$ electrons described as core electrons for conventional Be K-edge EELS calculations using CASTEP. Firstly, to validate the accuracy of the new pseudopotential, geometry optimisation and density of states calculations were performed using the two pseudopotentials, for the seven structures belonging to the Be_xO_y system as listed in the last chapter. Secondly, the new approach was applied for the Be K-edge EELS calculations, with and without core hole, and the resulting spectra were compared with the ones using the conventional approach. Finally, we made a comparison of the onset energies calculated using Mizoguchi's method for the conventional approach with CASTEP, using the ΔSCF method for the new approach with CASTEP and for the all-electron method with WIEN2k [49].

7.1 A Brief Outline of the Methodology

EELS originates from the interaction between the incident electron and the atomic electrons. Similar effects could be achieved by an electromagnetic wave incident onto the specimen. And thus, intrinsically EELS is related to the optical constants which are described by the dielectric function ε [2, 25]:

$$\varepsilon = \varepsilon_1 + i\varepsilon_2 \tag{7.1}$$

In EELS, the double differential scattering cross section (DDSCS) is measured, which describes the fraction of the incident electrons being scattered per unit solid angle $d\Omega$ losing an energy between ΔE and $\Delta E + dE$. And the DDSCS is related to the dielectric function by [114]:

$$\begin{aligned} \frac{d^2\sigma}{d\Omega dE} &= \frac{1}{(\pi e a_0)^2}\frac{1}{q^2}\mathrm{Im}\left[\frac{-1}{\varepsilon}\right] \\ &= \frac{1}{(\pi e a_0)^2}\frac{1}{q^2}\left[\frac{\varepsilon_2}{{\varepsilon_1}^2 + {\varepsilon_2}^2}\right] \end{aligned} \tag{7.2}$$

where a_0 is the first Bohr radius (0.529 Å) and q is the momentum transferred by the incident electron.

The imaginary part of the dielectric function is calculated by a method described by Pickard as described in the methodology chapter [114]:

$$\varepsilon_2(\omega) = \frac{4\pi}{q^2\omega}\sum_{v,c,\mathbf{k}}\left|\left\langle \phi_{c\mathbf{k}}\middle| e^{i\mathbf{q}.\mathbf{r}}\middle|\phi_{v\mathbf{k}}\right\rangle\right|^2 \delta(\epsilon_{c\mathbf{k}} - \epsilon_{v\mathbf{k}} - \omega) \tag{7.3}$$

The dipole operator describes the probability of transition from the initial occupied state to the final unoccupied state. In the low-loss EELS, the initial states

correspond to the valence states and the final states correspond to the conduction states. For the Be K-edge EELS, the transition is between the Be $1s$ states and the unoccupied states above the Fermi energy. For calculations discussed in this chapter, the independent particle approximation is adopted which is based on the assumption that the off-diagonal elements of the dielectric matrix are zero (the local field (LF) effects are ignored).

ε_1 is also required to fully evaluate the loss function, which is calculated using the Kramers-Krönig relation [26] in the low-loss calculations. For the core-loss calculation, the situation is simpler as the system is not strongly polarised and thus ε_1 is close to unity.

A key question is that for the pseudopotential method, the frozen core approximation is employed and the wavefunctions of the valence electrons are pseudised. Equation 7.3 involves the overlap of the core state and the valence state. The wavefunction of the core electrons in a pseudopotential is identical to the true AE version. However, for the valence state in a pseudopotential, it is pseudised close to the nucleus and thus differs from the AE one. Since the core state is localised close to the nucleus, the integral is weighted to the region close to the nucleus, exactly where the valence state is not physical. The problem is solved by reconstructing the AE wavefunctions from the calculated pseudo wavefunctions of the valence electrons, based on the Projector Augmented Wave (PAW) method as described in Pickard's thesis [114]. Since the pseudo wavefunctions are correct beyond the core radius r_c of the pseudopotential, only the wavefunctions within r_c need to be corrected. The correction is known as the PAW correction, such that the integral is evaluated with AE accuracy. To include the effect of the core hole which will be further discussed later in this chapter, the core orbital is first obtained from an all-electron calculation of an isolated single atom. And the excited pseudopotential is modified by removing an electron from the core orbital

and the wave functions of the final states are calculated by using the excited pseudopotential for one atom in a supercell [138].

As for beryllium, it has four electrons. The default OTF pseudopotential treats all four electrons as valence electrons. The potential near the core is pseudised such that the pseudo wavefunctions are considerably smoother than the true wavefunctions and thus reduce the number of planewaves required. For the new pseudopotential generated (referred to as the modified pseudopotential), the $1s$ electrons are treated as core electrons. A comparison of the electronic configurations of a single beryllium atom using the OTF pseudopotential, the modified pseudopotential, and the all-electron method in WIEN2k is shown in Figure 7.1.

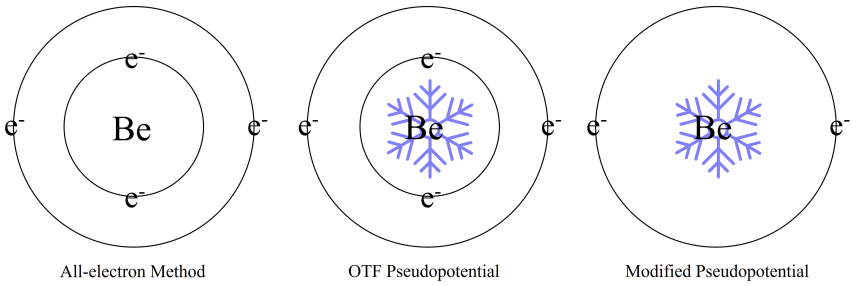


Figure 7.1: Comparison of the all-electron method, the OTF pseudopotential, and the modified pseudopotential. The ice symbol corresponds to the Frozen Core Approximation.

For the simulation of the low-loss spectrum, no significant difference is expected using the two pseudopotentials as the plasmon excitation involves only the outer valence electrons, for which the wavefunctions should be identical in both pseudopotentials and the integral is evaluated close to the Fermi energy. For the Be K-edge spectrum, the conventional approach using the modified pseudopotential calculates only the imaginary part of the dielectric function ε_2, with PAW correction applied to the pseudised wavefunctions of the $2s$ electrons within r_c. As for the new approach, the Be K-edge spectrum is calculated together with the low-loss spectrum via the low-loss scheme, for which both ε_2 and ε_1 are calculated. In

the new approach, no PAW correction is added. For simplicity, the conventional method is referred to as the core-loss method and the new approach is referred to as the low-loss method later in this chapter.

7.2 Accuracy of the Modified Pseudopotential

The default OTF pseudopotential uses a cutoff radius $r_c = 1.0\,a_0$ and treats all four electrons as valence electrons. The modified pseudopotential increases the cutoff radius to $r_c = 1.8\,a_0$, with the $1s$ electrons treated as core electrons instead and only the valence $2s$ electrons react to the crystal environment. Increasing the cutoff radius could lead to lower accuracy and transferability of the pseudopotential. Thus, to begin with, the accuracy of the modified pseudopotential is tested and compared with the OTF pseudopotential. Ultrasoft PBE functionals are used and the calculation details can be found in the Appendix.

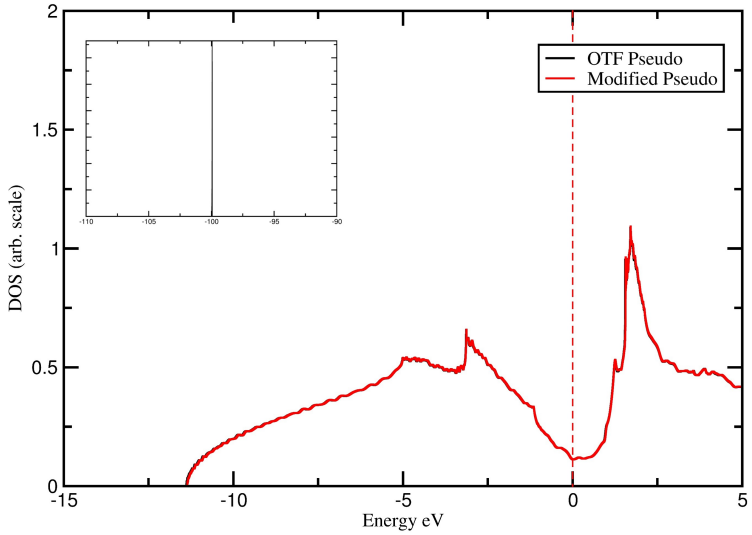
Structure	Structure	Parameter	OTF (Å)	Modified (Å)
Be	Hexagonal	a	2.258	2.248
		c	3.583	3.569
BeH_2	BCC	a	8.970	8.934
		b	4.157	4.142
		c	6.248	6.225
BeO	Hexagonal	a	2.711	2.702
		c	4.404	4.390
BeO	Tetragonal	a	4.642	4.629
		c	2.702	2.693
BeO_2	FeS_2	a	4.315	4.308
$Be(OH)_2$	Tetragonal	a	4.845	4.835
		c	8.839	8.817
$Be(OH)_2$	Orthorhombic	a	4.588	4.587
		b	6.317	6.193
		c	6.735	6.883

Table 7.1: Geometry optimisation of the candidate structures using the OTF and the modified pseudopotentials. For computational efficiency, the smallest unit cells were used and the associated lattice parameters are listed in the table.

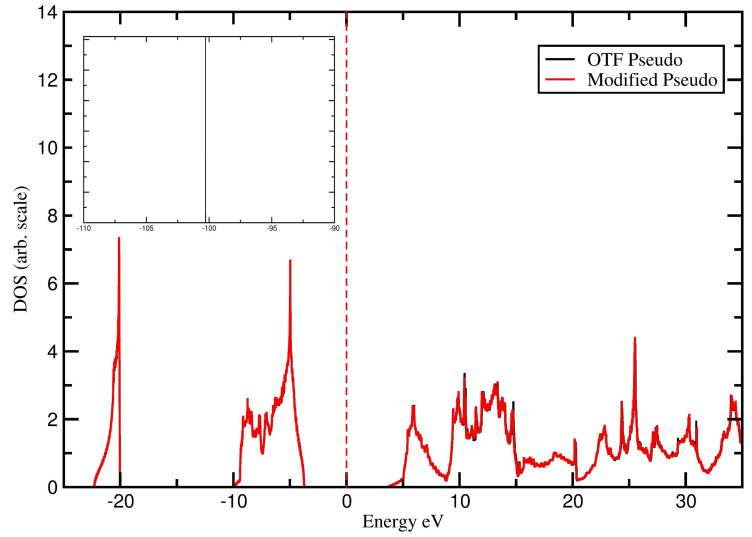
The calculated cell parameters using the modified pseudopotential at the theo-

retical equilibrium for the candidate structures that were discussed in the last chapter are reported in Table 7.1. These values agree well with the calculated values using the default OTF pseudopotential, which validates the accuracy of the modified pseudopotential for ground-state structures. For all structures, smaller lattice parameters are predicted using the modified functional, with a difference of less than 0.5% except the orthorhombic $Be(OH)_2$, for which the largest difference of 2.2% is observed for the c parameter. As PBE functional has a tendency to overestimate the lattice constants by $1-2\%$ [165–168], it indicates that using the modified pseudopotential predicts better results for the geometry optimisation. However, the OTF pseudopotential was developed in order to minimize the error with respect to fully converged all-electron DFT calculations. For calculations discussed in the rest of the chapter, the geometry-optimised structures with the default OTF pseudopotential were used.

In addition, as EELS is closely related to the optical properties of materials, calculations of the DOS using the two pseudopotentials were also performed for comparison. As shown in Figure 7.2, almost identical DOS is calculated using the different pseudopotentials. The only difference is that for the OTF pseudopotential, there is an additional sharp peak at around -100 eV for both Be metal and hexagonal BeO which corresponds to the $1s$ states. This agrees with the fact that the $1s$ electrons are treated as core electrons for the modified pseudopotential and are pseudised, which results in the missing of sharp peak.



(a) Be metal



(b) Hexagonal BeO

Figure 7.2: Comparison of the calculated DOS using the OTF (Black) and the modified (Red) pseudopotentials. The inset corresponds to the DOS in the lower-energy range (-110 to -90 eV).

7.3 EELS Modelling using the New Approach

The simulated EELS using different approaches is shown in Figure 7.3. The low-loss scheme is the proposed new approach which uses the OTF pseudopotential that treats all Be electrons as valence electrons. The core-loss scheme is the conventional approach that uses the modified pseudopotential that treats the $1s$ electrons as core electrons. In addition, as discussed earlier in this chapter, reconstruction of the full all electron wavefunctions is required for the conventional core-loss scheme, which involves the PAW correction. Thus, the core-loss scheme is subdivided into one with the PAW correction and one without. As shown in Figure 7.3, very similar results are given by the low-loss and core-loss schemes, especially when the PAW correction is removed.

Another important factor to consider when simulating the core-loss EELS are the core hole effects, due to the interaction between the core hole and the excited electron. The exact description of the excitation process, which involves the actual time-dependent evolution of the core electron into its final excited state is not feasible within the single particle electronic structure methods. In this thesis, the method proposed in Pickard's thesis [114] is adopted. It is based on the assumption that the lattice does not have time to relax once the core electron is excited, while the relaxation of the valence electrons due to the presence of the core hole and the associated screening of the core hole by the valence electrons are instantaneous. In the conventional core-loss scheme, to include the effects of the core hole, a $1s$ electron is removed from the core state to generate a specially designed excited pseudopotential. In the proposed new approach using the low-loss scheme, as all four electrons are described as valence electrons, the $1s$ electron is removed from the valence state which generates a valence hole.

The results are shown in Figure 7.4. Similar spectra are simulated with the new approach using the low-loss scheme, compared to those using the conventional

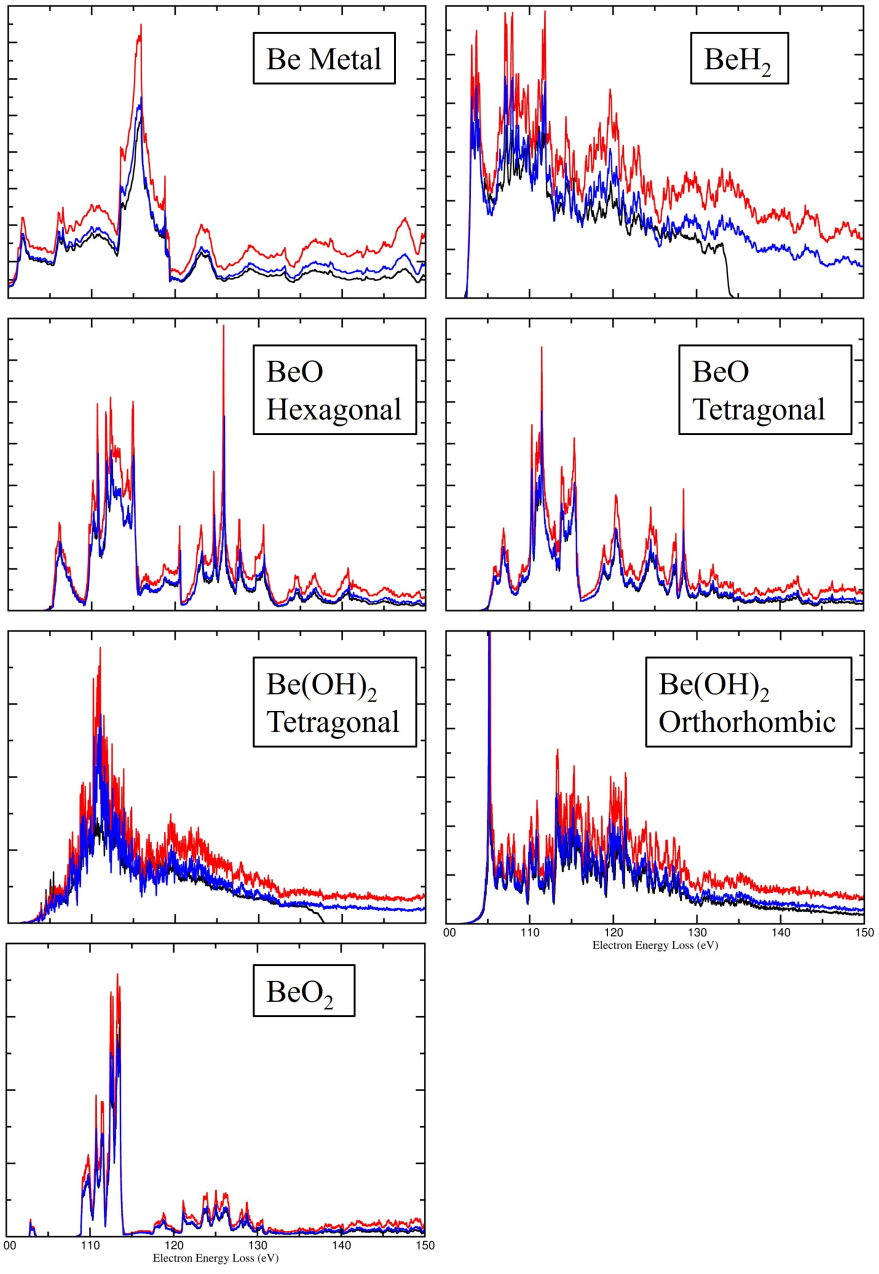


Figure 7.3: Comparison of the simulated EELS for the candidate structures using the low-loss scheme (Black) and the core-loss scheme with the PAW corrections (Red). For the core-loss scheme, additional calculations were performed by removing the PAW corrections during the pseudopotential reconstruction (Blue).

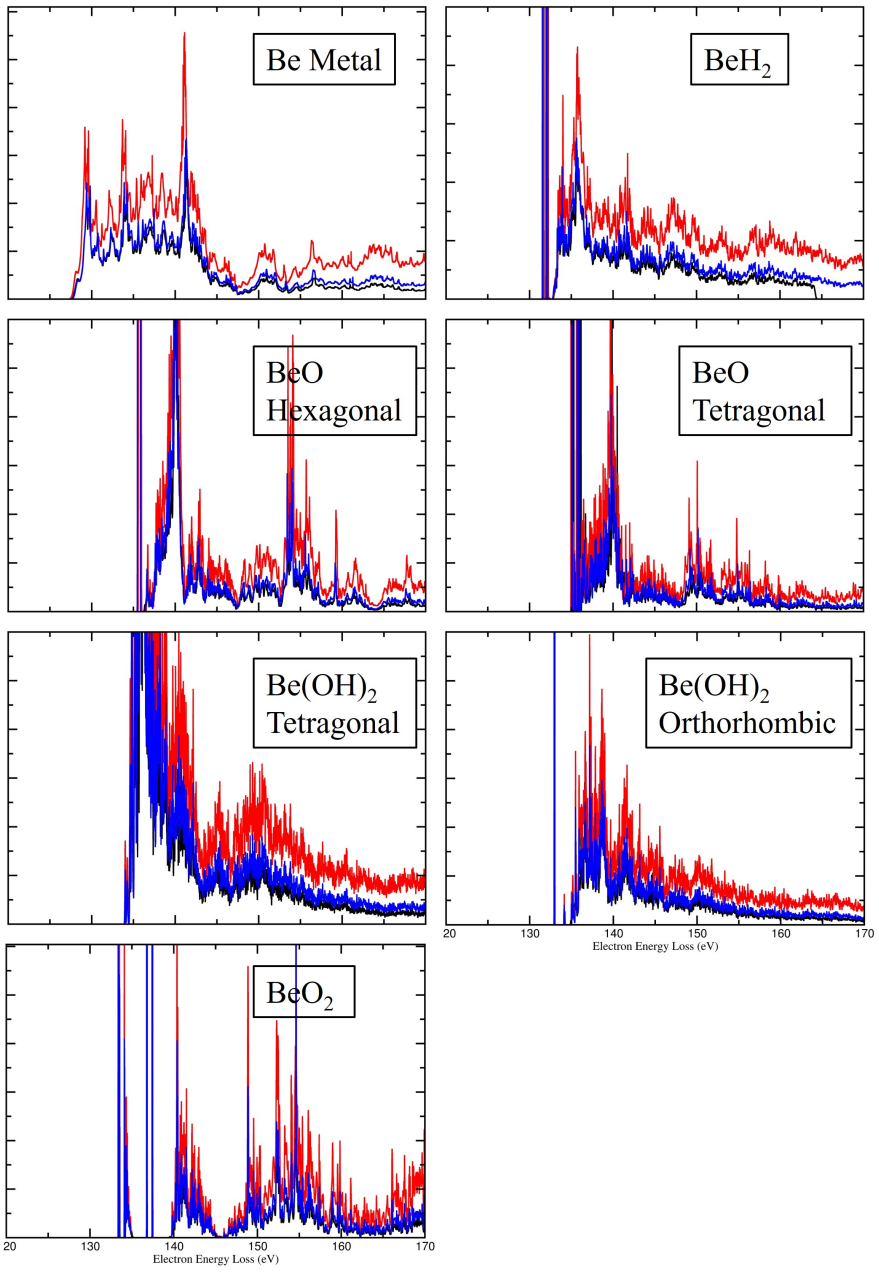


Figure 7.4: Comparison of the simulated EELS for the candidate structures using the low-loss scheme (Black) and the core-loss scheme with (Red) and without (Blue) the PAW corrections. The effects of the core hole are included.

core-loss scheme when PAW corrections are removed. The major effect of adding the PAW corrections is an increase in intensity. However, such a small intensity difference could be neglected when compared with the experimental results, especially when broadening is applied. For both sets of spectra with and without the core hole effects, the intensity of the spectrum using the new approach is always lower than that using the core-loss scheme. There are two main reasons for the discrepancy: first of all, the $1s$ states of the OTF pseudopotential that is used in the new approach are pseudised and thus deviate from the $1s$ states of the modified pseudopotential applied in the conventional approach, which is identical to the AE wavefunctions. Secondly, in the core-loss scheme, the real part of the dielectric function is approximated to be one as there is no polarisation response at such high energy. However, in the low-loss scheme, the real part is calculated separately. For example, in the case of hexagonal BeO as shown in Figure 7.5, the real part is approaching unity with an increase in energy. The fact that the real part is smaller than one for the low-loss scheme, however, will result in a higher intensity difference between the simulated spectra due to Equation 7.2. In the case of hexagonal BeO, the calculation of the real part in the new approach results in a higher intensity of around 7.76% compared to the conventional approach which approximates the real part to be one.

7.4 Predicted Transition Energy

The proposed new method has been shown to correctly reproduce the spectral features. Another important aspect to be examined is that if the new method can also be used to derive the predicted transition energy (PTE). The calculation of PTE is indispensable for mainly two reasons. Firstly, an element may appear at different sites within a single structure and be subject to different chemical environments. It is thus vital to calculate PTE, to sum up the individual spectra for

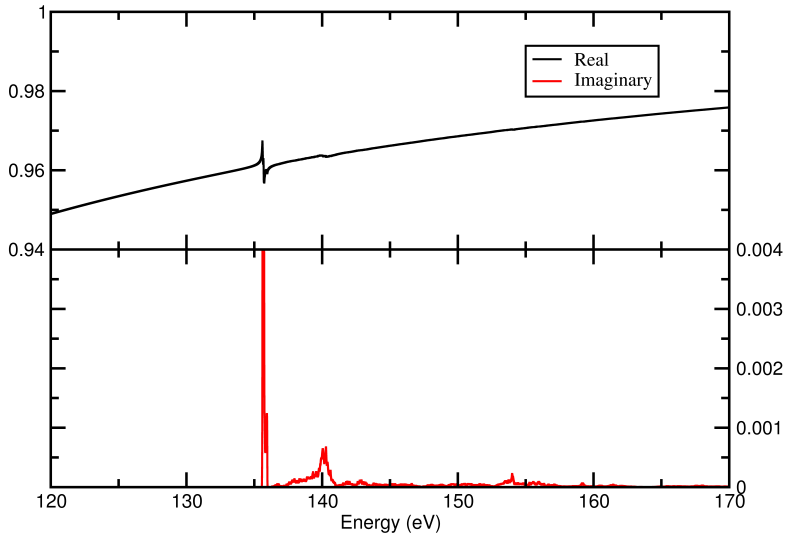


Figure 7.5: Real (Black) and imaginary (Red) part of the dielectric function of hexagonal BeO calculated using the low-loss scheme.

each individual site for comparison with the experiment. Secondly, as it is already shown in the previous chapter, for systems with different structures, the shape of the peaks and the relative positions of the peaks are equally important.

In this chapter, we make a comparison of PTE calculated using our new approach, with those using the standard methodologies and with the experimental values. There are several existing methodologies for calculating PTE. For all-electron methods like WIEN2K, the ΔSCF method is adopted, which is straightforward as the calculation involves the description of both the valence electrons and the core electrons. The WIEN2k presented in this thesis was performed by Professor Rebecca Nicholls. For pseudopotential methods like CASTEP, as the core electrons are pseudised, the PTE is calculated using the method proposed by Mizoguchi [138] which requires additional all-electron calculations for the single atom. In our new approach to calculating the core-loss EELS, there are two methods to calculate PTE. Firstly, as the core-loss spectrum is calculated together with the low-loss spectrum, theoretically the core-loss spectrum starts at

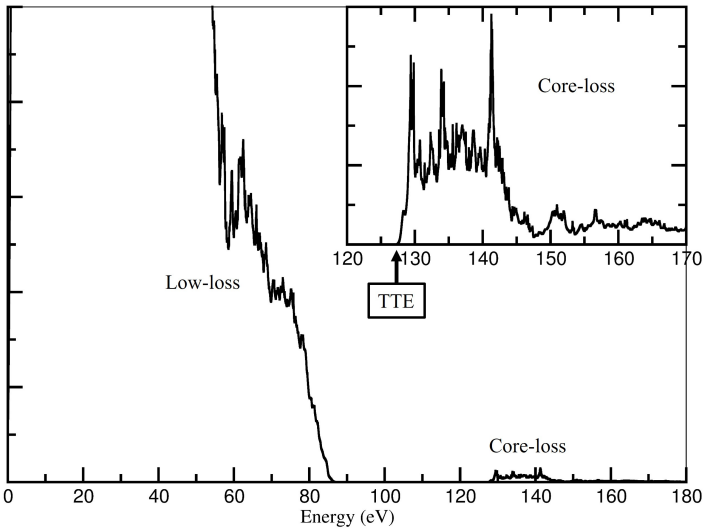


Figure 7.6: Simulated low-loss and core-loss EELS of Be using the new approach with the low-loss scheme. The left-hand side of the graph (below 90 eV) is the low-loss region and the small peaks above 120 eV are the core-loss region. The inset is an enlarged version of the core-loss region and the predicted transition energy (PTE) is the starting point of the core-loss peaks.

a certain energy that corresponds to PTE as shown in Figure 7.6. Secondly, as the pseudopotential of beryllium used in our approach treats all four electrons as valence electrons which are explicitly described, the ΔSCF method can also be applied for this pseudised all-electron method. The results are shown in Table 7.2:

The most different results are given by the values reading directly from the simulated spectra using the new approach with the low-loss scheme. This is due to the fact that these values correspond to the energy difference between the Be $1s$ state and the bottom of the conduction band. However, DFT is a ground-state theory and the single-electron eigenvalues have no physical meaning and are only used as a good approximation when constructing the band structure. In addition, the notorious band gap problem also challenges the validity of the method. Furthermore, the larger value is due to the fact that when calculating

Formula	Structure	Exp.[1]	WIEN2k[2]	CASTEP[3]	Graph[4]	Pseudo AE[5]
Be	Hexagonal	112.1	109.4	100.4	128.0	101.8
BeH_2	BCC	\	\	106.9	131.7	117.1
BeO	Hexagonal	119.3	109.9	101.5	135.6	105.6
BeO	Tetragonal	\	110.5	102.0	135.3	106.5
BeO_2	FeS_2	\	109.9	101.3	133.4	103.3
$Be(OH)_2$	Tetragonal	\	\	105.8	134.0	112.7
$Be(OH)_2$	Orthorhombic	\	\	107.3	133.0	116.5

Table 7.2: Comparison of the predicted transition energy calculated using different methods.
1: experimental values taken from the EELS of the metallic and oxide region of as-received sample as discussed in previous chapter.
2: WIEN2k (all-electron) calculations with the ΔSCF method.
3: conventional CASTEP (pseudopotential) core-loss calculations using the Mizoguchi's method.
4: core-loss calculations using the new approach (pseudised all-electron) with the low-loss scheme. PTE is directly given in the spectra.
5: core-loss calculations using the new approach. PTE is calculated using the ΔSCF method.

through the low-loss scheme, a core hole is added which attracts the $1s$ state and makes the difference larger. Thus, the PTE directly given in the spectra is not reliable.

From Table 7.2, there is a difference between the experimental values and the calculated WIEN2k values. Such difference is suggested in Reference [137], in which the author stated that PTE obtained using the ΔSCF method for the all-electron calculations is only valid for the relative positions of different spectra, but not the absolute positions. In other words, using such calculated PTE could correctly align the peaks from different spectra, but to compare with the experimental spectra, an additional constant shift of a few eV is needed. Thus, when comparing the PTE predicted using different methods, instead of focusing on the absolute values, we focus on the relative values. However, in our results, the shift is not constant for the calculated and experimental spectra of Be metal and hexagonal BeO. It could be due to the fact that we are comparing a metal and a semiconductor and that the ΔSCF method is only valid within semiconductors.

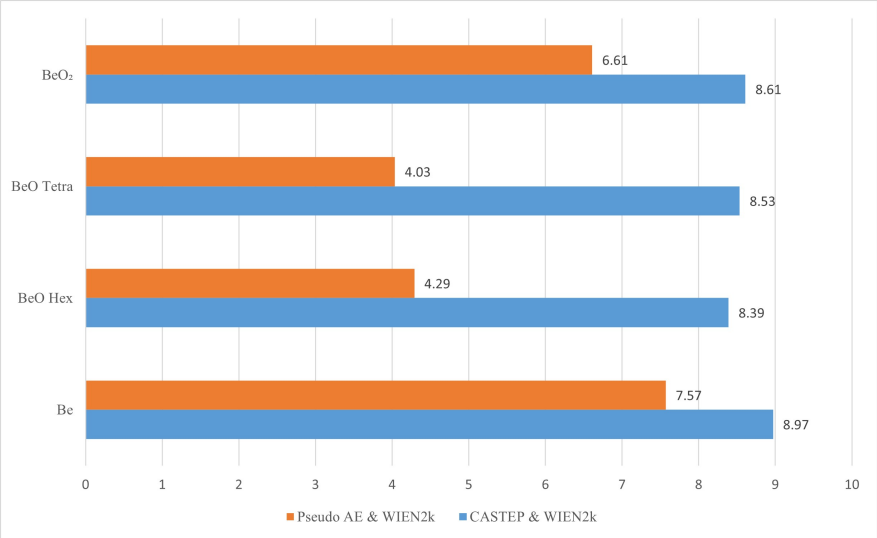


Figure 7.7: Difference of the calculated PTE using the new approach (Column 7 in Table 7.2), the conventional pseudopotential approach (Column 5) and the standard all-electron method (Column 4).

To prove the validity of the ΔSCF method for the Be_xO_y system requires further support of the experimental data, which are currently unavailable. At the moment, further discussion will be based on the assumption that the all-electron ΔSCF method is still the correct and standard method to calculate PTE.

The conventional CASTEP calculations using Mizoguchi's method are in good agreement with the WIEN2k results using the ΔSCF method. As shown in the blue bars in Figure 7.7, a relatively constant difference is seen with a difference of less than 1 eV. For the proposed new method using the ΔSCF method, however, the calculated values disagree with the standard all-electron ΔSCF method. As shown in the orange bars in Figure 7.7, the difference is not consistent, which is also seen if we compare the values for the rest of the structures with those using conventional CASTEP.

7.4.1 Costs of Calculations

In this section we make a comparison of the relative costs of calculations using different methods, taking beryllium metal as an example as shown in Table 7.3.

The calculation times listed below are all based on converged parameters. For the core-loss calculations, one important parameter that requires a convergence test is the size of the supercell. A $5 \times 5 \times 5$ supercell is used for CASTEP calculations while a $5 \times 5 \times 3$ supercell is used for WIEN2k calculations. The CASTEP calculations were performed on the YOUNG cluster supported by the UK Materials and Molecular Modelling Hub using the message passing interface (MPI) programs, and the WIEN2k calculations were performed on a local machine named Kohn.

Code	Method	Time (s)	No. of Processes	Time Converted (hour)
CASTEP	Core Hole	7270.34	96	193.9
CASTEP	Valence Hole	14852.79	48	198.0
WIEN2k	Core Hole	326117	4	362.4

Table 7.3: Comparison of the calculation time of the core-loss EELS of beryllium metal using different methods. The time converted column corresponds to the total time of all processes, converted into hours.

As shown in Table 7.3, the costs are similar for CASTEP calculations using the conventional core-loss method with OTF pseudopotential (Core hole) and using the new low-loss method with modified pseudopotential (Valence hole). As expected, both pseudopotential methods are significantly cheaper than the all-electron method using WIEN2k. The result suggests that the proposed new method is capable of doing an all-electron calculation with the cost of conventional pseudopotential calculations.

7.5 Summary

In this chapter, we propose a new method to calculate EELS via the low-loss scheme. At the moment the method is limited to beryllium, but potentially it could also be applied to other elements with semi-core electrons, for example, the K-edge of lithium ($1s$ electrons) and the L-edge of sodium and magnesium ($2s$ and $2p$ electrons).

In the new method, a pseudopotential that treats all four electrons of Be as valence electrons is used and thus all electrons are explicitly described. The Be K-edge spectrum is then calculated together with the low-loss spectrum. It is shown that the Be K-edge spectra simulated using the new approach are able to regenerate all the features seen in the spectra calculated using the conventional core-loss scheme, whether core hole is included or not, with no additional cost. As for the predicted transition energy, it can be obtained by either using Mizoguchi's method for pseudopotentials or the ΔSCF method for AE calculations.

Chapter 8

Simulating EELS within DFT

DFT is capable of predicting numerous physical properties, such as geometries, DOS, band structure diagrams and the low-loss and core-loss peaks of EELS. A key part of DFT is the treatment of the exchange and correlation functional and various methods have been developed. However, as described in the methodology chapters, a major limitation of DFT is that it is a ground-state theory and thus the calculations of excited-state properties are not guaranteed to work. One well-known issue is the underestimation of the band gaps of materials. In addition, as discussed in Chapter 5, there are some discrepancies between the experimental and simulated spectra, which indicate that DFT may not be good enough to model EELS. In this chapter, we study the simulation of EELS, within independent particle approximation, using functionals that are reported to make better predictions of band gaps: the Becke-Johnson functional (BJ), the Tran-Blaha functional (TB) and the RSCAN functional and make a comparison with the standard PBE functional.

To make a comprehensive comparison, we have selected eight candidate structures: the standard benchmark structures are diamond, silicon, and graphite which correspond to an insulator, a semi-conductor and a conductor. In addi-

tion, we have also studied LiF which is reported to have a large band gap of 14.20 eV [169]. A major problem of the low-loss EELS calculations using DFT is its failure in the high energy range (above 30 eV) when the structures involve *d*-state electrons. And thus rutile titanium dioxide is brought into the discussion. Finally, the initial incentive of this thesis is to identify the metal/oxide interface layer that appears during the oxidation of zirconium-based alloys. The bulk oxidation product, ZrO_2, known as zirconia and two computationally predicted stable structures of ZrO, the hexagonal and orthorhombic polymorphs [18, 170] are calculated. We start with the geometries of the structures predicted using different approaches, followed by the band structures and finally the low-loss region of EELS.

8.1 Geometry Optimisation

The DFT calculations discussed in this chapter have been performed with the CASTEP code [48] using ultrasoft pseudopotentials. As for the geometry optimisation, the original structures are taken from ICSD [154] and the Materials Project [171] except the hexagonal and orthorhombic ZrO which are from reference [18]. Two types of functionals are used: the PBE functional and the RSCAN functional. For the BJ and TB functionals, as their expressions are not derivable as the functional derivative of any known exchange and correlation energy functional, the total energy and the forces are not well correlated and cannot be used for geometry optimisation. For this reason, the subsequent band structure, DOS and low-loss EELS calculations using the BJ and TB functionals are based on a PBE-optimised structure.

As we can see from Table 8.1, both PBE and RSCAN yield very good results of geometry predictions with a difference less than 2.0%, except for the *c* parameter of graphite. The severe overestimation of the *c* value of graphite using PBE is

Structure	Parameter	PBE (Å)	RSCAN (Å)	Expt. (Å)
Diamond	a	3.571	3.554	3.567
Graphite	a	2.466	2.450	2.464
	c	8.511	7.046	6.711
LiF	a	4.063	3.983	4.028
Silicon	a	5.469	5.439	5.431
Rutile	a	4.643	4.590	4.594
	c	2.962	2.946	2.959
ZrO_2 Monoclinic	a	5.177	5.144	5.182
	b	5.245	5.213	5.248
	c	5.359	5.318	5.363
	β	99.60	99.35	99.71
ZrO Hexagonal	a	5.302	5.276	\
	c	3.203	3.186	\
ZrO Orthorhombic	a	3.246	3.213	\
	b	12.176	12.091	\
	c	8.591	8.558	\

Table 8.1: Structural parameters of a selection of metallic and semiconductor solids, computed using PBE and RSCAN functional at $T = 0$K. Experimental values were taken from ICSD [154], which are measured and reported at room temperature. As the hexagonal and orthorhombic ZrO are computationally predicted structures [18], no experimental data is available for comparison.

because of the lack of description of the van der Waals interactions, which keeps the graphite layer together. RSCAN gives a better prediction of the atomic distance in graphite layers. Overall, PBE has a tendency to overestimate the lattice constants, which agrees with previous studies [165–167]. As for RSCAN, it tends to underestimate the lattice constants. However, since the experimental values listed are taken at room temperature while the modelling results are simulated at 0K, the actual difference is larger and it is only reasonable to make the conclusion that its overall performance is good.

8.2 Band Structures

The major improvement of the meta-GGA functional over standard PBE functional is the description of electronic band structures and in particular, the band gaps. For the band structure calculations, there are four different functionals: PBE, Becke-Johnson (BJ), Tran-Blaha (TB), and RSCAN.

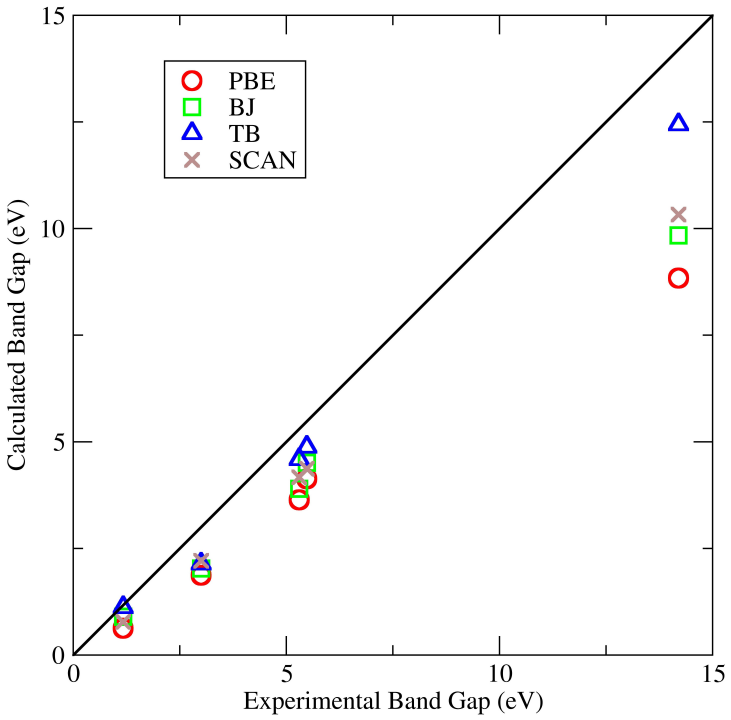


Figure 8.1: The band gaps of selected semiconductors and insulators from PBE (Red), BJ (Green), TB (Blue) and RSCAN (Brown) are plotted against the experimental values (Black) using the data in Table 8.2.

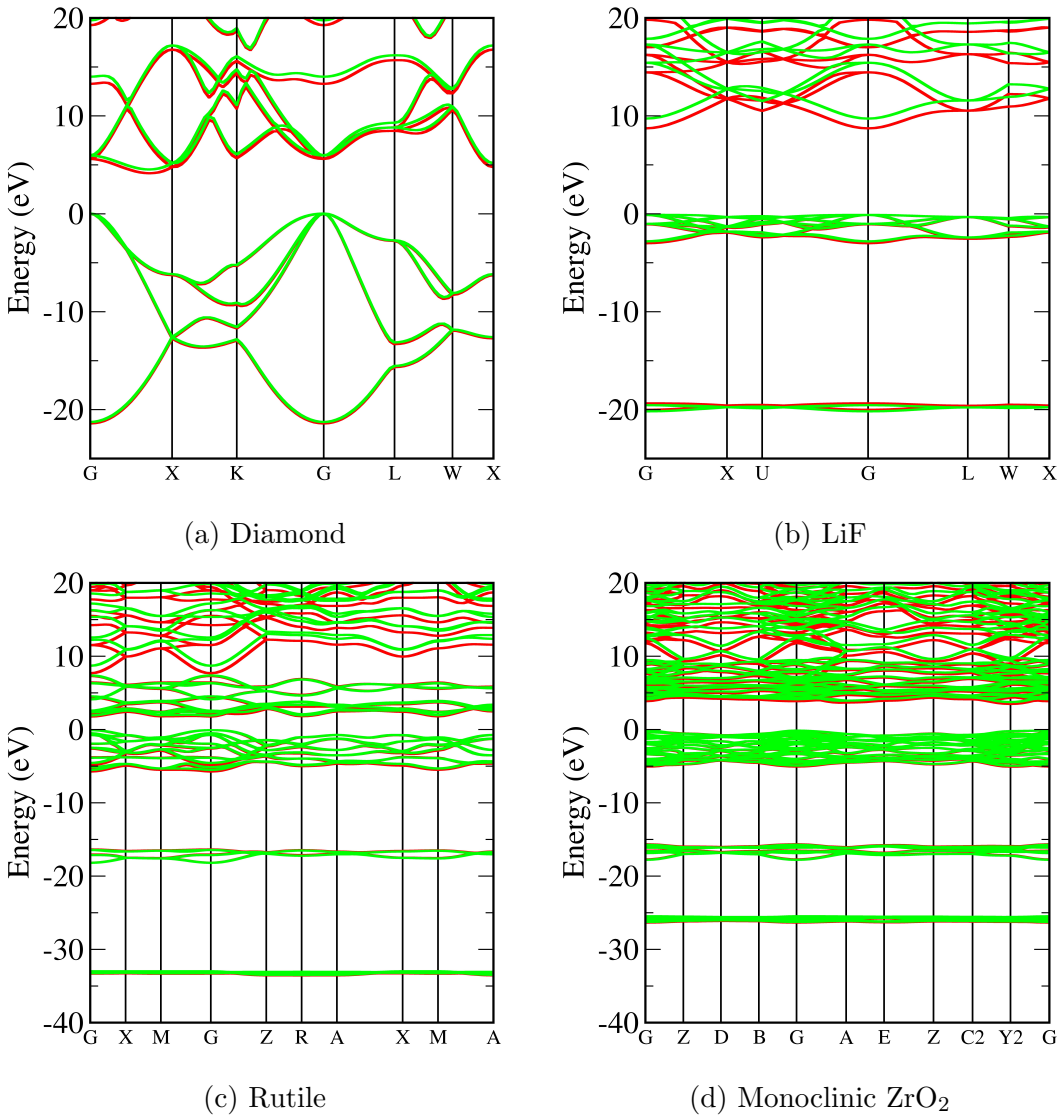
For the simulated band gaps, as shown in Figure 8.1 and Table 8.2, TB tends to produce the band gaps that is closest to the experimental values except for rutile. BJ and RSCAN show some improvements compared to PBE, but it is hard to make the judgment about which one works better, which is materials dependent. The above observations agree with the conclusion from reference [69]. However, even for the best results produced by TB, there is still an underestimation of the

Structure	PBE	BJ	TB	RSCAN	Expt.
Diamond	4.13	4.51	4.88	4.37	5.48
LiF	8.84	9.84	12.44	10.33	14.20
Silicon	0.63	0.90	1.12	0.78	1.17
Rutile	1.87	2.03	2.14	2.21	3.00
ZrO_2 Monoclinic	3.64	3.90	4.59	4.17	5.30

Table 8.2: Calculated band gaps of the candidate structures in eV. The experimental data are collected from [62, 172–176]

band gaps. In addition, for the TB calculation, a separate convergence test is required for the c parameter as described by equation 4.29 using a self-consistent method proposed in paper [92] and is further discussed in the Appendix. As for the d-block elements, harder pseudopotentials than the standard ones are also required to reach the convergence and thus make TB calculations expensive to run.

Next, we made an investigate of how these different functionals are able to predict more accurate band gaps than PBE by comparing the band structures. As shown in Figure 8.2, the valence bands predicted by PBE and BJ are almost identical. The major improvement that BJ has made is an upward shift of the conduction bands, both for structures involving and not involving d-states and for conductors and semi-conductors, which results in larger band gaps than PBE.



(a) Diamond

(b) LiF

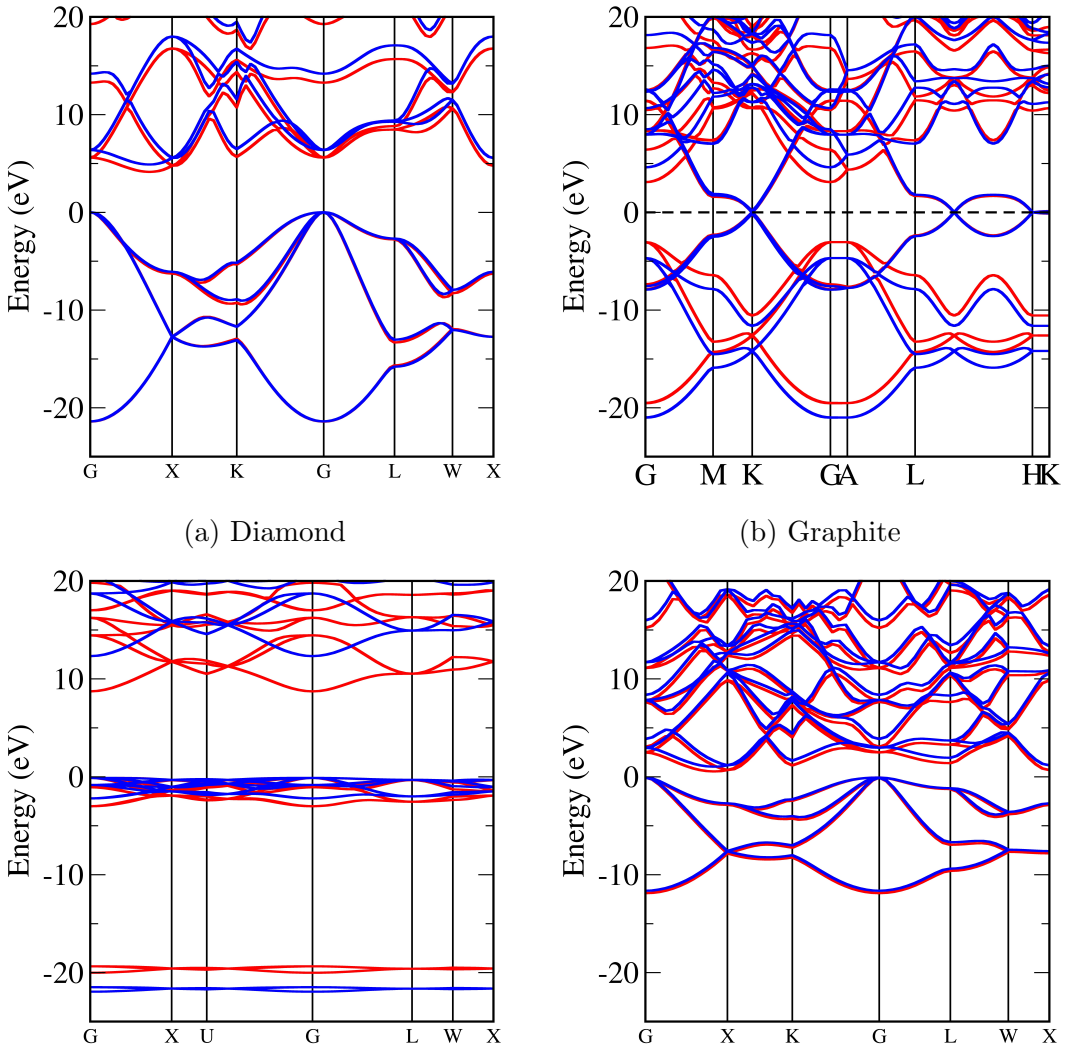
(c) Rutile

(d) Monoclinic ZrO_2

Figure 8.2: Comparison of band structures of selected candidate structures calculated using PBE (Red) and BJ (Green) functionals. For semiconductors, the valence band top is at 0 eV. For metals, the Fermi energy is plotted at 0 eV (Black Dashed).

For TB shown in Figure 8.3, a larger upward shift of the conduction bands is observed, which results in the best band gaps among the four functionals. In addition, for graphite, the valence band is pushed down in energy with TB. As for LiF and for the valence band lying 0 to 3 eV below the Fermi energy, which corresponds to the F $2p$ bands, TB underestimates its bandwidth. However, the F $2s$ bands (around 20 eV below the Fermi level) are better positioned with TB than with LDA as confirmed by the GW results in the next chapter and also from

reference [177].



(a) Diamond

(b) Graphite

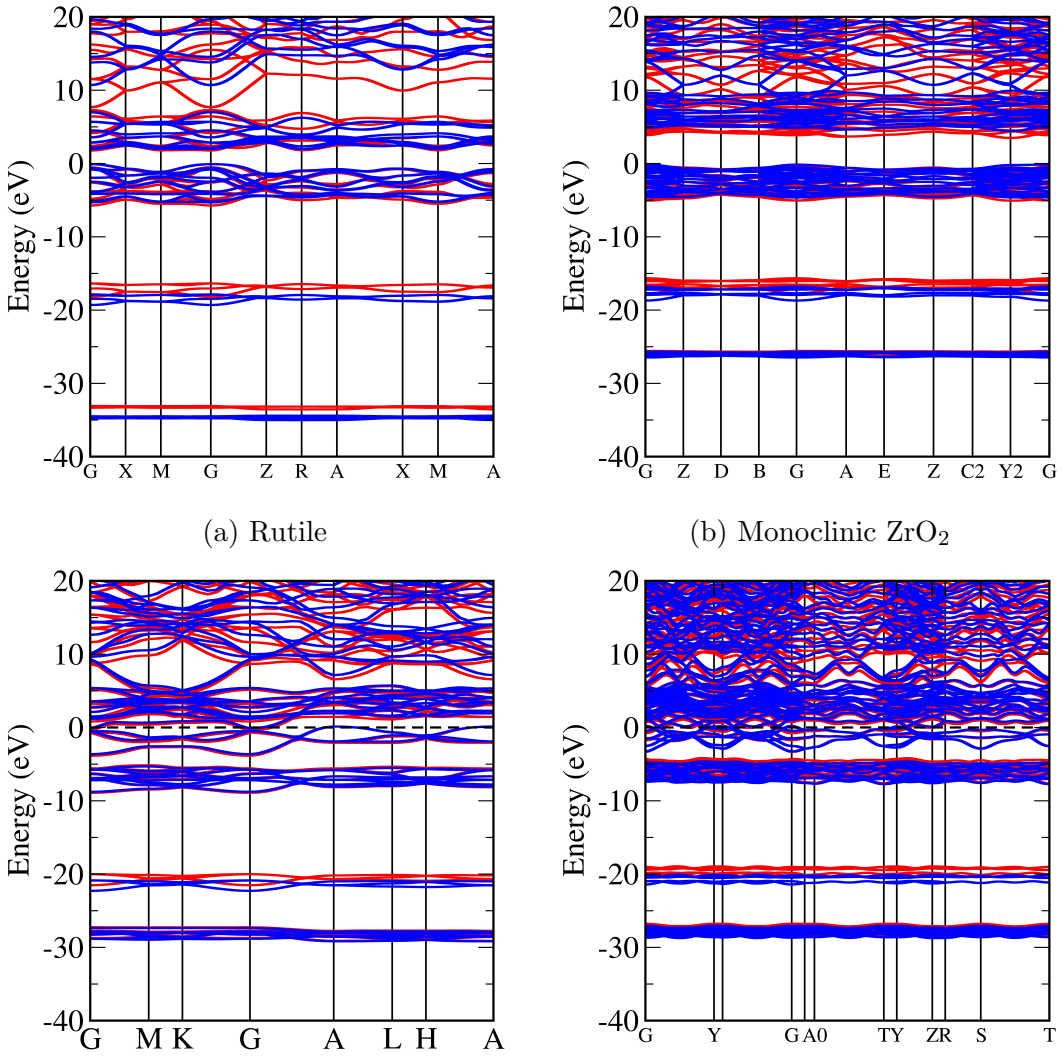
(c) LiF

(d) Silicon

Figure 8.3: Comparison of band structures of candidate structures calculated using PBE (Red) and TB (Blue) functionals. For semiconductors, the valence band top is at 0 eV. For metals, the Fermi energy is plotted at 0 eV (Black Dashed).

As for the transition metal oxides as shown in Figure 8.4, we can see that in addition to the upward shift of the conduction bands, there is also a downward shift of the valence bands around -20 eV which are mostly of O 2s character with a little hybridisation with the Ti s, p, d states and Zr s, p, d states respectively. Besides, the lower lying bands (around -35 eV for rutile and between -25 to -30 eV for the polymorphs of ZrO) are the Ti 3p and Zr 4p sates, which are predicted

to be lower by 1.5 eV using TB. As for the upper valence band near the Fermi energy, there is a very strong hybridisation between the O $2p$ and the transition metal d-states (Ti $3d$ and Zr $4d$) with the bandwidth underestimated by TB. Another thing to mention is that for the conduction bands in rutile, there is a band separation predicted by TB at around 10 eV, which is due to an upward shift of the Ti $4p$ bands.



(a) Rutile

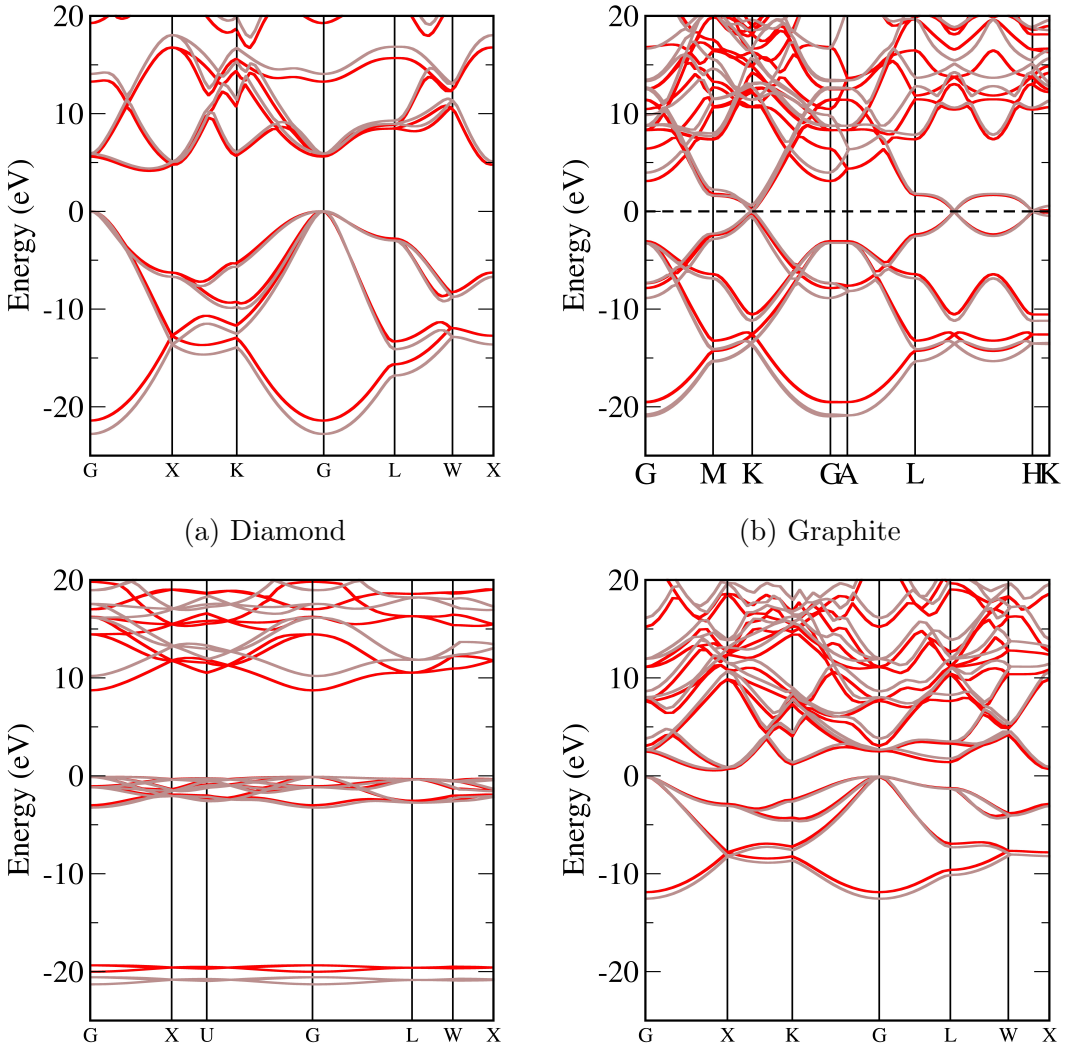
(b) Monoclinic ZrO_2

(c) Hexagonal ZrO

(d) Orthorhombic ZrO

Figure 8.4: Comparison of band structures of candidate structures involving d-states electrons, calculated using PBE (Red) and TB (Blue) functionals. For semiconductors, the valence band top is at 0 eV. For metals, the Fermi energy is plotted at 0 eV (Black Dashed).

In the case of RSCAN as shown in Figure 8.5, for diamond, graphite, and silicon, it tends to predict a larger valence bandwidth for bands close to the Fermi energy. For LiF, a downward shift of the F 2s bands (around 20 eV below the Fermi level) is observed, similar to what is predicted by TB. In all four cases, the larger band gap by RSCAN is due to an upward shift of the conduction bands.

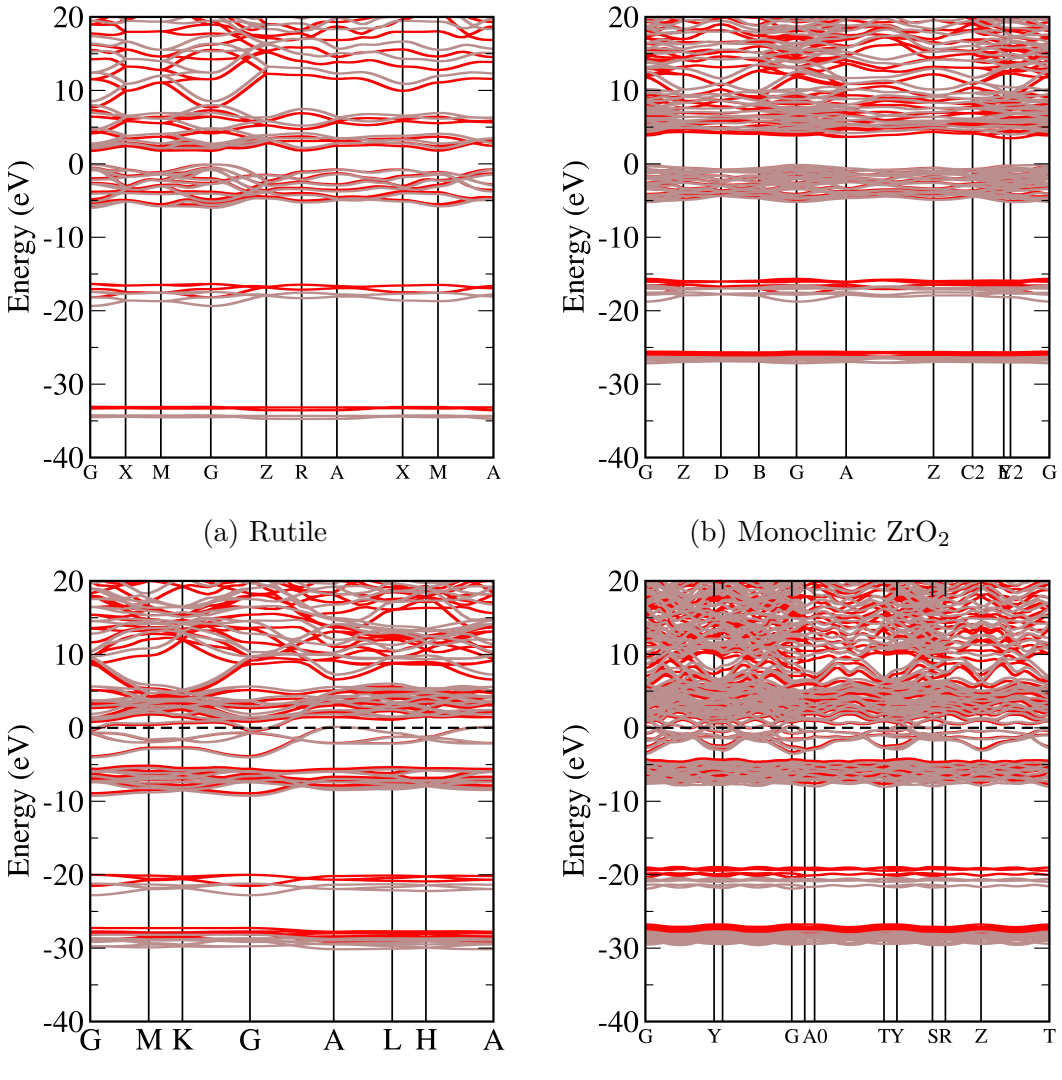


(a) Diamond (b) Graphite

(c) LiF (d) Silicon

Figure 8.5: Comparison of band structures of candidate structures calculated using PBE (Red) and RSCAN (Brown) functionals. For semiconductors, the valence band top is at 0 eV. For metals, the Fermi energy is plotted at 0 eV (Black Dashed).

Similarly, for transition metals as shown in Figure 8.6, RSCAN gives a larger width for the valence bands that are close to the Fermi energy. For all four transition metals, RSCAN shows a lower position for the O 2*s*-states (around -20 eV) and the *d*-states (-25 to -35 eV).



(a) Rutile

(b) Monoclinic ZrO_2

(c) Hexagonal ZrO

(d) Orthorhombic ZrO

Figure 8.6: Comparison of band structures of candidate structures involving *d*-states electrons, calculated using PBE (Red) and RSCAN (Brown) functionals. For semiconductors, the valence band top is at 0 eV. For metals, the Fermi energy is plotted at 0 eV (Black Dashed).

As the prediction of the EEL spectrum is closely related to the transition between states as described in the methodology chapters, due to the different band structures predicted by PBE, BJ, TB and RSCAN, we are expecting a difference

in the modelled EELS other than just a rigid shift due to the band gaps. Since the low-loss EELS is directly associated with the valence excitations close to the Fermi energy, we focus on the low-loss region of the modelled EELS to investigate the influence of different functionals.

8.3 Low-loss EELS within IPA

In this section, we present our results of the modelled low-loss EELS with different functionals, using the independent particle approximation (IPA). There are four functionals used: PBE, BJ, TB, and RSCAN. The resulting spectra of each material are shown as follows.

8.3.1 Diamond

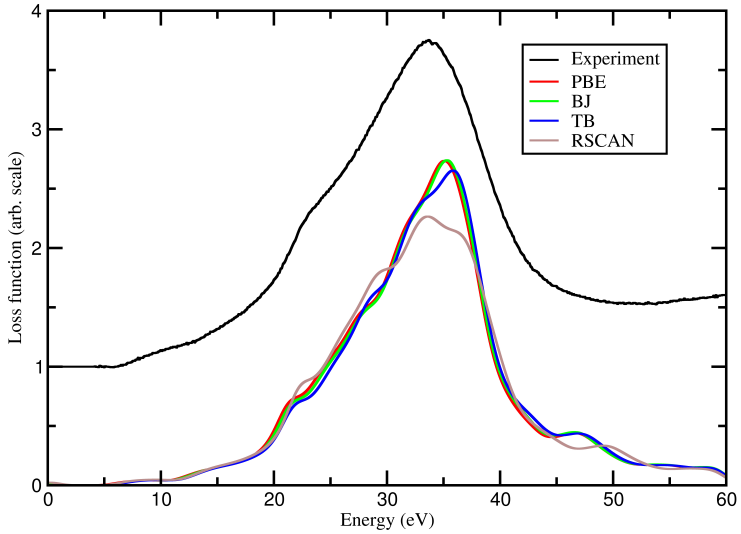


Figure 8.7: Calculated EELS of diamond using PBE (Red), BJ (Green), TB (Blue) and RSCAN (Brown). The experimental spectrum (Black) is taken from the EELS Data Base [178], which was originally taken from Reference [179]. The zero-loss peak is ignored and the spectrum is background subtracted with power law on selected low-loss region.

Method	PBE	BJ	TB	RSCAN	Experiment
Plasmon Peak	35.0	35.3	35.9	33.6	33.8
Plasmon Shoulder	21.5	21.6	22.0	22.6	23.6

Table 8.3: Position of the low-loss peaks of diamond using different functionals.

The simulated EELS of diamond is shown in Figure 8.7. The experimental spectrum consists of two main features: a broad peak at 33.8 eV and a small shoulder at 23.6 eV. Both features are associated with the collective excitation of the valence electrons. The broad main peak indicates the existence of plasmon damping as a result of single-electron excitation. We have collected the positions of the peaks predicted using different functionals as shown in Table 8.3. From the position side, PBE, BJ, and TB all tend to overestimate the plasmon energy of the main broad peak while underestimating that of the shoulder. RSCAN gives the positions of the plasmon peaks that are in best agreement with the experimental values. As for the shapes, very similar spectra are given by PBE, BJ, and TB and all four functionals show line shapes close to the experimental spectrum while they also give features that are not seen experimentally, which come from the band structure effects. In addition, with the same broadening used for all four functionals, RSCAN gives more fine features than the others and also predicts a lower intensity of the main broad peak. Overall, RSCAN makes better predictions regarding the position of the peak but gives poor performance regarding the shape due to the additional fine features.

8.3.2 Graphite

Method	PBE	BJ	TB	RSCAN	Experiment
Plasmon Peak	22.9	23.4	24.6	26.5	26.7
$\pi - \pi^*$ transition	5.8	5.9	6.1	6.2	6.6

Table 8.4: Position of the low-loss peaks of graphite using different functionals.

For graphite as shown in Figure 8.8, it has a plasmon peak at 26.7 eV and a

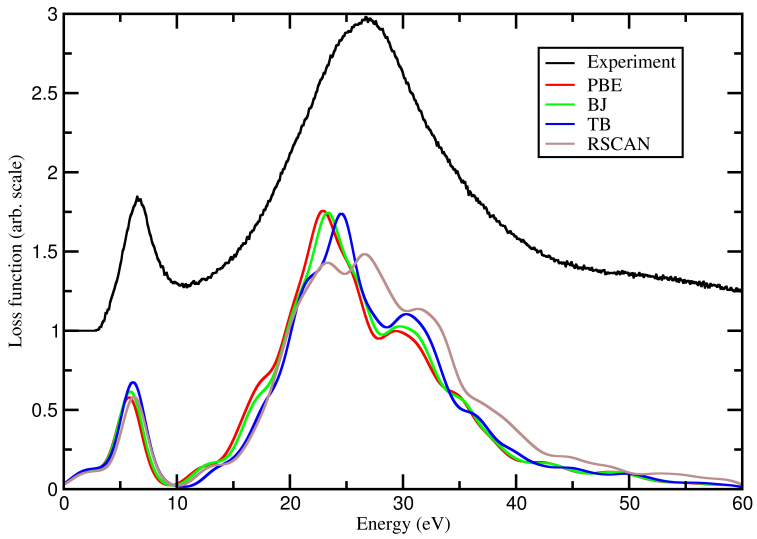


Figure 8.8: Calculated EELS of graphite using PBE (Red), BJ (Green), TB (Blue) and RSCAN (Brown). The experimental spectrum (Black) is taken from the EELS Data Base [178]. The zero-loss peak is removed with a fitted logarithm tail between 2 and 4 eV and the background is subtracted using power law.

large additional peak at 6.6 eV which corresponds to the transitions between the π and π^* states. Comparing the positions of the two peaks of the simulated spectra with the experimental one as shown in Table 8.4, all four functionals tend to underestimate the energies of both the plasmon and the $\pi - \pi^*$ peaks. BJ, TB , and RSCAN do improve the positions of the PBE peaks, which is due to an increase in the bandwidth as discussed in the band structures section. Regarding the shape of the peaks, the $\pi - \pi^*$ peak in the experimental spectrum is perfectly replicated by all four functionals. However, as for the plasmon peaks, the calculated spectra show an additional shoulder at around 30 eV which is not seen in the experiment. The spectra obtained using PBE and BJ are very similar and almost indistinguishable. In addition, RSCAN predicts more fine structures, and the plasmon peak is split into two peaks with lower intensity. Overall, TB produces better results than the PBE with a more accurate position of the plasmon peak. RSCAN gives better positions but a worse shape of the

plasmon peak.

8.3.3 LiF

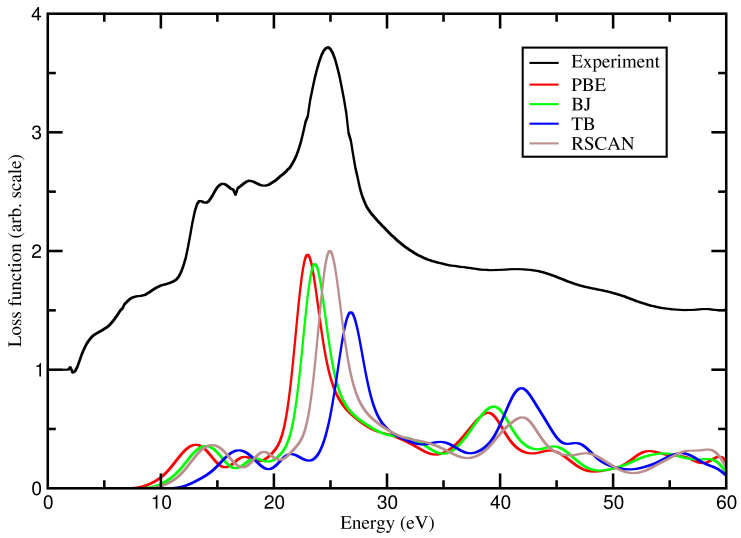


Figure 8.9: Calculated EELS of LiF using PBE (Red), BJ (Green), TB (Blue) and RSCAN (Brown). The experimental spectrum (Black) is taken from the EELS Atlas [180]. The zero-loss peak is ignored and the spectrum is background subtracted with power law on selected low-loss region.

Method	PBE	BJ	TB	RSCAN	Experiment
Conduction Shoulder	13.0	13.9	17.9	14.6	17.7
Plasmon Peak	23.0	23.6	26.8	24.9	24.8
Plasmon Shoulder	38.9	39.4	41.9	42.0	42.2

Table 8.5: Position of the low-loss peaks of LiF using different functionals.

In the case of LiF, the experimental spectrum (Figure 8.9) consists of a sharp plasmon peak at 24.8 eV, which indicates low plasmon damping and is a typical feature of alkali metals, and a plasmon shoulder at around 42.2 eV. In addition, there is another shoulder at 17.7 eV which corresponds to the electron transition from the top of the valence band to the bottom of the conduction band, i.e. crossing the band gap. Comparing the position of the low-loss peaks as listed in

Table 8.5, we could see that TB gives the best position of the conduction shoulder. It agrees with the fact that TB makes the best band gap prediction. As for the main plasmon peak and the plasmon shoulder, both PBE and BJ underestimate the plasmon energy. TB works well with the plasmon shoulder but shifts the main plasmon peak by around 2 eV to the right. The best positions of the plasmon peaks are given by RSCAN with a difference less than 0.2 eV.

All four functionals give distinguishable spectra for LiF, while the ones obtained by PBE and BJ are still very similar. Comparing the shapes of the peaks, we can see that the height difference between the two plasmon peaks of the TB spectrum is smaller than those predicted by PBE, BJ, and RSCAN. The largest height difference is given by RSCAN which best aligns with the experiment. Furthermore, as for the experimental spectrum, there are some fine structures lying below the energy of the band gap, which is not seen from the modelling spectra. Potentially it could be an artifact created when removing the zero-loss peak, or it could be an indication of the Rydberg series of states caused by excitons. Since within DFT the excitonic effect is not included, we will make further discussion in the next chapter when talking about BSE. Overall, the best conduction shoulder is given by TB as a result of the best band gap predicted while the plasmon peaks are best modelled with RSCAN.

8.3.4 Silicon

Method	PBE	BJ	TB	RSCAN	Experiment
Plasmon Peak	16.7	16.9	17.0	16.5	16.6

Table 8.6: Position of the low-loss peaks of silicon using different functionals.

The silicon specimen has a plasmon peak at 16.6 eV as shown in Figure 8.10. There is an additional peak at around 33 eV which is around twice the energy of the main plasmon peak. That peak is caused by plural scattering and thus is not seen in the modelling spectra. The plasmon peak also represents a sharp

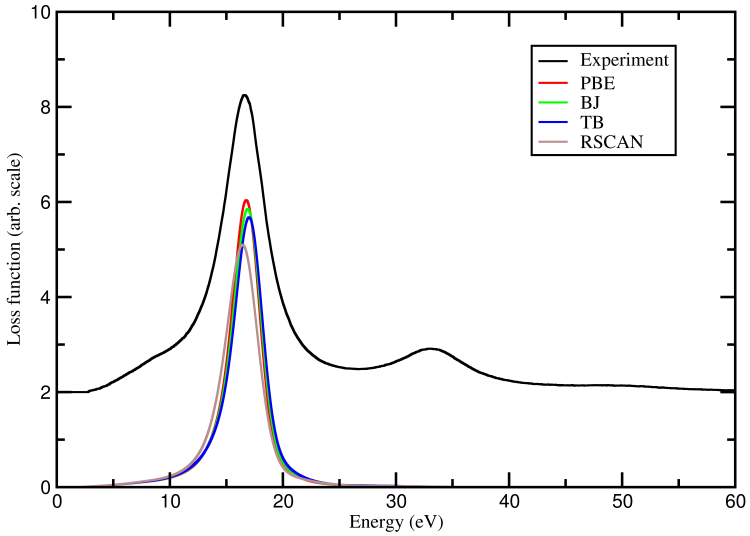


Figure 8.10: Calculated EELS of silicon using PBE (Red), BJ (Green), TB (Blue) and RSCAN (Brown). The experimental spectrum (Black) is taken from the EELS Data Base [178], which was originally taken from Reference [181]. The zero-loss peak is removed with a fitted logarithm tail between 2 and 4 eV and the background is subtracted using power law.

resonance in silicon and low dampening. Comparing the modelling results with the experimental one (Table 8.6), all four functionals give similar positions of the plasmon peak. The spectra of PBE, BJ, and TB are very similar and almost indistinguishable. The RSCAN spectrum is different due to a lower intensity than the other spectra.

8.3.5 Rutile

Method	PBE	BJ	TB	RSCAN	Experiment
Plasmon Peak 1	11.1	11.1	11.1	11.7	11.9
Plasmon Peak 2	24.4	24.7	27.3	25.6	25.9
Transition	40.9	41.3	42.8	42.6	48.3

Table 8.7: Position of the low-loss peaks of rutile using different functionals.

For rutile, experimentally there are three main features in the EEL spectrum as shown in Figure 8.11: two plasmon peaks at 11.9 eV and 25.9 eV and a third

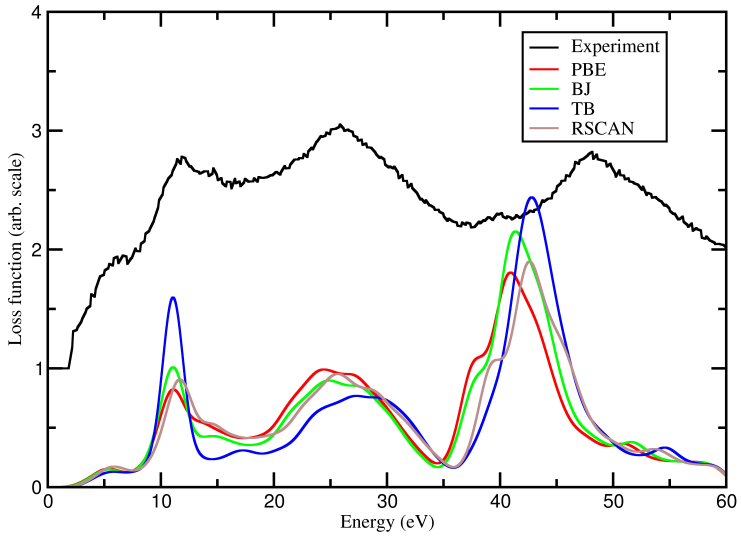


Figure 8.11: Calculated EELS of rutile using PBE (Red), BJ (Green), TB (Blue) and RSCAN (Brown). The experimental spectrum (Black) is taken from the EELS Data Base [178]. The zero-loss peak is removed using the reflected tail method and the background is subtracted using power law.

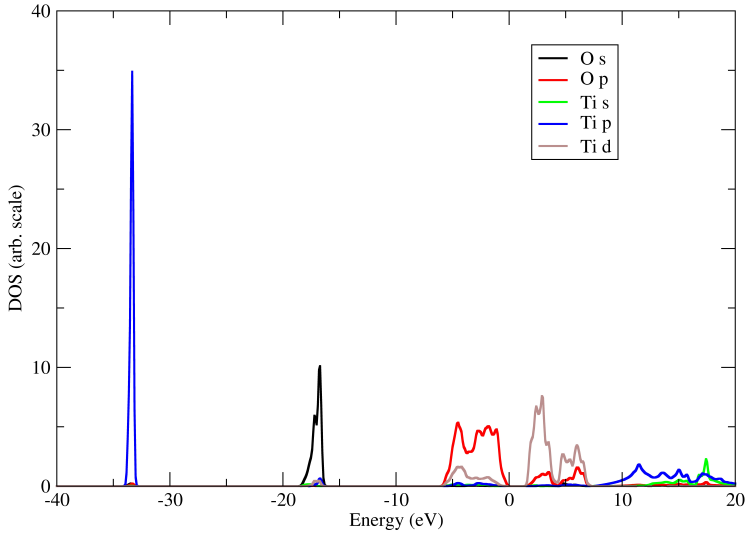


Figure 8.12: The projected density of states (PDOS) of rutile calculated using the PBE functional. The top of the valence band is set to zero.

peak in the higher energy range at 48.3 eV. Combined with the PDOS shown in Figure 8.12, it can be deduced that the first plasmon peak at 11.9 eV is caused by the valence electrons close to the Fermi energy. The second plasmon peak at about 25.9 eV is due to a broad collective excitation stemming from the oxygen $2s$ orbitals. And the third peak at 48.3 eV is a result of the transitions from the Ti $3p$ states to the bottom of the valence bands which are the unoccupied Ti $3d$ states.

Distinctive spectrum is given by different functionals. Compared with the simulated EELS, as for the positions, PBE, BJ, and TB all give exactly the same position for the first plasmon peak, which underestimates the energy of the experimental peak. RSCAN improves the position of that peak. For the second plasmon peak, PBE and BJ tend to underestimate the plasmon energy while TB overestimates that. The best prediction is still given by RSCAN. However, all four functionals predict a sharp peak at around 42 eV for the third transition peak, which disagrees with the experimental spectrum. As for the shapes, PBE, BJ, and RSCAN predict similar shapes for the first and the second plasmon peaks, which give a good approximation of the experimental peaks. As for TB however, the intensity of the first peak is much higher than the experimental one. This is caused by the underestimation of the valence bandwidth as discussed in the previous section.

In conclusion, using all four different functionals with IPA, no satisfactory results are obtained due to the failure to model the transition peak in the higher energy range.

8.3.6 Monoclinic ZrO_2

As shown in Figure 8.13 and 8.14, similar to rutile, experimentally monoclinic ZrO_2 has a valence plasmon peak at 15.3 eV, a collective excitation peak at 25.4

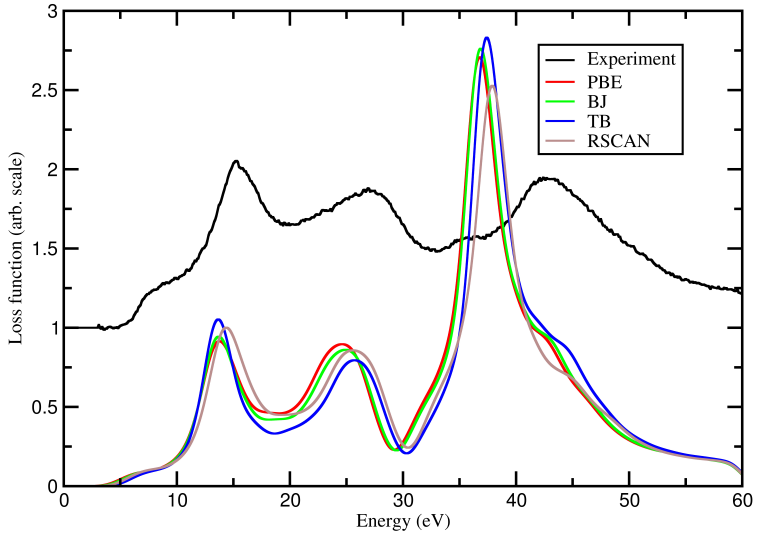


Figure 8.13: Calculated EELS of monoclinic ZrO_2 using PBE (Red), BJ (Green), TB (Blue) and RSCAN (Brown). The experimental spectrum (Black) is taken from the EELS Data Base [178], which was originally taken from Reference [62]. The zero-loss peak is ignored and the spectrum is background subtracted with power law on the selected low-loss region.

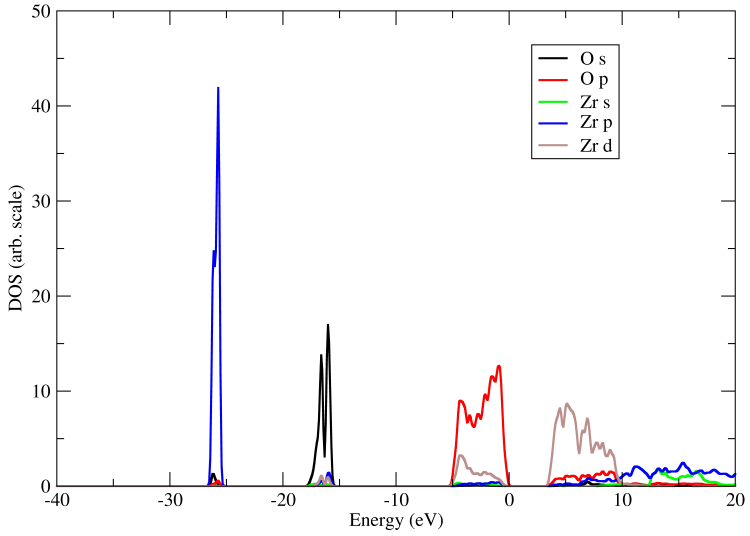


Figure 8.14: The projected density of states (PDOS) of monoclinic ZrO_2 calculated using the PBE functional. The top of the valence band is set to zero.

Method	PBE	BJ	TB	RSCAN	Experiment
Plasmon Peak 1	13.8	13.7	13.7	14.4	15.3
Plasmon Peak 2	24.6	24.9	25.8	25.6	25.4
Transition	36.8	36.9	37.4	37.9	42.7

Table 8.8: Position of the low-loss peaks of rutile using different functionals.

eV due to the O 2s states and a transition peak at 42.7 eV corresponding to the zirconium 4p excitations.

On the simulation side, very similar spectra are predicted using PBE and BJ functionals. For the first two plasmon peaks, RSCAN gives the result that is in best alignment with the experimental spectrum, both in position and shape. PBE and BJ tend to underestimate the plasmon energies. As for TB, although it predicts a more accurate band gap, the simulated spectrum is not improved: the first plasmon peak is at a similar position compared to PBE and BJ while the second peak overestimates the associated energy. In addition, a larger difference in the peak heights is observed for the TB spectrum, due to the underestimation of the valence bandwidth. As for the transition peak, all four functionals fail to simulate the experimental feature. Sharper peaks at lower energies are modelled, which deviate from the broad peak observed experimentally, similar to what we have seen with rutile.

8.3.7 Hexagonal and Orthorhombic ZrO

Experimental	Hex(P)	Hex(R)	Orth(P)	Orth(R)
Plasmon Peak 1 (6.6)	5.4	5.9	6.2	6.7
Plasmon Peak 2 (14.6)	13.9	14.7	14.4	15.0
Plasmon Shoulder (24.2)	23.2	24.4	\	\
Transition (40.4)	36.4	37.2	36.0	37.0

Table 8.9: Comparison of the position of the low-loss peaks of hexagonal and orthorhombic ZrO using PBE (P) and RSCAN (R) functionals. Experimental values are shown in the bracket.

Both hexagonal and orthorhombic ZrO are computationally predicted structures

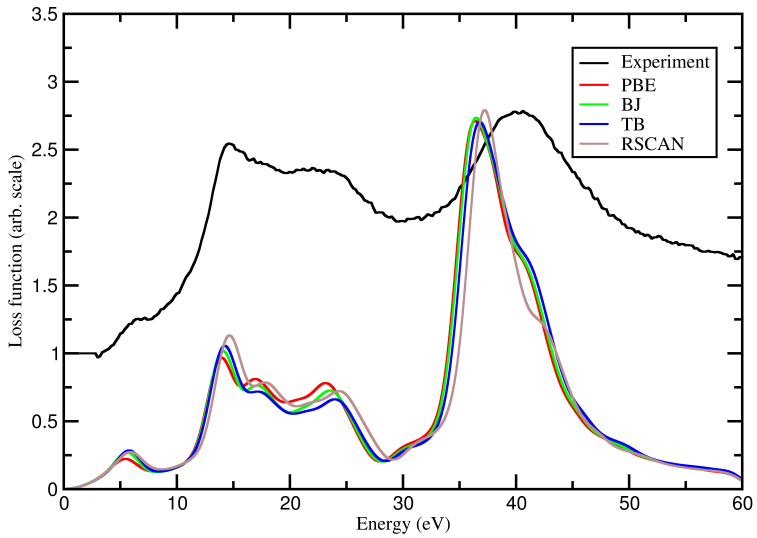


Figure 8.15: Calculated EELS of hexagonal ZrO using PBE (Red), BJ (Green), TB (Blue) and RSCAN (Brown). The experimental spectrum (Black) is from Reference [18]. The zero-loss peak is removed with a fitted logarithm tail between 2 and 4 eV and the background is subtracted using power law.

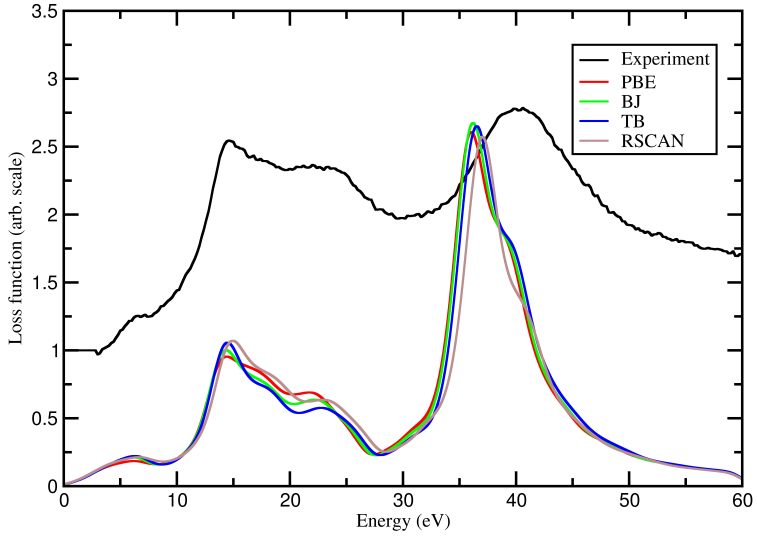


Figure 8.16: Calculated EELS of orthorhombic ZrO using PBE (Red), BJ (Green), TB (Blue) and RSCAN (Brown). The same experimental spectrum (Black) from Reference [18] is used.

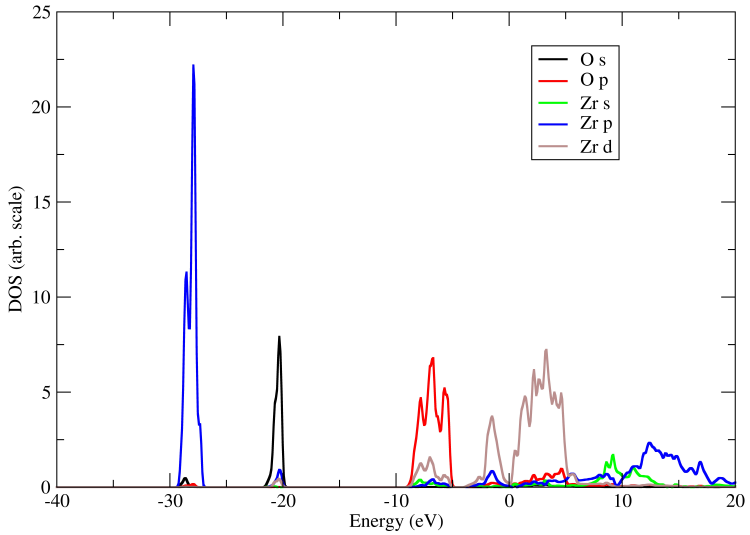


Figure 8.17: The projected density of states (PDOS) of hexagonal ZrO calculated using the PBE functional. The Fermi energy is set to zero.

from Reference [18]. The experimental spectrum is also given by the author of the same article, with the sample being a thin interface layer between the zirconium metal and the monoclinic ZrO_2 oxide. In that article, the author compared the low-loss spectrum simulated using the PBE functional with the experimental spectrum up to 30 eV and claimed that the interface layer is hexagonal ZrO.

From the experimental spectrum as shown in Figure 8.15, we can identify four main features: a small plasmon peak at 6.6 eV, a sharp plasmon peak at 14.6 eV, a plasmon shoulder at 24.2 eV and a transition peak at 40.4 eV. From Figure 8.17, we could easily assign the first small plasmon peak to be the valence excitation of Zr 4*d* orbitals. The major sharp peak and the plasmon shoulder are the results of the collective excitation of the O 2*p* and 2*s* states respectively and the transition peak is caused by the Zr 4*p* excitations, similar to rutile and monoclinic ZrO_2.

Comparing the simulated spectra of the hexagonal and orthorhombic ZrO as

shown in Figure 8.15 and 8.16 and Table 8.9, for both hexagonal and orthorhombic ZrO, similar results are given by all four different functionals, with additional fine features for the RSCAN functional. For the orthorhombic ZrO structure, although a better-positioned small plasmon peak is simulated, the plasmon shoulder is missing. For the high energy range of the spectrum, we are still encountering the same problem for rutile and monoclinic ZrO_2 that the simulated spectra can not accurately reproduce the experimental feature.

Method	PBE	BJ	TB	RSCAN	Experiment
Plasmon Peak 1	5.4	5.6	5.8	5.9	6.6
Plasmon Peak 2	13.9	14.1	14.2	14.7	14.6
Plasmon Shoulder	23.2	23.5	24.0	24.4	24.2
Transition	36.4	36.5	36.8	37.2	40.4

Table 8.10: Position of the low-loss peaks of hexagonal ZrO using different functionals.

For the hexagonal ZrO, when comparing peak positions with different functionals shown in Table 8.10, the best spectrum is given by RSCAN. Compared to PBE, BJ and TB only slightly improve the peak positions. Once again, no satisfactory result is produced for the simulation of the transition peak using the four functionals.

8.3.8 Costs of Calculations

Finally, we make a comparison of the relative costs of calculations using different functionals, taking diamond as an example as shown in Table 8.11. Here we make the approximation that the costs of the convergence tests of the energy cutoff, the k-point sampling, the spectral k-point sampling, and the number of unoccupied bands are the same for different functionals, and converged parameters are used for the final low-loss EELS calculations. The calculations were performed on the YOUNG cluster supported by the UK Materials and Molecular Modelling Hub using the message passing interface (MPI) programs, parallelised over 24

processes.

Functional	PBE	BJ	TB	RSCAN
Calculation Time	655	8669	8618	1381
c Convergence Time	\	\	25934	\
Total Time	655	8669	34552	1381

Table 8.11: Comparison of the calculation time (wall time in seconds) of the low-loss EELS of diamond using different functionals.

As shown in Table 8.11, the costs of the final low-loss EELS calculations using BJ and TB functionals are roughly the same, which are about 13 times higher than that of a standard PBE calculation. The calculation time difference is mainly due to the difference in computing the spectral properties. However, for the TB functional, an additional self-consistent c convergence test is required. A TB calculation of the low-loss EELS is about 40 times more expensive than a PBE calculation. In addition, as discussed earlier, a harder pseudopotential is required for the d-block element to reach a converged c parameter for the TB functional. Thus, the cost is anticipated to be even higher for materials with transition metals. As for an RSCAN calculation, the cost is about double that of a PBE calculation.

8.4 Summary

In this chapter, we compared the geometry optimisation, band structures (band gaps) and the EELS simulated using PBE, BJ, TB and RSCAN functional. For the geometry optimisation, the correlation between energy and force is missing for BJ and TB and thus the two functionals can not be used. Both PBE and RSCAN yield good results of the lattice constants except for the atomic distance between the graphite layers using PBE (the c parameter). PBE tends to overestimate the lattice constants while RSCAN tends to underestimate them.

As for the band gaps, TB gives the best performance among the four functionals

except for rutile. RSCAN and BJ both improve the band gaps predicted by PBE, but they produce better results for different materials. On the band structure side, the improvement in band gaps is caused by an upward shift of the valence band. Band structures simulated by PBE and BJ are similar. As for TB, although it predicts better band gaps, for certain materials it tends to underestimate the valence bandwidth. For RSCAN, other than improved band gaps, negative shifts of the positions of the lower valence bands are also observed.

The simulated EELS discussed in this chapter are obtained using the independent particle approximation. Among the four functionals, RSCAN makes better predictions regarding the position of the peaks. However, additional fine features are seen in the RSCAN results which make it poor in accurately predicting the shape of the spectra. TB gives the best modelling results for LiF but for most other structures, no sharp difference is seen with different functionals. In addition, all four functionals fail to give an accurate representation of the transition peak in the higher energy range of the spectra of materials that involve d-state electrons. Regarding the cost of calculations, PBE and RSCAN calculations are similar while BJ and TB calculations are significantly more expensive. It is thus suggested that for the band gaps prediction, TB makes better predictions with additional cost. For the low-loss EELS calculations, no functional tends to give the best overall performance and PBE should still be used in most cases given its relatively lower cost.

Chapter 9

Simulating EELS Beyond DFT

no functional tends to give the best overall performance and PBE should still be used in most cases given its relatively lower cost.

In the last chapter I have shown that within the independent particle approximation (IPA), no meta-GGA functionals tend to give the best overall performance and PBE should still be used given its relatively lower cost. Although DFT serves as a good starting point to model the EEL spectrum, there are still some discrepancies, i.e. the exact positions of the peaks and fine features that appear at energies smaller than the band gap. The most distinctive difference is in the high energy range of the low-loss EEL spectrum of materials that are composed of transition metals. Both the standard PBE and the meta-GGAs fail to accurately produce such features.

To improve the simulated EEL spectrum, there are two questions waiting to be solved. The first one is that if DFT is sufficient to model EELS. Since DFT is a ground-state theory while EEL spectroscopy involves the excitation of electrons, it is obvious that theoretically DFT is not enough. In this chapter, we will tackle this question by using theories beyond DFT that are directly related to the excited properties of materials, the time-dependent density functional theory (TDDFT)

and the GW method.

The second question is that if IPA is adequate to model EELS. Theoretically the answer is no since in theory the electrons and holes are not independent but correlated. To solve this problem, in this chapter, I will start with the local field effects (LFE) which are vital for inhomogeneous systems. The next approach is the linear-response theory which helps simplify the TDDFT method. To finalise this chapter, I will present the BSE method that runs on top of the GW method.

9.1 Low-loss EELS with LFE

In the previous chapter, the ground-state calculations were performed with the CASTEP code and the EEL spectrum calculations were done with OptaDOS. In OptaDOS, the imaginary part of the microscopic dielectric function is calculated based on IPA, using the method proposed in Pickard's thesis [114] as described in the methodology chapter:

$$\varepsilon_2(\omega) = \frac{4\pi}{q^2\omega} \sum_{v,c,\mathbf{k}} \left| \left\langle \phi_{c\mathbf{k}} \middle| e^{i\mathbf{q}.\mathbf{r}} \middle| \phi_{v\mathbf{k}} \right\rangle \right|^2 \delta(\epsilon_{c\mathbf{k}} - \epsilon_{v\mathbf{k}} - \omega) \tag{9.1}$$

for which the matrix elements and the transition energies are obtained from the eigenvalues and eigenfunctions of the Kohn-Sham equation of the ground-state DFT calculations. The real part of the dielectric function is then calculated with the Kramers-Krönig relation.

For calculations shown in this chapter, the ground-state calculations were performed with Quantum Espresso [112, 113] while the excited-state calculations were done with the YAMBO code [105]. In addition, we also used YAMBO for the associated spectroscopy simulation. In YAMBO, the microscopic dielectric function is obtained by solving the Dyson equation for the independent particle

susceptibility [99, 123]:

$$\varepsilon_{\mathbf{GG'}}(\mathbf{q},\omega) = \delta_{\mathbf{GG'}} - v_{\mathbf{G}}(\mathbf{q})\chi^{0}_{\mathbf{GG'}}(\mathbf{q},\omega) \tag{9.2}$$

for which the susceptibility χ^0 describes the transitions between occupied and empty states.

Up to this step, the calculated microscopic dielectric function using the two different approaches should be identical in nature. The major difference between OptaDOS and YAMBO is the following construction of the energy loss function. In OptaDOS, it is assumed that microscopic dielectric function is diagonal in the reciprocal space and the macroscopic dielectric function is just the zeroth element of the dielectric matrix [99]:

$$\varepsilon'_{M}(\omega) = \lim_{\mathbf{q}\to 0} \varepsilon(\mathbf{q},\omega)_{\mathbf{G}=\mathbf{G'}=\mathbf{0}} \tag{9.3}$$

However, such an approximation is not true if the system is inhomogeneous. The off-diagonal elements of the dielectric matrix could be non-zero and must be taken into account in the matrix inversion as described by [99]:

$$\varepsilon_{M}(\omega) = \lim_{\mathbf{q}\to 0} \frac{1}{[\varepsilon^{-1}(\mathbf{q},\omega)]_{\mathbf{G}=\mathbf{G'}=\mathbf{0}}} \tag{9.4}$$

The local field effects (LFE) corresponds to the discrepancy between the macroscopic dielectric functions calculated using the two different approaches. The effects are reported to have influence on the positions of the valence plasmon peaks of silicon [182] and the transition peaks at higher energies of rutile [63]. The contribution of the LFE depends on both the microscopic inhomogeneities and the microscopic polarisability of the system [99]. To simplify the notation, we refer the approximations in YAMBO that involve the LFE as the random phase

approximation (RPA) while the approximations in OptaDOS as the independent particle approximation (IPA), which is essentially RPA without the LFE.

As for the ground-state DFT calculations which are performed with Quantum Espresso, the norm-conserving (NC) pseudopotentials were used as a requirement for the subsequent YAMBO calculations. The PBE functional is used for a direct comparison with the CASTEP results. We have also used the LDA functional for subsequent comparison with the TDDFT and GW methods since the only available type of TDDFT functional is the adiabatic LDA functional.

As expected, the NC PBE pseudopotential gives very similar results to the ultra-soft (US) PBE pseudopotential has a tendency to overestimate the cell parameters while LDA tends to underestimate. As for the spectral calculations the results are presented as follows, which are split into two groups: the non-transition elements (diamond, graphite, LiF, and silicon) and the transition elements (rutile, monoclinic ZrO_2 and hexagonal and orthorhombic ZrO).

9.1.1 Non-transition Elements

As shown in Figure 9.1, the EELS of diamond using the independent particle approximation and simulated with NC PBE (YAMBO) and US PBE (CASTEP) are very similar, concerning the position and the shape of the peaks. The US PBE peak is higher than the NC PBE peak, which could potentially be caused by the different pseudopotentials, the different broadening schemes, or the different methods used to calculate the loss function. The LDA IP is worse than the PBE IP as it further shifts the major plasmon peak to the right, which deviates from the experimental spectrum. As expected, no significant change is seen by adding the LFE to either LDA or PBE, as the system is homogeneous.

For graphite, the EELS simulated using US PBE and NC PBE as shown in Figure 9.2 are also very similar. A broadened plasmon peak at higher energy

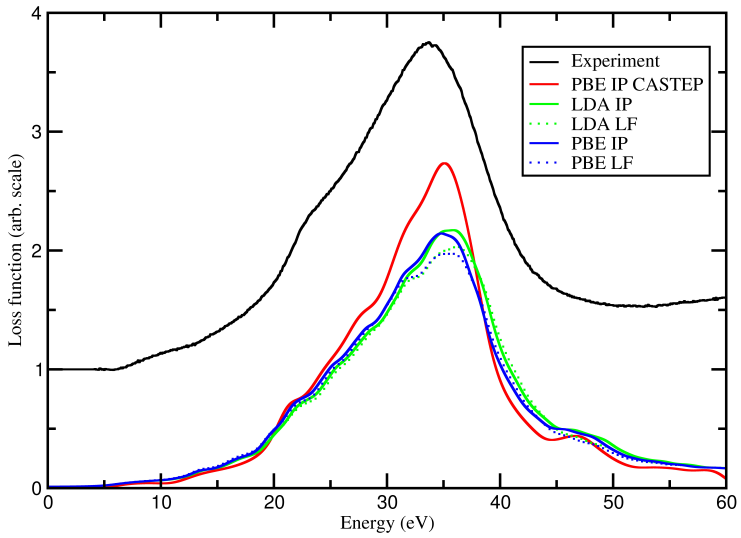


Figure 9.1: Calculated EELS of diamond using PBE IP (Red), LDA IP (Green-solid), LDA LF (Green-dotted), PBE IP (Blue-solid) and PBE LF (Blue-dotted), where IP represents the independent particle approximation while LF corresponds to including the LFE. The experimental spectrum (Black) is the same as the one shown in Figure 8.7 [179].

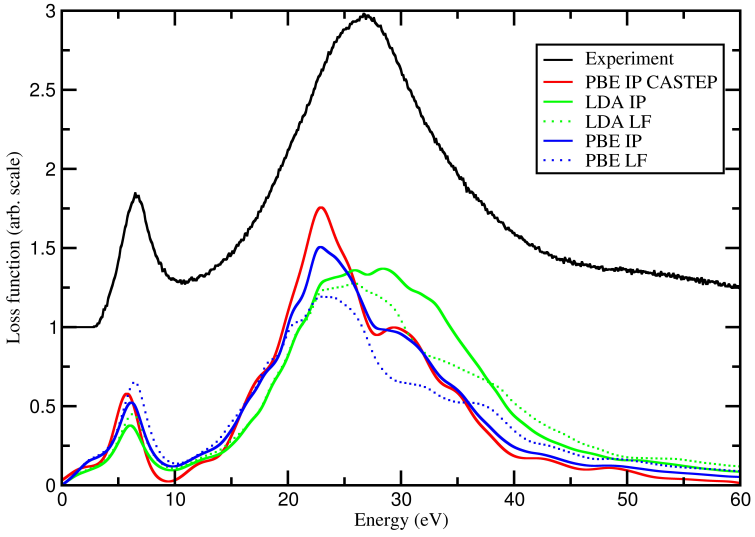


Figure 9.2: Calculated EELS of graphite using PBE IP CASTEP (Red), LDA IP (Green-solid), LDA LF (Green-dotted), PBE IP (Blue-solid) and PBE LF (Blue-dotted). The experimental spectrum (Black) is the same as the one shown in Figure 8.8 [178].

is seen in the NC LDA spectrum, which is closer to the experimental one. The fact that LDA tends to produce a better spectrum is caused by the difference in the geometry optimised structures used. The inter-atomic distance between the graphite layer predicted by LDA is closer to the experimental value, which results in different predicted band structures and EELS. This difference in the predicted spectra using the two types of pseudopotentials indicates a strong dependence of the spectrum features of graphite on the layer separation. When including the LFE, a larger difference is seen for graphite than diamond as the system is less homogeneous.

For both LiF and silicon, similar spectra are simulated using US PBE pseudopotential and NC PBE pseudopotential except for the intensity difference. For LiF, the LDA functional predicts better plasmon energy of the main peak than PBE. As for the LFE, no significant difference in the positions of the prominent peak is seen while there is a drastic decrease in the intensity of the peak, which agrees with the result from Reference [182]. The results are in agreement with the fact that both materials are homogeneous and the inclusion of LFE should only have a minor effect on the simulated spectra.

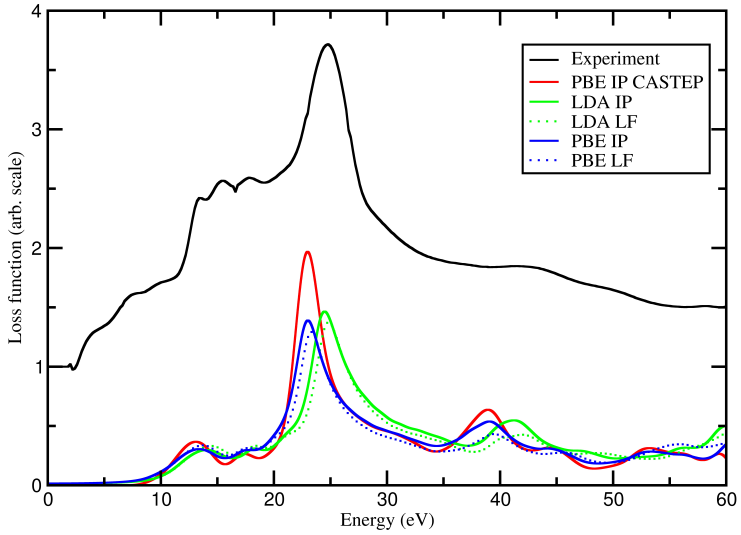


Figure 9.3: Calculated EELS of LiF using PBE IP CASTEP (Red), LDA IP (Green-solid), LDA LF (Green-dotted), PBE IP (Blue-solid) and PBE LF (Blue-dotted). The experimental spectrum (Black) is the same as the one shown in Figure 8.9 [180].

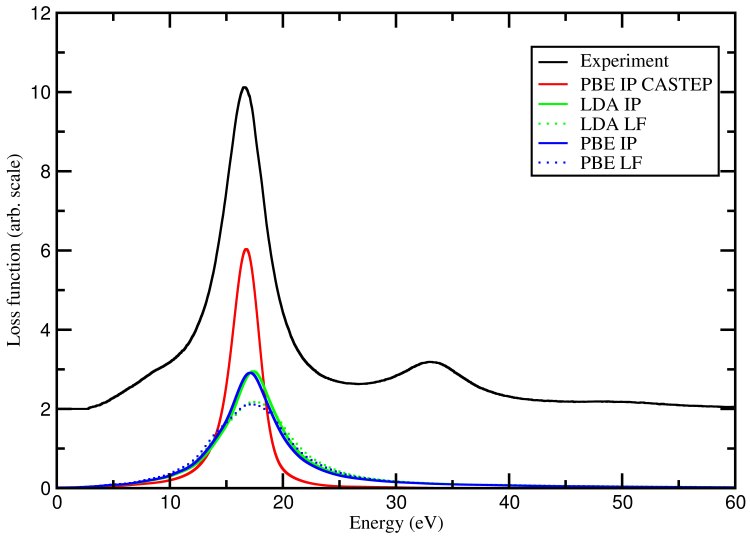


Figure 9.4: Calculated EELS of silicon using PBE IP CASTEP (Red), LDA IP (Green-solid), LDA LF (Green-dotted), PBE IP (Blue-solid) and PBE LF (Blue-dotted). The experimental spectrum (Black) is the same as the one shown in Figure 8.10 [178].

9.1.2 Transition Elements

Previous studies have suggested that for the low-loss EELS, it is vital to include the LFE with materials that involve transition elements (zirconia in reference [62], rutile in reference [63], and zirconia and rutile in reference [123]). Comparable findings are observed in this thesis. As shown in Figure 9.5 for rutile and Figure 9.6 for monoclinic ZrO_2, involving the LFE slightly increases the intensity of the valence plasmon peak and the collective excitation at around 25 eV. The most significant improvement is for the transition peaks in the semi-core region of the EEL spectrum. The peak heights are reduced and the line shapes are changed, and the peaks are shifted to higher frequencies which are in agreement with the experimental spectra. Similar results are also seen with hexagonal and orthorhombic ZrO structures. The results suggest that to accurately model the high energy range of the low-loss EEL spectrum where the transitions from the localised semi-core states are involved, and the inclusion of LFE is vital.

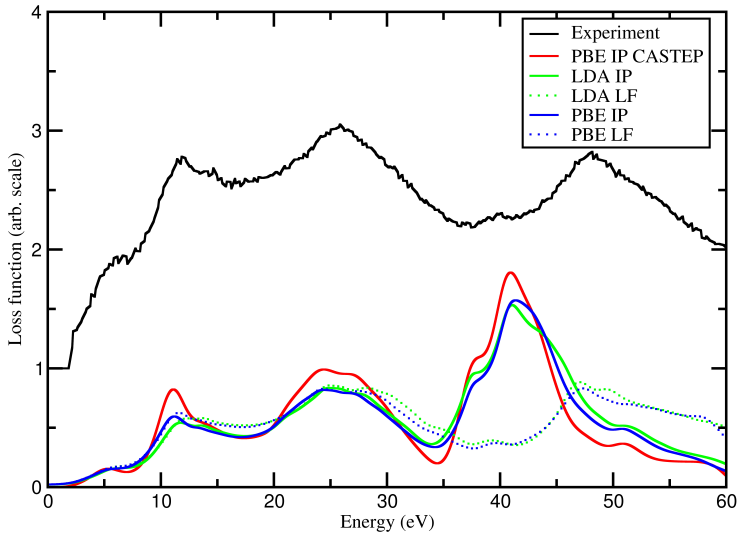


Figure 9.5: Calculated EELS of rutile using PBE IP CASTEP (Red), LDA IP (Green-solid), LDA LF (Green-dotted), PBE IP (Blue-solid) and PBE LF (Blue-dotted). The experimental spectrum (Black) is the same as the one shown in Figure 8.11 [178].

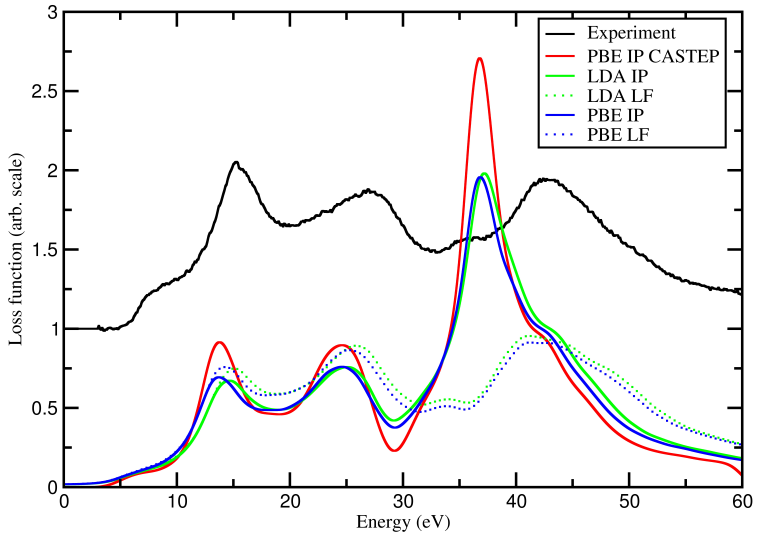


Figure 9.6: Calculated EELS of monoclinic ZrO_2 using PBE IP CASTEP (Red), LDA IP (Green-solid), LDA LF (Green-dotted), PBE IP (Blue-solid) and PBE LF (Blue-dotted). The experimental spectrum (Black) is the same as the one shown in Figure 8.13 [178].

9.2 Low-loss with TDDFT

Including the LFE has made some improvements to the computationally modelled spectra of systems that are inhomogeneous. It also has drastic effects on the simulated semi-core peaks which lie in the higher energy range of the low-loss EEL spectrum for materials that are composed of transition elements. However, there are still some discrepancies in the positions and the shapes of the peaks between the experimental and simulated spectra. By including the LFE, we have taken variation of the Hartree potential into account while the microscopic polarisability χ^0 is still independent. It means that the induced electrons and holes are independent and have no effects on the polarisability. If the exchange and correlation effects in the response are not neglected, the density-response function χ appears which takes the form:

$$\chi = (1 - \chi^0 v - \chi^0 f_{xc})^{-1} \chi^0 \tag{9.5}$$

where f_{xc} is the exchange and correlation kernel which is the functional derivative of the time-dependent exchange and correlation potential with respect to the time-dependent density. In this section, the results obtained within time-dependent DFT in the adiabatic local density approximation (ALDA) are presented.

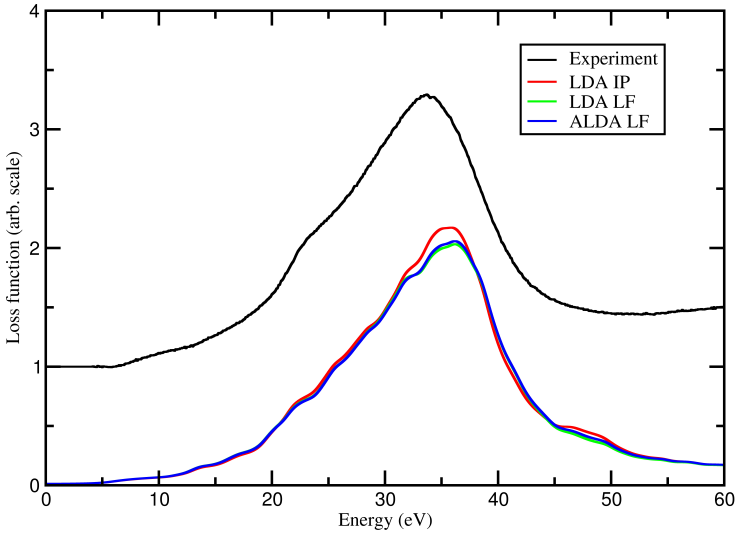


Figure 9.7: Calculated EELS of diamond using LDA IP (Red), LDA LF (Green) and ALDA LF (Blue). The experimental spectrum (Black) is the same as the one shown in Figure 8.7 [179].

As shown in Figure 9.7, the inclusion of the exchange and correlation kernel has only a minor effect on the simulated spectrum of diamond. The same phenomena are also observed with graphite and silicon. As for LiF, by using ALDA the valence plasmon peak exhibits a small shift towards lower frequencies which actually worsens the simulated spectrum. More visible effects are seen with rutile and hexagonal ZrO as shown in Figure 9.9 and 9.10. The valence plasmon peak and the collective excitation peak at around 25 eV are still unaffected by the addition

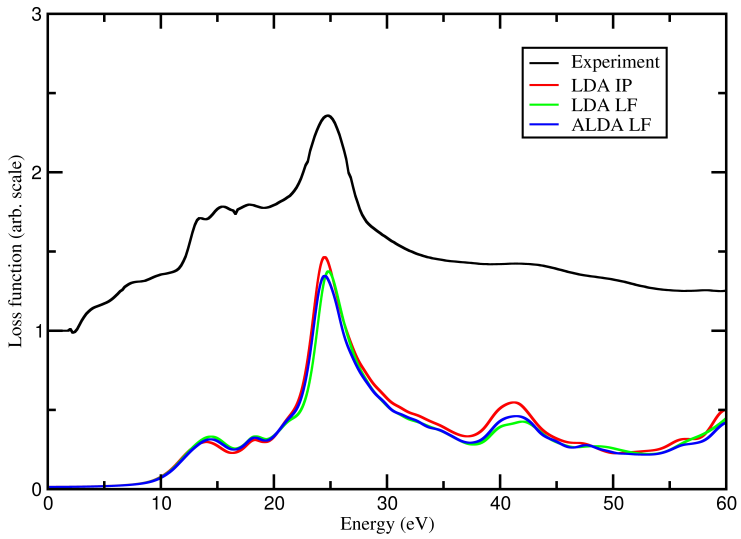


Figure 9.8: Calculated EELS of LiF using LDA IP (Red), LDA LF (Green) and ALDA LF (Blue). The experimental spectrum (Black) is the same as the one shown in Figure 8.9 [180].

of the kernel, whereas there is an increase in intensity for the transition peak at higher energy for both materials. However, similar trends are not seen in either monoclinic ZrO_2 (Figure 9.11) or orthorhombic ZrO for which the spectra look almost identical. In conclusion, TDDFT does not have much impact on the simulated spectrum of RPA and in some occasions, it even produces less agreement with the experiment in terms of the position of the peaks.

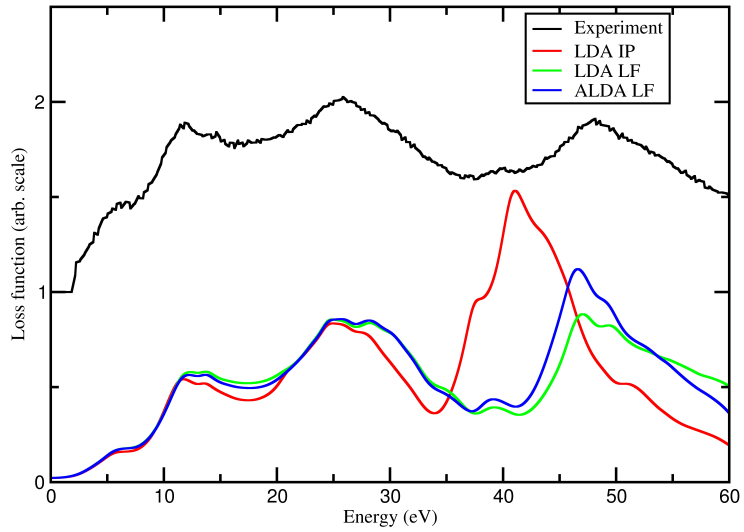


Figure 9.9: Calculated EELS of rutile using LDA IP (Red), LDA LF (Green) and ALDA LF (Blue). The experimental spectrum (Black) is the same as the one shown in Figure 8.11 [178].

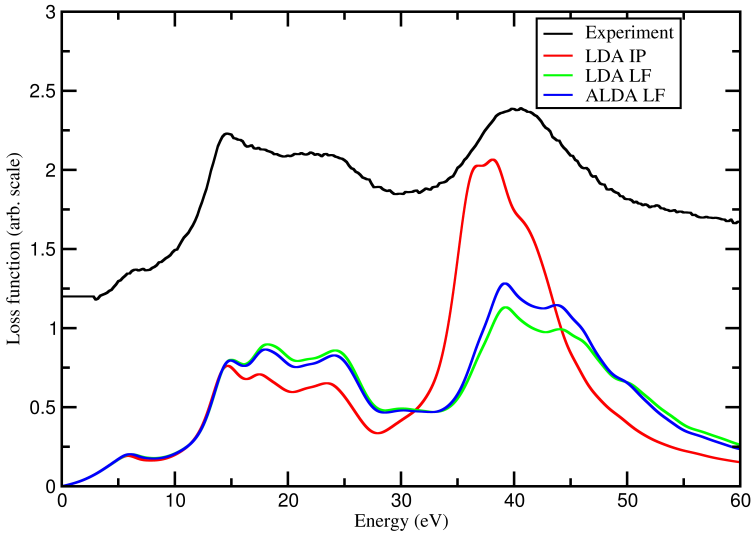


Figure 9.10: Calculated EELS of hexagonal ZrO using LDA IP (Red), LDA LF (Green) and ALDA LF (Blue). The experimental spectrum (Black) is the same as the one shown in Figure 8.15 [18].

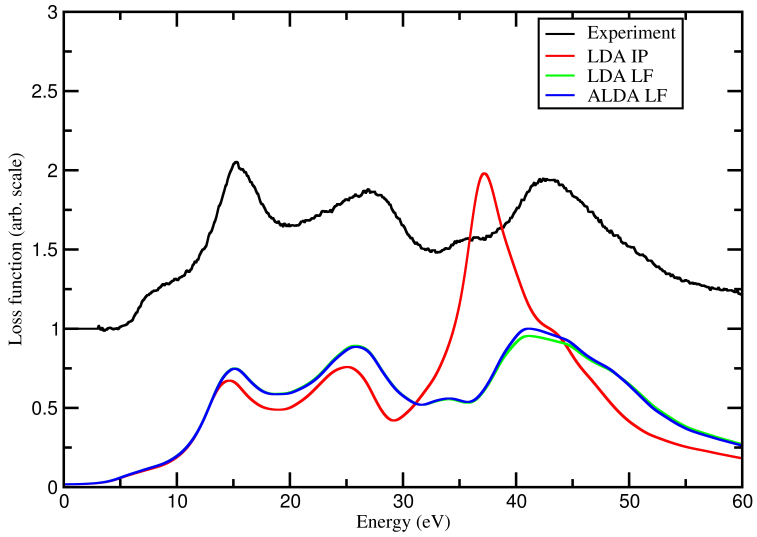


Figure 9.11: Calculated EELS of monoclinic ZrO_2 using LDA IP (Red), LDA LF (Green) and ALDA LF (Blue). The experimental spectrum (Black) is the same as the one shown in Figure 8.13 [178].

9.3 Low-loss EELS with GW + RPA

Structure	PBE	TB	RSCAN	LDA	GW(LDA)	Expt.
Diamond	4.13	4.88	4.37	4.23	5.53	5.48
LiF	8.84	12.44	10.33	9.76	14.56	14.20
Silicon	0.63	1.12	0.78	0.46	1.11	1.17
Rutile	1.87	2.14	2.21	1.88	3.53	3.00
ZrO_2 Monoclinic	3.64	4.59	4.17	3.74	5.63	5.30

Table 9.1: Calculated band gaps of the candidate structures. The PBE, TB, RSCAN, and experimental results are the same as the ones from Table 8.2. The GW approximations are calculated on top of LDA.

The major limitation of DFT is that it is a ground-state theory and thus is intrinsically not necessarily suitable for any excited states properties. The next level of approximation is the GW method which is based on the single-particle Green's function that describes the propagation of a particle that enters an electronic system. The GW approximation is currently the state-of-the-art method for predictive calculations of the band gaps and many other excited state prop-

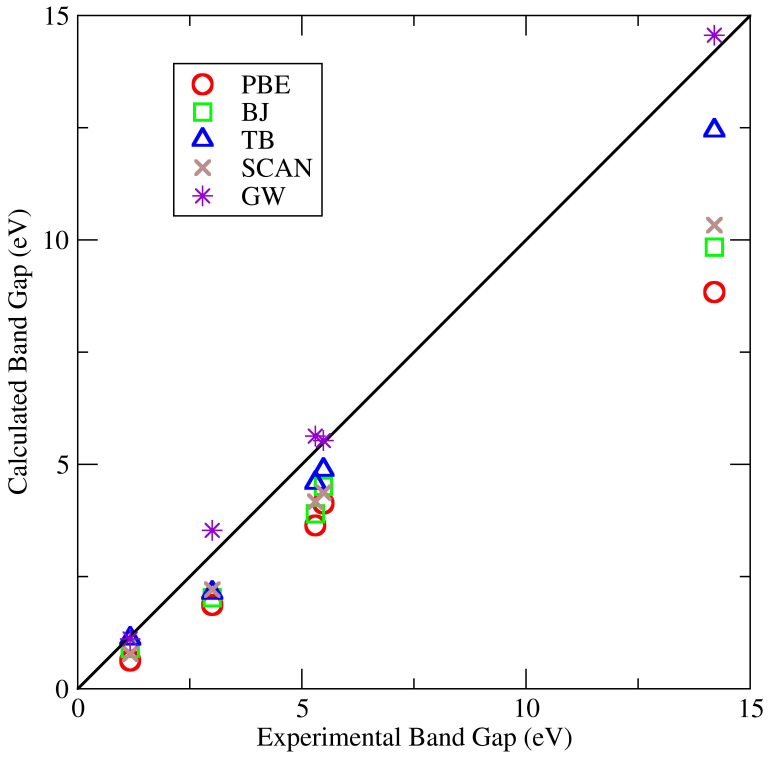


Figure 9.12: The band gaps of selected semiconductors and insulators from LDA (Green), PBE (Red), TB (Blue) RSCAN (Brown) and GW (Purple) are plotted against the experimental values (Black) using the data in Table 9.1

erties.

To begin with, we make a comparison of the band gaps predicted with DFT and with GW. As shown in Table 9.1 and Figure 9.12, the best-predicted band gap results are given by GW approximation, which slightly overestimates the experimental values. Compared to the best results given within the DFT functionals using the TB functional, significant improvement can be seen with the GW approximation. More accurate prediction of band gaps indicates that the GW method is better at dealing with excited state properties, which should also be able to predict better EELS. However, this is not the case as shown in Figure 9.13, 9.14, 9.15 and 9.16. The simulation of EELS of monoclinic ZrO_2 using the GW approximation and RPA is beyond the computational resources available

which will be further discussed in a later section.

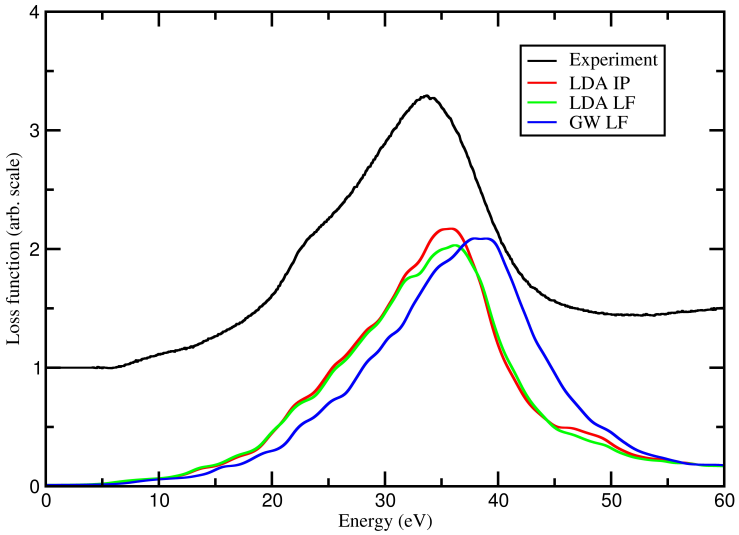


Figure 9.13: Calculated EELS of diamond using LDA IP (Red), LDA LF (Green) and GW LF (Blue). The experimental spectrum (Black) is the same as the one shown in Figure 8.7 [179].

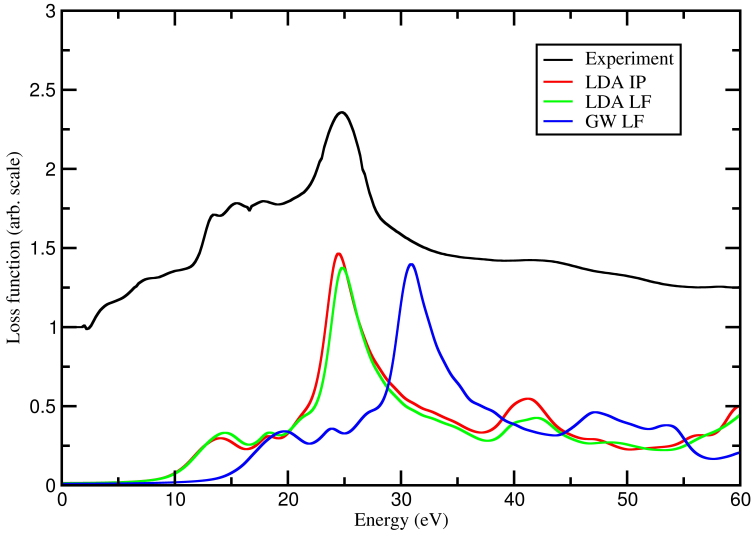


Figure 9.14: Calculated EELS of LiF using LDA IP (Red), LDA LF (Green) and GW LF (Blue). The experimental spectrum (Black) is the same as the one shown in Figure 8.9 [180].

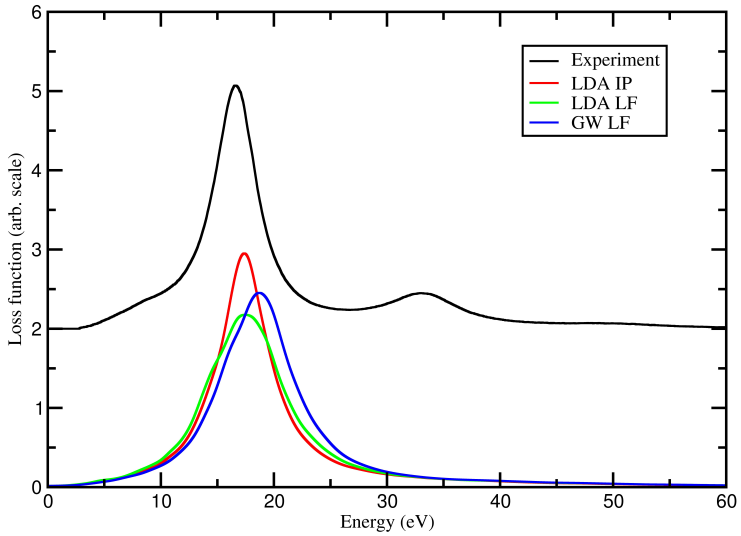


Figure 9.15: Calculated EELS of silicon using LDA IP (Red), LDA LF (Green) and GW LF (Blue). The experimental spectrum (Black) is the same as the one shown in Figure 8.10 [178].

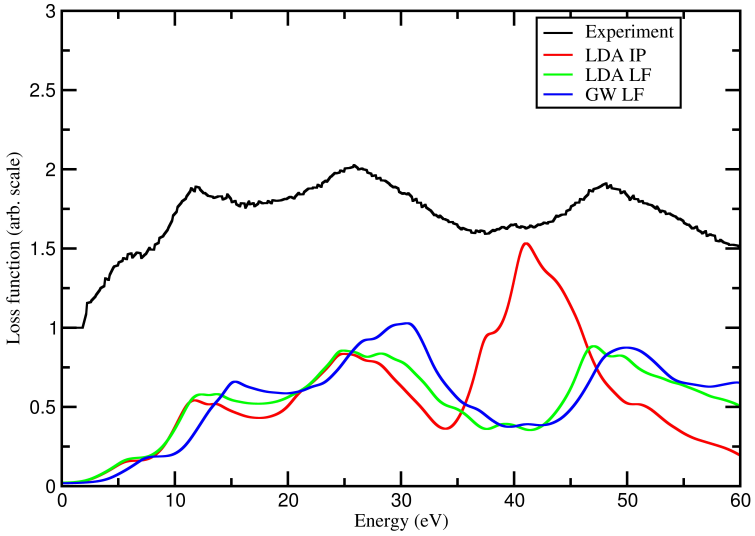


Figure 9.16: Calculated EELS of rutile using LDA IP (Red), LDA LF (Green) and GW LF (Blue). The experimental spectrum (Black) is the same as the one shown in Figure 8.11 [180].

Compared to the standard DFT+RPA calculations, the GW+RPA calculations replace the DFT eigenvalues with the quasi-particle energies which are the true excitation energies. However, the major effect to the simulated spectra by applying the GW corrections is an almost rigid shift of the DFT+RPA spectra towards higher energy, with minor modifications to the spectrum features. Compared to the experimental spectra, the positions of the peaks of the simulated spectra using the GW approximations are worse than those of the DFT+RPA spectra. This is because in both GW+RPA and DFT+RPA calculations, the propagations of electrons and holes are independent. In reality, when an electron is excited to the conduction state, it is attracted by the hole that it left behind in the valence state , and the two form a bound state known as the exciton. The attraction shifts the plasmon peak towards lower energy. On the other hand, DFT severely underestimates the band gap which is the separation of the conduction state and the valence state and the better predictions of the positions of the peaks in the simulated EELS are mostly fortuitous.

9.4 Low-loss with GW+BSE

Using only the GW-corrected quasi-particle energies in the simulation of EELS makes the predictions worse. The next step is to include the electron-hole interaction using the Bethe-Salpeter equation (BSE). The macroscopic dielectric function ε_M is computed from the two-particle correlation function of the interacting particles L as described by equation 5.35, which is calculated solving the Bethe-Salpeter equation through the introduction of an effective excitonic Hamiltonian defined as [64, 99]:

$$H^{exc}_{(vc)(v'c')} = \begin{pmatrix} H^{reso}_{(vc)(v'c')} & H^{coupling}_{(vc)(c'v')} \\ -\left[H^{coupling}_{(vc)(c'v')}\right]^* & -\left[H^{reso}_{(vc)(v'c')}\right]^* \end{pmatrix} \tag{9.6}$$

where the diagonal elements H^{reso} and $-\left[H^{reso}\right]^*$ correspond to the resonant part, which contains the valence-to-conduction transitions of positive frequency, and the anti-resonant part, which contains the conduction-to-valence transitions of negative frequency. The off-diagonal matrices $H^{coupling}$ are the coupling terms that describe the mixing of the positive and negative frequency transitions [64, 99, 128, 134]. The results are shown as follows.

9.4.1 Diamond

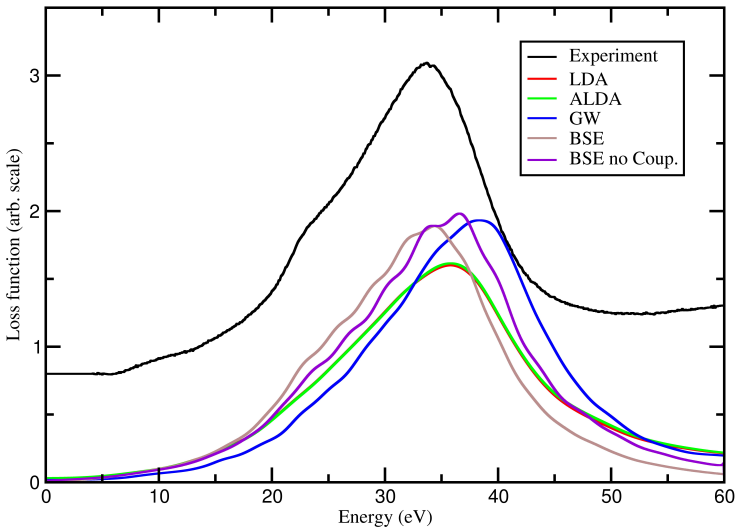


Figure 9.17: Calculated EELS of diamond using LDA (Red), ALDA (Green), GW (Blue), BSE (Brown) and BSE neglecting the coupling terms (Purple). The LFE is included in all the calculation results. The experimental spectrum (Black) is the same as the one shown in Figure 8.7 [179].

As discussed in the previous section, including the many-body effects via the GW approximation while neglecting the electron-hole interactions worsens the simulated EEL spectrum with respect to the DFT+RPA one, regarding the position of the plasmon peak. The inclusion of the excitons introduces fine features to the simulated spectra and shifts the plasmon peak towards lower energy. The coupling terms further shift the peak to the left. As for the position of the plasmon

peak, the best result is given by the GW+BSE method with the coupling terms. However, regarding the line shapes and the fine features such as the plasmon shoulder at 23.6 eV experimentally, it is hard to say if the simulated GW+BSE spectrum improves as several oscillations are observed within the energy range of 20 to 30 eV and it is hard to judge which one corresponds to the experimental plasmon shoulder.

9.4.2 LiF

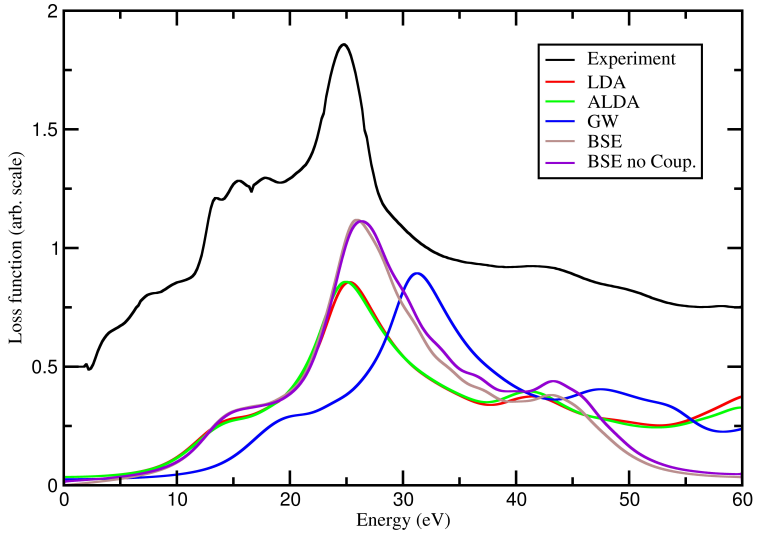


Figure 9.18: Calculated EELS of LiF using LDA (Red), ALDA (Green), GW (Blue), BSE (Brown) and BSE neglecting the coupling terms (Purple). The LFE is included in all the calculation results. The experimental spectrum (Black) is the same as the one shown in Figure 8.9 [180].

As shown in Figure 9.18, including the excitonic effect improves the GW+BSE spectrum. In the case of LiF, no significant change is seen when adding the coupling term. As for the position of the central plasmon peak at 24.8 eV experimentally, the best result is given by the LDA+RPA or ALDA+RPA calculations. However, GW+BSE calculation improves the spectrum with better positions of conduction shoulder at 17.7 eV and plasmon shoulder at 42.2 eV which are seen

experimentally.

9.4.3 Silicon

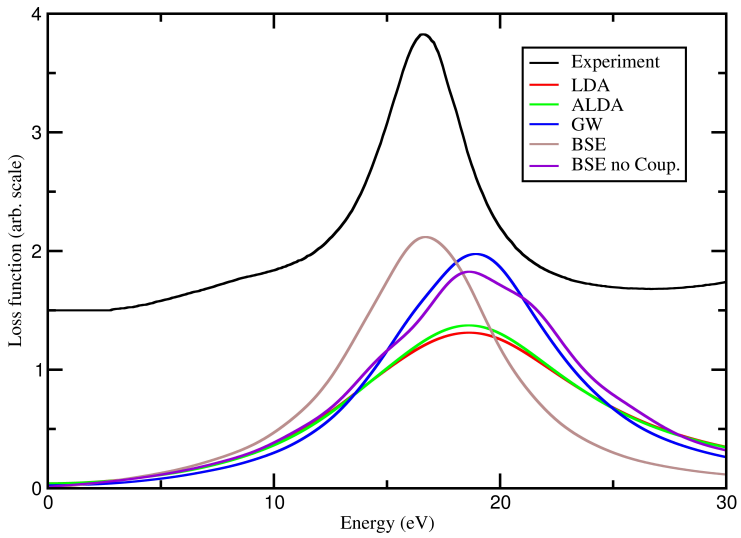


Figure 9.19: Calculated EELS of silicon using LDA (Red), ALDA (Green), GW (Blue), BSE (Brown) and BSE neglecting the coupling terms (Purple). The LFE is included in all the calculation results. The experimental spectrum (Black) is the same as the one shown in Figure 8.10 [178].

The most significant improvement to the simulated EEL spectrum when solving the BSE is seen with silicon as shown in Figure 9.19. For the simulated spectrum including the effects of the electron-hole interaction and the coupling terms, both the position of the plasmon peak and the shape of the line are in best agreement with the experimental spectrum, among all five types of calculations. If the coupling term is neglected, the resulting spectrum does not make any improvement with respect to the GW+RPA spectrum and even worsens regarding the line shape. Thus in the case of silicon, the coupling terms are vital to accurately reproduce the spectrum features. The results agree well with the previous study conducted by Olevano [64].

9.4.4 Rutile

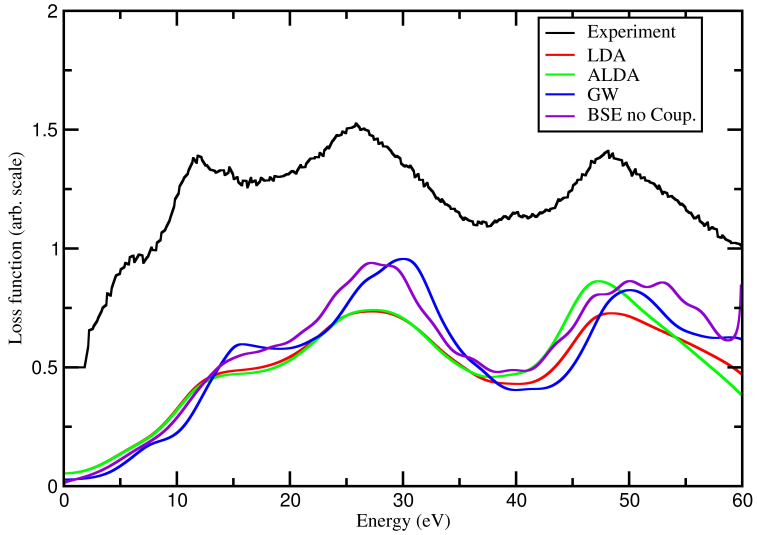


Figure 9.20: Calculated EELS of rutile using LDA (Red), ALDA (Green), GW (Blue) and BSE neglecting the coupling terms (Purple). The LFE is included in all the calculation results. The experimental spectrum (Black) is the same as the one shown in Figure 8.11 [178]. Due to the limitation of computational resources, the BSE without coupling spectrum is only converged up to 50 eV.

For rutile, due to the limitation of computational resources, which will be discussed further in the next section, only the BSE calculation without the coupling terms is performed and it is converged up to 50 eV. As shown in Figure 9.20, adding the electron-hole interaction does improve the spectrum with respect to the GW calculations regarding the position of the plasmon peaks. Compared to the the LDA+RPA or the ALDA+RPA spectra, the BSE spectrum improves in the positions of the plasmon peak at 25.9 eV and the transition peak at 48.3 eV experimentally. However, a less sharper plasmon peak (or more like a shoulder) is seen at 12.2 eV, which is in less good agreement with the experimental spectrum with respect to the LDA+RPA or the ALDA+RPA spectra.

9.5 Costs of Calculations

In this section, we make a comparison of the relative costs of different methods and discuss why certain calculations are beyond the current limit of the computational capabilities. For calculations shown in this chapter, the ground-state calculations were performed with Quantum Espresso [112, 113] while the excited-state calculations and the EELS simulations were done with the YAMBO code [105]. The calculation times listed below are all based on converged parameters.

Band Structure	Time	EELS	Time	Total Time
Ground-State (DFT)*	3min	IP/LF*	3min	6min
		ALDA*	4min	7min
GW*	11h13min	GW+RPA*	4min	11h17min
		GW + BSE†	9h19min	20h32min
		GW + BSE††	19h36min	30h49min

Table 9.2: Comparison of the calculation time (wall time) of the low-loss EELS of LiF using different methods. The calculations marked with $*$ were ran using the YOUNG cluster supported by the UK Materials and Molecular Modelling Hub using the message-passing interface (MPI) programs and parallelised over 48 processes (except the Ground State calculation in which 24 processes were used). The calculations marked with † used the University of Oxford Advanced Research Computing (ARC) facility [183]. The GW + BSE† corresponds to the GW+BSE calculation without coupling and the calculation was parallelised over 64 processes while the GW + BSE†† represents the GW+BSE calculation including the coupling terms and the calculation was parallelised over 128 processes.

There are two methods used for the band structure calculation: the ground-state calculation using the LDA functional and the GW calculation that runs on top of the ground-state calculation. It is obvious that compared to the ground-state DFT calculations, the GW calculations are much more expensive. Using the GW approximation to obtain the band gaps is much cheaper because the GW corrections only need to be applied to bands corresponding to the top of the valence band and the bottom of the conduction band at a specific k-point. As for the EELS simulation, calculations of the GW corrections for all the k-points are needed, together with all the valence bands and additional empty conduction

bands. This is the reason why the GW calculations of monoclinic ZrO_2 fail when increasing the k-point density to obtain a converged spectrum.

Regarding the calculations of the EELS, there are six methods discussed in this chapter: the independent particle (IP) approximation, the random phase approximation (RPA) which includes the local field (LF) effects, the adiabatic LDA (ALDA) corresponds to the time-dependent DFT, the GW+RPA method, the GW method followed by solving the Bethe-Salpeter equation (BSE) with and without the coupling terms. In YAMBO, the IP and LF calculations are performed simultaneously, which took around 3 minutes in the case of LiF. The ALDA and the RPA calculation using the GW-corrected quasi-particle energies took a similar amount of time. With respect to RPA calculations, the BSE calculations are much more expensive and including the coupling terms take about four times the computational resources than the BSE calculations without the coupling term (as it took doubled the number of processes and took a doubled amount of time). As for the GW+BSE calculation without the coupling term of rutile, the final calculation was parallelised over 360 processes and ran for 3 days 3 hours and 30 minutes to finish and if the coupling term is included, the amount of computational resources required will be incredibly large.

In addition, the random-access memory (RAM) and the storage space required will also be a problem for large BSE calculations. In the case of the GW+BSE calculation without the coupling term of rutile, 6.95 gigabytes of maximum memory is required per core and the job generates files of 5.2 terabytes. Thus regarding the computational resources available at the moment, it is not feasible to run such large calculations.

9.6 Summary

In this chapter, we compared the EELS simulated using the independent particle (IP) approximation with LDA and PBE functionals, the random phase approximation (RPA) which includes the local field (LF) effects with the ground-state DFT (LDA and PBE functionals) and the GW corrected quasi-particle energies, the linear-response theory associated with the time-dependent DFT using the ALDA functional and the Bethe-Salpeter equation (BSE) method with and without the coupling terms. Within the IP approximation, similar results are given by LDA and PBE functionals, which agree well with the experimental spectra except for the transition peak in the higher energy range of materials with *d*-state electrons. Previous studies [62, 63, 123] have suggested that incorporating local field effects (LFE) can significantly enhance the modelling of transition peak features. Our DFT+RPA calculations support this, demonstrating that including LFE is essential for accurately simulating the EELS of materials with *d*-state electrons. Regarding the TDDFT, we have shown that using the ALDA functional generates similar EELS compared to the DFT+RPA spectra, and the relative costs of calculations are also similar.

GW corrections significantly improve the predicted band gaps. However, if GW-corrected quasi-particle energies are used in the RPA calculations, the EELS simulated presents an almost rigid shift of the DFT+RPA spectra towards higher energy, with minor modifications to the spectrum features. Regarding the position of the plasmon peaks, the GW+RPA calculated spectrum is worse than the DFT+RPA one, which is due to the missing of electron-hole interaction. Applying the BSE method improves the GW+RPA spectrum, in which the coupling terms are important to accurately simulate the spectrum. GW+BSE with the coupling terms produces the best spectrum in the case of silicon, which agrees with what the author stated in reference [64]. However, minor improvements are

seen with respect to the simulated EELS of diamond and LiF and the simulated spectrum is even worse in the case of rutile in which the coupling term is neglected due to computational limitations.

Regarding the costs of calculations, using GW+BSE calculations to simulate EELS is too expensive and sometimes beyond the computational resources available for large systems with minor improvements on the simulated spectra. DFT+RPA and ALDA calculations produce very similar results with similar costs and make significant improvements to the position and shape of peaks in the higher energy range of simulated EELS of materials with transition elements. It is thus recommended that regarding the EELS simulation, DFT+RPA calculations including the local field effects generate accurate results at reasonable computational cost.

Chapter 10

Conclusions

10.1 Summary

Electron Energy Loss (EEL) Spectroscopy is an analytical technique incorporated into a (scanning) transmission electron microscope ((S)TEM), which analyses the energy distribution of electrons that have interacted inelastically with the specimen. There are three regions in an EEL spectrum (EELS) based on the energy range: the zero-loss region, the low-loss region and the core-loss region. To fully interpret experimental EELS, comparing the simulated EELS of known crystal structures is important and thus it is vital to develop a protocol to computationally model EELS. In this thesis, we have focused on improving the simulated low-loss region of EELS, using advanced functionals within the density functional theory (DFT) and methods beyond DFT (e.g. Time-dependent DFT, the GW approximation and the Bethe-Salpeter Equation (BSE)). In addition, we have also applied the EELS simulation technique to better understand the corrosion products of beryllium metal used in the nuclear reactor during which, we have discovered a new approach to model the core-loss spectrum.

The first study in Chapter 6 was aimed at analysing the corrosion products of

beryllium tiles taken from the Joint European Torus (JET) tokamak by comparing the experimental and computationally modelled EELS. Experimentally, two regions of a non-exposed beryllium sample and five regions from three JET samples were examined and the low-loss region, Be K-edge and O K-edge of the core-loss region were analysed. Theoretically, seven candidate structures were selected from the literature and the corresponding EELS were calculated using PBE functional. The experimental EELS of the non-exposed was used as a benchmark to test the accuracy of the modelling results. The results agreed well with the metallic region while there were some differences for the oxide region. Thus it was hard to set the standard as it was unclear if the discrepancies were caused by the limitation of DFT or by an unknown type of oxygen-containing beryllium oxide structure. However, we were able to show that for the JET samples, the main corrosion product was hexagonal or tetragonal BeO, which were computationally predicted to be equally stable, and if hydrogen did retain in the sample, it retained as BeH_2 but not as either polymorph of $Be(OH)_2$.

In Chapter 7 we proposed a new approach to calculate the core-loss region of EELS using the dielectric function, which was commonly used to simulate the low-loss region. The method could potentially be applied to the EELS simulation of elements with semi-core electrons. Using the new approach, we were able to perform all-electron calculations with the cost of conventional pseudopotential approaches, regenerating all the features seen in the simulated spectrum via the conventional pseudopotential core-loss scheme, with both core hole included and not.

In Chapter 8 we performed a systematic study of applying functionals within DFT to the simulation of band structures and EELS. Four functionals were examined: PBE, Becke-Johnson (BJ), Tran-Blaha (TB), and RSCAN functionals. Regarding the band gaps, the best agreement with the experimental values was calcu-

lated using TB functional, followed by RSCAN while for the simulated EELS, no functional gives the best overall performance. In addition, all four functionals failed to correctly reproduce the transition peaks that appeared in the high energy region of low-loss EELS of materials involving transition elements. It is thus suggested that it is worth running TB or RSCAN calculations for better band gap predictions while using PBE for low-loss EELS calculations.

The problem raised at the end of Chapter 8 was solved in Chapter 9 by going beyond the independent particle (IP) approximation adopted in the calculation of the dielectric function that was used for the EELS simulation discussed in Chapter 8. In this chapter, we have studied various methods to simulate EELS by calculating the macroscopic dielectric function: the IP approximation, the random phase approximation (RPA) which includes the local field (LF) effects with ground-state DFT and the GW corrected quasi-particle energies, the linear-response theory adopted in the time-dependent DFT and the BSE method with and without the coupling terms. We concluded that DFT+RPA calculations with the local field effects generate accurate results at a reasonable computational cost.

10.2 Outlook

There are several interesting questions that could be investigated further. The first one is regarding the corrosion product of beryllium and what is the unknown oxygen-containing beryllium oxide structure that is causing the difference in the spectrum. To solve the problem, one plausible approach could be to do an Ab initio Random Structure Searching (AIRSS) to search for new structures that could possibly be present in the Be-O-H system. Since the JET is operating at high temperature and high pressure, there is also a possibility for the existence of unknown high temperature/pressure phases.

The second question is whether using more advanced functional within DFT or methods beyond DFT will improve the core-loss region of simulated EELS if the core hole is taken into consideration. This will be a computationally challenging task because to include the effect of core hole, supercells are needed to minimise the mutual interaction of excited atoms.

The third question is if the simulated EELS of large systems could be further improved by including the coupling terms in the BSE method. With the advancement of computer science, both for computer capabilities and numerical algorithms, this question could potentially be solved in the future.

All in all, we hope that the work present in this thesis has demonstrated the capability of simulating EELS to assist experimental studies and the results can be used as a reliable protocol to select the suitable method to fulfill different simulation requirements.

Bibliography

[1] F Hofer, F P Schmidt, W Grogger, and G Kothleitner. Fundamentals of electron energy-loss spectroscopy. *IOP Conference Series: Materials Science and Engineering*, 109:012007, 2016.

[2] Ray Egerton. *Electron Energy-Loss Spectroscopy in the Electron Microscope*. Springer, 3rd ed. edition, 2011.

[3] P. Rez, J. Bruley, P. Brohan, M. Payne, and L. A.J. Garvie. Review of methods for calculating near edge structure. *Ultramicroscopy*, 59:159–167, 7 1995.

[4] C. Barry Carter and David B. Williams. Transmission electron microscopy: Diffraction, imaging, and spectrometry. *Transmission Electron Microscopy: Diffraction, Imaging, and Spectrometry*, pages 1–518, 8 2016.

[5] V. J. Keast. An introduction to the calculation of valence eels: Quantum mechanical methods for bulk solids. *Micron*, 44:93–100, 1 2013.

[6] Frank De Groot. Multiplet effects in x-ray spectroscopy. *Coordination Chemistry Reviews*, 249:31–63, 1 2005.

[7] G. Van Der Laan and B. T. Thole. Strong magnetic x-ray dichroism in 2p absorption spectra of 3d transition-metal ions. *Physical Review B*, 43:13401, 6 1991.

[8] B. T. Thole, G. Van Der Laan, J. C. Fuggle, G. A. Sawatzky, R. C. Karnatak, and J. M. Esteva. 3d x-ray-absarption lines and the 3d9 4fn+1 multiplets of the lanthanides. *Physical Review B*, 32:5107, 10 1985.

[9] John J Rehr, Joshua J Kas, Fernando D Vila, Micah P Prange, and Kevin Jorissen. Parameter-free calculations of x-ray spectra with feff9. *Physical Chemistry Chemical Physics*, 12:5503–5513, 5 2010.

[10] M. S. Moreno, S. Lazar, H. W. Zandbergen, and R. F. Egerton. Accuracy of the calculated unoccupied states in gan phases as tested by high-resolution electron energy-loss spectroscopy. *Physical Review B - Condensed Matter and Materials Physics*, 73:073308, 2 2006.

[11] John J. Rehr, Joshua J. Kas, Micah P. Prange, Adam P. Sorini, Yoshinari Takimoto, and Fernando Vila. Ab initio theory and calculations of x-ray spectra. *Comptes Rendus Physique*, 10:548–559, 7 2009.

[12] J. J. Rehr and R. C. Albers. Theoretical approaches to x-ray absorption fine structure. *Reviews of Modern Physics*, 72:621, 7 2000.

[13] Shang Peng Gao, Jun Jiang, Minghe Cao, Jing Zhu, and Jun Yuan. Unoccupied electronic states in cab6 studied by density functional theory and eels measurements. *Physical Review B - Condensed Matter and Materials Physics*, 69:214419, 6 2004.

[14] Shang Peng Gao, Aihua Zhang, Jing Zhu, and Jun Yuan. Anisotropic spectroscopy of nitrogen k-edge in group-iii nitrides. *Applied Physics Letters*, 84:2784–2786, 4 2004.

[15] C. Elsasser and S. Kostlmeier. Density-functional modelling of core-hole effects in electron energy-loss near-edge spectra. *Ultramicroscopy*, 86:325–337, 2 2001.

[16] D. N. Jayawardane, Chris J. Pickard, L. M. Brown, and M. C. Payne. Cubic boron nitride: Experimental and theoretical energy-loss near-edge structure. *Physical Review B*, 64:115107, 8 2001.

[17] Shang Peng Gao, Chris J. Pickard, Mike C. Payne, Jing Zhu, and Jun Yuan. Theory of core-hole effects in 1s core-level spectroscopy of the first-row elements. *Physical Review B - Condensed Matter and Materials Physics*, 77:115122, 3 2008.

[18] Rebecca J. Nicholls, Na Ni, Sergio Lozano-Perez, Andrew London, David W. McComb, Peter D. Nellist, Chris R M Grovenor, Chris J. Pickard, and Jonathan R. Yates. Crystal structure of the zro phase at zirconium/zirconium oxide interfaces. *Advanced Engineering Materials*, 17:211–215, 2015.

[19] David B. Williams and C. Barry Carter. *Transmission electron microscopy: A textbook for materials science.* 2009.

[20] Jordan A. Hachtel, Andrew R. Lupini, and Juan Carlos Idrobo. Exploring the capabilities of monochromated electron energy loss spectroscopy in the infrared regime. *Scientific Reports 2018 8:1*, 8:1–10, 4 2018.

[21] Ondrej L. Krivanek, Tracy C. Lovejoy, Niklas Dellby, and R. W. Carpenter. Monochromated stem with a 30 mev-wide, atom-sized electron probe. *Microscopy*, 62:3–21, 2 2013.

[22] Ondrej L. Krivanek, Tracy C. Lovejoy, Niklas Dellby, Toshihiro Aoki, R. W. Carpenter, Peter Rez, Emmanuel Soignard, Jiangtao Zhu, Philip E. Batson, Maureen J. Lagos, Ray F. Egerton, and Peter A. Crozier. Vibrational spectroscopy in the electron microscope. *Nature*, 514:209–212, 10 2014.

[23] R J Nicholls. Advances in modelling electron energy loss spectra from first principles. *Journal of Physics: Materials*, 4:024008, 3 2021.

[24] R. F. Egerton. Electron energy-loss spectroscopy in the tem. *Reports on Progress in Physics*, 72, 2009.

[25] Ludwig Reimer and Helmut Kohl. *Transmission Electron Microscopy Physics of Image Formation*, volume 51. Springer, 5th ed. edition, 2008.

[26] R. de L. Kronig. On the theory of dispersion of x-rays. *JOSA, Vol. 12, Issue 6, pp. 547-557*, 12:547–557, 6 1926.

[27] Duncan T L Alexander, Peter A Crozier, and James R Anderson. Brown carbon spheres in east asian outflow and their optical properties. *Science (New York, N.Y.)*, 321:833–6, 8 2008.

[28] J M Thomas, B G Williams, and T G Sparrow. Electron-energy-loss spectroscopy and the study of solids. *Acc. Chem. Res*, pages 324–330, 1985.

[29] T G Sparrow, B G Williams, J M Thomas, W Jones, P J Herley, and D A Jefferson. Plasmon spectroscopy as an ultrasensitive microchemical tool. *Journal of the Chemical Society-Chemical Communications*, pages 1432–1434, 1983.

[30] William Jones, Timothy G Sparrow, Brian G Williams, and Patrick J Herley. Evidence for the formation of single crystals of sodium metal during the decomposition of sodium aluminum hydride: an electron microscopic study. *Materials Letters*, 2:377–379, 1984.

[31] Brian G. Williams. Electron energy-loss spectroscopy. *Progress in Solid State Chemistry*, 17:87–143, 1987.

[32] Heinz Raether. Excitation of plasmons and interband transitions by electrons. *Springer Tracts in Modern Physics*, 88:4–13, 1980.

[33] Michael Isaacson. Interaction of 25 kev electrons with the nucleic acid bases, adenine, thymine, and uracil. *The Journal of Chemical Physics*, 56:1803–

1812, 1972.

[34] Ann-Lenaig Hamon, Jo Verbeeck, Dominique Schryvers, Jan Benedikt, and Richard M.C.M. van de Sanden. Elnes study of carbon k-edge spectra of plasma deposited carbon films. *Journal of Materials Chemistry*, 14:2030, 2004.

[35] Peter Atkin and Julio Paula. *Physical chemistry*. Oxford University Press, 8th ed. edition, 2006.

[36] R D Leapman and V E Cosslett. Extended fine structure above the x-ray edge in electron energy loss spectra. *Journal of Physics D: Applied Physics*, 9, 1976.

[37] Gatan. Digitalmicrograph eels analysis user's guide. *Gatan, Inc.*, 6 2003.

[38] Kayleigh L.Y. Fung, Michael W. Fay, Sean M. Collins, Demie M. Kepaptsoglou, Stephen T. Skowron, Quentin M. Ramasse, and Andrei N. Khlobystov. Accurate eels background subtraction - an adaptable method in matlab. *Ultramicroscopy*, 217, 10 2020.

[39] R.F. Egerton, B.G. Williams, and T.G. Sparrow. Fourier deconvolution of electron energy-loss spectra. *Proceedings of the Royal Society of London. A. Mathematical and Physical Sciences*, 398:395–404, 4 1985.

[40] R. F. Egerton and Z. L. Wang. Plural-scattering deconvolution of electron energy-loss spectra recorded with an angle-limiting aperture. *Ultramicroscopy*, 32:137–147, 2 1990.

[41] Frank M.F. de Groot, Hebatalla Elnaggar, Federica Frati, Ru pan Wang, Mario U. Delgado-Jaime, Michel van Veenendaal, Javier Fernandez-Rodriguez, Maurits W. Haverkort, Robert J. Green, Gerrit van der Laan, Yaroslav Kvashnin, Atsushi Hariki, Hidekazu Ikeno, Harry Ramanantoanina, Claude Daul, Bernard Delley, Michael Odelius, Marcus Lundberg,

Oliver Kuhn, Sergey I. Bokarev, Eric Shirley, John Vinson, Keith Gilmore, Mauro Stener, Giovanna Fronzoni, Piero Decleva, Peter Kruger, Marius Retegan, Yves Joly, Christian Vorwerk, Claudia Draxl, John Rehr, and Arata Tanaka. 2p x-ray absorption spectroscopy of 3d transition metal systems. *Journal of Electron Spectroscopy and Related Phenomena*, 249:147061, 5 2021.

[42] F. M.F. De Groot, J. C. Fuggle, B. T. Thole, and G. A. Sawatzky. 2p x-ray absorption of 3d transition-metal compounds: An atomic multiplet description including the crystal field. *Physical Review B*, 42:5459, 9 1990.

[43] Javier Fernández-Rodríguez, Brian Toby, and Michel Van Veenendaal. Xclaim: A graphical interface for the calculation of core-hole spectroscopies. *Journal of Electron Spectroscopy and Related Phenomena*, 202:81–88, 7 2015.

[44] M. W. Haverkort, G. Sangiovanni, P. Hansmann, A. Toschi, Y. Lu, and S. Macke. Bands, resonances, edge singularities and excitons in core level spectroscopy investigated within the dynamical mean-field theory. *Europhysics Letters*, 108:57004, 12 2014.

[45] W. G. Waddington, P. Rez, I. P. Grant, and C. J. Humphreys. White lines in the l23 electron-energy-loss and x-ray absorption spectra of 3d transition metals. *Physical Review B*, 34:1467, 8 1986.

[46] K. Jorissen, J. J. Rehr, and J. Verbeeck. Multiple scattering calculations of relativistic electron energy loss spectra. *Physical Review B - Condensed Matter and Materials Physics*, 81:155108, 4 2010.

[47] M. S. Moreno, K. Jorissen, and J. J. Rehr. Practical aspects of electron energy-loss spectroscopy (eels) calculations using feff8. *Micron*, 38:1–11, 1 2007.

[48] Stewart J Clark, Matthew D Segall, Chris J Pickard, Phil J Hasnip, Matt IJ Probert, Keith Refson, and Mike C Payne. First principles methods using castep. *Zeitschrift fuer Kristallographie*, 220:567–570, 2005.

[49] C. Hébert. Practical aspects of running the wien2k code for electron spectroscopy. *Micron*, 38:12–28, 2007.

[50] Peter Blaha, Karlheinz Schwarz, Fabien Tran, Robert Laskowski, Georg K.H. Madsen, and Laurence D. Marks. Wien2k: An apw+lo program for calculating the properties of solids. *Journal of Chemical Physics*, 152:74101, 2 2020.

[51] V. Milman, K. Refson, S. J. Clark, C. J. Pickard, J. R. Yates, S. P. Gao, P. J. Hasnip, M. I.J. Probert, A. Perlov, and M. D. Segall. Electron and vibrational spectroscopies using dft, plane waves and pseudopotentials: Castep implementation. *Journal of Molecular Structure: THEOCHEM*, 954:22–35, 8 2010.

[52] Teruyasu Mizoguchi, Isao Tanaka, Masato Yoshiya, Fumiyasu Oba, Kazuyoshi Ogasawara, and Hirohiko Adachi. Core-hole effects on theoretical electron-energy-loss near-edge structure and near-edge x-ray absorption fine structure of mgo. *Physical Review B*, 61:2180, 1 2000.

[53] K. Lie, R. Hoier, and R. Brydson. Theoretical site- and symmetry-resolved density of states and experimental eels near-edge spectra of alb2 and tib2. *Physical Review B*, 61:1786, 1 2000.

[54] S. D. Mo and W. Y. Ching. Ab initio calculation of the core-hole effect in the electron energy-loss near-edge structure. *Physical Review B*, 62:7901, 9 2000.

[55] Stefan Nufer, Thomas Gemming, Christian Elsässer, Sibylle Köstlmeier, and Manfred Rühle. Core-hole effect in the elnes of α-al2o3: experiment

and theory. *Ultramicroscopy*, 86:339–342, 2 2001.

[56] K. Van Benthem, C. Elsässer, and M. Rühle. Core-hole effects on the elnes of absorption edges in srtio3. *Ultramicroscopy*, 96:509–522, 9 2003.

[57] Francesco Mauri and Roberto Car. First-principles study of excitonic self-trapping in diamond. *Physical Review Letters*, 75:3166, 10 1995.

[58] Peter Rez, Jose R. Alvarez, and Chris Pickard. Calculation of near edge structure. *Ultramicroscopy*, 78:175–183, 6 1999.

[59] A. T. Paxton, A. J. Craven, J. M. Gregg, and D. W. McComb. Bandstructure approach to near edge structure. *Journal of microscopy*, 210:35–44, 4 2003.

[60] Z. L. Wang. Valence electron excitations and plasmon oscillations in thin films, surfaces, interfaces and small particles. *Micron*, 27:265–299, 6 1996.

[61] V. J. Keast, K. Birt, C. T. Koch, S. Supansomboon, and M. B. Cortie. The role of plasmons and interband transitions in the color of aual2, auin2, and auga2. *Applied Physics Letters*, 99:111908, 9 2011.

[62] L. K. Dash, Nathalie Vast, Philippe Baranek, Marie Claude Cheynet, and Lucia Reining. Electronic structure and electron energy-loss spectroscopy of zro2 zirconia. *Physical Review B - Condensed Matter and Materials Physics*, 70:1–17, 12 2004.

[63] Nathalie Vast, Lucia Reining, Valerio Olevano, Peter Schattschneider, and Bernard Jouffrey. Local field effects in the electron energy loss spectra of rutile tio2. *Physical Review Letters*, 88:4, 2002.

[64] Valerio Olevano and Lucia Reining. Excitonic effects on the silicon plasmon resonance. *Physical Review Letters*, 86:5962, 6 2001.

[65] Axel D. Becke and Erin R. Johnson. A simple effective potential for exchange. *The Journal of Chemical Physics*, 124:221101, 2006.

[66] Fabien Tran and Peter Blaha. Accurate band gaps of semiconductors and insulators with a semilocal exchange-correlation potential. *Physical Review Letters*, 102, 2009.

[67] Jianwei Sun, Adrienn Ruzsinszky, and Johnp Perdew. Strongly constrained and appropriately normed semilocal density functional. *Physical Review Letters*, 115:036402, 7 2015.

[68] Jianwei Sun, Richard C. Remsing, Yubo Zhang, Zhaoru Sun, Adrienn Ruzsinszky, Haowei Peng, Zenghui Yang, Arpita Paul, Umesh Waghmare, Xifan Wu, Michael L. Klein, and John P. Perdew. Accurate first-principles structures and energies of diversely bonded systems from an efficient density functional. *Nature Chemistry 2016 8:9*, 8:831–836, 6 2016.

[69] Pedro Borlido, Thorsten Aull, Ahmad W. Huran, Fabien Tran, Miguel A.L. Marques, and Silvana Botti. Large-scale benchmark of exchange-correlation functionals for the determination of electronic band gaps of solids. *Journal of Chemical Theory and Computation*, 15:5069–5079, 9 2019.

[70] J. C. Slater. A simplification of the hartree-fock method. *Physical Review*, 81:385, 2 1951.

[71] J. P. Perdew and Alex Zunger. Self-interaction correction to density-functional approximations for many-electron systems. *Physical Review B*, 23:5048–5079, 1981.

[72] John P. Perdew, Kieron Burke, and Matthias Ernzerhof. Generalized gradient approximation made simple. *Physical Review Letters*, 77:3865–3868, 10 1996.

[73] Albert P. Bartók and Jonathan R. Yates. Regularized scan functional. *The Journal of Chemical Physics*, 150:161101, 4 2019.

[74] Feliciano Giustino. *Materials modelling using density functional theory : properties and predictions*. Oxford University Press, 2014.

[75] Richard M Martin. *Electronic Structure: Basic Theory and Practical Methods*. Cambridge University Press, 2004.

[76] Richard M. Martin, Lucia Reining, and David M. Ceperley. *Interacting electrons : theory and computational approaches*. Cambridge University Press, 5 2016.

[77] P. Hohenberg and W. Kohn. Inhomogeneous electron gas. *Phys. Rev.*, 136:B864–B871, 1964.

[78] Marina Rucsandra Filip. Electronic excitations and rational design of novel light sensitisers for photovoltaics. *Thesis*, 2015.

[79] J. C. Slater. The theory of complex spectra. *Physical Review*, 34:1293, 11 1929.

[80] Eugen Merzbacher. *Quantum Mechanics*. Wiley, 3rd edition, 1998.

[81] John David Jackson. *Classical Electrodynamics*. Wiley, 3rd edition, 1998.

[82] W. Kohn and L. J. Sham. Self-consistent equations including exchange and correlation effects. *Physical Review*, 140, 1965.

[83] Charles Kittel. Introduction to solid state physics. *Solid State Physics*, page 703, 2005.

[84] D M Ceperley and B J Alder. Ground state of the electron gas by a stochastic model. *Phys. Rev. Lett.*, 45:566–569, 1980.

[85] Mermin and Ashcroft. *Solid State Physics*. Saunders College Publishing, 1976.

[86] Aron J. Cohen, Paula Mori-Sánchez, and Weitao Yang. Challenges for density functional theory. *Chemical Reviews*, 112:289–320, 1 2012.

[87] Dal Corso A, Pasquarello, Baldereschi, and Car. Generalized-gradient approximations to density-functional theory: A comparative study for atoms and solids. *Physical review. B, Condensed matter*, 53:1180–1185, 1 1996.

[88] V. Fock. Näherungsmethode zur lösung des quantenmechanischen mehrkörperproblems. *Zeitschrift für Physik 1930 61:1*, 61:126–148, 1 1930.

[89] T. W. Hollins, S. J. Clark, K. Refson, and N. I. Gidopoulos. Optimized effective potential using the hylleraas variational method. *Physical Review B - Condensed Matter and Materials Physics*, 85:235126, 6 2012.

[90] Fabien Tran, Peter Blaha, and Karlheinz Schwarz. How close are the slater and becke-roussel potentials in solids? *Journal of Chemical Theory and Computation*, 11:4717–4726, 8 2015.

[91] A. D. Becke and M. R. Roussel. Exchange holes in inhomogeneous systems: A coordinate-space model. *Physical Review A*, 39:3761, 4 1989.

[92] Albert P. Bartók and Jonathan R. Yates. Ultrasoft pseudopotentials with kinetic energy density support: Implementing the tran-blaha potential. *Physical Review B*, 99:235103, 6 2019.

[93] Tomáš Rauch, Miguel A.L. Marques, and Silvana Botti. Local modified becke-johnson exchange-correlation potential for interfaces, surfaces, and two-dimensional materials. *Journal of Chemical Theory and Computation*, 16:2654–2660, 4 2020.

[94] Eric B. Isaacs and Chris Wolverton. Performance of the strongly constrained and appropriately normed density functional for solid-state materials. *Physical Review Materials*, 2:063801, 6 2018.

[95] S Baroni and R Resta. Ab initio calculation of the low-frequency raman cross section in silicon. *Physical Review B*, 33, 1986.

[96] M. A. L. Marques, C. A. Ullrich, F. Nogueira, A. Rubio K., and E. K. U. Gross. *Time-Dependent Density Functional Theory*, volume 706. Springer, 2006.

[97] Silvana Botti, Arno Schindlmayr, Rodolfo Del Sole, and Lucia Reining. Time-dependent density-functional theory for extended systems. *Reports on Progress in Physics*, 70:357–407, 2007.

[98] Carsten A. Ullrich and Zeng hui Yang. A brief compendium of time-dependent density functional theory. *Brazilian Journal of Physics*, 44:154–188, 2 2014.

[99] Francesco Sottile. Response functions of semiconductors and insulators: from the bethe-salpeter equation to time-dependent density functional theory. *Thesis*, 2003.

[100] L. J. Sham and M. Schluter. Density-functional theory of the energy gap. *Physical Review Letters*, 51:1888, 11 1983.

[101] Dorothea Golze, Marc Dvorak, and Patrick Rinke. The gw compendium: A practical guide to theoretical photoemission spectroscopy. *Frontiers in Chemistry*, 7:377, 7 2019.

[102] Giovanni Onida, Lucia Reining, and Angel Rubio. Electronic excitations: density-functional versus many-body green's-function approaches. *Reviews of Modern Physics*, 74:601, 6 2002.

[103] Lars Hedin and Stig Lundqvist. Effects of electron-electron and electron-phonon interactions on the one-electron states of solids. *Solid State Physics - Advances in Research and Applications*, 23:1–181, 1 1969.

[104] F Aryasetiawan and O Gunnarsson. The gw method. *Reports on Progress in Physics*, 61:237, 3 1998.

[105] Andrea Marini, Conor Hogan, Myrta Grüning, and Daniele Varsano. yambo: An ab initio tool for excited state calculations. *Computer Physics Communications*, 180:1392–1403, 8 2009.

[106] Lars Hedin. New method for calculating the one-particle green's function with application to the electron-gas problem. *Physical Review*, 139:A796, 8 1965.

[107] C. Friedrich and A. Schindlmayr. *Many-Body Perturbation Theory: The GW Approximation*, volume 31. 2006.

[108] B. Holm and U. von Barth. Fully self-consistent gw self-energy of the electron gas. *Physical Review B*, 57:2108, 1 1998.

[109] P. García-González and R. W. Godby. Self-consistent calculation of total energies of the electron gas using many-body perturbation theory. *Physical Review B*, 63:075112, 1 2001.

[110] Wolf Dieter Schöne and Adolfo G. Eguiluz. Self-consistent calculations of quasiparticle states in metals and semiconductors. *Physical Review Letters*, 81:1662, 8 1998.

[111] Wei Ku and Adolfo G. Eguiluz. Band-gap problem in semiconductors revisited: Effects of core states and many-body self-consistency. *Physical Review Letters*, 89:126401, 8 2002.

[112] Paolo Giannozzi, Stefano Baroni, Nicola Bonini, Matteo Calandra, Roberto Car, Carlo Cavazzoni, Davide Ceresoli, Guido L. Chiarotti, Matteo Cococcioni, Ismaila Dabo, Andrea Dal Corso, Stefano De Gironcoli, Stefano Fabris, Guido Fratesi, Ralph Gebauer, Uwe Gerstmann, Christos Gougoussis, Anton Kokalj, Michele Lazzeri, Layla Martin-Samos, Nicola Marzari, Francesco Mauri, Riccardo Mazzarello, Stefano Paolini, Alfredo Pasquarello, Lorenzo Paulatto, Carlo Sbraccia, Sandro Scandolo, Gabriele Sclauzero, Ari P. Seitsonen, Alexander Smogunov, Paolo Umari, and Renata M. Wentzcovitch. Quantum espresso: a modular and open-source software project for quantum simulations of materials. *Journal of physics. Condensed matter : an Institute of Physics journal*, 21, 2009.

[113] P. Giannozzi, O. Andreussi, T. Brumme, O. Bunau, M. Buongiorno Nardelli, M. Calandra, R. Car, C. Cavazzoni, D. Ceresoli, M. Cococcioni, N. Colonna, I. Carnimeo, A. Dal Corso, S. De Gironcoli, P. Delugas, R. A. Distasio, A. Ferretti, A. Floris, G. Fratesi, G. Fugallo, R. Gebauer, U. Gerstmann, F. Giustino, T. Gorni, J. Jia, M. Kawamura, H. Y. Ko, A. Kokalj, E. Kücükbenli, M. Lazzeri, M. Marsili, N. Marzari, F. Mauri, N. L. Nguyen, H. V. Nguyen, A. Otero-De-La-Roza, L. Paulatto, S. Poncé, D. Rocca, R. Sabatini, B. Santra, M. Schlipf, A. P. Seitsonen, A. Smogunov, I. Timrov, T. Thonhauser, P. Umari, N. Vast, X. Wu, and S. Baroni. Advanced capabilities for materials modelling with quantum espresso. *Journal of physics. Condensed matter : an Institute of Physics journal*, 29, 10 2017.

[114] C J Pickard. Ab initio electron energy loss spectroscopy. *Thesis*, 9 1997.

[115] D. R. Hamann, M. Schlüter, and C. Chiang. Norm-conserving pseudopotentials. *Physical Review Letters*, 43:1494, 11 1979.

[116] David Vanderbilt. Soft self-consistent pseudopotentials in a generalized eigenvalue formalism. *Physical Review B*, 41:7892, 4 1990.

[117] Chris G. Van De Walle and P. E. Blöchl. First-principles calculations of hyperfine parameters. *Physical Review B*, 47:4244, 2 1993.

[118] R. W. Godby and R. J. Needs. Metal-insulator transition in kohn-sham theory and quasiparticle theory. *Physical Review Letters*, 62:1169, 3 1989.

[119] Tonatiuh Rangel, Mauro Del Ben, Daniele Varsano, Gabriel Antonius, Fabien Bruneval, Felipe H Da Jornada, Michiel J Van Setten, Okan K Orhan, David D O'regan, Andrew Canning, Andrea Ferretti, Andrea Marini, Gian-Marco Rignanese, Jack Deslippe, Steven G Louie, and Jeffrey B Neaton. Reproducibility in g0w0 calculations for solids. *Computer Physics Communications*, 255:107242, 2020.

[120] R J Nicholls, A J Morris, C J Pickard, and J R Yates. Optados - a new tool for eels calculations. *Journal of Physics: Conference Series*, 371:012062, 7 2012.

[121] Andrew J. Morris, Rebecca J. Nicholls, Chris J. Pickard, and Jonathan R. Yates. Optados: A tool for obtaining density of states, core-level and optical spectra from electronic structure codes. *Computer Physics Communications*, 185:1477–1485, 5 2014.

[122] H. Ehrenreich and M. H. Cohen. Self-consistent field approach to the many-electron problem. *Physical Review*, 115:786, 8 1959.

[123] Francesco Sottile, Fabien Bruneval, A. G. Marinopoulos, L. K. Dash, Silvana Botti, Valerio Olevano, Nathalie Vast, Angel Rubio, and Lucia Reining. Tddft from molecules to solids: The role of long-range interactions. *International Journal of Quantum Chemistry*, 102:684–701, 1 2005.

[124] Stephen L. Adler. Quantum theory of the dielectric constant in real solids. *Physical Review*, 126:413, 4 1962.

[125] Nathan Wiser. Dielectric constant with local field effects included. *Physical Review*, 129:62, 1 1963.

[126] D. Sangalli, A. Ferretti, H. Miranda, C. Attaccalite, I. Marri, E. Cannuccia, P. Melo, M. Marsili, F. Paleari, A. Marrazzo, G. Prandini, P. Bonfà, M. O. Atambo, F. Affinito, M. Palummo, A. Molina-Sánchez, C. Hogan, M. Grüning, D. Varsano, and A. Marini. Many-body perturbation theory calculations using the yambo code. *Journal of Physics: Condensed Matter*, 31:325902, 5 2019.

[127] Giovanni Bussi. Effects of the electron-hole interaction on the optical properties of materials: The bethe-salpeter equation. *Physica Scripta T*, T109:141–151, 1 2004.

[128] Stefan Albrecht, Lucia Reining, Rodolfo Del Sole, and Giovanni Onida. Ab initio calculation of excitonic effects in the optical spectra of semiconductors. *Physical Review Letters*, 80:4510, 5 1998.

[129] Lorin X. Benedict, Eric L. Shirley, and Robert B. Bohn. Theory of optical absorption in diamond, si, ge, and gaas. *Physical Review B*, 57:R9385, 4 1998.

[130] F. Bechstedt, K. Tenelsen, B. Adolph, and R. Del Sole. Compensation of dynamical quasiparticle and vertex corrections in optical spectra. *Physical Review Letters*, 78:1528, 2 1997.

[131] Pierluigi Cudazzo and Lucia Reining. Correlation satellites in optical and loss spectra. *Physical Review Research*, 2:012032, 2 2020.

[132] W. Hanke. Dielectric theory of elementary excitations in crystals. *Advances in Physics*, 27:287–341, 1978.

[133] Albrecht Stefan. Optical absorption spectra of semiconductors and insulators: ab initio calculations of many-body effects. *Thesis*, 1999.

[134] Xavier Blase, Ivan Duchemin, Denis Jacquemin, and Pierre-Franc Ois Loos. The bethe-salpeter equation formalism: From physics to chemistry. *J. Phys. Chem. Lett*, 11:7371–7382, 2020.

[135] R. O. Jones and O. Gunnarsson. The density functional formalism, its applications and prospects. *Reviews of Modern Physics*, 61:689, 7 1989.

[136] Carlo Massobrio, Alfredo Pasquarello, and Roberto Car. First principles study of photoelectron spectra of cu clusters. *Physical Review Letters*, 75:2104, 9 1995.

[137] Zheng-Ling Wang, Yin Jian-Ping, Carlos A P Bengaly, Roy Maartens, Mario G Santos, A T Paxton, M Van Schilfgaarde, M Mackenzie, and A J Craven. The near-edge structure in energy-loss spectroscopy: many-electron and magnetic effects in transition metal nitrides and carbides. *Journal of Physics: Condensed Matter*, 12:729, 2 2000.

[138] Teruyasu Mizoguchi, Isao Tanaka, Shang-Peng Gao, and Chris J Pickard. First-principles calculation of spectral features, chemical shift and absolute threshold of elnes and xanes using a plane wave pseudopotential method. *Journal of Physics: Condensed Matter*, 21:104204, 3 2009.

[139] Jorge E. Müller and John W. Wilkins. Band-structure approach to the x-ray spectra of metals. *Physical Review B*, 29:4331, 4 1984.

[140] John C. Fuggle and John E. Inglesfield, editors. *Unoccupied Electronic States*, volume 69. Springer, 1992.

[141] Yoyo Hinuma, Giovanni Pizzi, Yu Kumagai, Fumiyasu Oba, and Isao Tanaka. Band structure diagram paths based on crystallography. *Computational Materials Science*, 128:140–184, 2 2017.

[142] D R Hamann. Optimized norm-conserving vanderbilt pseudopotentials. *Physical Review B*, 88:85117, 2013.

[143] Carmen Makepeace. Fuel retention in plasma facing materials of the jet iter-like wall. *Thesis*, 2021.

[144] James Michael Beal. Erosion, deposition and material migration in the jet divertor with carbon and iter-like walls. *Thesis*, 2016.

[145] K. Heinola, A. Widdowson, J. Likonen, E. Alves, A. Baron-Wiechec, N. Barradas, S. Brezinsek, N. Catarino, P. Coad, S. Koivuranta, G.F. Matthews, M. Mayer, and P. Petersson. Fuel retention in jet iter-like wall from post-mortem analysis. *Journal of Nuclear Materials*, 463:961–965, 8 2015.

[146] D.E. Dombrowski, E.B. Deksnis, and M.A. Pick. Thermomechanical properties of beryllium. *Atomic and plasma-material interaction data for fusion*, 1994.

[147] J. Roth, R. Doerner, M. Baldwin, T. Dittmar, H. Xu, K. Sugiyama, M. Reinelt, Ch. Linsmeier, and M. Oberkofler. Oxidation of beryllium and exposure of beryllium oxide to deuterium plasmas in pisces b. *Journal of Nuclear Materials*, 438:S1044–S1047, 7 2013.

[148] C. Makepeace, C. Pardanaud, P. Roubin, I. Borodkina, C. Ayres, P. Coad, A. Baron-Wiechec, I. Jepu, K. Heinola, A. Widdowson, S. Lozano-Perez, and J.E.T. Contributors. The effect of beryllium oxide on retention in jet iter-like wall tiles. *Nuclear Materials and Energy*, 19:346–351, 5 2019.

[149] K. Schmid, M. Baldwin, and R. Doerner. Modeling of beryllium deposition from a beryllium-seeded deuterium plasma. *Journal of Applied Physics*, 97:064912, 3 2005.

[150] V.M. Sharapov, V.Kh. Alimov, and L.E. Gavrilov. Deuterium accumulation in beryllium oxide layer exposed to deuterium atoms. *Journal of Nuclear Materials*, 258-263:803–807, 10 1998.

[151] M. Mayer. Codeposition of deuterium with beo at elevated temperatures. *Journal of Nuclear Materials*, 240:164–167, 1 1997.

[152] Rion A Causey and David S Walsh. Codeposition of deuterium with beryllium. *Journal of Nuclear Materials*, 254:84–86, 3 1998.

[153] S. Zalkind, M. Polak, and N. Shamir. Effects of preadsorbed hydrogen on the adsorption of o2, co and h2o on beryllium. *Surface Science*, 539:81–90, 8 2003.

[154] G. Bergerhoff and I. D. Brown. Inorganic crystal structure database. *Acta Crystallographica Section A Foundations of Crystallography*, 37, 1981.

[155] R. A. Belyaev, Yu I. Danilov, and S. A. Furaev. Corrosion of beryllium oxide products of extended length in high-moisture vapor streams communication 2. *Soviet Atomic Energy*, 27:1360–1362, 12 1969.

[156] A. L. Ivanovskii, I. R. Shein, Yu. N. Makurin, V. S. Kiiko, and M. A. Gorbunova. Electronic structure and properties of beryllium oxide. *Inorganic Materials*, 45:223–234, 3 2009.

[157] Shoutao Zhang, Fei Li, Haiyang Xu, and Guochun Yang. Pressure-induced stable beryllium peroxide. *Inorganic Chemistry*, 56:5233–5238, 5 2017.

[158] G. J. Brendel, E. M. Marlett, and L. M. Niebylski. Crystalline beryllium hydride. *Inorganic Chemistry*, 17:3589–3592, 12 1978.

[159] Gordon S. Smith, Quintin C. Johnson, Deane K. Smith, D.E. Cox, Robert L. Snyder, Rong-Sheng Zhou, and Allan Zalkin. The crystal and molecular structure of beryllium hydride. *Solid State Communications*, 67:491–494, 8 1988.

[160] Kenneth A. Walsh and Edgar E. Vidal. *Beryllium chemistry and processing*. ASM International, 2009.

[161] IJ Bear and AG Turnbull. The heats of formation of beryllium compounds. i. beryllium hydroxides. *The Journal of Physical Chemistry*, 69:2828–2833, 1965.

[162] D. K. Smith, C. F. Cline, and S. B. Austerman. The crystal structure of β-beryllia. *Acta Crystallographica*, 18:393–397, 1965.

[163] J. Paméla, G. F. Matthews, V. Philipps, and R. Kamendje. An iter-like wall for jet. *Journal of Nuclear Materials*, 363-365:1–11, 6 2007.

[164] A. Baron-Wiechec, A. Widdowson, E. Alves, C. F. Ayres, N. P. Barradas, S. Brezinsek, J. P. Coad, N. Catarino, K. Heinola, J. Likonen, G. F. Matthews, M. Mayer, P. Petersson, M. Rubel, W. Van Renterghem, and I. Uytdenhouwen. Global erosion and deposition patterns in jet with the iter-like wall. *Journal of Nuclear Materials*, 463:157–161, 7 2015.

[165] Philipp Haas, Fabien Tran, and Peter Blaha. Calculation of the lattice constant of solids with semilocal functionals. *Physical Review B - Condensed Matter and Materials Physics*, 79:085104, 2 2009.

[166] Laurids Schimka, Judith Harl, and Georg Kresse. Improved hybrid functional for solids: The hsesol functional. *J. Chem. Phys*, 134:24116, 2011.

[167] Roberto Peverati and Donald G. Truhlar. Performance of the m11-l density functional for bandgaps and lattice constants of unary and binary semiconductors. *The Journal of Chemical Physics*, 136:134704, 4 2012.

[168] Gabor I. Csonka, John P. Perdew, Adrienn Ruzsinszky, Pier H. T. Philipsen, Sebastien Lebegue, Joachim Paier, Oleg A. Vydrov, and Janos G. Angyan. Assessing the performance of recent density functionals for bulk solids. *Physical Review B - Condensed Matter and Materials Physics*, 79, 3 2009.

[169] M. Piacentini, D. W. Lynch, and C. G. Olson. Thermoreflectance of lif between 12 and 30 ev. *Physical Review B*, 13:5530, 6 1976.

[170] Jin Zhang, Artem R Oganov, Xinfeng Li, Huafeng Dong, and Qingfeng Zeng. Novel compounds in the zr-o system, their crystal structures and mechanical properties. *Physical chemistry chemical physics : PCCP*, 17:17301–10, 7 2015.

[171] Anubhav Jain, Shyue Ping Ong, Geoffroy Hautier, Wei Chen, William Davidson Richards, Stephen Dacek, Shreyas Cholia, Dan Gunter, David Skinner, Gerbrand Ceder, and Kristin A. Persson. Commentary: The materials project: A materials genome approach to accelerating materials innovation. *APL Materials*, 1:011002, 7 2013.

[172] Hong Jiang. Band gaps from the tran-blaha modified becke-johnson approach: A systematic investigation. *J. Chem. Phys*, 138:134115, 2013.

[173] J. Pascual, J. Camassel, and H. Mathieu. Resolved quadrupolar transition in tio2. *Physical Review Letters*, 39:1490, 12 1977.

[174] M. Shishkin and G. Kresse. Self-consistent gw calculations for semiconductors and insulators. *Physical Review B - Condensed Matter and Materials Physics*, 75:235102, 6 2007.

[175] David Koller, Fabien Tran, and Peter Blaha. Merits and limits of the modified becke-johnson exchange potential. *Physical Review B - Condensed Matter and Materials Physics*, 83:195134, 5 2011.

[176] David Koller, Fabien Tran, and Peter Blaha. Improving the modified becke-johnson exchange potential. *Physical Review B - Condensed Matter and Materials Physics*, 85:155109, 4 2012.

[177] Neng Ping Wang, Michael Rohlfing, Peter Krüger, and Johannes Pollmann. Quasiparticle band structure and optical spectrum of lif(001). *Physical Review B*, 67:115111, 3 2003.

[178] Philip Ewels, Thierry Sikora, Virginie Serin, Chris P. Ewels, and Luc Lajaunie. A complete overhaul of the electron energy-loss spectroscopy and x-ray absorption spectroscopy database: Eelsdb.eu. *Microscopy and Microanalysis*, 22:717–724, 2 2016.

[179] V. Serin, Eric Beche, R. Berjoan, D. Dorignac, David Rats, Julien Fontaine, Lionel Vandenbulcke, Chantal Germain, and A. Catherinot. Xaes, xps, eels and raman spectroscopy of polycrystalline to amorphous films with various sp2 to sp3 bondings. pages 126–141, 1998.

[180] C. Ahn, O. Krivanek, R. P. Burgner, M. Disko, and P. Swann. *EELS atlas : a reference collection of electron energy loss spectra covering all stable elements*. Gatan, Inc., 1983.

[181] Philip Edward Batson. Current trends for eels studies in physics. *Microscopy Microanalysis Microstructures*, 2:395–402, 4 1991.

[182] Steven G Louie, James R Chelikowsky, and Marvin L Cohen. Local-field effects in the optical spectrum of silicon. *Physical Review Letters*, 34, 1975.

[183] Andrew Richards. University of oxford advanced research computing. 8 2015.